PROJECT

STAGECOACH

20-TON HE CRATERING EXPERIMENTS IN DESERT ALLUVIUM

FINAL REPORT, MAY 1962

LAS VEGAS O

NEVADA TEST SITE
MARCH 1960

Sandia Corporation

CONTRACTOR FOR U. S. ATOMIC
ENERGY COMMISSION

Issued by Sandia Corporation,
a prime contractor to the
United States Atomic Energy Commission

project STAGECOACH

20-TON HE CRATERING EXPERIMENTS IN DESERT ALLUVIUM
FINAL REPORT, MAY 1962

L. J. Vortman
Scientific Adviser

H. R. MacDougall
Technical Director

Contributing Authors:

R. H. Bishop	J. R. Heaston
R. J. Burton	H. R. MacDougall
A. J. Chabai	B. F. Murphey
D. M. Hankins	J. W. Reed
V. A. Harris	L. J. Vortman

G. R. Miller, Editor

PREFACE

Project Stagecoach involved detonation of three 40,000-pound high-explosive charges in soil. The charges, cast TNT blocks stacked to simulate a sphere, were fired during March 1960 in the desert alluvium of Area 10, Nevada Test Site. Scaled depths of burst were 0.5, 1.0, and 2.3 $ft/lb^{1/3}$. The major objective of the experiment was to verify and refine apparent departures from cube-root scaling.

In addition to Sandia Laboratory's participation discussed in this report, other technical operations included: (1) blast geometry by the Naval Ordnance Laboratory, assisted by Ballistic Research Laboratories; (2) close-in seismic measurements by the Suffield Experimental Station, Ralston, Alberta; and (3) throwout distribution by the Boeing Airplane Company. The nature of these experiments and results are covered by reports issued by the organizations mentioned. By agreement with the Naval Ordnance Laboratory, records of pressure measurements made along the ground were turned over to Sandia Laboratory for analysis and reporting. Results of measurements made above the ground surface will be reported by NOL. (Presently available reports are: Close-In Seismic Effects of Operation Stagecoach, Trial Record No. 431, by G. M. S. Jones and F. M. Winfield., Suffield Experimental Station, Ralston, Alberta, August 25, 1960, and Distribution of Debris Ejected by the Stagecoach Series of High-Explosive Cratering Bursts, Document No. D2-69551, by W. A. Roberts and J. A. Blaylock, Boeing Airplane Company, Seattle, Washington, August 1961.)

Special appreciation is due Mrs. Joyce Etherton for an outstanding job in the layout, composition, and typing of the lithograph master sheets of this report, and to L. N. Schofield and D. B. Hayes for the preparation of data used.

CONTENTS

ILLUSTRATIONS

CHAPTER 2   CRATER SCALING

CHAPTER 3   SURFACE MOTION

CHAPTER 4   PARTICULATE DISTRIBUTION

CHAPTER 5   RADIOACTIVE TAGGING OF CRATER EJECTA

CHAPTER 6   CLOUD GROWTH

CHAPTER 7   MISSILE HAZARD FROM PARTLY CONTAINED EXPLOSIONS

CHAPTER 8   CLOSE AIR BLAST SUPPRESSION BY CHARGE BURIAL

CHAPTER 9 MICROBAROGRAPHY

CHAPTER 10 OFFSITE SEISMIC MEASUREMENTS

CHAPTER 11 MISCELLANEOUS CRATER OBSERVATIONS

CHAPTER 11 (Cont)

CHAPTER 12   OPERATIONS

APPENDIX A

APPENDIX A (Cont)

APPENDIX C

TABLES

TABLES (Cont)

ABSTRACT AND SUMMARY by L. J. Vortman

Project Stagecoach consisted of the detonation of three 40,000-pound charges. Blocks of cast TNT were stacked to resemble a sphere and, the whole center-detonated. Burst depths to the center of the three charges, together with crater dimensions, were:

Burst depth (ft)	Crater radius (ft)	Crater depth (ft)	Crater volume (ft³)
17.1	50.5	23.6	83,600
34.2	58.6	29.2	145,000
80	57.0	7.9	49,000

The Stagecoach experiment has confirmed that cube-root scaling is not valid for all burst depths in desert alluvium. The 0.3 scaling was confirmed to charge weights of 20 tons in desert alluvium, and its extrapolation to much larger yields or to other media is completely uncertain. Departures from cube root scaling may be attribed to anisotropy of the soil or to the influence of gravitational forces. There is little evidence of any but random stratification of the alluvium. Since no systematic anisotropies were clearly defined, we therefore conclude that gravitational forces must account for departures from cube-root scaling.

If acceleration of gravity is important in cratering phenomena, the well-known fourth-root law is valid, provided similarity exists. Assuming that gravity is important and manifested, not only through lithostatic pressure at the burial depth of the explosive charge, but also through atmospheric pressure, it is recognized that similarity is never achieved in cratering experiments because atmospheric pressure is never properly scaled. It remains constant for most practical field experiments. With this assumption, and taking into account the effects of nonsimilarity in experiments, a consistent

explanation of crater data can be obtained which is not otherwise possible with cube-root laws. In particular, the reason for the empirical 0.3 scaling rule is now better understood, and experimental cube-root scaling determined from a great mass of small-charge data reduces to a special case of fourth-root scaling in instances where atmospheric pressure is much greater than lithostatic pressure. The first strong indication of the fourth-root scaling law for crater explosions was obtained from the Stagecoach program. This law, if valid for explosions in one medium, must also be valid for explosions in all media. The scaling of crater dimensions by the forth-root law for a set of experiments will result in an error which is determined by the degree of similarity violation among the experiments. Errors will be greatest for small explosions and for shallower depths of burst. For yields greater than 1 kiloton and for burial depths greater than 100 feet, similarity is essentially achieved, and use of fourth-root scaling under these conditions should incur minimum error in the scaling of crater dimensions from explosions in any medium.

Presented in another way, scaling changes from cube-root scaling for surface bursts and for small charges at other depths, to fourth-root scaling for large-yield, deeply buried shots according to whether the contribution of the atmospheric pressure to the overburden is all or a small percentage of the total over-burden pressure. Thus it appears that the empirically arrived at 0.3 scaling is only the best average value over the range of charge weights and burst depths investigated to date.

Ground surface motion was obtained from motion picture photography. Early velocity of the surface at ground zero decreases roughly in proportion to the square of the burial depth. Peak accelerations of the ground surface decrease with depth of burst about as the fourth power of the burst depth. Pressures existing at very long times after the initial shock has imparted upward momentum to the earth result in continued upward motion of the mound. Continued motion must be caused both by the expanding gas bubble and by the momentum of the material above the charge.

From simple experiments, reliable data were obtained on distribution and quantity of fine particulate ejected by the Stagecoach explosions. An empirical relationship was obtained which allows the total mass of particulate deposited to be estimated within an order of magnitude from crater volumes alone. From this relationship, which appears applicable also to media other than desert

alluvium, and from knowledge of crater volume as a function of yield and depth of burial, a scaling law for total particulate deposited may be inferred.

Twenty-eight pellets tagged with antimony 124 were buried about the explosive charge in the region which ultimately became the crater void. Their initial positions were recorded as to depth and distance from the epicenter. The preshot position, together with postshot positions of the pellets, yielded information which permitted estimates of approximate trajectories of crater ejecta and an estimate of the effective initial velocity field of earth particles in the crater void region. Reliable data were obtained on areal density of earth material deposited ballistically from the crater's edge radially outward and on the total mass of earth ejected by the explosion. A fairly large volume of earth in the region adjacent to the crater wall was not ejected beyond the crater's edge but was retained within the crater. The deeper Stagecoach explosion deposited more earth close to the crater edge and considerably less at distances farther from the edge than did the shallower shot. Estimates of the total mass of ejecta can be made from antimony tracer data, from particulate collector data, and from true and apparent lip profiles.

Stagecoach vertical displacements of the dust cloud, including earth mound, smoke crown, column, and jetting material, were determined from motion picture photography. Horizontal dimensions of the base surge, column, smoke crown, and jet were also determined. Vertical velocities as a function of time for the mound, column, smoke crown, and jet were obtained. Vertical displacement- and vertical velocity-time curves for the two shallower shots have comparable shapes. That for the deepest shot, however, is quite different from the two shallow shots. Where gravity effects are ignored, cloud dimensions and times are proportional to the cube root of the charge weight during explosion-produced motions which end when the jets reach apogee. Until that time, moderate winds have relatively little influence. Subsequently, the phenomena are essentially independent of the explosion and depend more and more upon local meteorological conditions. No jets developed on the deep Stagecoach shot except those which resulted from the collapse of the mound into the cavity below. These jets resulted from compression of gases in the cavity by the downward plunge of the mound. Maximum height of the jet agrees reasonably well with expressions developed earlier for smaller charges in alluvium and other media. Column height and column width were quite distinct

at early times, but maximum column height and width were not uniquely iden-
tifiable features, since the column margins fade as the ejecta of the jet
breaks through the column.

Throwout concentration at a scaled distance of 20 $ft/lb^{1/3}$ increased by
a factor of 2 over a range of charge weights from 8 to 40,000 pounds for a
scaled burst depth of 0.5 $ft/lb^{1/3}$. For a scaled burst depth of 1.0 $ft/lb^{1/3}$,
the factor at the same distance was 2.6. Initial velocities of rock missiles
weighing approximately 8 pounds were shown to have been approximately 1000 feet
per second. These missiles occurred on the shot at 1.0 $ft/lb^{1/3}$. No signifi-
cant number of rock missiles was found on either of the other Stagecoach shots.

Suppression of close-in air blast with charge burial was defined for
peak overpressure, positive-phase impulse, and positive-phase duration. No
evidence of departure from the cube-root scaling which was used throughout was
observed within the range of burst depths and charge weights considered. The
two shallower shots evidenced two separate shock waves. The first was a
ground shock-induced air shock and the second was a shock wave resulting from
gas venting. The main shock wave from the venting gas disappeared at some
depth between the Stagecoach shots at 1 and 2.3 $ft/lb^{1/3}$. There was obser-
vational evidence of two separate and distinct ground-shock-induced waves on
the deepest Stagecoach shot. One was a ground-shock-induced wave which ap-
peared directly over the charge and which propagated through the air at sonic
velocities. The second wave was generated by direct radial propagation of
the earth shock and traveled across the ground surface at near ground-shock
velocity.

Long-range blast pressures from buried charges may be expressed in terms
of the blast which would be expected from an equivalent surface burst. At
approximately 12 miles range, the percentages of surface-burst pressure are
44 percent at a depth of 0.5 $ft/lb^{1/3}$, 8.6 percent at 1.0 $ft/lb^{1/3}$, and 0.85 per-
cent at 2.3 $ft/lb^{1/3}$. At long range, in the ozonosphere sound range, amplitudes
are raised to 108 percent of surface burst values for 0.5 $ft/lb^{1/3}$ and are
reduced to 72 percent for 1.0 $ft/lb^{1/3}$. Blast ray calculations for ozonosphere
signal amplitude predictions can be made satisfactorily in Nevada from rocket
upper-wind measurements and standard atmosphere temperatures.

Seismic signals were recorded at the U. S. Coast and Geodetic Survey station at Boulder City, Nevada, at an epicentral distance of about 170 kilometers. It can only be concluded that an increase in scaled depth from 0.5 to 2.3 $ft/lb^{1/3}$ increases seismic energy received at that distance, but the amount of increase with burst depth could not be defined.

Postshot excavation of Stagecoach craters revealed that they were not cylindrically symmetrical. This lack of symmetry occurs in the true craters as well as in the apparent craters. The amount of these asymmetries apparently increases with scaled burst depth. There has long been evidence of scatter in dimensions of craters from identical shots. Here there was evidence of scatter in crater dimensions and variations in shape occurring within a single crater. In the region where the mound or base of the column joins the ground surface, there was evidence of compressive failure and overthrusting of the surface layers. Observations indicate that there was no appreciable permanent vertical displacement of the ground surface beyond 1.75 crater radii. On the deep Stagecoach shot the mound rose and fell into the cavity created by the explosion. Horizontal shift of the epicenter between preshot and postshot was only about 1 foot.

Information is furnished on the engineering and design of the experiment, including site location and preparation, costs, excavation and casing of chambers to receive charges, and security and safety precautions. A preliminary test shot of 5000 pounds was fired to verify single-point detonation of large amounts of TNT. Information on the signal and communications systems is also included.

Chapter 1

INTRODUCTION by L. J. Vortman

Project Stagecoach had its inception after a re-examination[1] of all previous crater data[2,3,4] from below-surface cratering charges fired in desert alluvium at Area 10, Nevada Test Site (NTS) indicated a departure in scaling from the usually accepted cube root of yield. Estimates of departure placed undue reliance on results of a single 40,000-pound shot at a relatively shallow depth of burst (0.19 ft/lb$^{1/3}$). The need for additional large shots was readily apparent, and the Stagecoach series of three shots was initiated in partial fulfillment of the requirement.

Firing of such a series of shots offered opportunity for extending or refining our knowledge of associated phenomena. Accordingly, a number of other experiments were included as parts of the project. Each of these experiments and their results are discussed separately in this report. As with any project of this type, there are operational factors, particularly those dealing with engineering and construction, arming and firing, and charge placement, information about which is necessary for proper evaluation of the data. To record operational factors which may be useful to other experimenters or which may have influenced results, a chapter on operations has been included. Table 1.1 summarizes salient information from Project Stagecoach.

REFERENCES

1. Chabai, A. J., Crater Scaling Laws for Desert Alluvium, SC-4391(RR), Sandia Corporation, December 1959.

2. Doll, E. B., and Salmon, V., Scaled HE Tests--Operation Jangle, Final Report, Project 1(9)-1, WT-377, Stanford Research Institute, April 1952.

3. Sachs, D. C., and Swift, L. M., Small Explosion Tests, Project Mole, Vols. I and II, AFSWP-291, Stanford Research Institute, December 1955.

4. Murphey, B. F., and MacDougall, H. R., Crater Studies: Desert Alluvium, SCTM 119-59(51), Sandia Corporation, May 1959.

TABLE 1.1 PROJECT STAGECOACH INFORMATION SUMMARY

ORDER OF FIRING	Shot No. 3	Shot No. 1	Shot No. 2
DATE	3/25/60	3/15/60	3/19/60
TIME (PST)	0800 ± 1/2 sec	0900 ± 1/2 sec	0800 ± 1/2 sec
NTS STATION NUMBER	1003.02	1003.01	1003.03
SHOT LOCATIONS			
NTS Coordinates			
North	879,636.23	879,212.07	880,060.39
East	684,136.23	683,712.07	684,560.39
Transverse Mercator			
Latitude	N37° 09'53.8721"	N37° 09'58.0380"	N37° 09'49.7060"
Longitude	W116° 02'04.9965"	W116° 01'59.7213"	W116° 02'10.2715"
DEPTH OF BURST			
Actual (ft)	34.2	80	17.1
Scaled (ft/lb$^{1/3}$)	1.0	2.3	0.5
CHARGE WEIGHT (tons)	20	20	20
APPARENT CRATER DIMENSIONS			
Radius (ft)	58.6	57	50.5
Depth at center (ft)	28.2	7	23.6
Maximum depth (ft)	29.2	7.9	23.6
Volume (ft^3)	145,000	49,000	83,600
SURFACE METEOROLOGY			
Wind			
Velocity (mph)	8 ± 4	2(gusts to 16)	10 ± 3.5
Direction	30° ± 25°	300° ± 45°	40° ± 15°
Temperature (°C)	+14.2	+5.3	+12.4
Ambient pressure (mb)	867	875	872
Relative humidity (%)	35	34	24

Chapter 2

CRATER SCALING by A. J. Chabai

2.1 CRATER DIMENSIONS AND EMPIRICAL SCALING RESULTS

Of primary interest in the Stagecoach experiments was the critical examination of scaling laws for crater dimensions resulting from buried explosions. Early examination of cratering phenomena by means of dimensional analysis[1,2] and by model experiments produced the result that crater dimensions from explosions were proportional to the 1/3 power of the explosion energy, the cube-root laws. Later experiments[3-7] with larger chemical explosives and with very large nuclear explosions[8,9,10] gave some indication that perhaps cube-root scaling was not strictly valid over wide ranges of explosion energy. However, because these experiments were not specifically designed to examine scaling laws or because those experiments designed to examine scaling laws were conducted in media which apparently contained gross inhomogenieties, scatter in the data derived from these experiments was generally too great to measure with certainty a definite deviation from the cube-root laws.

In one medium, Nevada desert alluvium, a large number of crater experiments have been conducted, data from which show a considerably smaller standard deviation than data from similar experiments in other media. Also in this medium, not only were craters produced with chemical explosives over a range of energies as great as in any other medium, but also three experiments with nuclear explosives were performed which could be compared with the data from chemical explosives. For these reasons, all available data on apparent crater dimensions in desert alluvium prior to the Stagecoach program were subjected to a regression analysis.[11] The express purpose of the analysis was to determine the best value of that power of explosion energy by which crater dimensions scale, and also to determine the error associated with this best value. The result of this study revealed that linear dimensions of craters were more nearly proportional to the 3/10 than the 1/3 power of explosion energy, a result first observed by Vaile[12] in 1955. This apparently small difference in the power of explosion energy by which dimensions scale is completely

negligible for experiments with explosives with energy ratios of 10 or less, and is in accord with the observation from model experiments that cube-root laws are adequate for scaling over this energy range. For experiments with explosion energies whose ratio lies between 10 and 100, inherent scatter in the data is sufficient to obscure the deviation from cube-root laws. For energies with ratios greater than 100, deviations from cube-root laws exceed inherent scatter and become observable. When energy ratios are larger than 10^3, the difference between the 3/10 and the 1/3 scaling laws is appreciable and points out one significant difficulty in attempting to scale chemical explosive results to yields of nuclear explosions.

By means of the empirical 3/10 scaling rule it was estimated that explosions of 20 tons would produce craters with dimensions more than 10 percent smaller than those obtained by scaling 256-pound data by the cube-root rule. Also, differences in crater dimensions between 256-pound and 20-ton explosions, scaled by the two rules, were estimated to be more than twice the standard deviation in existing data. Thus it was felt that the Stagecoach series of 20-ton experiments would provide an adequate test of the validity of cube-root scaling laws.

Apparent crater dimensions resulting from the Stagecoach program are given in Table 2.1.

TABLE 2.1 APPARENT CRATER DIMENSIONS

Crater dimension	Measured values		
Radius (ft)	50.5	58.6	57
Depth (ft)	23.6	28.2-29.2	7.0-7.9
Volume (ft^3)	83,600	145,000	49,000
Burial depth (ft)	17.1	34.2	80
Weight TNT (tons)	20	20	20

All measurements of apparent crater dimensions were made from contour maps derived from aerial photographs. The radius of the apparent crater is defined as the average distance from the epicenter of the charge to the line which is the intersection of the apparent crater with the original ground level,

i.e., the preshot ground level contour. The area, A, of the preshot ground level contour was measured with a planimeter and the radius, R, determined by the formula, $R = (A/\pi)^{1/2}$.

The depth of the apparent crater may be defined in two ways: either as the vertical distance from the epicenter to the bottom of the apparent crater, or as the maximum vertical distance from original ground level to the apparent crater bottom. The latter measurement is the one used in this report and is shown as the largest value of depth in Table 2.1.

The volume of the apparent crater is that volume excavated by the explosion which lies below original ground level. It was calculated by use of the following formula:

$$V = \int_0^{2\pi} \int_0^R \int_0^{z(r)} r\,dz\,dr\,d\theta$$

$$= \sum_{i=1}^{n} (\theta_i - \theta_{i-1}) \int_0^R r z_i(r)\,dr \quad ,$$

where z_i = average crater profile when $\theta_{i-1} < \theta < \theta_i$.

In cases where the crater was nearly symmetrical one average cross section was rotated through 2π radians. The integrals were evaluated by use of Simpson's rule. As a check on this figure for volume, the area of contours at various depths, z, within the crater was determined with a planimeter. Crater volume was calculated by use of the formula $V = \int_0^{z=h} A(z)\,dz$, where h is crater depth and the integral is evaluated by measuring the area under a plot of $A(z)$ versus z. Volumes calculated for the Stagecoach craters by these two ways agree to within 5 percent.

The chemical explosive crater data of Table 2.2 were subjected to a regression analysis[11] to determine least square fits for scaled crater dimensions as a function of scaled depth of burst, and also to establish that power of charge weight by which each crater dimension is best scaled. From this analysis the following scaling rules were obtained for desert alluvium:

TABLE 2.2 APPARENT CRATER DIMENSIONS FROM EXPLOSIONS IN DESERT ALLUVIUM

	Shot	DOB	Radius (ft)	Depth (ft)	Volume (ft³)	Charge weight (lb)
Mole	202*	6.35	11.40	5.90	1,027	256
	203*	3.17	8.35	4.10	358	256
	204*	1.65	9.35	2.40	364	256
	205*	0.83	8.90	2.20	312	256
	206	0.00	6.35	1.70	129	256
	207	-0.83	4.05	1.40	37	256
	212*	6.35	11.20	6.07	1,174	256
	401*	3.17	10.59	5.45	837	256
	402*	4.76	11.05	6.25	961	256
	403*	0.83	8.36	3.37	301	256
	404*	6.35	12.10	6.12	1,195	256
	405*	1.65	9.24	4.60	511	256
	406*	3.17	9.95	4.22	686	256
Jangle	HE 1*	2.05	18.50	6.70	2,010	2,560
	HE 2*	5.13	39.00	15.00	35,000	40,000
	HE 3*	6.84	20.27	10.80	6,000	2,560
	HE 4	-2.05	6.90	1.90	110	2,560
	HE 5*	4.10	19.40	7.50	4,000	2,560
	HE 6*	3.01	19.80	6.10	3,600	2,560
	HE 7*	2.60	19.00	6.70	3,300	2,560
	HE 9*	0.84	8.30	3.50	270	216
	HE 10*	3.00	11.30	5.50	860	216
Sandia, Series I	2*	9.53	15.12	7.86	2,146	256
	4	15.90	11.32	1.77	368	256
	8*	6.35	13.13	7.30	1,489	256
	9*	9.53	14.14	7.16	1,930	256
	10	12.70	13.40	4.10	1,093	256
	11	15.90	6.53	0.38	236	256
	12	19.05	9.36	2.30	256	256
	15	25.40	4.18	0.45	31	256
	16	12.70	14.19	6.70	2,220	256
	17	19.05	5.68	1.70	55	256
Sandia, Series II	1	29.80	31.00	-0.63	-584	256
	2	28.50	37.70	-0.83	-1,079	256
	3	26.10	32.30	-1.03	-1,187	256
	4	25.50	2.35	1.15	16.4	256
	5	23.30	3.03	0.30	17.9	256
	6	22.60	4.39	1.00	170	256
	7	19.70	8.13	1.01	121	256
	8	19.00	10.07	1.60	297	256
	9	16.40	14.29	2.61	716	256
	10	16.10	14.10	4.55	1,077	256
	11	13.10	14.69	5.43	1,670	256
	S-12	0.00	8.57	2.49	161	256
	S-13	0.00	8.34	2.60	267	256
Stagecoach	I	80.0	57.0	7.9	49,000	40,000
	II*	17.1	50.5	23.6	83,600	40,000
	III*	34.2	58.6	29.2	145,000	40,000
5000 LB		0.00	18.50	4.75	2,950	5,000
3000 LB*		14.31	26.2	13.9	12,000	3,000
Jangle	S	-3.48	45.0	19.0	49,270	2.4×10^6
	U*	17.00	130.0	53.0	9.73×10^5	2.4×10^6
Teapot	S*	67.0	146	90.0	2.6×10^6	2.4×10^6

*Data used to compute standard deviations discussed in Section 2.3 following.

$$V/W^{q_1} = 7.85\,\Lambda^{0.753} \quad,$$

$$R/W^{q_2} = 2.23\,\Lambda^{0.174} \quad, \hspace{3cm} (2.1)$$

$$h/W^{q_3} = 1.14\,\Lambda^{0.373} \quad,$$

where $(0.2 < \Lambda = d/W^{q_4} < 2)$, and $(250 \leq W \leq 4 \times 10^4)$. Apparent crater volume, radius, and depth are represented by V, R, and h, respectively, depth of burial by d, and charge weight by W. Values of q_1, q_2, q_3, and q_4 give that power of charge weight by which crater dimensions are best scaled. It is recalled that cube-root scaling gives $q_1 = 1$ and $q_2 = q_3 = q_4 = 1/3$. Regression analysis values of each q and its standard deviation, σ, are given in Table 2.3.

TABLE 2.3   REGRESSION ANALYSIS VALUES

	q_1	σ_1	q_2	σ_2	q_3	σ_3	q_4	σ_4
Before Stagecoach[1]	0.898	0.062	0.291	0.016	0.298	0.036	0.299	0.021
With Stagecoach results	0.897	0.063	0.299	0.009	0.294	0.026	0.299	0.021

It can be seen that the values of q are less than predicted by cube-root scaling. While the q values were not appreciably altered by Stagecoach data, a noticeable reduction is apparent in standard deviations, σ_2 and σ_3, for the radius and depth scaling exponents. The Stagecoach experiments have confirmed that deviations from cube-root scaling are systematic (i.e., cube-root scaled crater dimensions for Stagecoach are all less than similar scaled quantities for 256- and 2560-pound explosives), and that deviations from cube-root scaling are greater than the inherent scatter of the data. Consequently, it is concluded that cube-root scaling laws are not adequate for accurately predicting crater dimensions in desert alluvium and that the empirically determined 3/10 scaling rule correlates present chemical explosive data better than does the cube-root law.

Desert alluvium crater dimensions scaled by rules obtained from the regression analysis are shown in Figs. 2.1, 2.2, and 2.3. The solid lines of positive slope in these illustrations are plots of Eqs. (2.1). For $\Lambda > 2$ the

solid lines of negative slope are straight line fits. The data for $\Lambda > 2$ were not subjected to a regression analysis, there being only two charge weights, 256 and 40,000 pounds, at these deeper burst depths.

2.2 SCALING LAWS WHEN GRAVITATIONAL ACCELERATION IS NOT NEGLECTED

The Stagecoach craters have shown conclusively that cube-root scaling is not valid in desert alluvium. This experimental result casts doubt on our ability to scale crater dimensions in other media. If cube-root scaling is incorrect for desert alluvium craters, it may well be inadequate for craters in other geologic media as well. Also, there is little evidence to indicate that the empirical 3/10 law of desert alluvium may be assumed without error for other media. The 3/10 scaling law has been established only for charge weights between 250 and 40,000 pounds, and use of the 3/10 law for extrapolation to yields in the high kiloton range is completely uncertain.

In order to understand whether crater dimensions can be accurately scaled in any medium, and particularly from model studies to the large yields of nuclear explosions, we inquire into the reasons for the departures from cube-root scaling observed in desert alluvium experiments. Two possibilities immediately suggest themselves. Assume that desert alluvium is homogeneous on a scale large compared to crater dimensions, which is evidenced by visual observation and by the fact that scatter in crater data is relatively smaller for this medium than for others. Departure from cube-root scaling may then be due to the anisotropic nature of the medium, e.g., variations in density, moisture content, porosity, or geologic stratification with depth; or the departure may be due to the influence of gravitational forces during crater formation. Since neither anisotropy nor gravitational acceleration can be scaled in field experiments, either or both of these conditions may account for the fact that crater sizes do not scale by cube-root laws.

Few quantitative data are available on the anisotropic nature of alluvium. Data on density and moisture content with depth (see Tables C.1 and C.2) suggest that the medium is essentially isotropic. There is geologic stratification (see Fig. C.5) in the medium but, generally, it appears to be more random than uniform over the region of the test area where experiments were conducted. Shoemaker[13] observes sand and gravel layers 15 to 25 feet below the surface at the Teapot Ess and Jangle-U sites and a more or less uniform medium below

these depths. Drilling logs (Fig. C.5) at the Stagecoach sites indicate layers or lenses of caliche, clay, and sand appearing at various depths down to 80 feet. Few if any of these layers can be identified as uniform and continuous throughout the test area. Seismic velocity logs[14] indicate that the medium is quite uniform down to a depth of 100 feet. If the geologic stratification is random, as appears to be the case, then it is difficult to see how this layering could influence crater formation in such a consistent manner as to result in the 3/10 scaling rule. In any case, should the apparently small anisotropy of the medium be responsible for departure from cube-root laws, an elaborate theory of cratering which takes account of medium variations with depth is required to explain the 3/10 rule.

Based on qualitative data, we assume that desert alluvium is uniform with depth, and we next examine the question as to how the effect of gravity may alter crater scaling laws. In the absence of a cratering theory the question is most easily considered by means of dimensional analysis.[15]

Assume that the following physical variables (dimensions in parentheses) are sufficient to describe the phenomena of cratering:

<u>Medium Properties</u>

ρ = (ML^{-3}), density of undisturbed medium

Y = $(ML^{-1}T^{-2})$, a yield strength of medium

ν = $(ML^{-1}T^{-1})$, a viscosity or dissipation variable of medium

<u>Independent Variables</u>

d = (L), depth of burial of explosive charge

p = $(ML^{-1}T^{-2})$, ambient pressure at depth, d

E = (ML^2T^{-2}), energy required to form crater

Dependent Variables

r = (L), linear crater dimension

t = (T), time

u = (LT^{-1}), velocity of medium particle during crater formation

a = (LT^{-2}), acceleration of medium particle during crater formation

Constants

g = (LT^{-2}), gravitational acceleration

Other variables could also be included. Dimensionless quantities such as strain, void ratio, or moisture content can simply be inserted into the final result (see Eq. 2.2 below) and do not affect the analysis on the listed variables. Quantities such as sonic velocity, c, of medium which have dimensions identical to a listed variable appear in the final result as dimensionless ratios such as u/c. Since crater volume is proportional to the cube of the linear crater dimension, r, it is redundant to include a variable representing crater volume. Any other variables which are considered significant to cratering may be added to the list without difficulty, provided the dimensions involve mass, length, and time only. However, as will be seen, those variables listed are sufficient to indicate the effect of gravity, which is our present concern.

Although it is not known whether the yield strength (compressive or tensile), Y, is significant to cratering phenomena in soils, it has been included for generality. For continuous rock media one expects this variable to be important, since the mechanism of crater formation in rock involves a spallation process[16] into which tensile strength enters. Similarly, for the sake of generality, a dissipation variable in the form of a viscosity has been assumed. If these variables are not significant, they can be discarded from consideration after completion of the analysis. Omission of these variables, should they be significant, leads to erroneous conclusions. The relevance of these variables must ultimately be determined by experiment. In any event, results of a dimensional analysis will allow their influence in cratering to be examined qualitatively.

While the meaning of variables which describe medium properties, gravitational acceleration, and energy required to form a crater is precise, some ambiguity exists in the interpretation of those dependent variables which we wish to have describe crater dynamics, u, a, t, and crater size, r. Also, the pressure variable, p, may be given several interpretations. For example, it is difficult to know initially whether the variable, r, represents a crater dimension or some radial distance from the explosion, whether u and a are the velocity and acceleration of particles being ejected from the crater region or are the motions of a particle due to the radiated stress wave. Similarly the variable p may refer to radial stress, peak shock pressure, and explosive detonation pressure as well as to ambient pressure in the medium. These ambiguities are characteristic in a dimensional analysis of a complex phenomenon such as cratering, since the complete differential equations and the equations of state of the medium which describe the phenomena are not known. The correctness of interpretation assigned to variables entering a dimensional analysis can only be justified by the accuracy of conclusions drawn from the analysis and by experimental verification.

Since we are interested in the mechanisms of crater formation which are dominant in soil, let the variables, u and a, refer to velocity and acceleration experienced by a soil particle which is ejected by an explosion and not to velocity and acceleration imparted to a soil particle by the seismic or shock disturbance. These variables are to be correlated with motion of up-heaved earth at times long compared to shock arrival time at the ground surface and to the motion of missiles that are discharged from the region which eventually becomes the crater void. We want the variable, t, to describe the time of an event in crater formation and not the period of seismic waves or the shock wave decay time. The variable, r, represents a crater dimension or the radial position of an ejected particle at time, t. Let p be ambient pressure at depth, d, and not radial stress or shock pressure. Take E as the energy utilized to form the crater; it is clear that E is less than the total energy of explosion, W, since energy is also partitioned to other phenomena such as ground shock and air blast.

From a dimensional analysis[15] on the variables assumed to be important, a general relationship describing cratering is obtained:

$$F \left\{ \frac{p}{\rho g d} \ , \ \frac{p r^3}{E} \ , \ \frac{r}{d} \ , \ \frac{Y}{p} \ , \ \frac{v}{(\rho^3 E^2 p)^{1/6}} \ , \right.$$

$$\left. t \left(\frac{p^5}{E^2 \rho^3} \right)^{1/6} \ , \ u \left(\frac{\rho}{p} \right)^{1/2} \ , \ a \left(\frac{\rho^3 E}{p^4} \right)^{1/3} \ , \ \ldots \right\} = 0 \ , \qquad (2.2)$$

where the arguments of F are dimensionless quantities and the dots indicate where other desired variables in appropriate dimensionless form may be inserted, e.g., strain, moisture content, velocities, c, in the form, c/u, pressures, P, as P/p, volumes as V/r^3, etc.

Equation 2.2 reveals how the physical variables involved must be altered in order to perform model or small-scale experiments. The model experiment is said to be <u>similar</u> to the prototype only if all dimensionless quantities in Eq. 2.2 have the same numerical values for both experiments. If one or more of the dimensionless quantities are not numerically identical for both experiments, then similarity does not exist and the model experiment will not exactly duplicate phenomena of the prototype experiment.

Writing Eq. 2.2 in the form

$$r = \left(\frac{E}{p} \right)^{1/3} f \left\{ \frac{p}{\rho g d} \ , \ \frac{r}{d} \ , \ \frac{Y}{p} \ , \ \frac{v}{(\rho^3 E^2 p)^{1/6}} \ , \right.$$

$$\left. t \left(\frac{p^5}{E^2 \rho^3} \right)^{1/6} , \ u \left(\frac{\rho}{p} \right)^{1/2} , \ a \left(\frac{\rho^3 E}{p^4} \right)^{1/3} , \ \ldots \right\} \qquad (2.3)$$

allows the scaling law for the variable, r, to be examined. Dimensional analysis does not provide the analytic form of f in Eq. 2.3. Without a theory this must come from experiment. It can be seen that the usual presentation of crater data, r = r(W, d), is the simplest assumed form of Eq. 2.3 (see Eq. 2.1 and Figs. 2.1, 2.2, and 2.3).
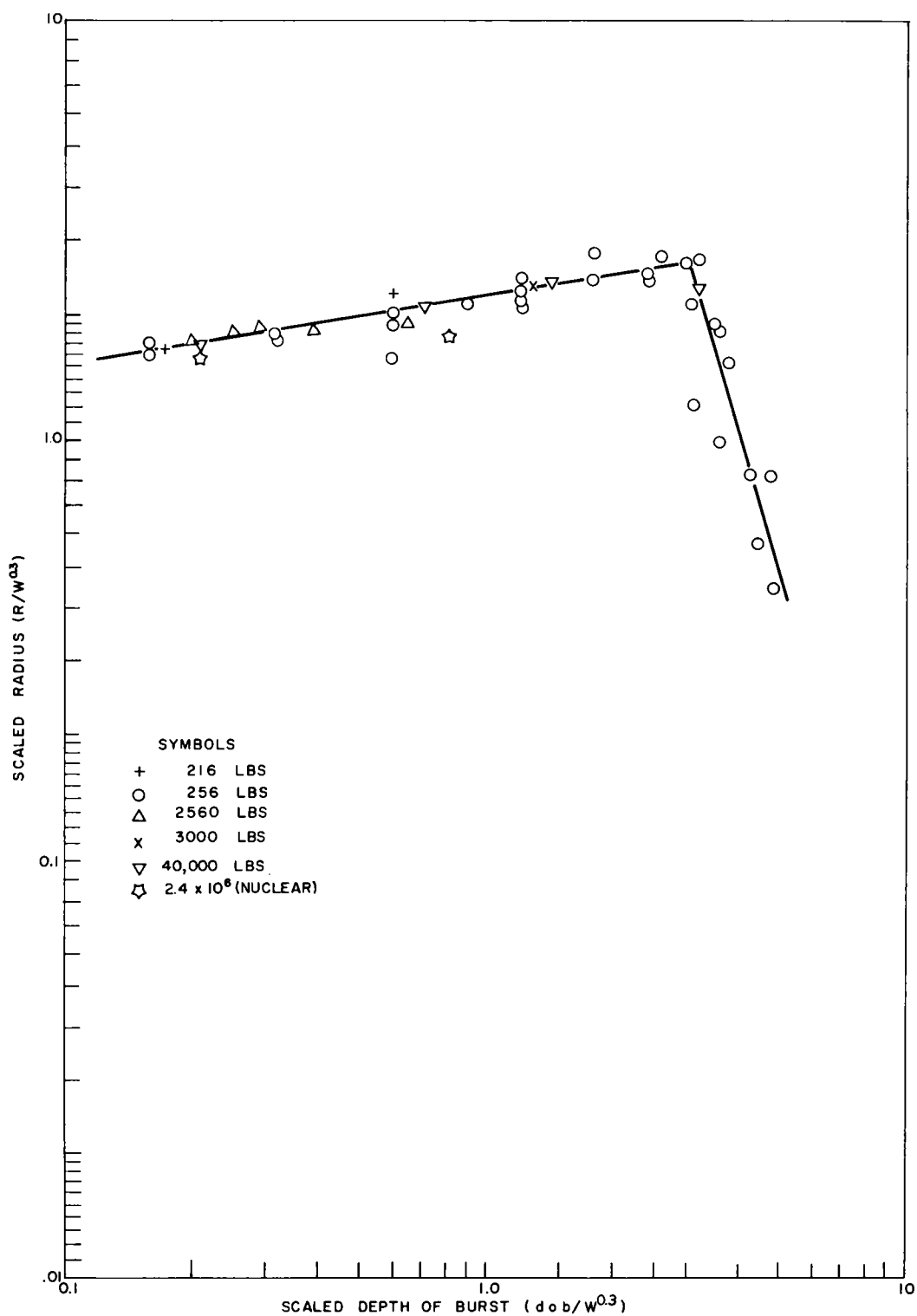
Fig. 2.1 Scaled crater radius versus scaled depth of burst; desert alluvium, 3/10 scaling.

Fig. 2.2 Scaled crater depth versus scaled depth of burst:
desert alluvium, 3/10 scaling.
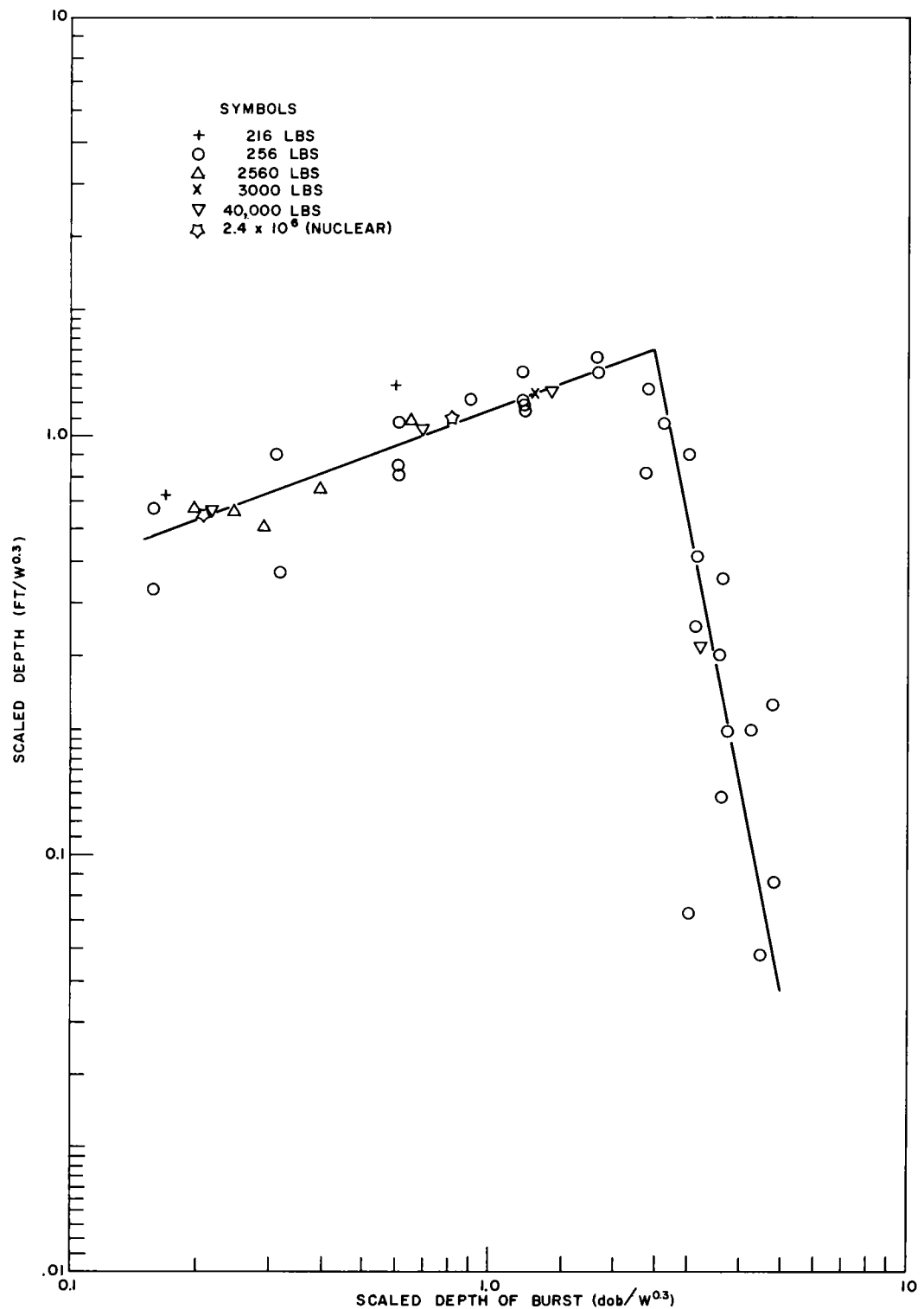
Fig. 2.3 Scaled crater volume versus scaled depth of burst; desert alluvium, 3/10 scaling.
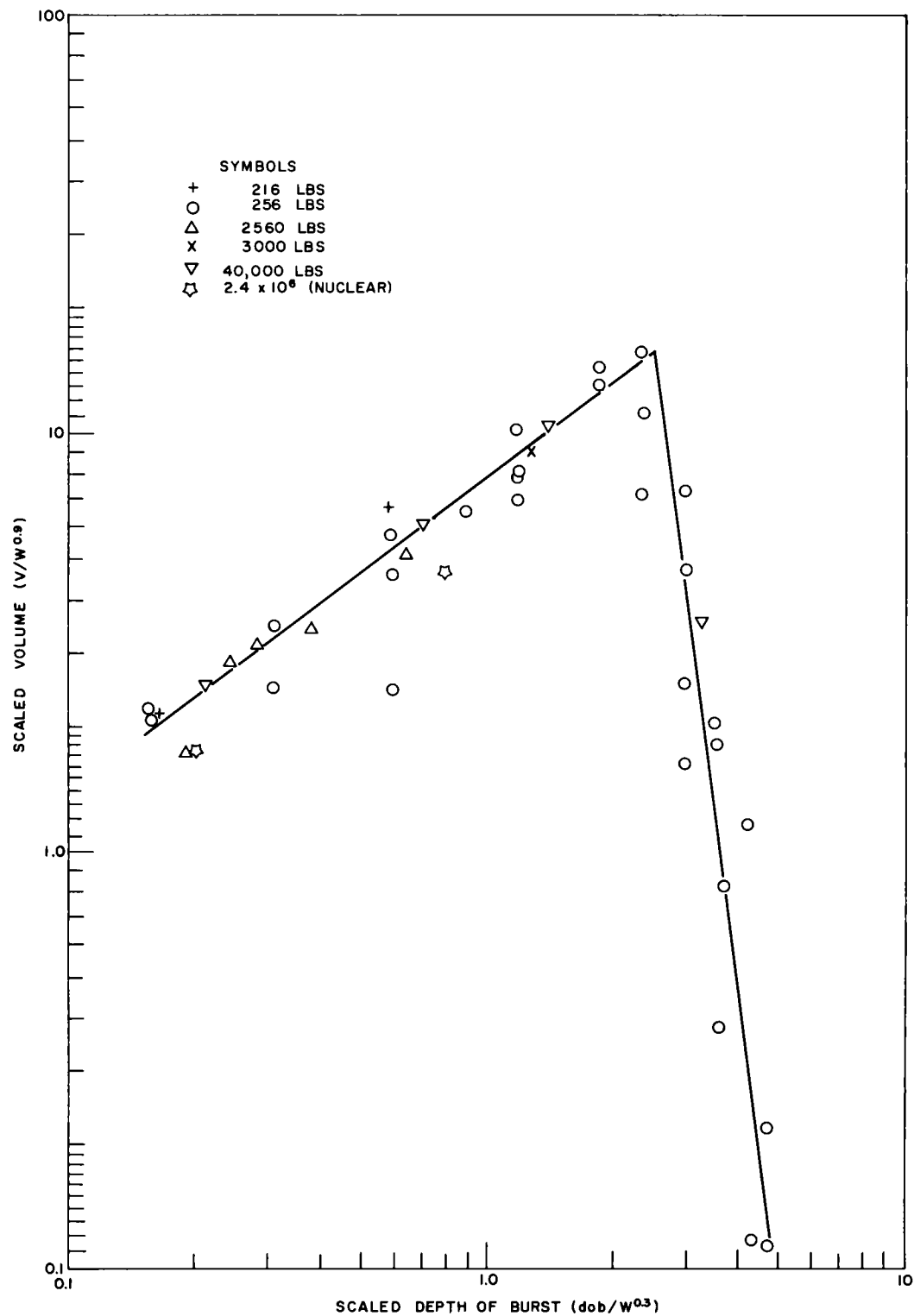
Throughout our consideration of Eq. 2.3 we take ρ, g, Y, ν, . . . to be constant in accordance with experimental conditions. If two cratering experiments with energies E_1 and E_2 are performed, <u>and</u> <u>if</u> similarity exists, the ratio of resulting crater dimensions will be

$$\frac{r_1}{r_2} = \left(\frac{E_1}{E_2}\right)^{1/3} \left(\frac{p_2}{p_1}\right)^{1/3} . \tag{2.4}$$

Since the two experiments are similar, the arguments of f in Eq. 2.3 are numerically equal for both experiments; consequently the function f is identical for both experiments and Eq. 2.4 follows. The fraction of total energy utilized in forming a crater is constant for all experiments which are similar. Thus in Eq. 2.4, we may substitute the ratio of total energies, W_1/W_2 for E_1/E_2.

The condition that two experiments be similar for Eq. 2.4 to be valid is never actually attained in practice. This point is immediately obvious by noting that for similarity the medium properties, Y and ν, must be scaled according to $Y_1/Y_2 = p_1/p_2$, and $\nu_1/\nu_2 = (E_1/E_2)^{1/3}(p_1/p_2)^{1/6}$. Since medium properties are not scaled in field experiments, the scaling law of Eq. 2.4 will be in error to the extent that similarity is not realized. Inclusion of medium perperties such as yield strength and viscosity in a dimensional analysis show that if these properties cannot be scaled, scaling laws for crater dimensions such as Eq. 2.4 will not be correct, and deviations from the scaling laws are expected. This is true whether or not gravitational acceleration is considered important to cratering.

The effect of not being able to scale viscosity and yield strength may be examined qualitatively to see if it can account for observed deviations from cube-root scaling. It seems reasonable to assume that for a given energy, E, crater dimensions increase when medium properties ν or Y decrease. Then, by Eq. 2.3, an increase in r is obtained for decreases in either of the dimensionless quantities, $\nu/(\rho^3 E^2 p)^{1/6}$ or Y/p. When the medium viscosity is constant, a decrease in the quantity $\nu/(\rho^3 E^2 p)^{1/6}$ also results from an increase in E, whereby a larger crater is produced. Thus the viscous effects of a medium are

more pronounced for smaller explosions, and model experiments with small explosions can be expected to produce smaller scaled craters than do large explosions. Similar consideration of yield strength and explosions at the same scaled depth indicate that smaller explosions will produce smaller scaled crater dimensions. Thus inability to scale viscosity or yield strength results in larger scaled crater dimensions for the larger explosions, an effect which is just opposite to what is observed in desert alluvium when dimensions are scaled by the cube-root law. We conclude, then, that medium properties such as viscosity and yield strength cannot account for deviation from cube-root scaling.

It may be the case that for experiments involving energies, E, greater than a certain value, similarity is nearly achieved. This implies that the manner in which the quantities $v/(\rho^3 E^2 p)^{1/6}$ and Y/p occur in the function f of Eq. 2.3 is such that the function has nearly an asymptotic value for these larger values of E. If this is correct. Eq. 2.4 will be a good approximation.

It seems logical that $v/(\rho^3 E^2 p)^{1/6}$ and Y/p can never be completely insignificant no matter how large the value of E, since it is these quantities, together with density, seismic velocity, moisture content, porosity, etc., that describe differences in media. For example, since v, Y, and ρ are greater for rock media than for soil, Eq. 2.3 shows that crater dimensions in rock will be smaller than those in soil if both experiments are otherwise identical. Moisture content and porosity, assuming they are constant throughout the medium, do not violate the similarity requirement as do yield strength and viscosity.

Equation 2.4 states that the cube-root scaling law, $r_1/r_2 = (E_1/E_2)^{1/3}$, is modified by the factor $(p_2/p_1)^{1/3}$ when gravity is not neglected. If two crater experiments are similar and the medium properties as well as gravity are constant, then regarding p as the lithostatic pressure, $\rho g d$, we have $p_2/p_1 = d_2/d_1 = r_2/r_1$, and Eq. 2.4 reduces to $r_1/r_2 = (E_1/E_2)^{1/4}$ or fourth-root scaling. When p is taken as the sum of lithostatic and atmospheric pressures, $\rho g d + \rho g K$, at depth (where K is that depth of earth equivalent to one atmosphere, 18 feet for desert alluvium), Eq. 2.4 becomes

$$\frac{r_1}{r_2} = \left(\frac{E_1}{E_2}\right)^{1/3} \left(\frac{d_2 + K}{d_1 + K}\right)^{1/3} . \qquad (2.5)$$

From the dimensionless quantities pr^3/E, $p/\rho gd$, and r/d we see that to insure similarity we must have for two experiments

$$\frac{r_1}{r_2} = \left(\frac{E_1}{E_2}\right)^{1/3} \left(\frac{d_2 + K}{d_1 + K}\right)^{1/3} = \frac{d_1}{d_2} = \frac{d_1 + K}{d_2 + K} \; , \qquad (2.6)$$

which can only be realized when atmospheric pressure is scaled according to

$$\frac{K_1}{K_2} = \frac{d_1}{d_2} = \frac{r_1}{r_2} = \left(\frac{E_1}{E_2}\right)^{1/4} \; , \qquad (2.7)$$

in which case fourth-root scaling obtains. When p is taken as lithostatic pressure alone, the dimensionless quantity, $p/\rho gd$, is identically one for all cratering experiments and never violates the requirement of similarity. When p is taken as lithostatic plus atmospheric pressure, or as the atmospheric pressure alone, the quantity, $p/\rho gd$, is never similar for experiments unless atmospheric pressure can be scaled. Since K is of the order of 20 feet of soil, and many of the alluvium experiments were conducted at depths of this magnitude or less, it is possible that our inability to scale crater dimensions properly may be a result of similarity violation by not scaling atmospheric pressure.

With the interpretation that p is lithostatic pressure alone, crater dimensions must scale by the fourth root of energy for all values of E. This conclusion is contradicted by data from model experiments of small E where cube-root scaling is found to be correct. This interpretation of p must consequently be incorrect.

When p includes atmospheric pressure, results of model experiments can be understood. For model experiments the values of E are small, and corresponding values of burial depth, d, are much less than K. In Eq. 2.5, then, one obtains cube-root scaling for small charges by neglecting d in comparison with K.

Considering the latter interpretation of p to be correct, the following conclusions can be drawn from the dimensional analysis:

1. In the limit of very small charges where the burial depth is much less than K, cube-root scaling results: $r \propto E^{1/3}$ for $K \gg d$ and as $E \to 0$.

2. Crater dimensions from surface bursts of any energy release scale by the cube-root rule: $r \propto E^{1/3}$ as $d \to 0$ for all E.

3. For very large charges and for depths where lithostatic pressure is much greater than atmospheric pressure, fourth-root scaling prevails: $r \propto E^{1/4}$ for $d \gg K$ as $E \to$ large.

4. For certain ranges of explosive energies, E, when $d \approx K$, $r \propto E^m$, $1/4 < m < 1/3$.

5. In the limiting case of completely contained explosions, r can be taken as the radius of a camouflet which must certainly depend on the overburden according to Eq. 2.4. Cube-root scaling laws cannot describe the dependence of camouflet radii on overburden, and a serious impasse is encountered on this point.

6. When $v = Y = 0$, crater scaling results reduce to the scaling laws for gas bubbles from underwater explosions.

Model experiments[17] with small charges corroborate item 1, above. Surface burst data[17,18] appear to verify item 2. Item 4 was observed in the previous section from the regression analysis. Scaling laws obtained from the special case of item 6 are well known,[19] and there is considerable evidence to show that hydrostatic as well as atmospheric pressure significantly influence explosion gas bubble phenomena.

There appear to be few data by which item 5 may be verified. Camouflet experiments[20] in which $d \ll K$ show, as expected (Eq. 2.5), that cavity radii scale by the cube-root law. At extreme depths, $d \gg K$, camouflet radii should scale by the fourth-root law. Data[9] from four contained nuclear explosions in volcanic tuff (Tamalpais, Rainier, Logan, Blanca), where $d \gg K$, indicate the camouflet scaling law, $r = 58 W^{1/4}$ (r in feet, W in kilotons). For contained explosions of different energies but identical depths, $d \gg K$, similarity is not achieved. However, from Eq. 2.5, one might expect that camouflet radii would be approximately proportional to the cube root of energy release. From three nuclear explosions in volcanic tuff meeting these conditions, the

camouflet radius has been found[9] to scale as $r = 50 \, W^{1/3}$ (r in feet, W in kilotons). For nonsimilar explosions of equal energy release but at different depths, $d \gg K$, the approximation $r_1/r_2 \cong (d_2/d_1)^{1/3}$ from Eq. 2.5 indicates that the shallower explosions will create the larger camouflets, which result is in keeping with our intuitive feeling about the dependence of cavity size on overburden.

Of the six items listed for which we have at least qualitative experimental evidence, only the first two can be explained by cube-root scaling laws.

2.3 FOURTH-ROOT SCALING

In Figs. 2.4 through 2.6 are presented desert alluvium crater data scaled by the fourth root of the explosive energy release in pounds. Total energy release, W, rather than energy, E, partitioned to crater formation, is used to scale data, since E is unknown. Because similarity is not achieved in the alluvium experiments, use of W for E is a necessary approximation in order to test the hypothesis that fourth-root scaling is correct. The lines in each graph are drawn to connect the 40,000-pound data points.

Crater data from nuclear explosions plotted indicate that differences in crater formation between nuclear and large chemical explosions are not as great as previously supposed. Only by assuming the validity of cube-root scaling does an unaccountably great difference appear between scaled crater dimensions of nuclear and chemical explosions.

Deviations from strict fourth-root scaling as seen in the illustrations are expected because of lack of similarity. However, the direction of deviations is described by considerations contained in the last section. Larger charges generally have greater scaled dimensions, deviations being greatest at the shallower burst depths where the effect of atmospheric pressure is more pronounced in comparison to lithostatic pressure. At scaled depths larger than 1.5, it appears that the condition of similarity is being approached for charges greater than about 5000 pounds, and also that nuclear explosions are becoming more similar to chemical explosions.

To examine the standard deviations in data scaled by 1/3, 3/10, and 1/4 rules, those data of Table 2.2 marked by asterisks were subjected to a
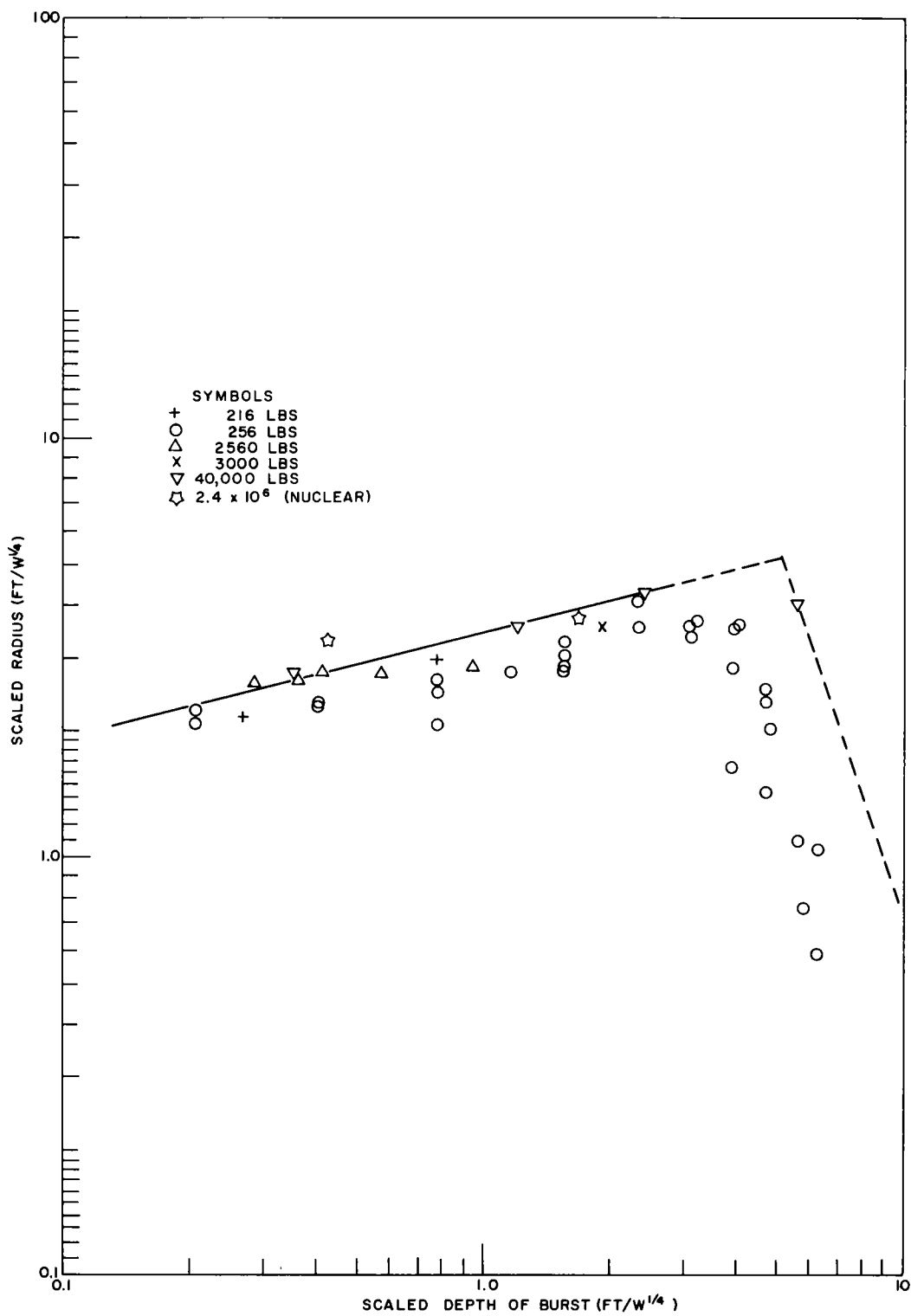
Fig. 2.4 Scaled crater radius versus scaled depth of burst; desert alluvium, fourth-root scaling.
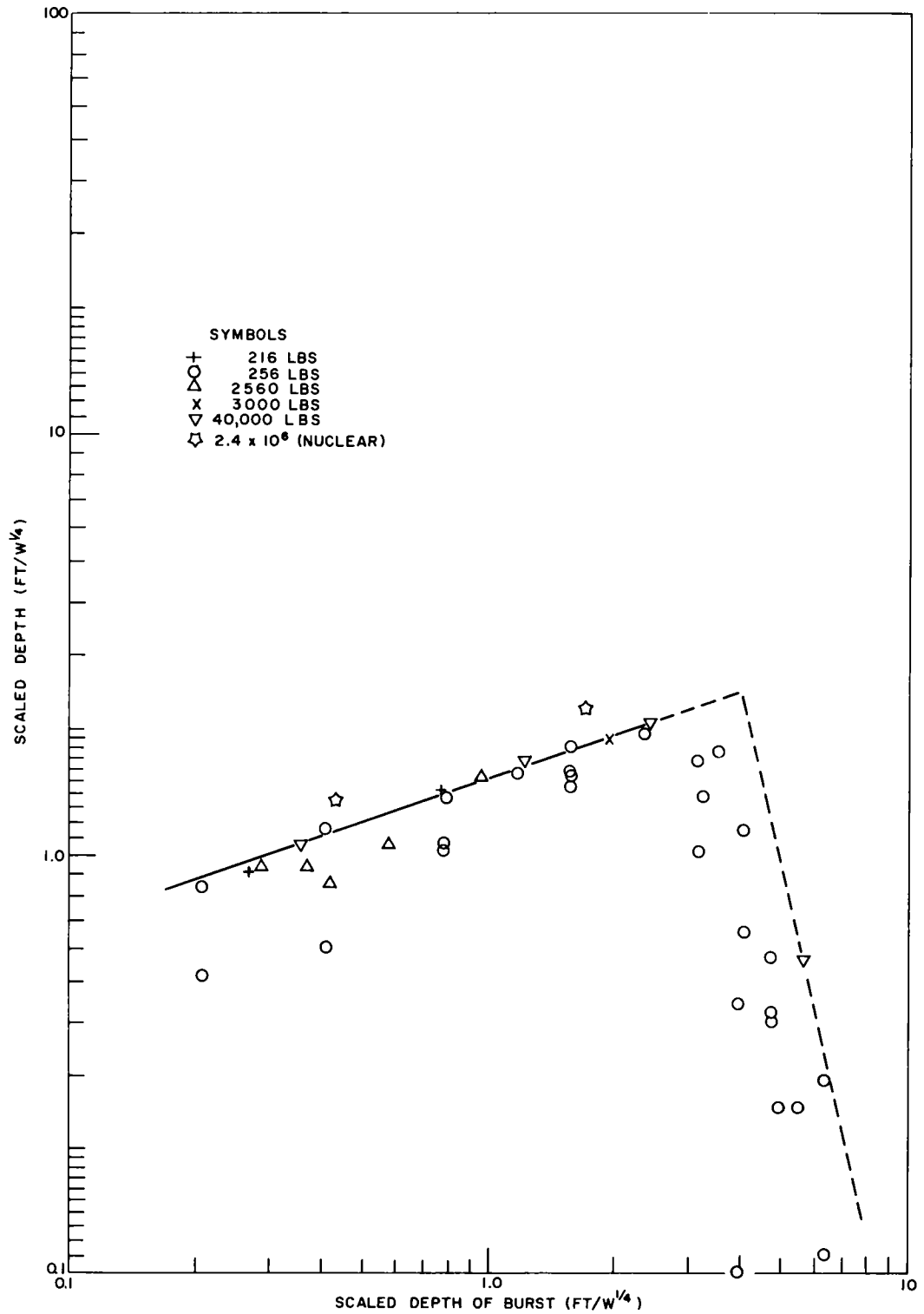
Fig. 2.5 Scaled crater depth versus scaled depth of burst; desert alluvium, fourth-root scaling.

100

SCALED VOLUME (FT³/W¾)

10

1.0

SYMBOLS

+   216 LBS
○   256 LBS
△   2560 LBS
x   3000 LBS
▽   40,000 LBS
✧ 2.4 x 10⁶ (NUCLEAR)

0.1

0.1   1.0   10

SCALED DEPTH OF BURST (FT/W¼)
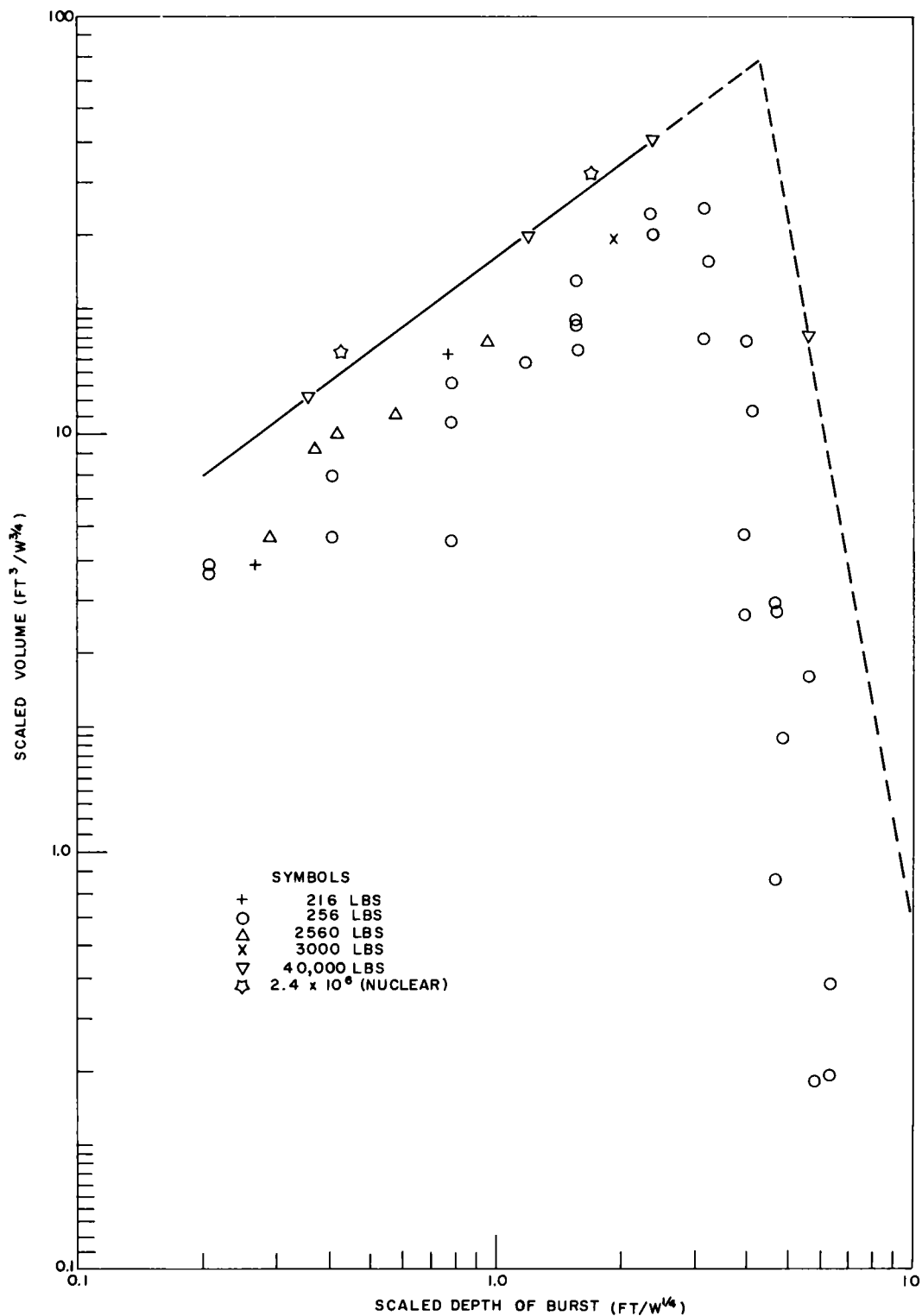
Fig. 2.6 Scaled crater volume versus scaled depth of burst;
desert alluvium, fourth-root scaling.

41

least squares fit, assuming the existence of a linear relation between the logarithm of scaled crater dimension and the log of scaled burst depth. Results are shown in Table 2.4.

TABLE 2.4   COMPARISON OF STANDARD DEVIATIONS IN CRATER DATA SCALED BY 1/3, 3/10, AND 1/4 RULES

	Scaling		
Dimension	1/3	3/10	1/4
Radius	0.058	0.038	0.055
Depth	0.073	0.066	0.075
Volume	0.148	0.090	0.145

From information in the above table, it is clear that for the range of explosion energies examined, $2 \times 10^2 < W < 2 \times 10^6$, 3/10 scaling is the best choice. Except for volume dimension, standard deviations in data scaled by cube-root rule are less than for fourth-root scaled data. However, since the deviations obtained are heavily weighted by the more numerous 256-pound data, and because it is asserted that these 256-pound experiments are not similar to experiments of the larger charge weights, one cannot argue in favor of cube-root scaling over fourth-root scaling on the basis of a comparison of these standard deviations. If, in the context that we wish to be able to extrapolate to large yields, fourth-root scaling correctly describes explosive cratering, the cube-root deviations are larger than 3/10 deviations, since cube-root scaling is incorrect. The fourth-root deviations are larger than those of 3/10 scaling because similarity was not achieved in the experiments. That scatter of 3/10 scaled data is less than fourth-root scaled data demonstrates that similarity is not realized in the experiments.

A more meaningful comparison on the basis of standard deviations is made by examining those data from explosions among which similarity was most nearly achieved. In Table 2.5 are presented standard deviations for data from explosions where $W \geq 4 \times 10^4$ pounds. The first Stagecoach shot is not included, since the datum from this experiment lies to the right of that burial depth at which crater dimensions are a maximum (see Figs. 2.4 through 2.6).

Comparing standard deviations for radius and volume data from Tables 2.4 and 2.5, it is seen that, for the larger explosions, deviations are about the same as those for all explosions when data are scaled by the cube-root rule.

TABLE 2.5   COMPARISON OF STANDARD DEVIATIONS IN CRATER DATA
SCALED BY 1/3, 3/10, AND 1/4 RULES

Dimension	Scaling		
	1/3	3/10	1/4
Radius	0.053	0.032	0.026
Depth	0.036	0.031	0.045
Volume	0.143	0.076	0.029

Note: Only explosions with $W \geq 4 \times 10^4$ pounds are considered.

When scaled by the 3/10 rule, deviations for radius and volume data are less for the larger explosions than for all explosions. The greatest reduction in deviations for these same dimensions occurs when data are scaled by the fourth-root law. This smaller scatter in data for the larger explosions scaled by fourth-root laws is interpreted as a confirmation of the argument that similarity is realized to a greater extent in those experiments with larger explosives and deeper burial depths.

From listings for depth in Tables 2.4 and 2.5, it is seen that for crater depth data the reduction in standard deviations is greatest in 3/10 scaling and least in 1/4 scaling. This result perhaps is an indication that similarity for the large explosive experiments considered, $4 \times 10^4 < W < 2 \times 10^6$ pounds, is still not sufficiently achieved. Such an explanation seems reasonable when burial depths, d, are compared with atmospheric depth, K; i.e., for these experiments the condition of similarity expressed as $d \gg K$ is not fully met.

A best choice of scaling made from a comparison of deviations in Table 2.5 is fourth-root scaling, especially for the radius and volume dimensions. It is expected that as more data are obtained from still larger explosions, $W > 2 \times 10^6$ pounds, and where $d \gg K$, standard deviations for 1/3 and 3/10 scaling in Table 2.5 will increase and those for 1/4 scaling will decrease, confirming the indication here that fourth-root laws more correctly describe scaling of deeply buried explosion craters.

Data from the 256-pound explosions, all of which had burial depths of the same order of magnitude as the atmospheric depth, K = 18 feet, are less reliable for scaling to large yields than are, for instance, the 2560-pound data, since violation of similarity is greatest in scaling from 256-pound results. Consequently, those data from the 256-pound experiments should not be relied upon to establish scaled crater curves (dimensions versus depth of burst) valid for all yields. This point is well illustrated by noting that

the scaled depth of burst for 256-pound explosions which results in maximum
crater dimensions is less than that for larger charges (see Stagecoach data
point at $d/W^{1/4} = 5.7$). It is believed that for experiments with charge
weights less than 256 pounds, optimum scaled depth will be less than that
for 256-pound charges. In order to determine the correct scaled depth at
which maximum crater dimensions are obtained from large charges, further ex-
periments are required.

To account in some degree for the effect of atmospheric pressure and
the lack of similarity in experiments, alluvium crater dimensions have been
scaled[21] by the formula $X(d + K)^{1/3}/W^{1/3}$, where X is a linear crater dimen-
sion. Since this scaled quantity can be written

$$X(d + K)^{1/3}\Big/ W^{1/3} = (X/W^{1/4}) \left[(d + K)/W^{1/4}\right]^{1/3} ,$$

we see that as one goes to larger yields, W, and corresponding greater depths,
d, the constant, K, becomes less significant and the condition of similarity
is more nearly realized. In the limit for those energies, W, where $d \gg K$,
the quantity $(d + K)/W^{1/4}$ approaches a constant scale factor. Results of the
author's report on alluvium scaling laws,[11] divided by the factor

$$\left[(d + K)/W^{1/4}\right]^{1/3} ,$$

then reduce to fourth-root scaled crater data of Figs. 2.4 through 2.6.

Figures 2.7 and 2.8 are presented to demonstrate the difficulty in ac-
curately scaling crater dimensions when similarity does not exist. In Fig.
2.7 we take as datum the crater depth of the shallowest 20-ton explosion
and in Fig. 2.8 the crater depth of the deepest 20-ton explosion in desert
alluvium. Lines through each datum represent the various scaling rules.
Arrowed lines show the limits in yield, greater and less than 20 tons, within
which two compared scaling rules give the same crater dimension to within 10
percent. Shaded areas indicate roughly the range of yields over which a par-
ticular scaling rule is most applicable. Note that, in estimating crater
depth for some yield from the 20-ton datum by a particular scaling rule,
depth of burial for that yield is determined by the same scaling rule.
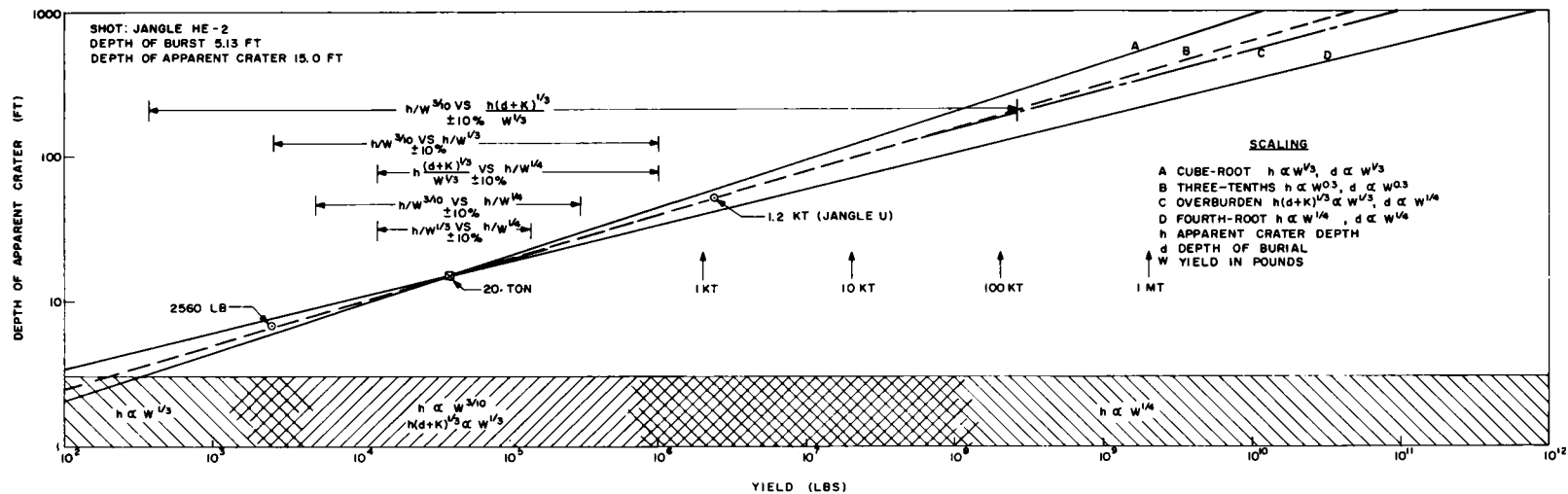
Fig. 2.7 Comparison of scaling rules. Crater depths h scaled from shallowest 20-ton explosion.
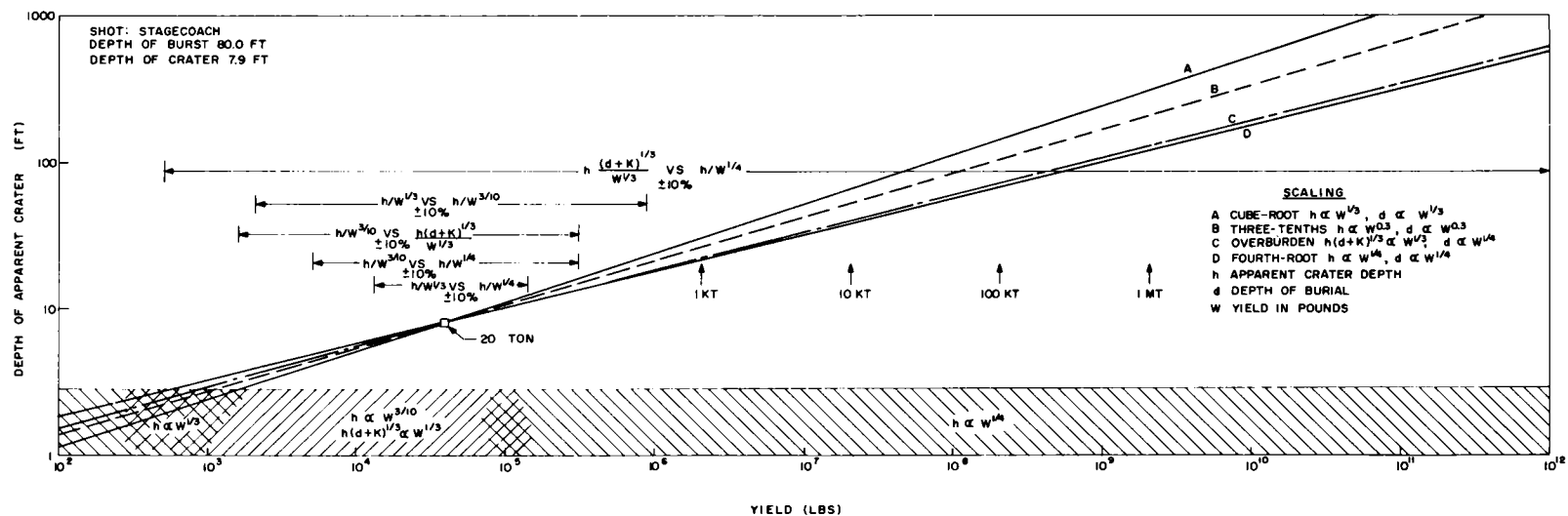
Fig. 2.8 Comparison of scaling rules. Crater depths h scaled from deepest 20-ton explosion.

In Fig. 2.7 we see that the 3/10 scaling rule closely approximates the "overburden" scaling rule of the author's alluvium report[11] over a wide range of yields,[*] and also that the results of shot HE-2 could be scaled to yields greater than 10 kt by 3/10 scaling but not by 1/4 scaling. For depths of burst corresponding to that of the 80-foot Stagecoach shot in Fig. 2.8, the 3/10 scaling rule cannot be extended with confidence even to 1 kt. In this instance fourth-root, or the essentially equivalent "overburden," scaling should be most accurate. The reason for inadequacy of the 1/4 scaling law at the shallower burst depth is that similarity is greatly violated for the shallower shot, since the burst depth of 5 feet is considerably less than the atmospheric depth, K, of 18 feet.

Inasmuch as similarity cannot be achieved in field experiments, no single scaling rule can be relied upon to scale crater dimensions over any arbitrary range of yields. For charge weights $W < 10^3$ pounds, cube-root scaling is sufficiently accurate. For charges, $10^3 < W < 10^6$ pounds, "overburden" scaling should be used in preference to 3/10 scaling, since 3/10 scaling is a less accurate approximation, particularly for the deeper depths of burst. For charges $W > 10^6$ pounds and burial depths greater than about 100 feet, fourth-root scaling should be more accurate.

2.4 CONCLUSIONS

Experimental data have shown that cube-root laws are not valid for scaling crater dimension resulting from buried explosions. If acceleration of gravity is important in cratering phenomena, then the well known[22,23] fourth-root law is valid, provided similarity exists. Assuming that gravity is important and manifested not only through lithostatic pressure at the burial depth of the explosive charge but also through atmospheric pressure, it is then recognized that similarity is never achieved in cratering experiments because atmospheric pressure is never properly scaled. With this assumption, and taking into account the effects of nonsimilarity in experiments, a consistent explanation of all crater data can be obtained, which is not otherwise possible with cube-root laws. In particular, the reason for the empirical

---

[*]In Figs. 2.7 and 2.8, depths of burial for the "overburden" scaling rule are scaled by the fourth root of the yield, whereas in the author's alluvium report[11] burial depth was scaled in the same way as crater dimensions; i.e., $d(d + K)^{1/3} \propto W^{1/3}$. The difference in resulting crater dimensions is negligible.

3/10 scaling rule is now better understood, and the experimental cube-root scaling rule determined from a great mass of small-charge data is found to be a special case of fourth-root scaling when atmospheric pressure is much greater than lithostatic pressure. Also, scatter in crater data scaled by the fourth-root law is accounted for by arguments concerning the lack of similarity among experiments.

The first strong indication that fourth-root scaling laws are correct for very large explosion craters has been obtained from the Stagecoach program. This law, if valid for buried explosions in one medium, must also be valid for explosions in all media. Scaling crater dimensions by the fourth-root law for a set of experiments will result in some error which is determined by the degree of similarity violation among experiments. Errors will be greatest for smaller explosions and for shallower depths of burst. For yields greater than 1 kiloton and burial depths greater than 100 feet, similarity is essentially achieved, and use of the fourth-root law should incur minimum error in scaling crater dimensions from explosions in any medium.

REFERENCES

1. Lampson, C. W., "Explosions in Earth," Effects of Impact and Explosion, Vol. I, Part II, Chapter 3, Office of Scientific Research and Development, Washington, D. C., 1946, p. 110.

2. Underground Explosion Theory, Operation Jangle, WT-369, Office of Technical Services, Dept. of Commerce, Washington 25, D. C., 1952.

3. High Explosive Tests, Operation Jangle, WT-365, Armed Forces Special Weapons Project, 1952.

4. Doll, E. G., and Salmon, V., Scaled HE Tests, Final Report, AFSWP-123, Stanford Research Institute, 1952.

5. Sachs, D. C., and Swift, L. M., Small Explosions Tests, Project Mole, Final Report, AFSWP-291, Stanford Research Institute, 1955.

6. Murphey, B. F., and MacDougall, H. R., Crater Studies: Desert Alluvium, SCTM 119-59(51), Sandia Corporation, 1959.

7. Underground Explosion Test Program, Vol. I--Soil, Final Report, Engineering Research Associates, Inc., Arlington, Va., 1952.

8. Lewis, J. G., Crater Measurements, WT-1105, Armed Forces Special Weapons Project, 1955.

9. Johnson, G. W., Higgins, G. H., and Violet, C. E., Underground Nuclear Detonations, UCRL-5626, University of California Lawrence Radiation Laboratory, 1959.

10. Shelton, A. V., Nordyke, M. D., and Goeckermann, R. H., The Neptune Event, A Nuclear Explosive Cratering Experiment, UCRL-5766, University of California Lawrence Radiation Laboratory, 1960.

11. Chabai, A. J., Crater Scaling Laws for Desert Alluvium, SC-4391(RR), Sandia Corporation, 1959.

12. Vaile, R. B., Crater Survey, Operation Castle, WT-920, Stanford Research Institute, 1955.

13. Shoemaker, E. M., Impact Mechanics at Meteor Crater, Arizona, U. S. Geological Survey, Menlo Park, California, 1959.

14. Rugg, A. M., Seismic Refraction Survey for Nye County, Nevada, WT-327, United Geophysics Co., Inc., Los Angeles, California, 1951.

15. Bridgman, P. W., Dimensional Analysis, Yale University Press, 1949.

16. Duvall, W. I., and Atchison, T. C., Rock Breakage by Explosives, Bureau of Mines Report No. 5356, U. S. Department of the Interior, 1957.

17. Compendium of Crater Data, Tech. Rpt. No. 2-547, Report 1, U. S. Army Engineer Waterways Experiment Station, Corps of Engineers, Vicksburg, Mississippi, 1960.

18. Jones, G. H. S., Spackman, N., and Winfield, F. H., Cratering by Ground Burst TNT, Suffield Technical Paper No. 158, Suffield Experiment Station, Ralston Alberta, 1959.

19. Cole, R. H., Underwater Explosions, Princeton University Press, 1948.

20. Randall, C., and Stresau, R. H., Camouflet Experiments in Ice, NAVORD Rpt. 4548, U. S. Naval Ordnance Laboratory, 1958.

21. Chabai, A. J., Gravity Scaling Laws for Explosion Craters, SC-4541(RR), Sandia Corporation, 1960.

22. Haskell, N. A., Some Considerations on the Modelling of Crater Phenomena in Earth, Air Force Surveys in Geophysics No. 67, TN-55-205, Air Force Cambridge Research Center, 1955.

23. Sedov, L. I., Similarity and Dimensional Methods in Mechanics, Academic Press, New York and London, 1959, p. 256.

Chapter 3

SURFACE MOTION by B. F. Murphey

3.1 GROUND SURFACE DISPLACEMENT

Displacement of the ground surface was determined as a function of time from motion picture photography. Details of camera types and locations are described in Appendix A. Initial displacements were read vertically above the charge center, and data plots are shown in Fig. 3.1. Note the change in time scale. Times for vertical displacement to be 10 feet increase from 22 msec to 97 msec to 480 msec. Vertical motions have been differentiated to provide velocity versus time and acceleration versus time. Early vertical particle velocities for each shot are plotted in Fig. 3.2. The approximately steady velocities decrease from 600 feet per second for the 17-foot depth of burst explosion to 28 feet per second for the 80-foot depth of burst explosion. Thus, early velocity of the surface at ground zero decreases roughly in proportion to the square of the depth of burial. It is notable in Fig. 3.2 that, for the deepest explosion, velocity is still increasing at 0.7 second.

3.2 VERTICAL MOTION

Acceleration-time plots of vertical motion are shown in Fig. 3.3. Peak accelerations decrease with depth of burst about as the fourth power of depth of burst.

Several frames from motion pictures of the 34-foot depth of burst explosion are shown in Fig. 3.4. Gas venting begins to occur at 110 msec. Vertical motion still evident at 200 msec can only be followed qualitatively.

Some frames from movies of the 80-foot depth of burst explosion are shown in Fig. 3.5. Venting of the high pressure gas bubble begins at 1.54 seconds. That the material moved farther on the side of venting can be seen in the crater photo (Appendix A, Fig. A.6) where more debris is apparent on the right. (The fence visible on the left is 200 feet from surface ground zero.)
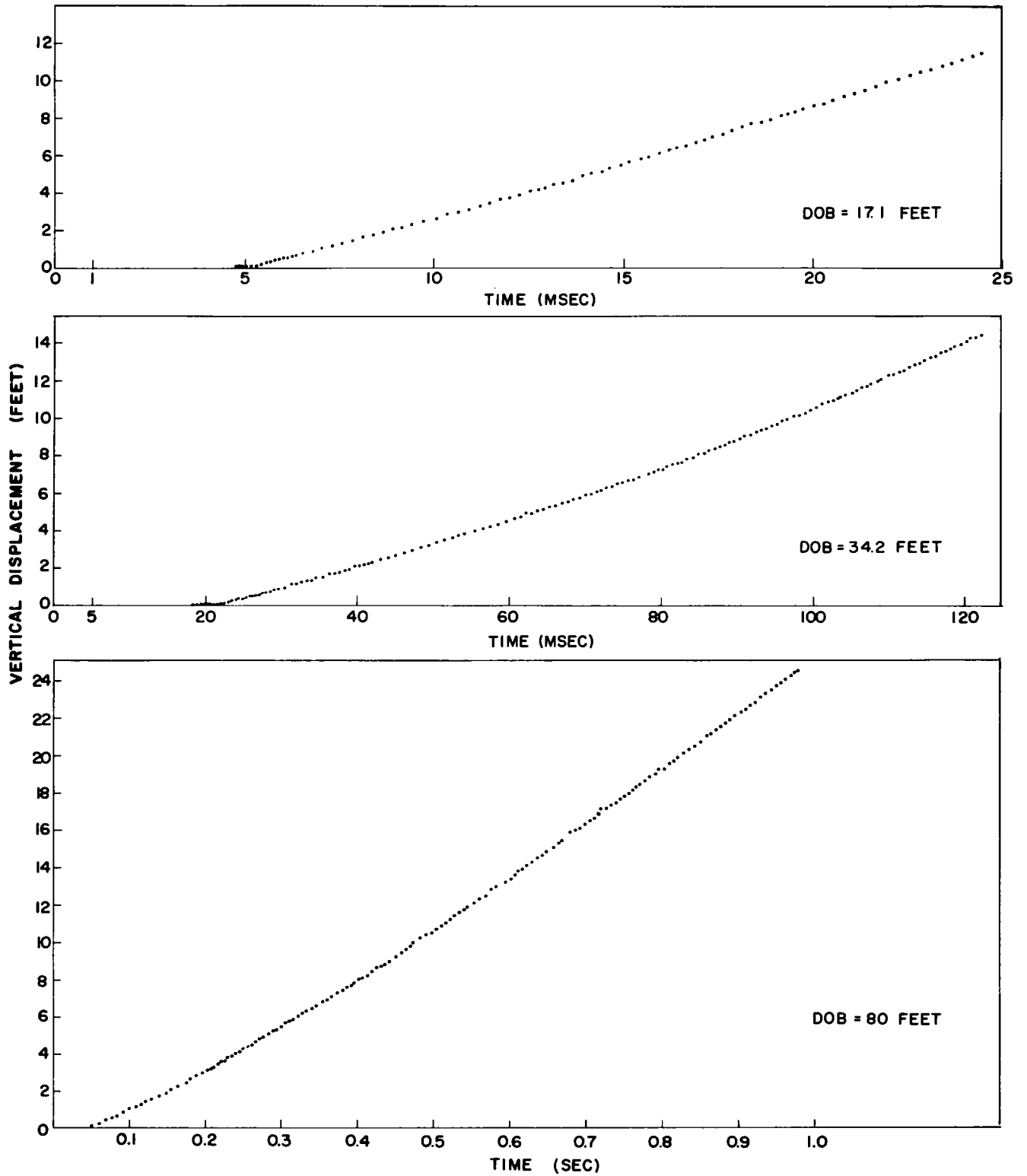
Fig. 3.1 Vertical displacements versus time.

50
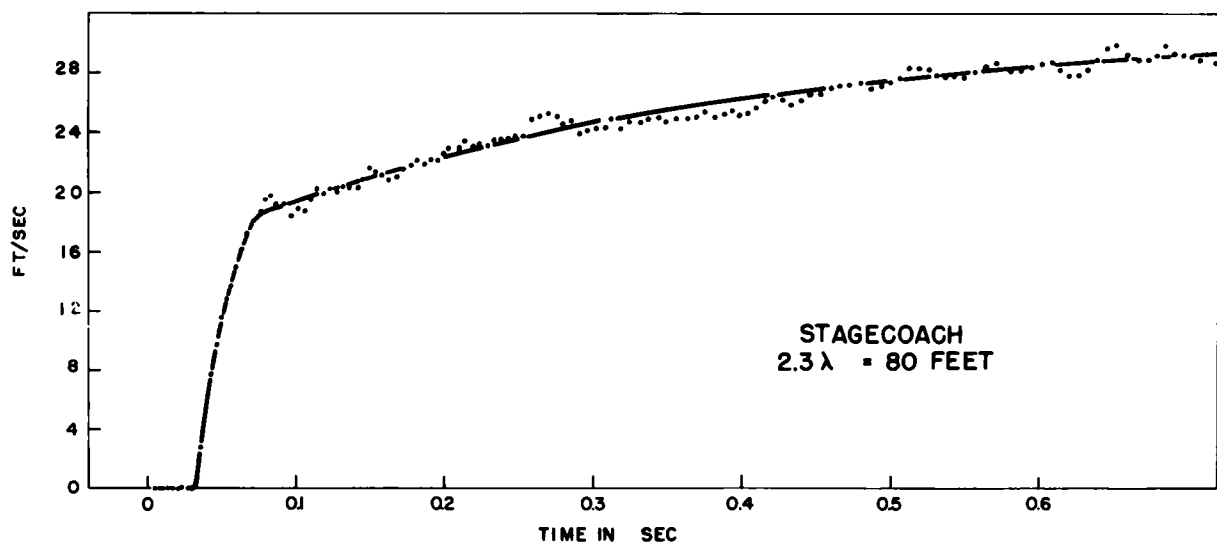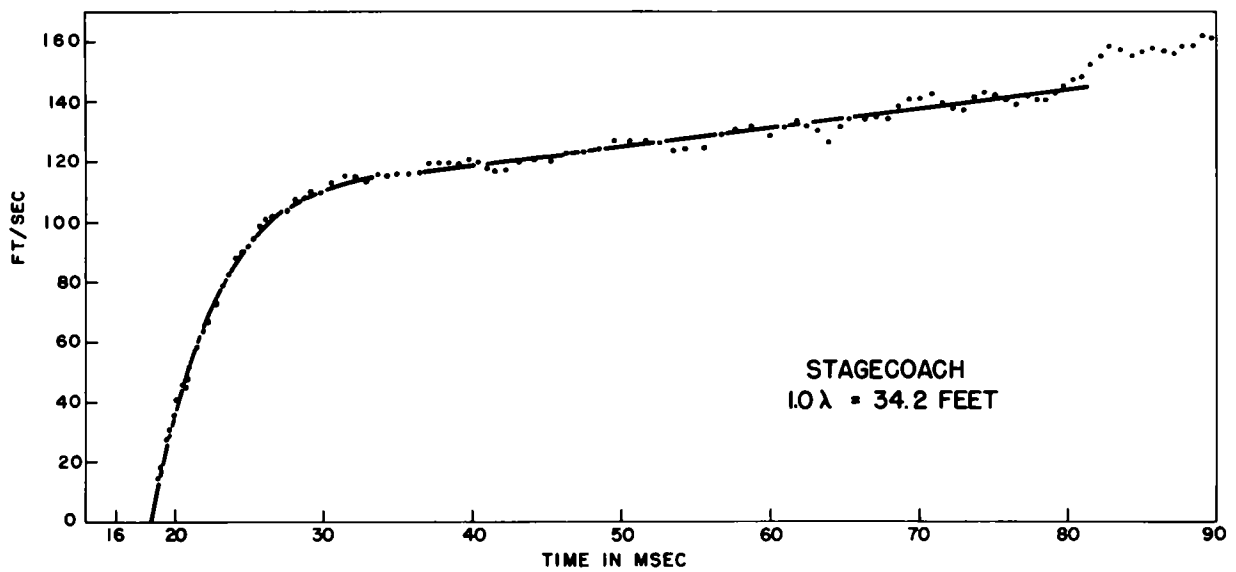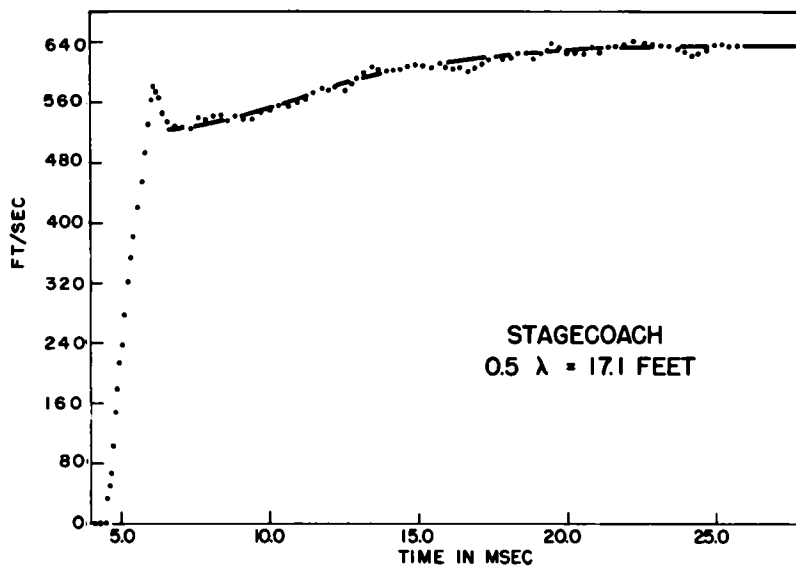
Fig. 3.2 Initial vertical surface velocities.
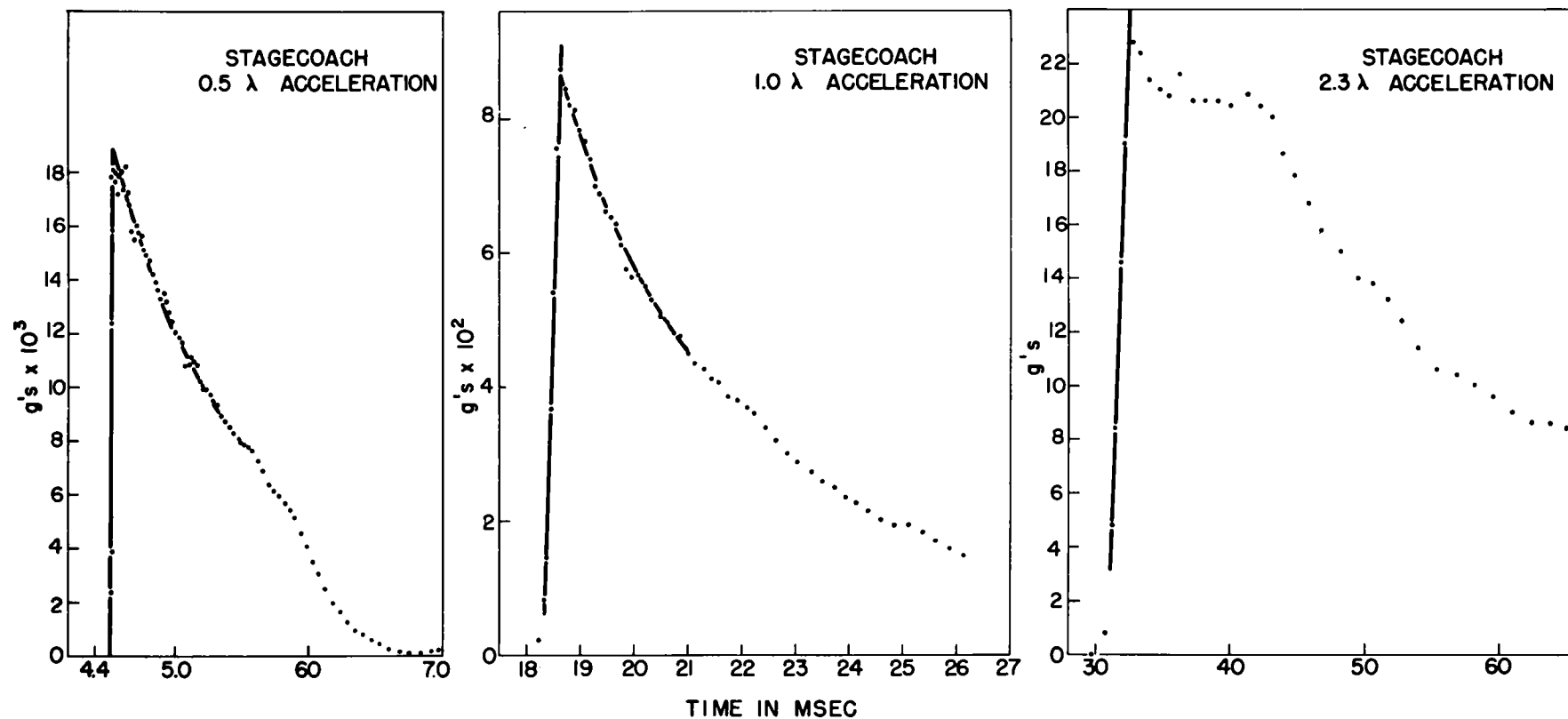
Fig. 3.3 Initial vertical surface accelerations.
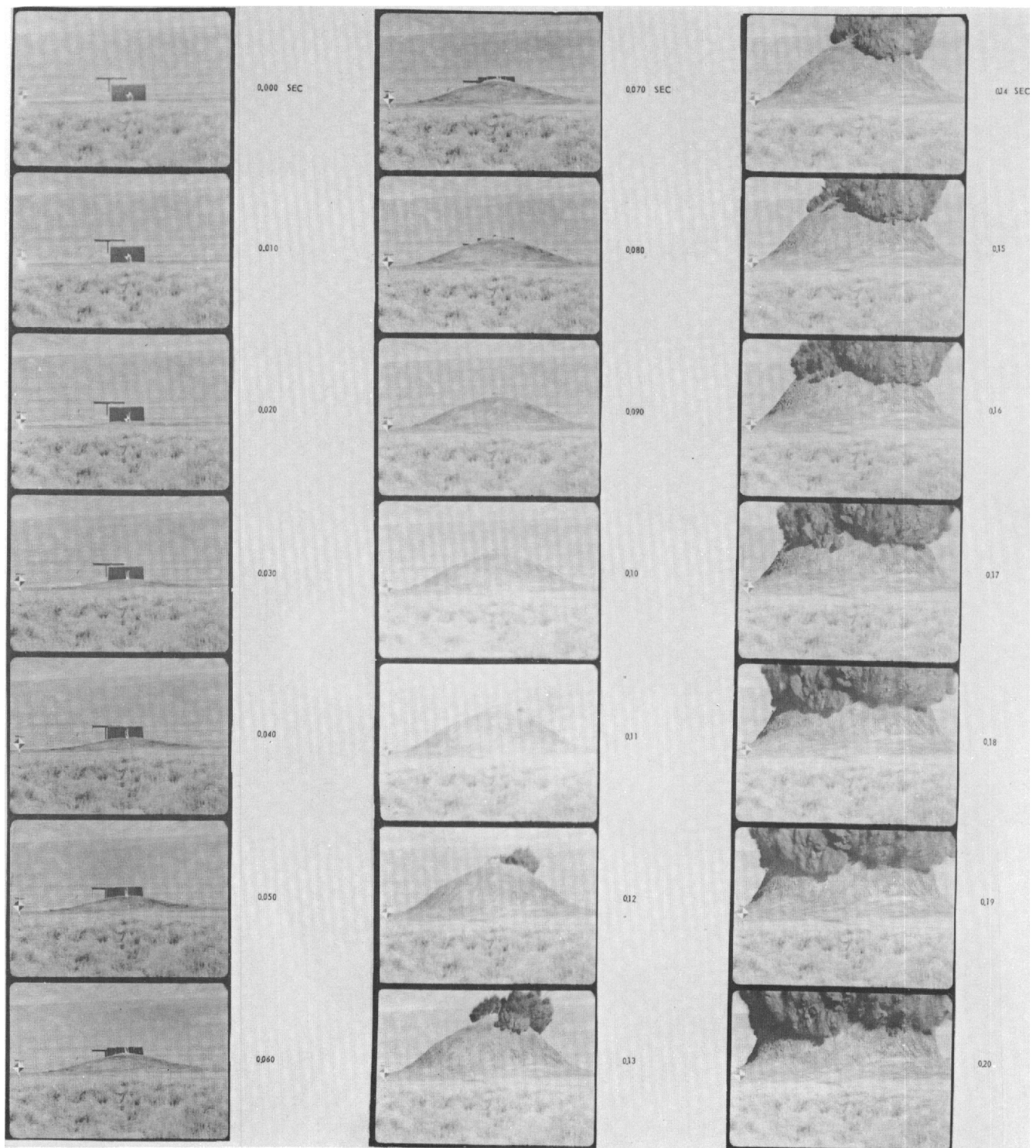
Fig. 3.4   Frames from 35-mm surface motion photography for 20 tons burst at depth of 34 feet. Width of field of view is 104 feet.
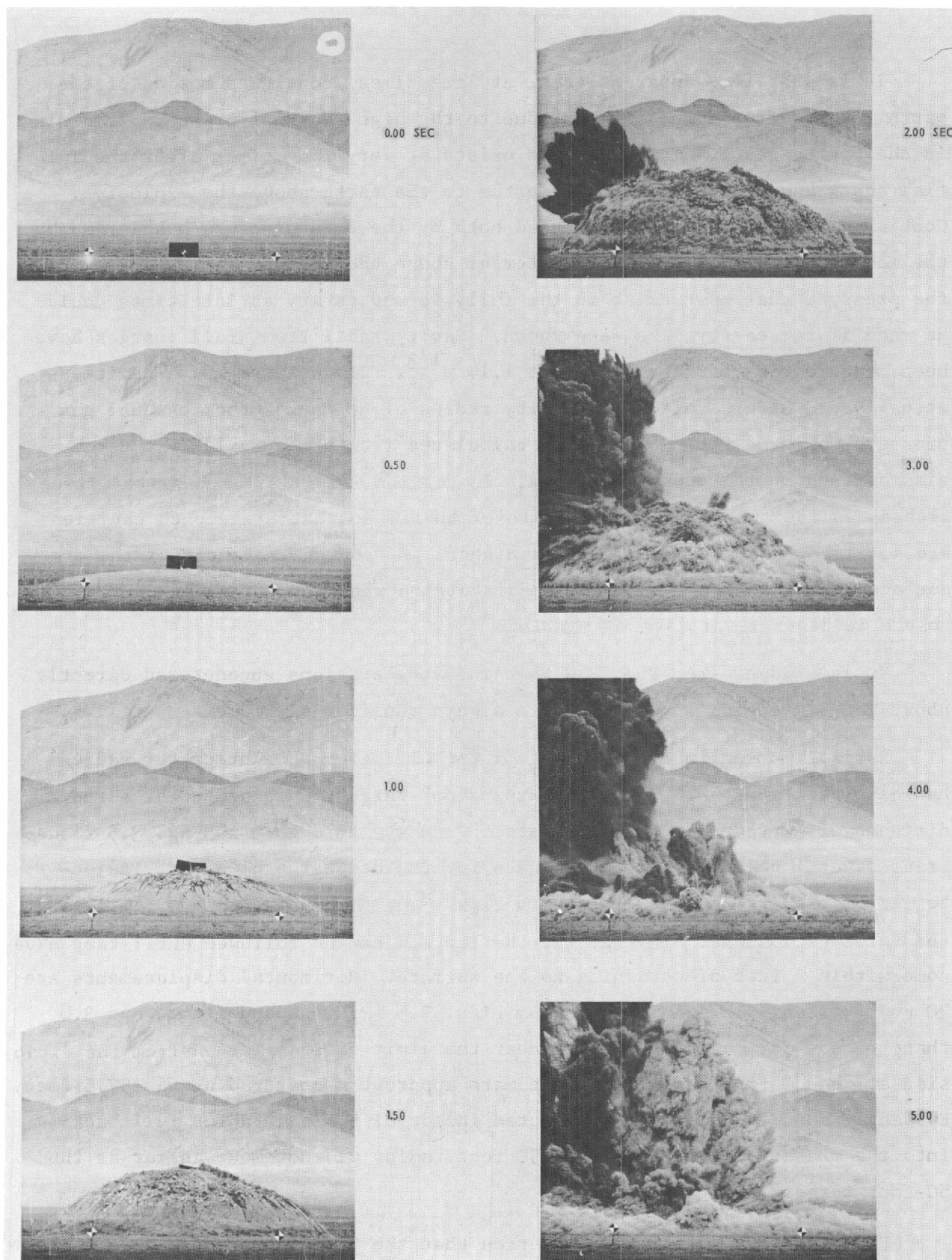
Fig. 3.5 Selected frames from 35-mm surface motion photography for 20 tons burst at depth of 80 feet. Width of field of view is 174 feet.

It is therefore apparent that, at late times, continued motion of the earth results from forces in part due to the high residual pressure remaining in the cavity space. This pressure exists at very long times after the initial shock has imparted upward momentum to the earth above the explosive. Continued late motion must be caused both by the expanding gas bubble and by the momentum trapped in all the material above the charge. An estimate of the pressure that must exist in the fully formed cavity at late times could be made if the cavity size were known. Cavity radii from small charges have been measured in other soils[1] to be $1.14 \ W^{1/3}$. If the Stagecoach cavities actually did attain this size (cavity radius of 38 feet), the residual gas pressure would be near 300 psi, as calculated from $p = (\gamma - 1)E/V$. Cavity size depends on the depth of burial. In section 2.2 it is argued that it decreases as the cube root of the depth of burst, so that Stagecoach cavities are smaller than this and pressures higher. Of course, movement of the free surface allows cavity expansion and distortion with an ultimate drop to atmospheric pressure at time of venting.

It is evident from Fig. 3.3 that the accelerations encountered directly above the Stagecoach explosions were always considerably in excess of 1 g.

Surface motion in the vicinity of the ultimate apparent crater radius has also been analyzed. For each explosion, targets were placed at a radial distance of 50 feet from surface zero. Frames 2 through 5 in Fig. 3.5 illustrate several positions of the targets for the deepest explosion. Trajectories of these targets are shown in Figs. 3.6, 3.7, 3.8, and 3.9 for each of the three explosions. In Fig. 3.9 the targets can be followed until they have come within 2 feet of returning to the surface. Horizontal displacements are 30 and 35 feet. It is apparent from Figs. 3.5 (2.00-second frame) and 3.8 that, except for dust, 30 feet is near the limit of translation from the explosion at the 80-foot depth. The ultimate apparent crater radius was 57.5 feet. Evidently most of the material ejected inside of 50 feet radius fell back into the crater. Material beyond 50 feet radius did not move as far as the 50-foot targets.

From Fig. 3.4, it may be inferred that the 50-foot targets moved horizontally considerably more than 30 feet for the 34-foot-depth explosion. Other information on particle trajectories may be inferred from data in Chapter 5.
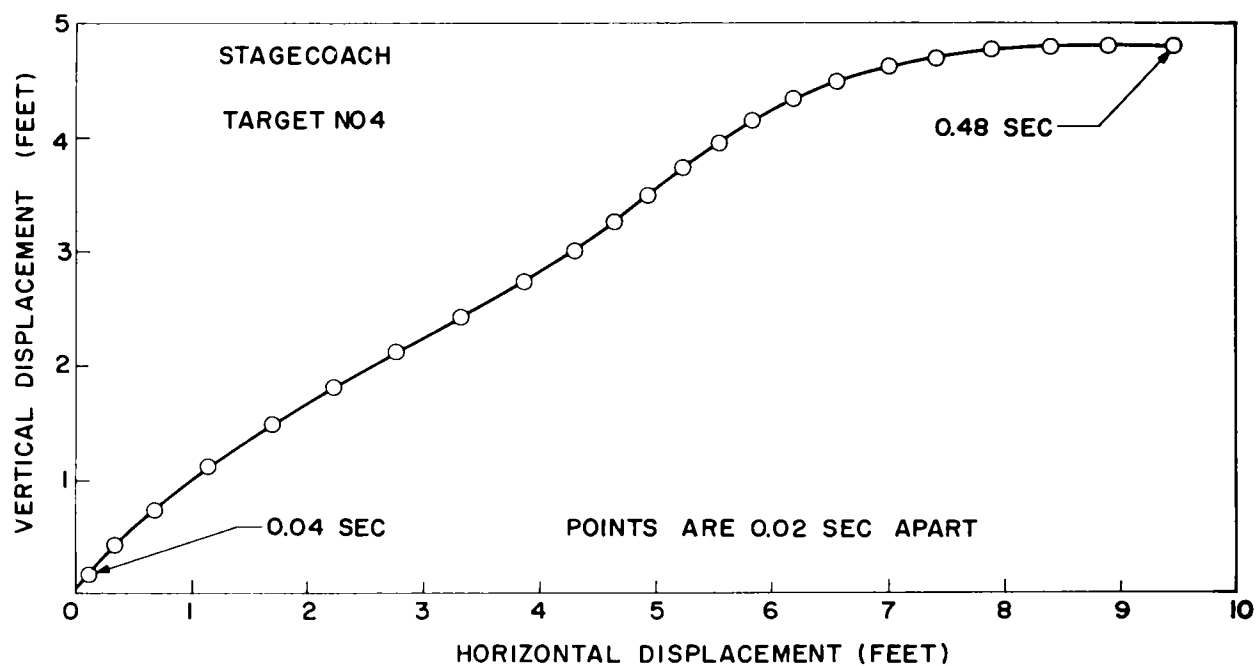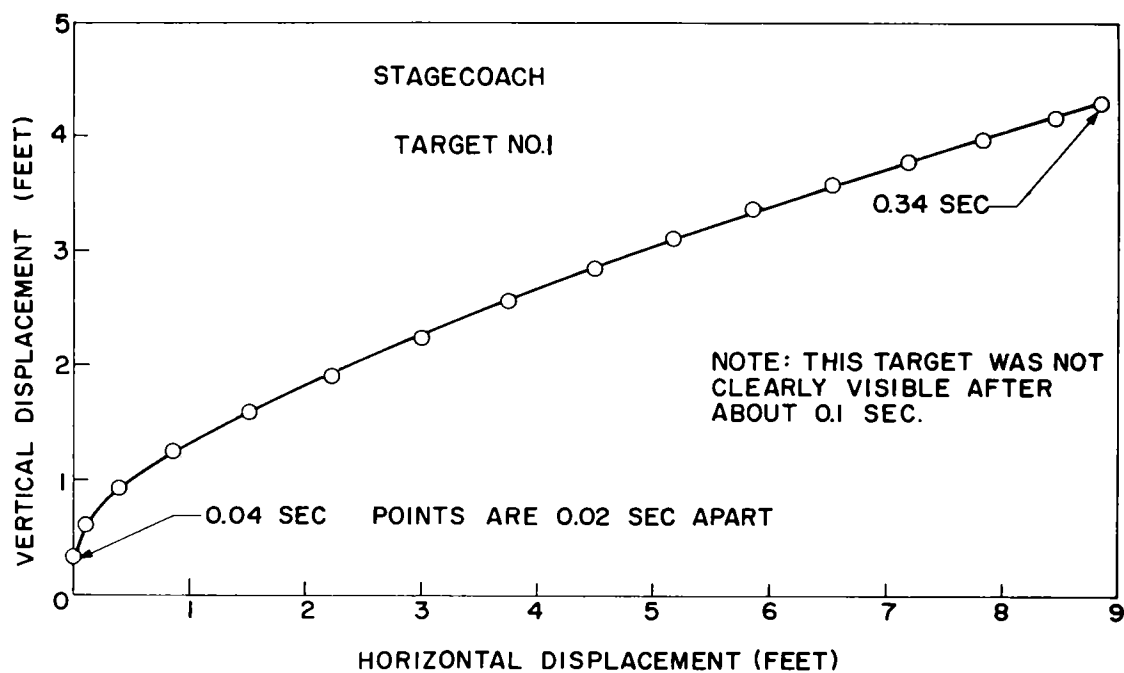
Fig. 3.6 Trajectories of targets at 50 feet from surface
zero, 17.1-foot DOB.
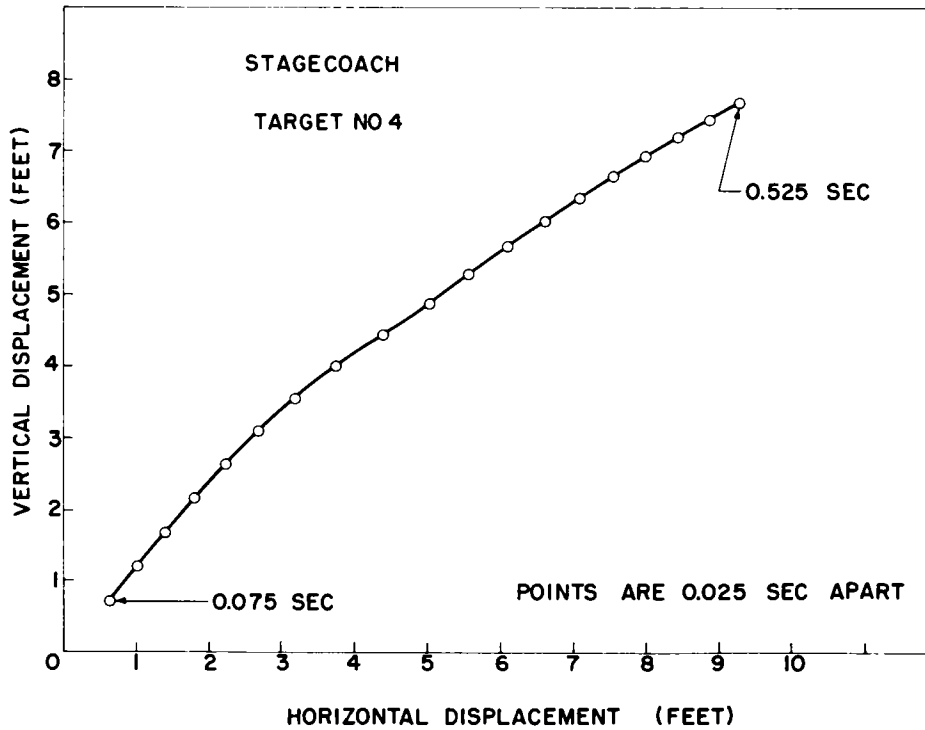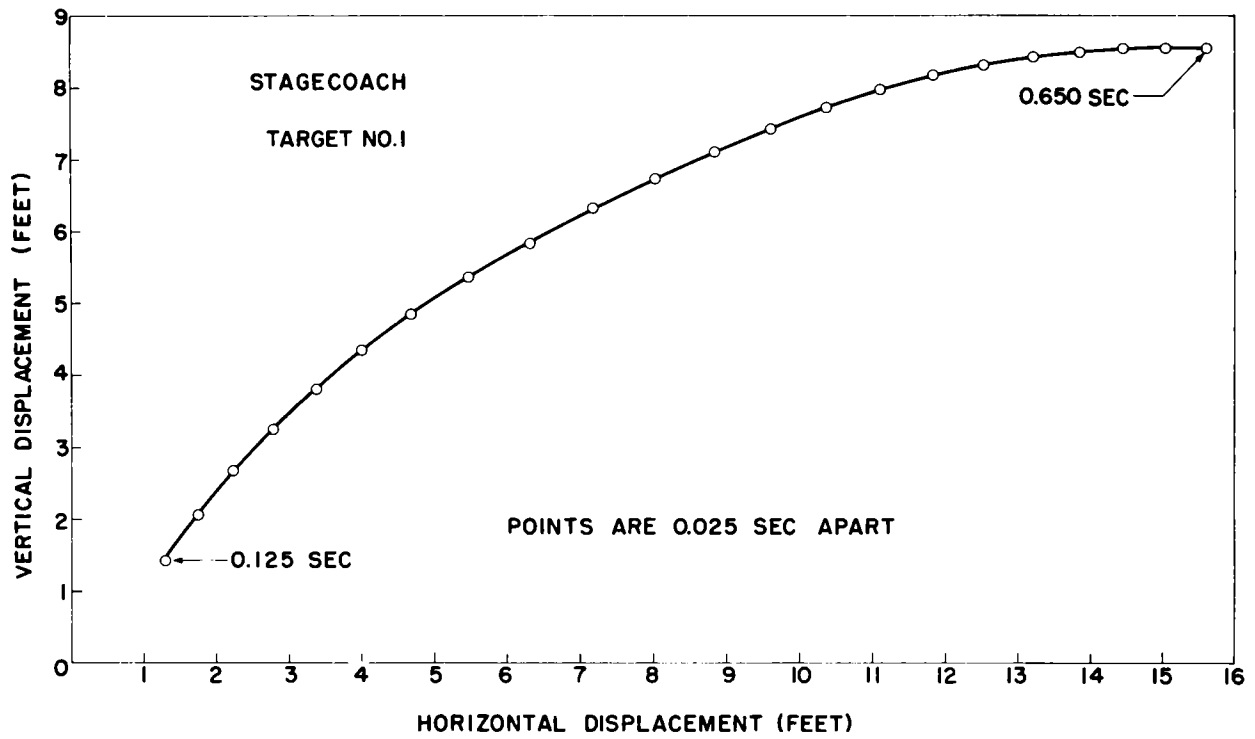
Fig. 3.7 Trajectories of targets at 50 feet from surface zero, 34.2-foot DOB.
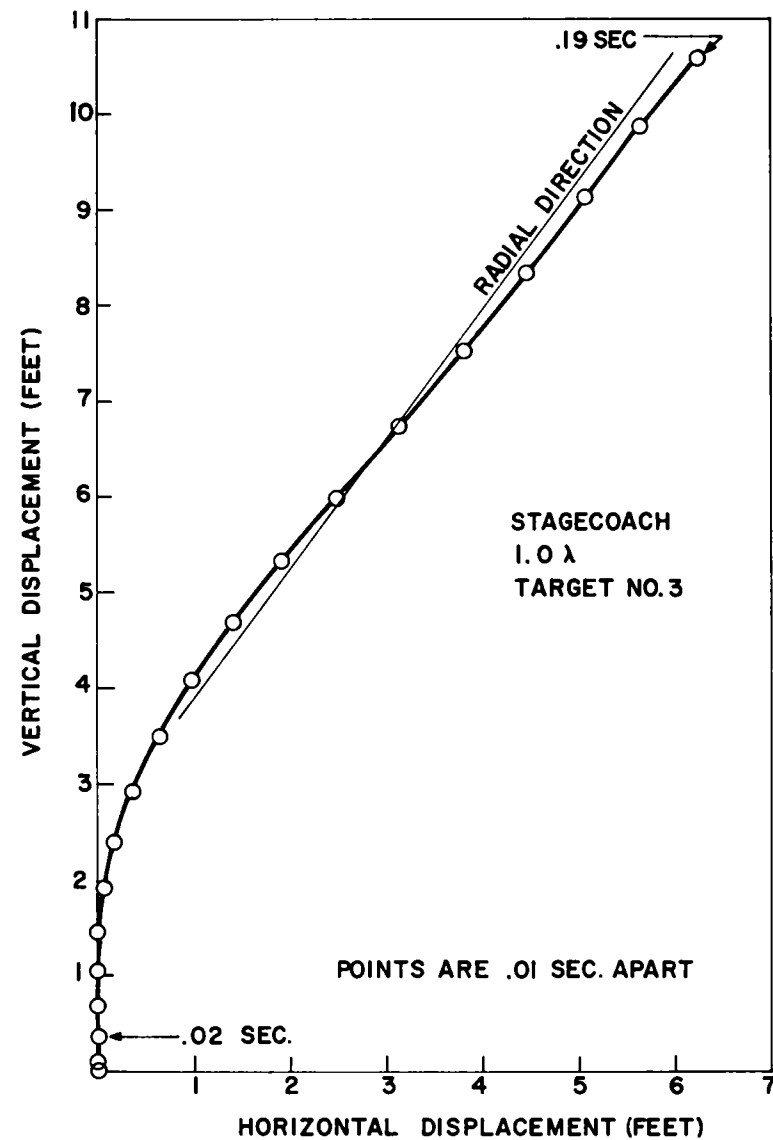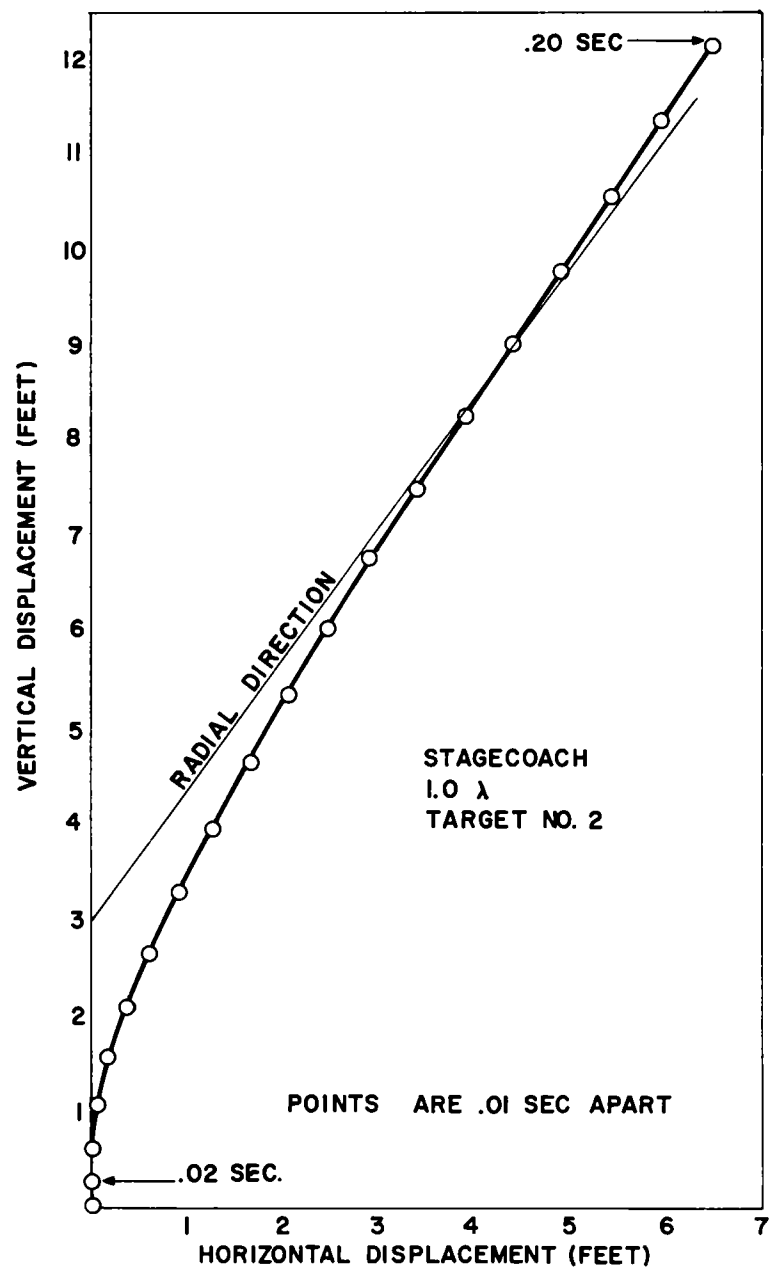
Fig. 3.8 Trajectories of targets at 25 feet from surface zero, 34.2-foot DOB.
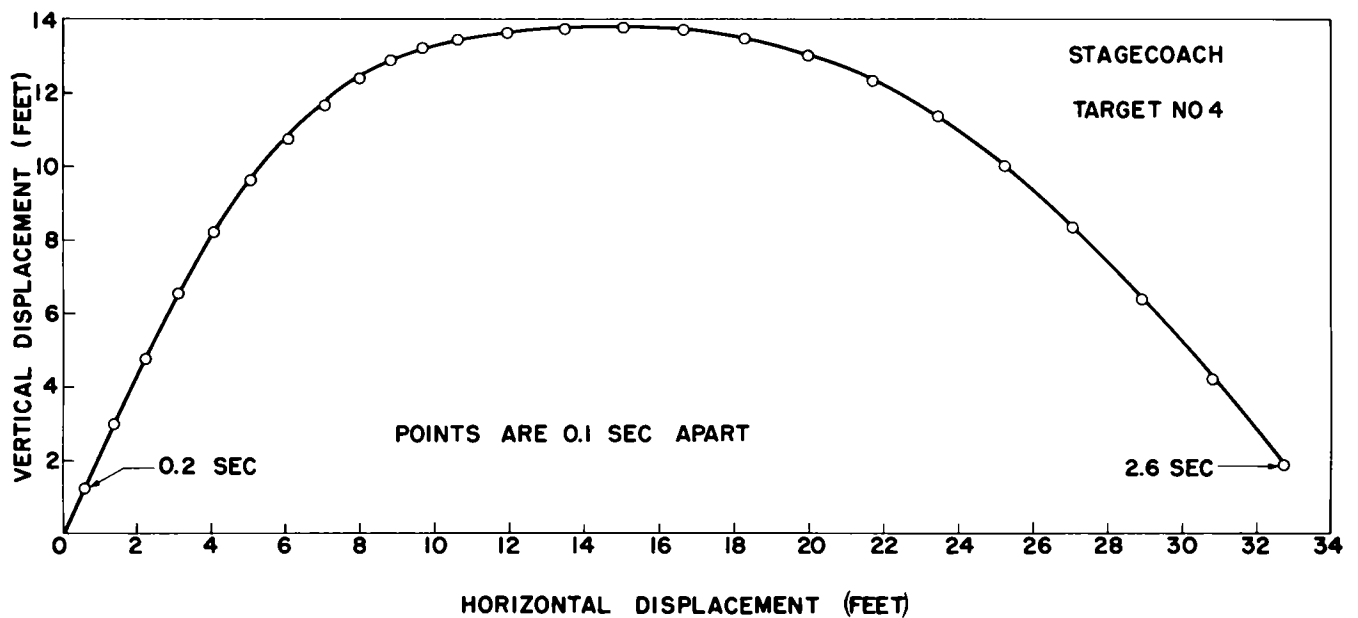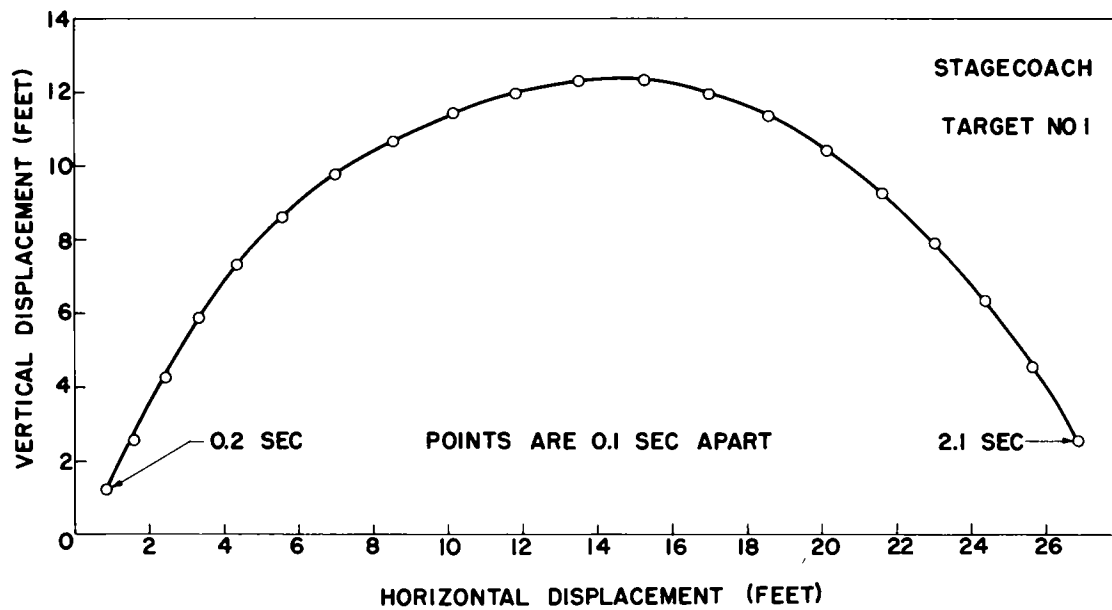
Fig. 3.9 Trajectories of targets at 50 feet from surface
zero, 80-foot DOB.

3.3 MECHANISM OF CRATER FORMATION

Several qualitative statements about the mechanism of crater formation can be made from examination of surface motion. The beginning of two of the three acceleration pulses are consistent with time of arrival of the shock at the surface:

Depth of burst (ft)	Depth to HE surface (ft)	Time of arrival (msec)	Sonic velocity (ft/sec)
17.1	11.6	4.52	2570
34.2	28.7	18.2	1580
80.0	74.5	30	3000

Thus, initial high accelerations are to be attributed to the reflected stress at the surface. Magnitude of initial vertical velocity ought to be twice observed peak particle velocity in the medium.

Examination of Fig. 3.2 shows that at such time as the peaks of the stress wave reached the surface, the peak particle velocities must have been 280 ft/sec at 17.1 feet, 50 ft/sec at 34.2 feet, and 9 ft/sec at 80 feet.

Time duration of the radial stress pulse (using data scaled from Project Scooter) was about 80 msec; the exact value varies with distance from the source. In the case of the 80-foot depth of burst, surface velocity continues to increase over a time at least 10 times the duration of the stress pulse. This observation confirms the earlier statement that residual cavity pressure contributes to the motion. For shallower depths of burst, this residual gas pressure may be considered a late part of the expanding explosion.

REFERENCE

1. Cratering Effects of Surface and Buried HE Charges in Loess and Clay, Technical Report No. 2-482, Waterways Experiment Station, Corps of Engineers, Vicksburg, Mississippi, June 1958.

Chapter 4

PARTICULATE DISTRIBUTION by A. J. Chabai

4.1 SCOPE OF THE EXPERIMENT

Investigation of particulate distribution from Stagecoach explosions represents part of a systematic effort to obtain data which will be useful in future Plowshare nuclear cratering events. The purpose of the Stagecoach experiments in particulate distribution was to procure quantitative information on the particulate fallback pattern, the surface area covered by fallback material, concentration of fallback at radial distances from the explosion hypocenter, and on the total mass of material deposited as fallback. The terms, particulate, fallback, and dust, are used here interchangeably to describe earth material ejected by the explosions and collected for analysis. Because of the relatively great distance of collectors from the explosions, most of the material collected was fine particulate the maximum diameter of which was much less than 1 cm; its motion during descent from the dust cloud was highly influenced by wind velocity and direction. At positions of collectors nearest the explosions, in addition to the fine particulate deposited by winds, some projectiles or missiles were also collected, as was earth material deposited by the base surge. No attempt is made to distinguish missiles (see Chapter 7) and base surge deposits from the fine particulate deposits caused by wind; however, as pointed out, at most of the collection stations the material collected is primarily fine particulate deposited by winds and is considered a good measure of fine particulate fallback.

4.2 DESCRIPTION OF EXPERIMENT AND METHOD

Particulate collectors for the 20-ton explosions at 17.1- and 34.2-foot depths were placed at intersections in a circular array as indicated in Fig. 4.1. A total of 112 collectors was used for each shot, two collectors being placed at the intersections with circles C, E, G, and H of radial lines 3, 6, 9, and 12. All collectors were placed in position the night before the shot was fired. Within an hour before firing time, several collectors were

LINE	DISTANCE (FT)
A	240
B	345
C	510
D	750
E	1095
F	1590
G	2325
H	3450
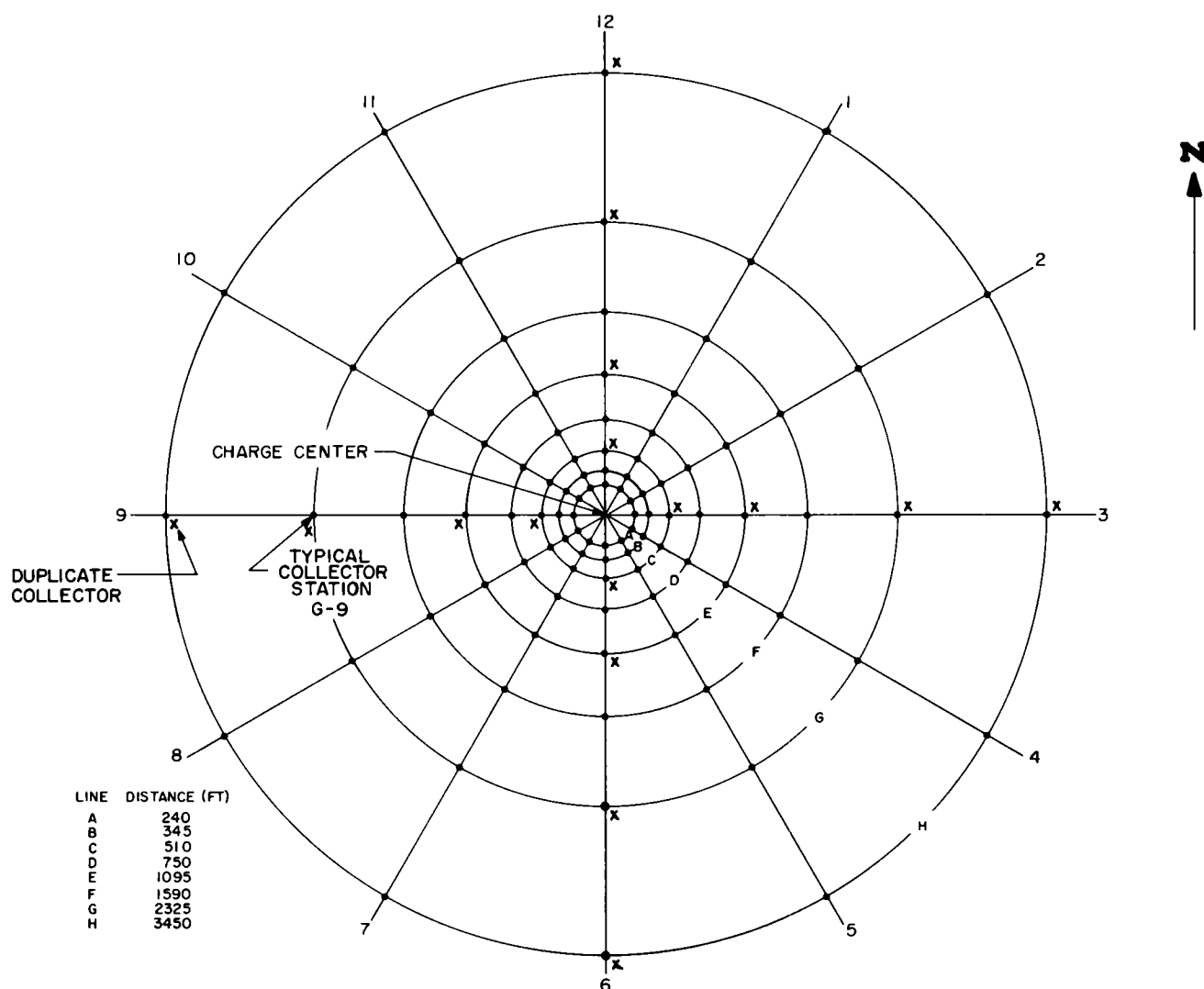
Fig. 4.1 Location of dust sampling stations.

examined to determine the amount of dust deposited overnight by wind action
and by preshot traffic within the collector array. The amount of dust deposited,
preshot, was negligible compared to the amount deposited postshot in every col-
lector examined. Particulate collectors were standard-size aluminum cake pans
(diameter - 9 inches, depth - about 1 inch). (See Fig. 12.21) Each pan was placed
on a 1-foot-square plywood board which was mounted on a stake driven into the
ground so that the bottom of the collector was level with the ground surface. An
area, approximately 6 feet in radius around each collector site, was leveled and
cleared of brush and vegetation. Fallback deposits were collected immediately
after each shot. Only necessary traffic was allowed into the array area before

collection of samples was completed. Material deposited in collectors was transferred to polyethylene bags. The bags were then sealed, marked with the station location and remarks relative to the postshot condition of the station, and then shipped to Albuquerque for analysis.

4.3 ANALYSIS OF DATA

Mass of fallback collected at each station is given in Tables 4.1 and 4.2. (See Chapter 7 for additional data.) Results of a sieve analysis on samples at nine locations from each shot are shown in Figs. 4.2 through 4.8. The isodensity contours of fallback shown in Figs. 4.9 and 4.10 were constructed from fallback collector data by use of the following procedure: Areal density of fallback (mass of material collected divided by area of collector pan) at collector stations was plotted on log-log paper as a function of radial distance of collector from hypocenter for each of the twelve radial lines on which collectors were placed. Radial distances for the particular density values used on these contours were then interpolated from the log-log plots. Similar plots of fallback density data along radial lines are shown in Figs. 5.9 and 5.10 of Chapter 5.

The total mass of fine particulates deposited by the Stagecoach explosions as a function of apparent crater volume is shown in Fig. 4.11, together with other alluvium data[1,2,3,4] and with data for dry sand,[5] dry clay,[5] and sandstone.[6] Total mass of fine particulates is defined and calculated in the following way: Average fallback density was obtained for each of the array circles, A to H, by taking the densities of the twelve stations on each circle and forming the arithmetic mean. This quantity was then used as an average fallback density at a radial distance equal to the radius of the circle for which it was computed. On a log-log plot of average density versus radial distance from hypocenter, a straight line was drawn through the data, the equation for which is given by $\rho(r) = Cr^m$ (see Figs. 4.12, 4.13, and 4.14). The mass of fine particulate was then obtained by means of the formula

$$M_F = M_o + 2\pi \int_{r_o}^{\infty} \rho(r) \, r dr \, , \qquad (4.1)$$

where M_o = the mass of fine particulate deposited within a circle of radius, $r_o \cong 7 \, W^{1/3}$ (r in feet and W in pounds), the mass having a constant density equal to Cr_o^m.

TABLE 4.1   PARTICULATE DISTRIBUTION OF MASS OF FALLBACK COLLECTED
AT VARIOUS STATIONS, STAGECOACH 17-FOOT SHOT

Charge weight: 40,000 lbs   <u>Apparent Crater Measurements</u>

Depth of burst: 17.1 ft

Medium: Desert alluvium   Radius: 50.5 ft

Size of collector: 9-inch diameter   Depth: 23.6 ft

Total fallout mass: 5.52×10^8 Volume: 83,600 ft^3

(Mass in grams.)

	A	B	C	D	E	F	G	H
1	222.74*	40.23	5.51	0	0	0	0	0
2	158.94*	63.09	14.96	3.38	0	0	0	0
3	123.16*	39.49	12.1 10.9	0	0.07 0	0	0 0	0 0
4	224.72*	98.95*	18.73	0.31	0.17	0.31	0	0
5	28.53*	110.87*	31.82	3.18	0	0	0	0
6	322.71*	48.95	344.37 192.98	9.93	13.4 12.3	4.38	0 0	0 0
7	23.43*	393.6	33.30*	54.40*	19.40	5.95	2.81	1.78
8	68.97*	287.17	204.05*	18.80*	26.12	8.39	2.58	1.83
9	184.50*	76.47*	69.3* 17.5*	62.81*	14.0 15.2	9.31	2.94 3.12	0.68 0.48
10	2875.7*	152.93*	34.51*	32.83	7.15	1.90	0	0
11	12.05*	19.62*	16.66*	17.24	0	0	0	0
12	178.17*	79.47*	19.8 23.6	0	0 0	0	0 0	0 0

*Collector was destroyed; sample was taken from 1- x 1-foot board on which
collector rested.

TABLE 4.2 PARTICULATE DISTRIBUTION OF MASS OF FALLBACK COLLECTED
AT VARIOUS STATIONS, STAGECOACH 34-FOOT SHOT

Charge weight: 40,000 lbs Apparent Crater Measurements

Depth of burst 34.2 ft

Medium: Desert alluvium Radius: 58.6 ft

Size of collector: 9-inch diameter Depth: 29.2 ft

Total fallout mass: 1.333×10^9 gm Volume: 145,000 ft^3

(Mass in grams.)

	A	B	C	D	E	F	G	H
1	X	131.00	44.33	4.68	0	0	0	0
2	771.42*	68.99*	93.73	29.39	0	0	0	0
3	X	X	19.70 18.20	5.13	0 0	0	0 0	0 0
4	X	X	92.02	54.39	14.81	0	0	0
5	X	377.49	0	19.47	7.66	5.42	0	0
6	X	X	176.93 X	64.09	17.30 10.21	7.60	0.64 0.58	0.27 0.50
7	2458.9*	1028.2	416.72	143.56	13.31	5.15	2.04	0.75
8	3010.9	1145.9	426.69	112.00	2058.7	6.43	2.58	0.38
9	1434.4*	1066.6*	X X	116.30*	14.79 13.95	5.73	4.90 4.44	0 0
10	710.99*	425.59	184.17	41.27	16.17	7.65	0	0
11	623.71	203.14	103.95	21.71	5.48	0	0	0
12	733.29*	113.57*	66.33 73.68	24.71	0 0	0	0 0	0 0

Note: X indicates station location where collector was destroyed; no sample was obtained.

*Collector was destroyed; sample was taken from 1- x 1-foot board on which collector rested.

U.S. STANDARD SERIES

PERCENT PASSING

○ 20 TONS, 17.1 FT
△ 20 TONS, 34.2 FT

0.42

2.0

.037   .074   .149   .297   .590   1.19   2.38   4.76   9.52

DIAMETER OF PARTICULATE (MILLIMETERS)
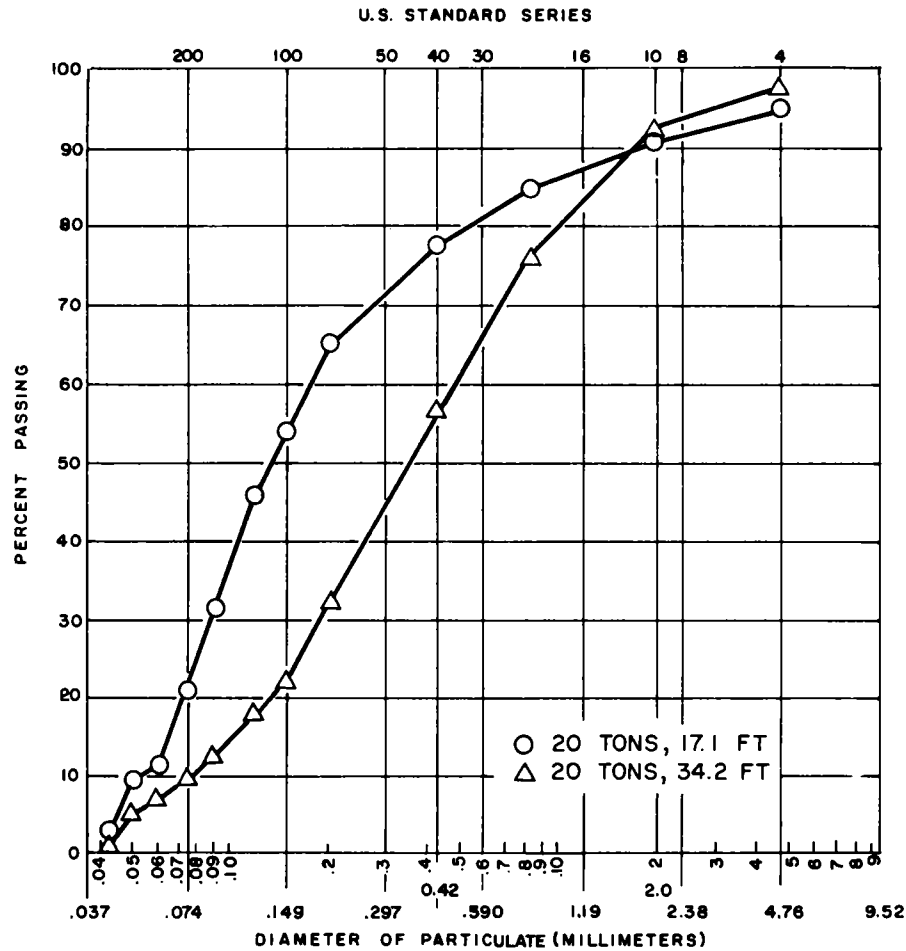
Fig. 4.2 Sieve analysis: Station A-1,
240 feet from ground zero.

U.S. STANDARD SERIES

PERCENT PASSING

○ 20 TONS, 17.1 FT
△ 20 TONS, 34.2 FT

0.42

2.0

.037   .074   .149   .297   .590   1.19   2.38   4.76   9.52

DIAMETER OF PARTICULATE (MILLIMETERS)
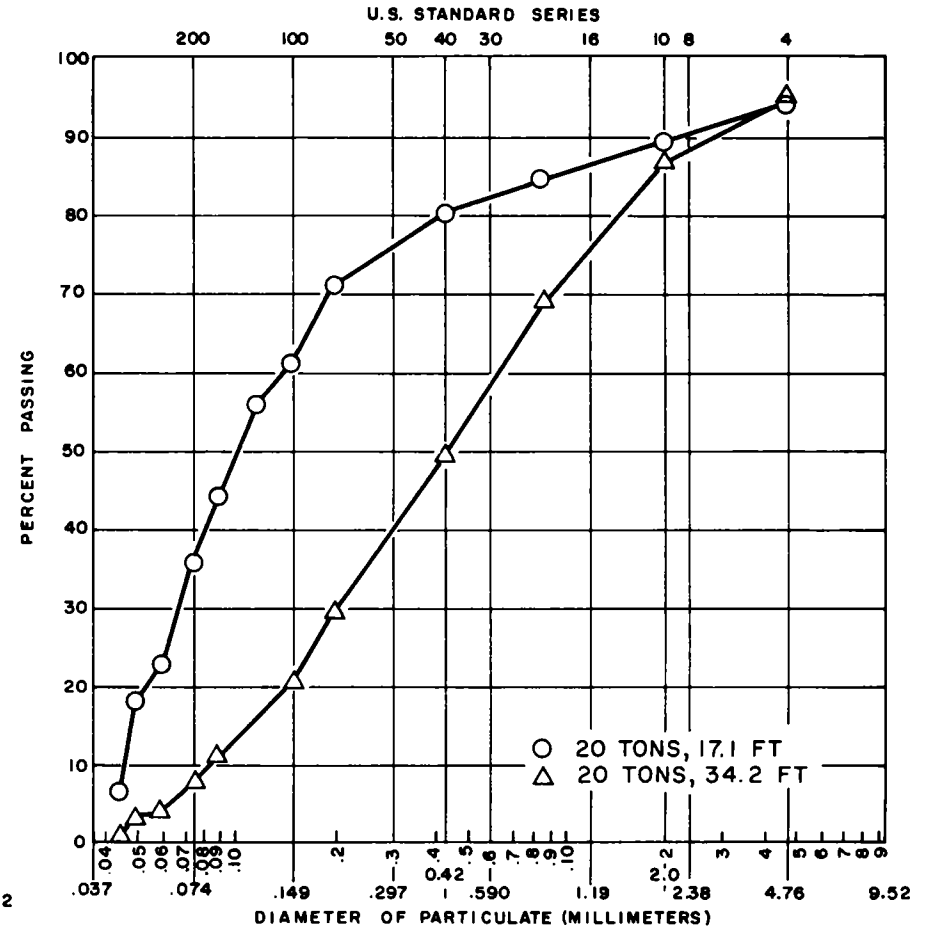
Fig. 4.3 Sieve analysis: Station B-1
345 feet from ground zero.
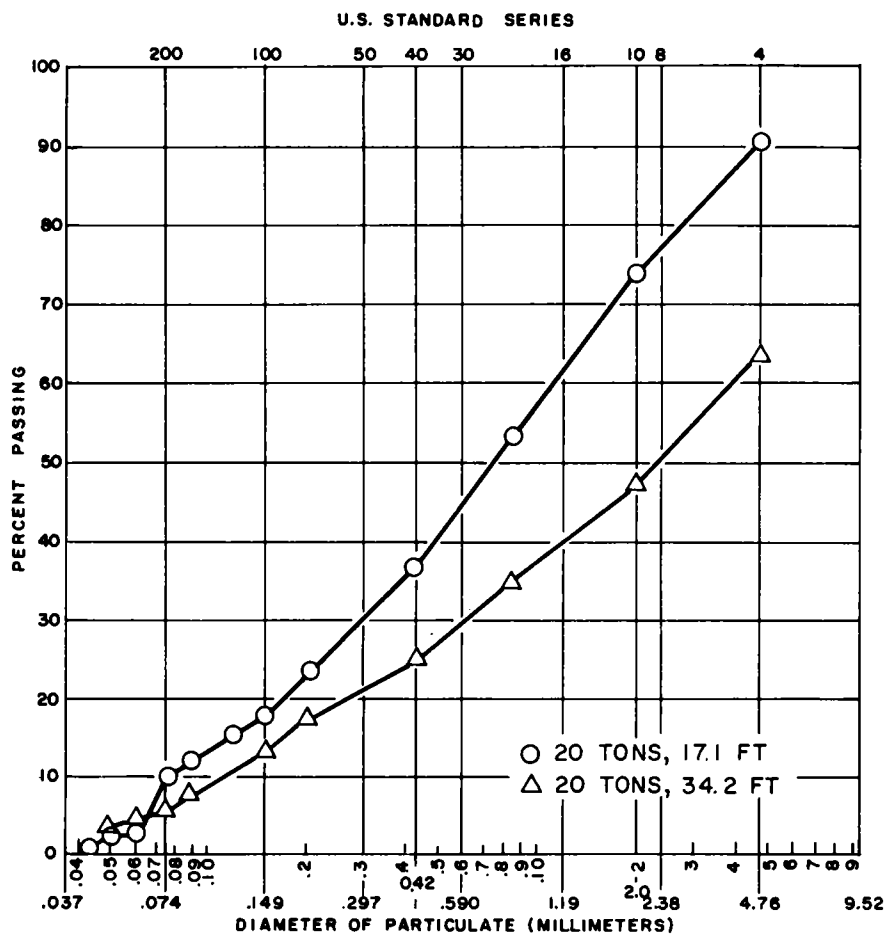
Fig. 4.4 Sieve analysis: Station B-7,
345 feet from ground zero.
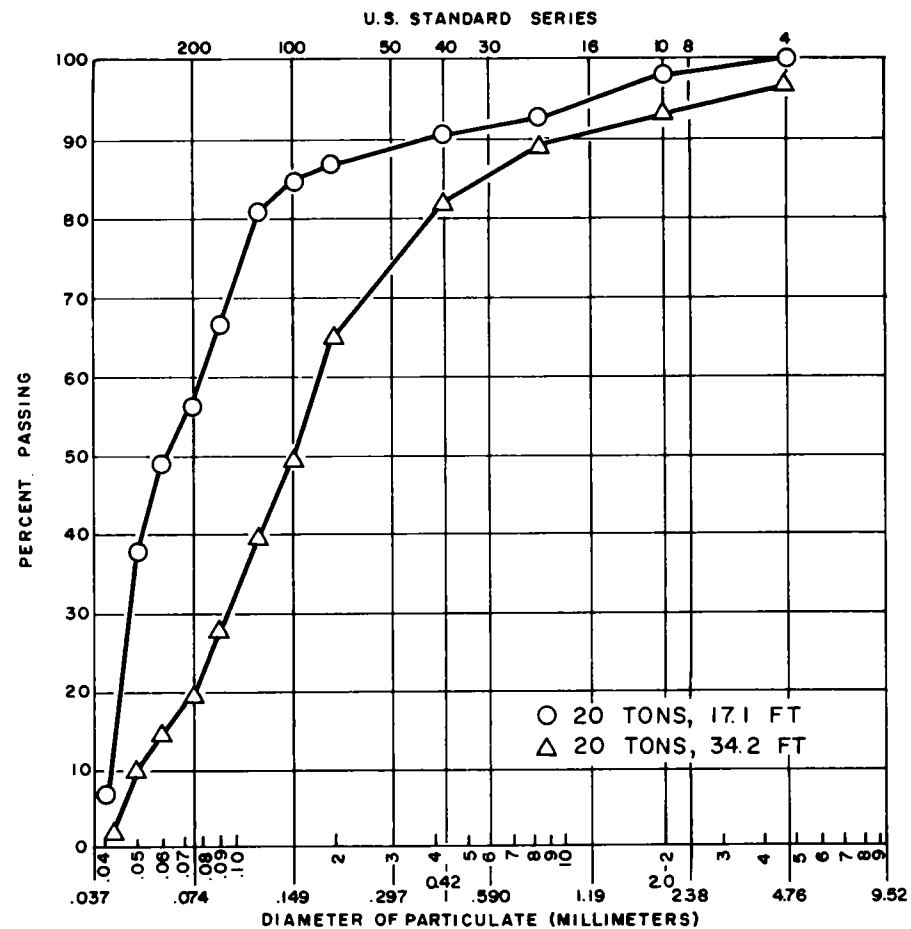
Fig. 4.5 Sieve analysis: Station C-1,
510 feet from ground zero.
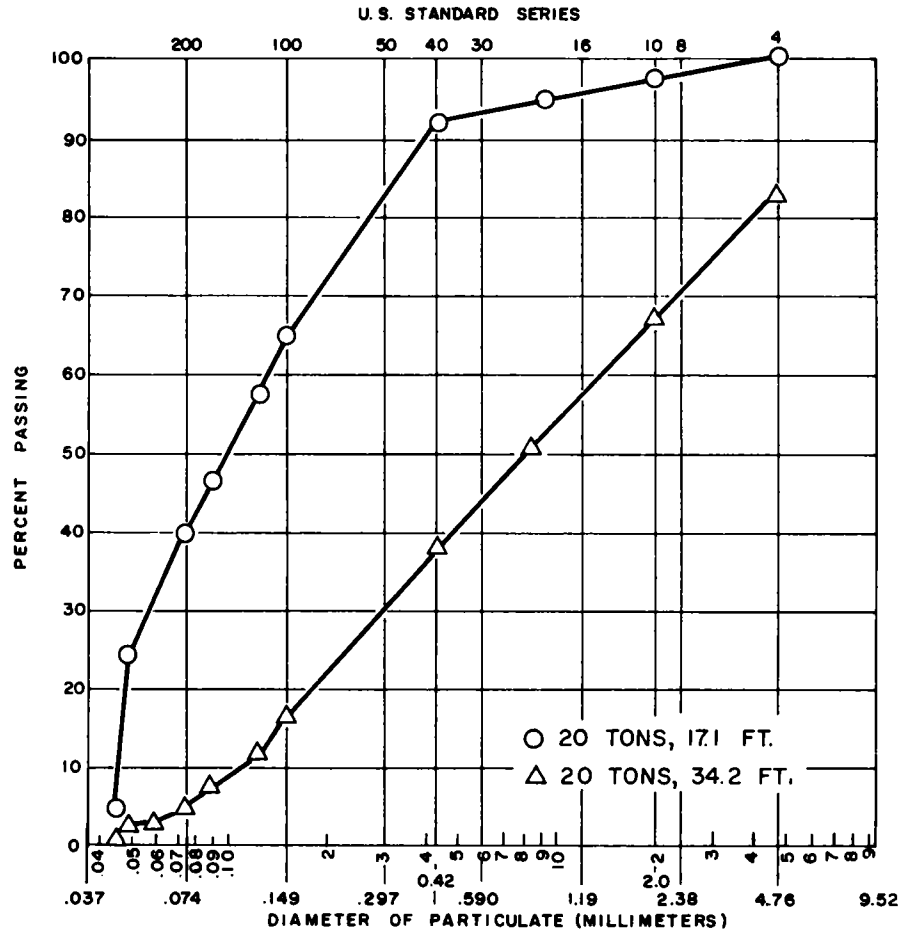
Fig. 4.6 Sieve analysis: Station C-7, 510 feet from ground zero.
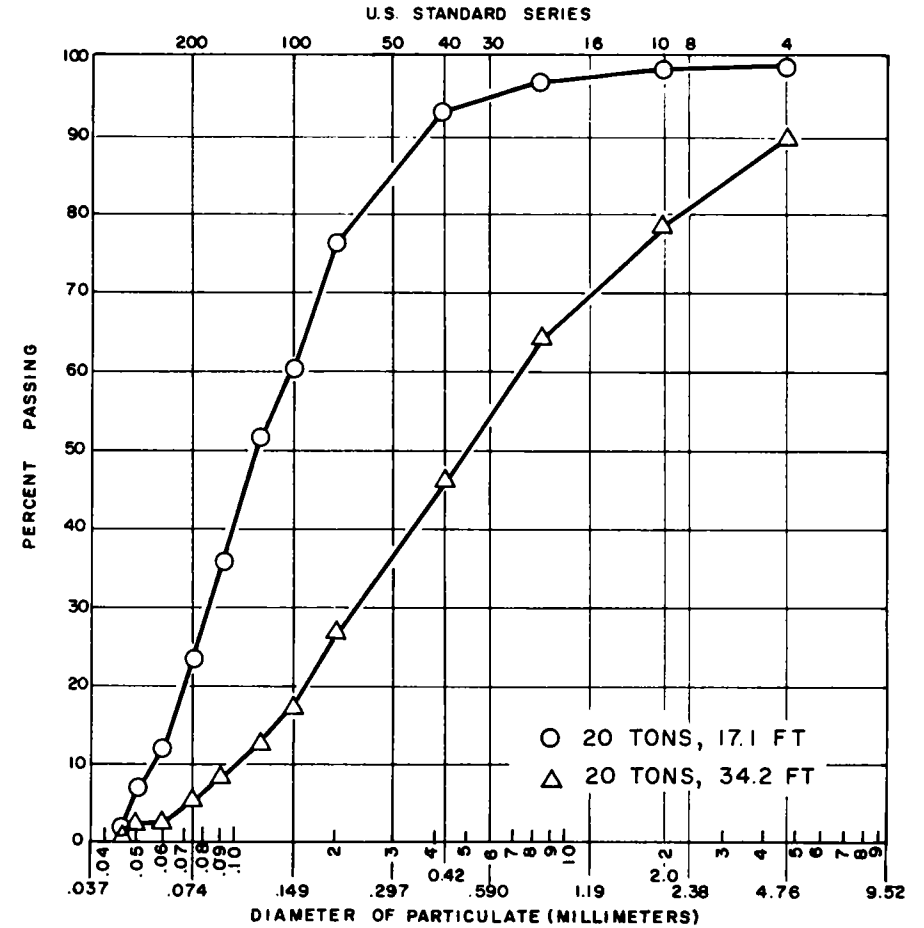
Fig. 4.7 Sieve analysis: Station D-7, 750 feet from ground zero.
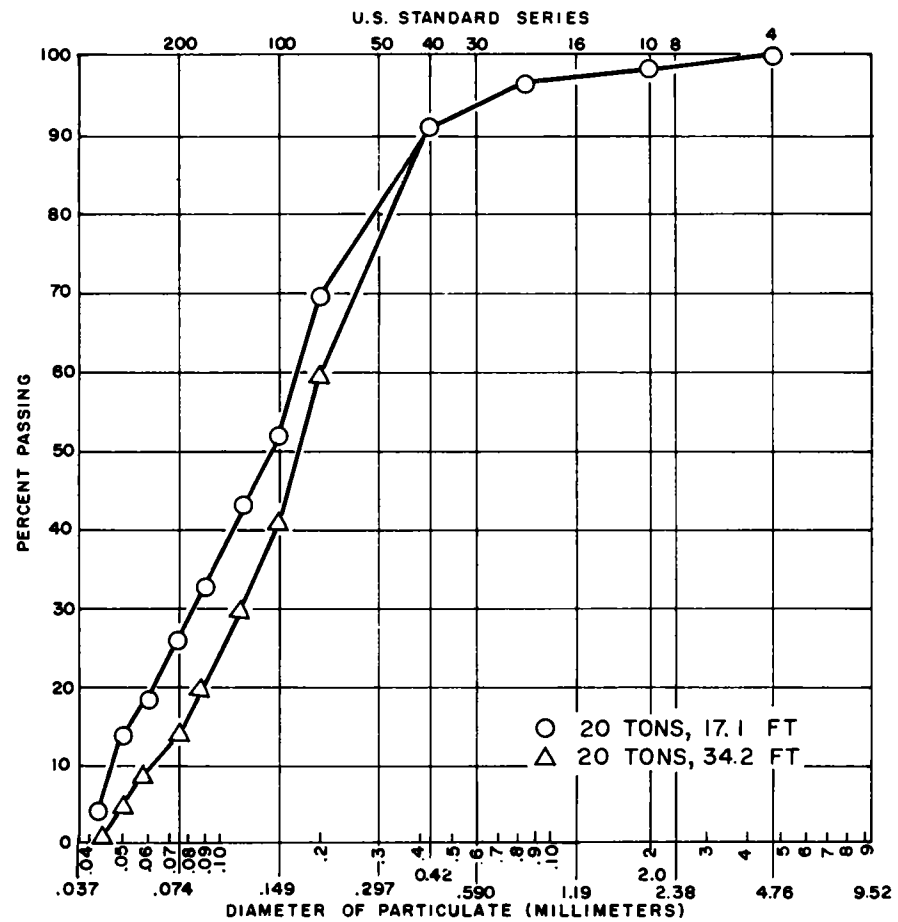
Fig. 4.8 Sieve analysis: Station E-7,
1095 feet from ground zero.
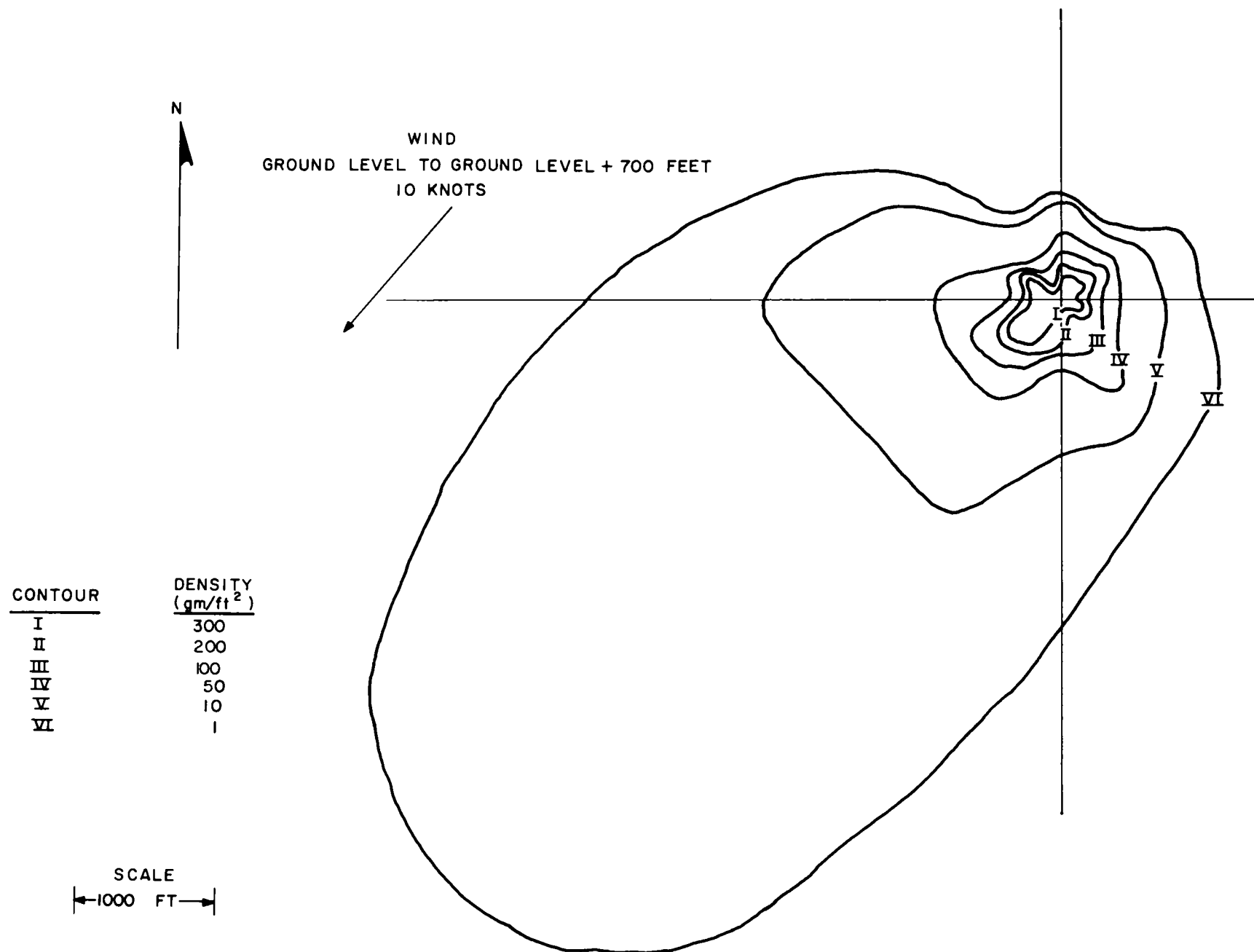
Fig. 4.9 Dust distribution pattern, 20 tons at 17.1 feet.

WIND
GROUND LEVEL TO GROUND LEVEL + 600 FEET
6 KNOTS

N

CONTOUR	DENSITY (gm/ft²)
I	1000
II	300
III	200
IV	100
V	50
VI	10
VII	1

SCALE

|←—1000 FT.—→|
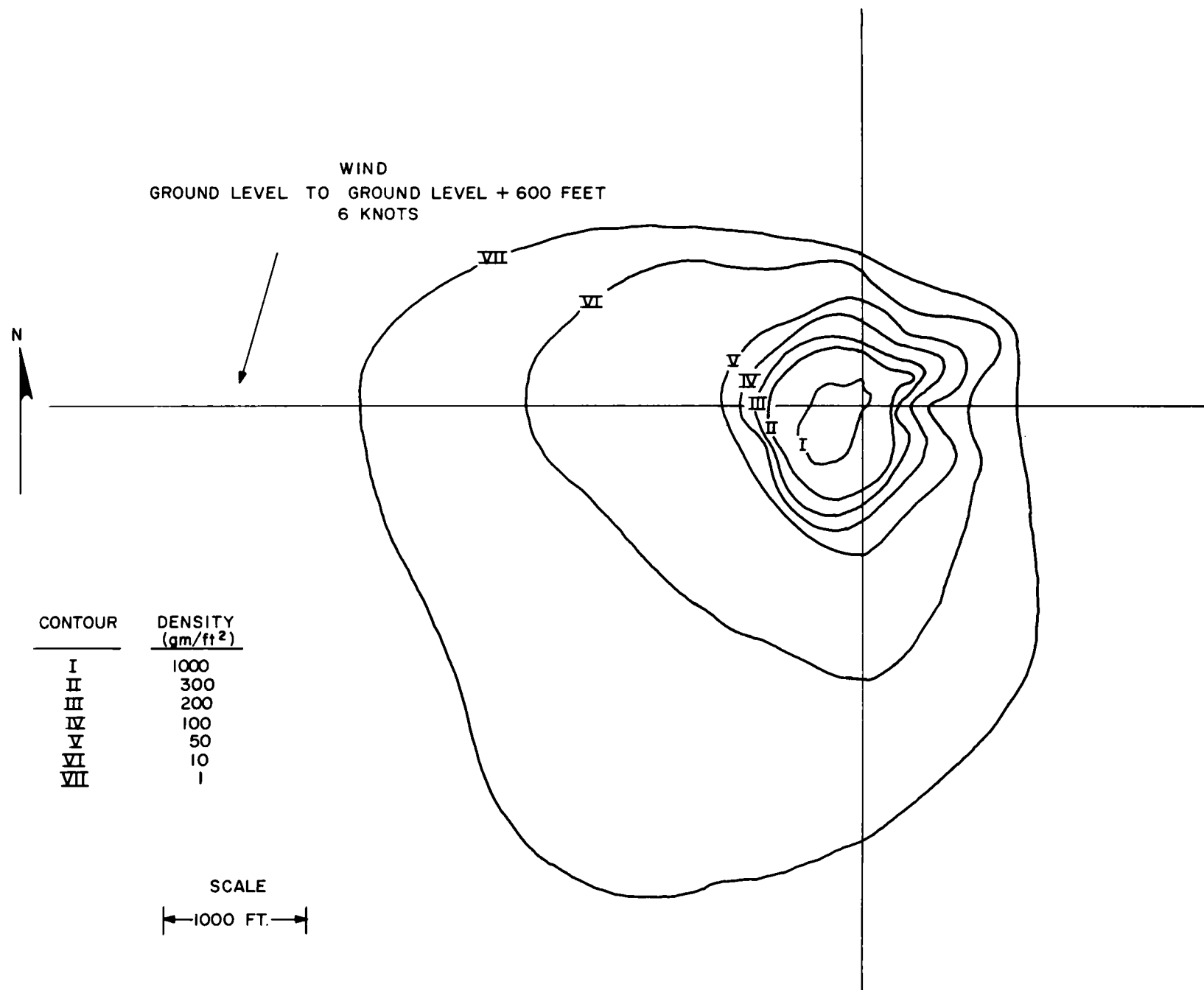
Fig. 4.10 Dust distribution pattern, 20 tons at 34.2 feet.
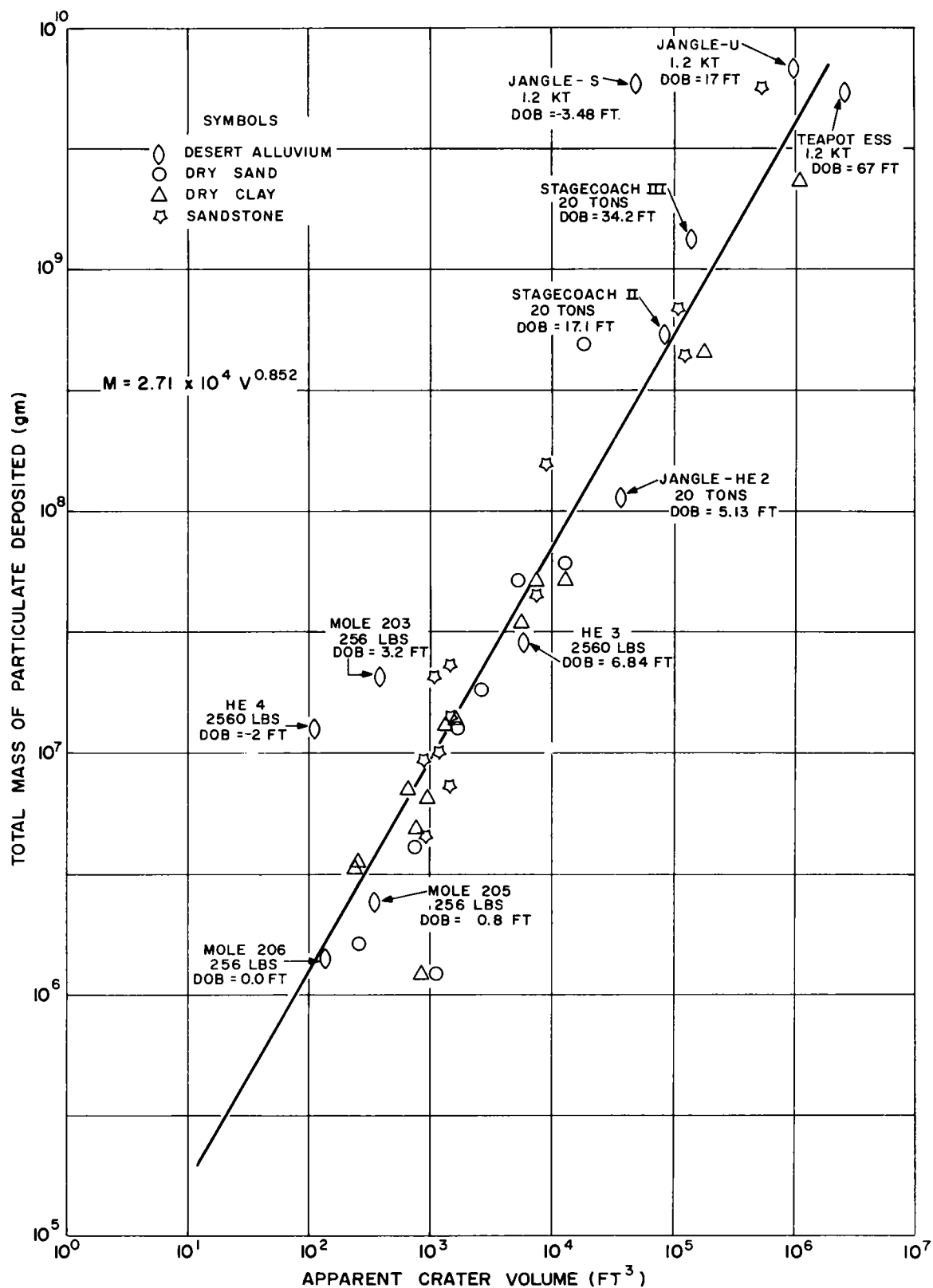
Fig. 4.11 Mass of particulate deposited versus apparent crater volume.
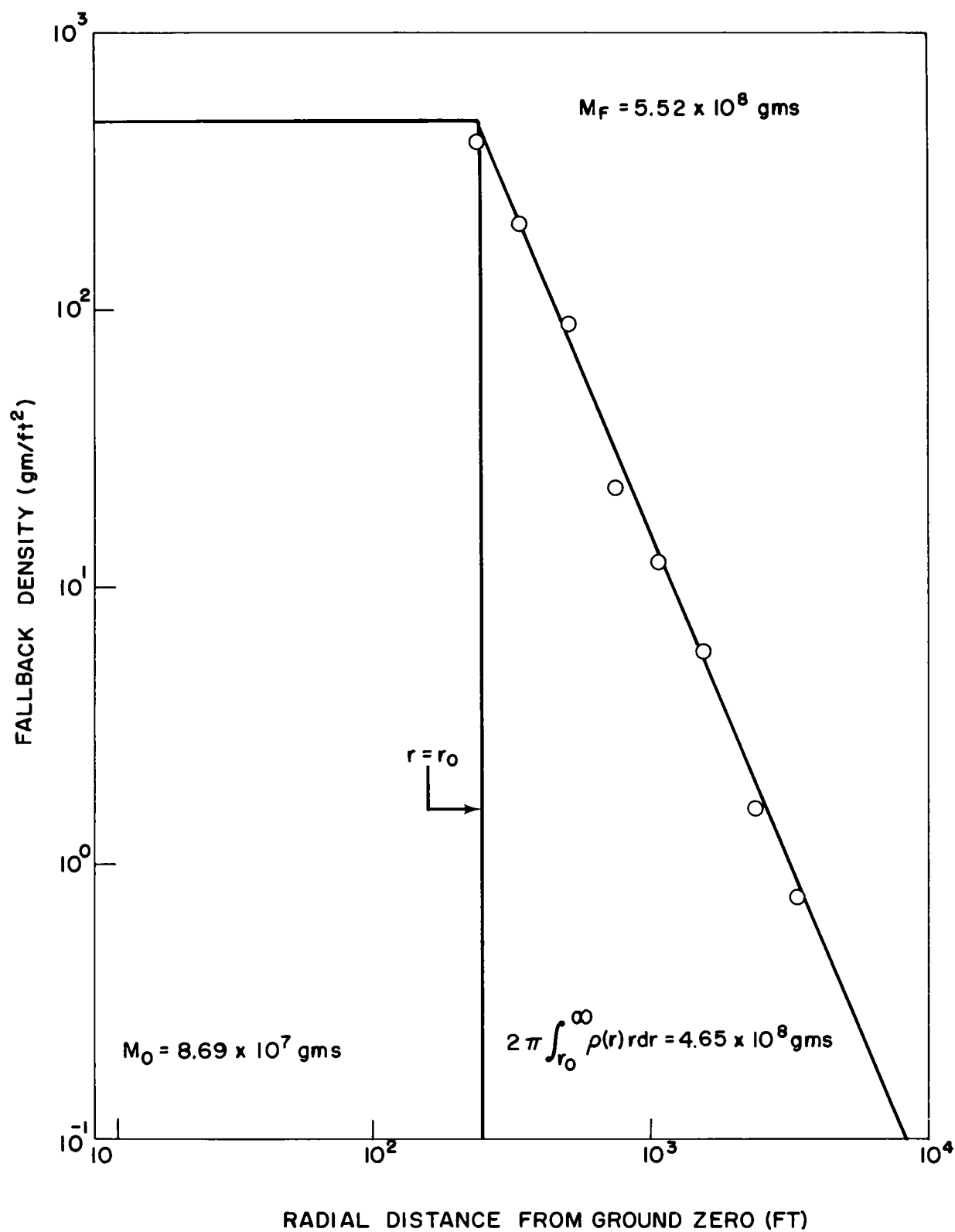
Fig. 4.12 Density of fallback versus radial distance from
ground zero, 20 tons at 17.1 feet.
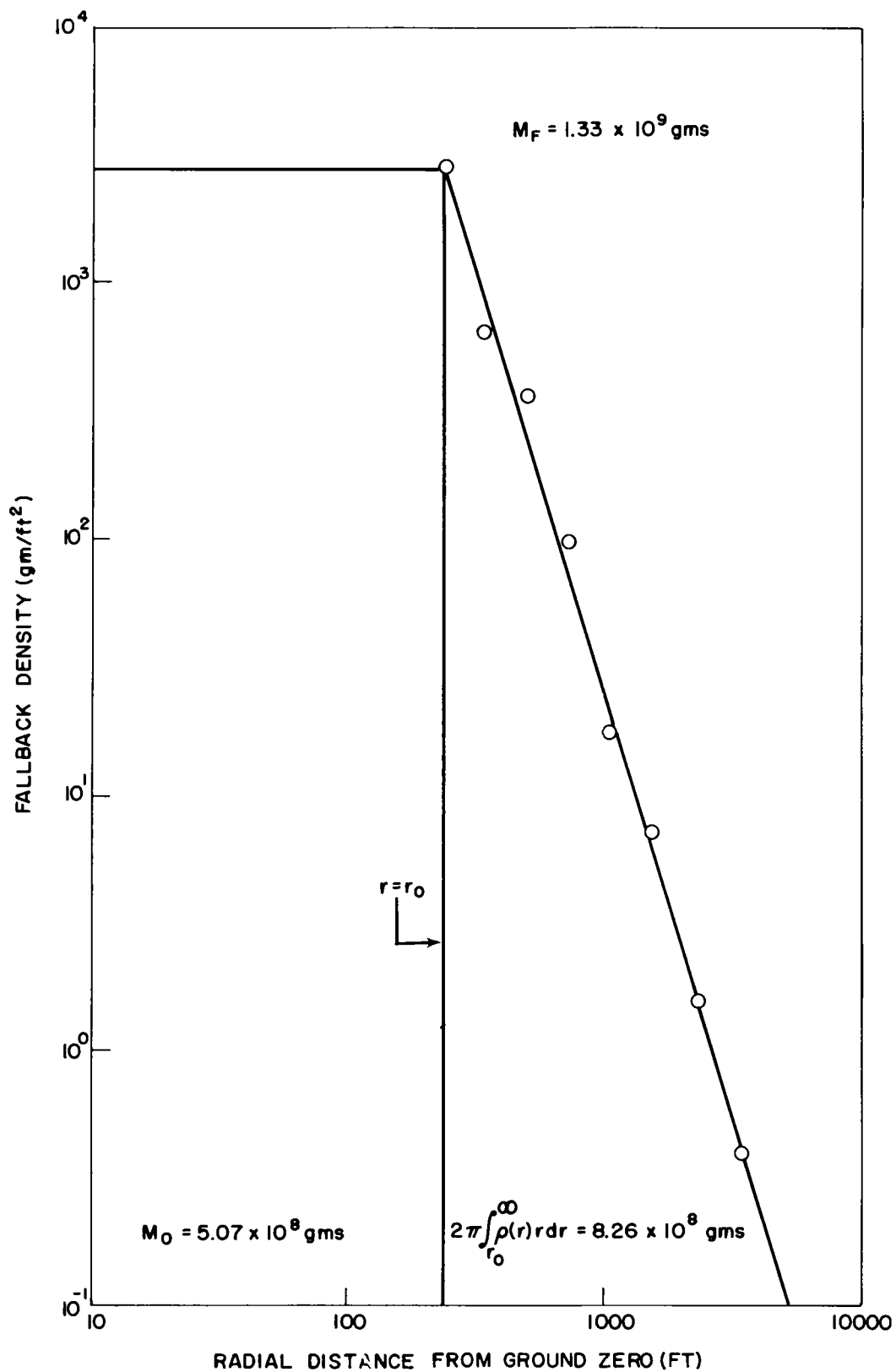
Fig. 4.13 Density of fallback versus radial distance from ground zero, 20 tons at 34.2 feet.
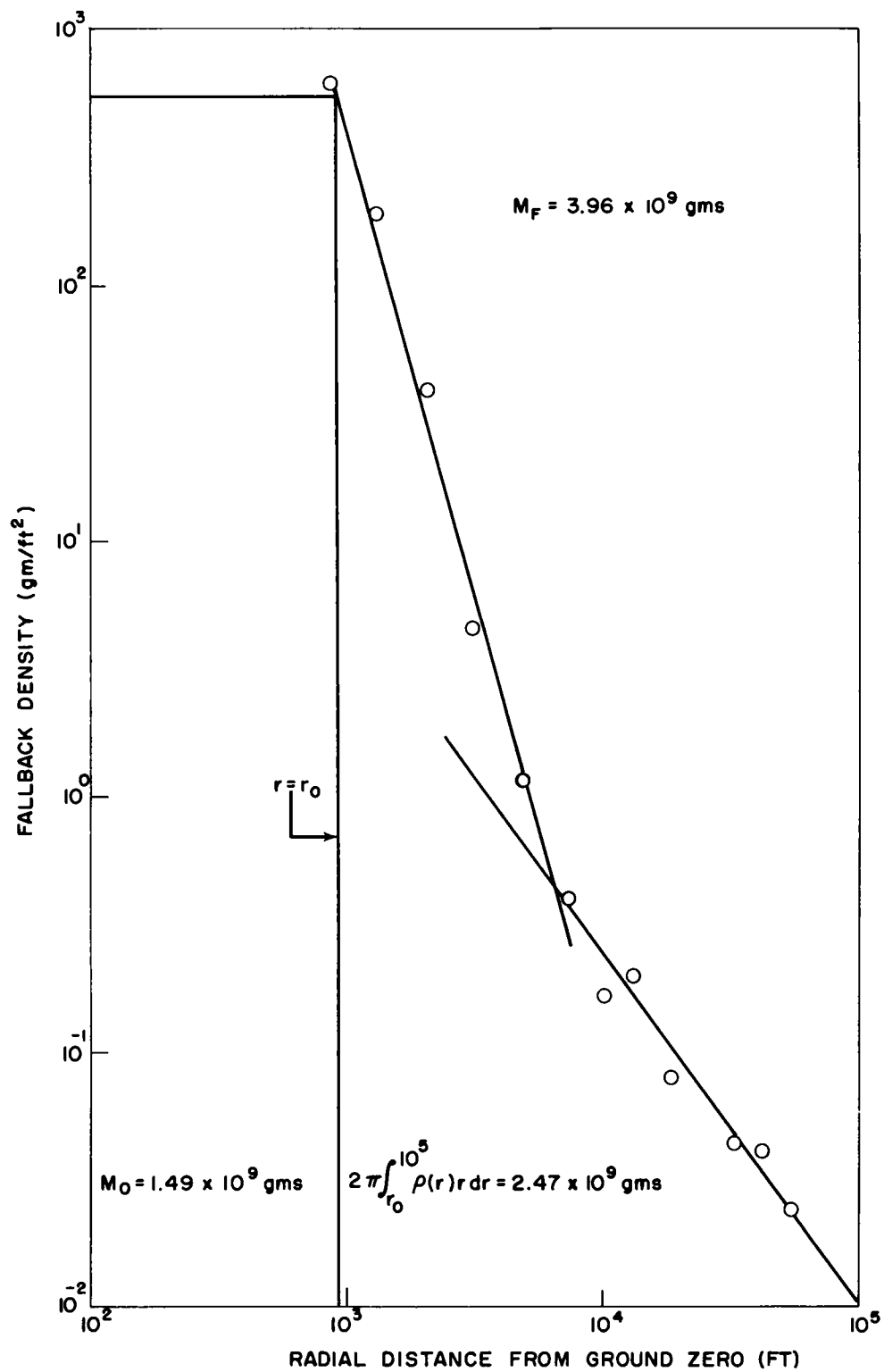
Fig. 4.14   Density of fallback versus radial distance from
ground zero, 1.2 kt at 67 feet, Teapot Ess.

The distance, r_o, is the radius of circle A for the Stagecoach experiments within which it is difficult to collect fallback deposits, since collectors are destroyed by missiles and air blast or are buried by ejecta. A constant fallback density for $r < 7 \ W^{1/3}$ is assumed in order to avoid the difficulty of extrapolating data from $r \cong 7 \ W^{1/3}$ to $r = 0$, where no data are available. With this assumption, it is seen that mass calculated by Eq. 4.1 will give a lower limit for _total_ mass of earth, including missiles, ejected. However, since our chief interest here is the mass of fine particulate deposited by winds, particularly at distant positions from the explosion, the mass figure arrived at by means of Eq. 4.1 is felt to be a good measure of fallback mass. (See Chapter 5 for total mass of ejecta calculations.) The method described for calculating fallback mass is simple and direct, and compares favorably in accuracy with calculations by other methods. (See, for example, the method used by Stetson, et al.[4]) The error in mass of fine particulate deposited is estimated to be less, certainly, than 25 percent and probably of the order of 5 to 10 percent.

The area covered with a given level (or greater) of fallback density may be estimated to within a factor of 2 by taking from Figs. 4.12 and 4.13 that radius, R, at which the given density level occurs and by letting the area equal πR^2.

An average of data plotted in Fig. 4.11 is given by the empirical relationship

$$M_F = 2.71 \times 10^4 \ V^{0.852} \ , \tag{4.2}$$

where M_F is mass of fine particulate in grams and V is apparent crater volume in cubic feet. It is seen that data from explosions in soil as well as those from explosions in rock are fairly well described by Eq. 4.2, and also that dependence of fallback mass on burial depth is largely removed by a plot such as shown in Fig. 4.11. With Eq. 4.2 and knowledge of crater volume as a function of explosive energy release and depth of burial, dependence of fallback mass on burial depth and yield may be inferred. For example, from Fig. 2.6, Chapter 2, crater volume data may be expressed approximately by the relations

$$V = 26.2 \left(\frac{d}{W^{1/4}}\right)^{0.74} W^{3/4} \, , \qquad W > 20 \text{ tons,} \quad 0.2 < \frac{d}{W^{1/4}} < 4 \, , \qquad (4.3)$$

$$V = 3.08 \times 10^5 \left(\frac{d}{W^{1/4}}\right)^{-5.68} W^{3/4} \, , \qquad W > 20 \text{ tons,} \quad \frac{d}{W^{1/4}} < 4 \, . \qquad (4.4)$$

Equations 4.3 and 4.4, substituted into Eq. 4.2 then yield empirical scaling rules for the mass of fine particulate in desert alluvium.

$$\frac{M_F}{W^{0.64}} = 4.4 \times 10^5 \left(\frac{d}{W^{1/4}}\right)^{0.628} \, , \qquad 0.2 < \frac{d}{W^{1/4}} < 4 \, , \qquad (4.5)$$

$$\frac{M_F}{W^{0.64}} = 1.28 \times 10^9 \left(\frac{d}{W^{1/4}}\right)^{-4.84} \, , \qquad \frac{d}{W^{1/4}} > 4 \, , \qquad (4.6)$$

where M_F is in grams when d is in feet and W in pounds.

No cake-pan measurements were made on the Stagecoach shot buried at 80 feet because it was felt that any array geometry which could collect a representative sample of fallback would be largely destroyed by the blast wave. From postshot observation at the site and from photographs, it appears that practically all of the fine particulate from the shot at the 80-foot depth was deposited within a circle of 500-foot radius.

4.4 CONCLUSIONS

From extremely simple experiments reliable data were obtained on distribution and quantity of fine particulate ejected by the Stagecoach explosions. An empirical relationship is obtained which allows the total mass of particulate deposit to be estimated within an order of magnitude from crater volumes alone. From this relationship, which appears applicable to media other than desert alluvium, and from knowledge of crater volume as a function of yield and depth of burial, a scaling law for total particulate deposited may be inferred.

REFERENCES

1. Operation Jangle: High Explosive Tests, WT-365, Armed Forces Special Weapons Project, 1951. (Uncl)

2. Doll, E. B., and Salmon, V., Scaled HE Tests, Final Report, AFSWP-123, Stanford Research Institute, 1952. (Conf)

3. Sachs, D. C., and Swift, L. M., Small Explosions Tests, Project Mole, Final Report, AFSWP-291, Stanford Research Institute, 1955. (Conf)

4. Stetson, R. L., et al., Distribution and Intensity of Fallout from the Underground Shot, Operation Teapot, WT-1154, U. S. Naval Radiological Defense Laboratory, 1955.

5. Underground Explosion Test Program, Vol. I, Soil, Final Report, Engineering Research Associates, Inc., Arlington, Va., 1952.

6. Underground Explosion Test Program, Vol. II, Rock, Final Report, Engineering Research Associates, Inc., Arlington, Va., 1953.

Chapter 5

RADIOACTIVE TAGGING OF CRATER EJECTA by A. J. Chabai

5.1 DESCRIPTION OF EXPERIMENT

In an effort to learn more about the manner in which earth is ejected (Fig. 5.1) by underground explosions, radioactive pellets of antimony 124 were buried about the explosive charge in the region which ultimately became the crater void. From knowledge of the initial and final positions of the radioactive pellets, information is obtained which yields the approximate trajectories of crater ejecta and an estimate of the effective initial velocity field of earth particles in the crater void region. In addition, reliable data are obtained on the areal density of earth material deposited ballistically from the crater's edge radially outward and on the total mass of earth (including fine particulate) ejected by the explosion.

Twenty pellets of stainless steel, each initially containing 600 milli-curies of Sb^{124}, were prepared for use in the two Stagecoach experiments burial depths of which were 17 and 34 feet. Strong Sb^{124} sources were chosen for three reasons. First, a source was required that was sufficiently strong that it could be easily detected in the background radiation field of the area (about 1 mR/hr). Second, the same pellets were to be used for both Stagecoach experiments and also for the Scooter experiment, and the possibility of delays between experiments had to be balanced against the half-life and source strength. Third and most important, the antimony pellets were expected to be buried under several feet of earth which would greatly attenuate their radiations and make their recovery difficult. A total of twenty-eight pellets were buried for both Stagecoach experiments and all were recovered.

Each pellet was a cylinder 3/8-inch in diameter and 3/8-inch long. The pellet wall was 1/16-inch thick. A stainless steel cap welded to the cylinder retained the antimony. Each pellet was inscribed with a number for the purpose of identification.
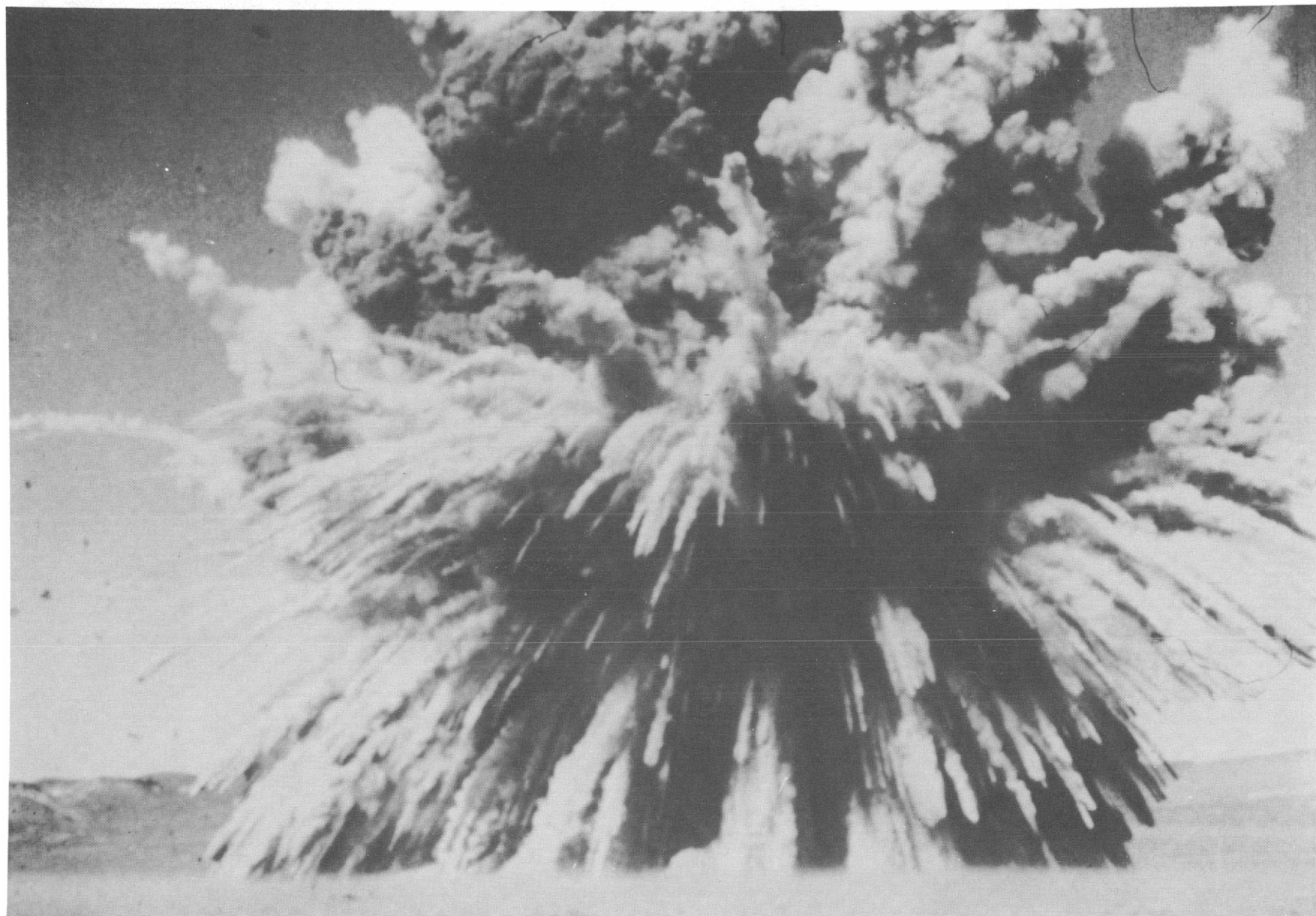
Fig. 5.1 Photo of ejecta from an underground explosion.

Initial location of antimony pellets for the Stagecoach shots is shown in Figs. 5.2 and 5.3. The pellets were buried in vertical 3-inch-diameter holes at the depths shown. Moistened earth was inserted and firmly tamped in each hole to the depth at which a pellet was to be buried. After placement of a pellet, the procedure was repeated until all pellets were buried. Previous investigations showed that this procedure of firmly tamping moistened earth in the holes adequately restored the original compaction of the soil medium and made the drill hole an insignificant perturbation to the explosive disturbance. By this precaution and by using small pellets, it was felt that a pellet would closely represent a soil particle and that its ejection from the crater region would be essentially that of an actual and similarly located soil particle.

Final positions of the radioactive pellets are shown in Figs. 5.2 and 5.3 and are also tabulated in Tables 5.1 and 5.2.

5.2 ANALYSIS OF DATA

In Figs. 5.4 and 5.5 are shown those volume segments of soil originally surrounding the charge which are ejected to the same epicentral distances. These figures were constructed by noting a pellet's epicentral distance of ejection at its initial burial position, then drawing lines representing equal distances of ejection through the data so as to produce some consistent picture. Although the lines of constant range in Figs. 5.4 and 5.5 are not unique, it was found that those variations which still gave a consistent picture did not greatly influence results derived from the contours. From Figs. 5.4 and 5.5, it is seen that a fairly large volume of earth in the region adjacent to the crater wall is not ejected beyond the crater's edge but is retained within the crater, partially filling the true crater void.

The areal density of ejecta was determined from Figs. 5.4 and 5.5 in the following manner. At the distance $(S_k + S_{k+1})/2$, shown in Fig. 5.6, the mass of earth per unit area is

$$\sigma = \rho_o (V_k - V_{k+1}) \Big/ \pi (S_{k+1}^2 - S_k^2) \ ,$$

where ρ_o is the soil density and V_k is the volume of soil enclosed by the
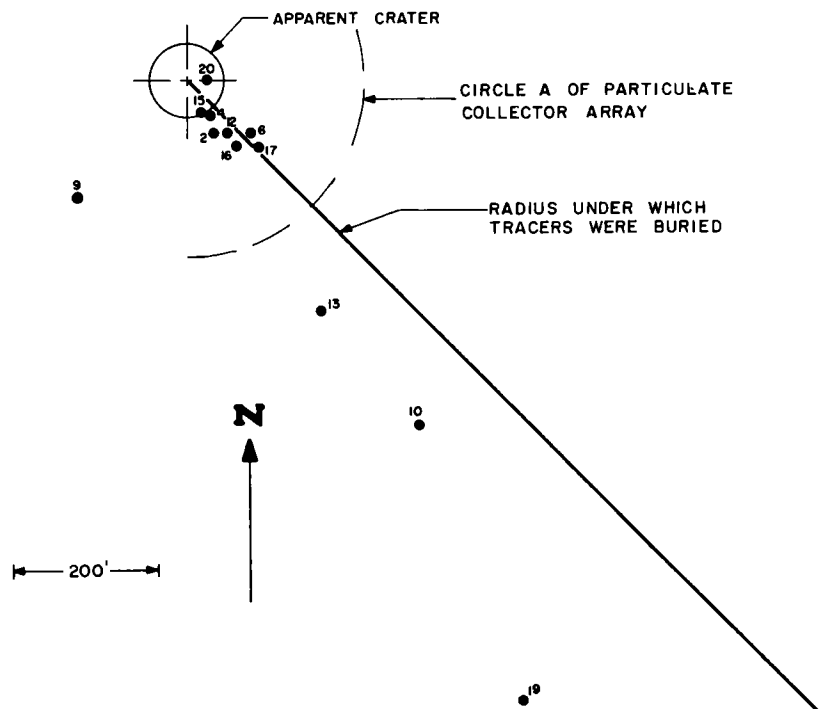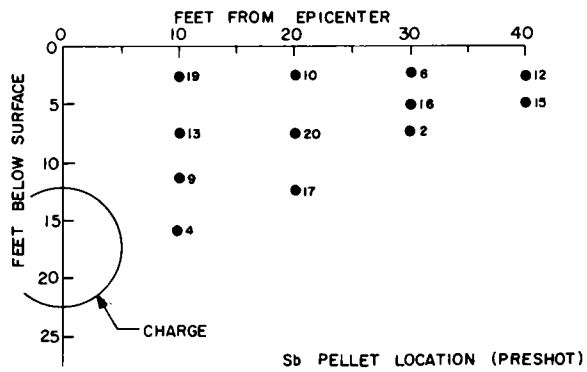
Fig. 5.2 Initial and final positions of antimony tracers for the 20-ton shot at 17-foot burst depth.
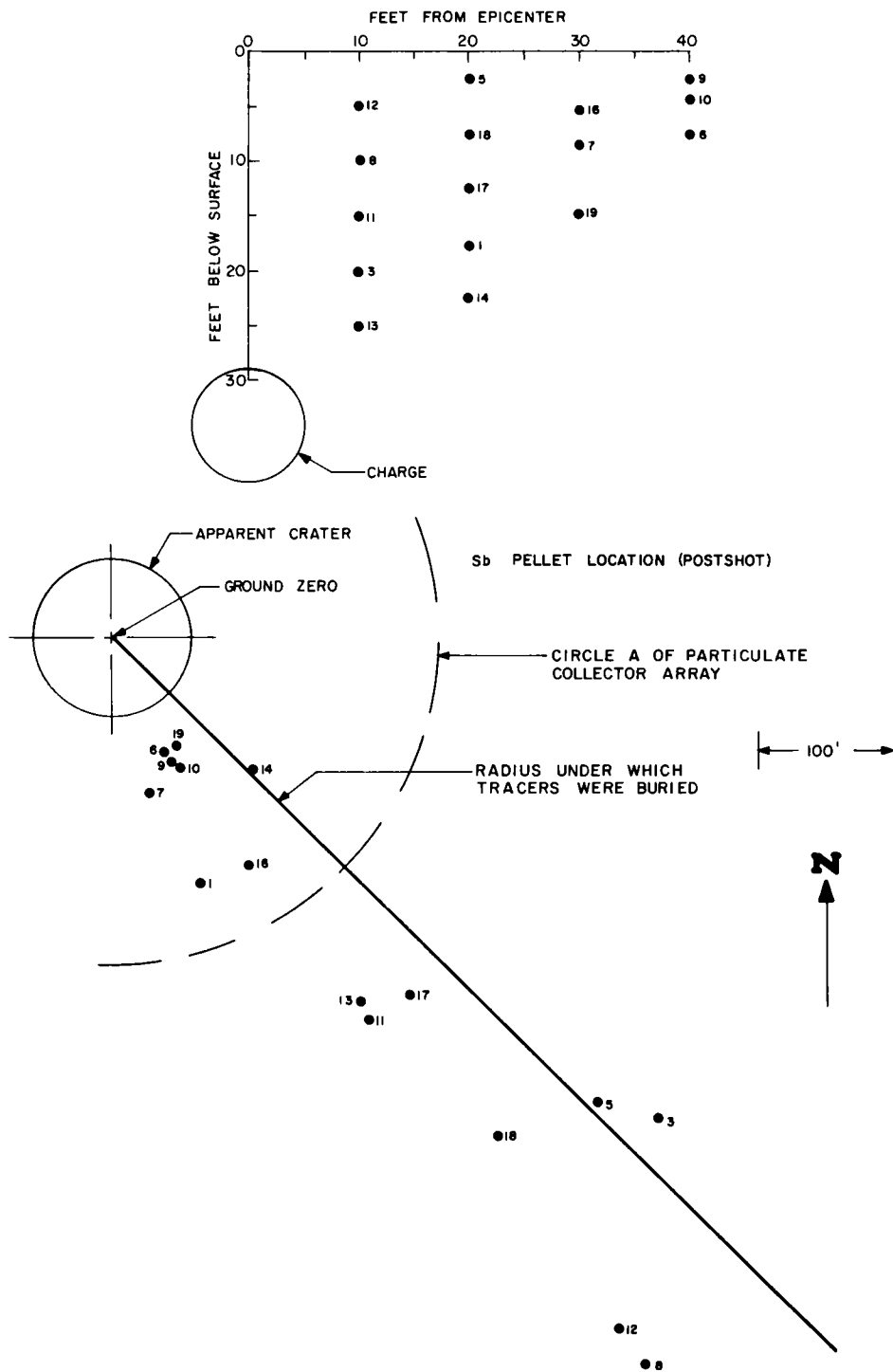
Fig. 5.3 Initial and final positions of antimony tracers
for the 20-ton shot at 34-foot burst depth.
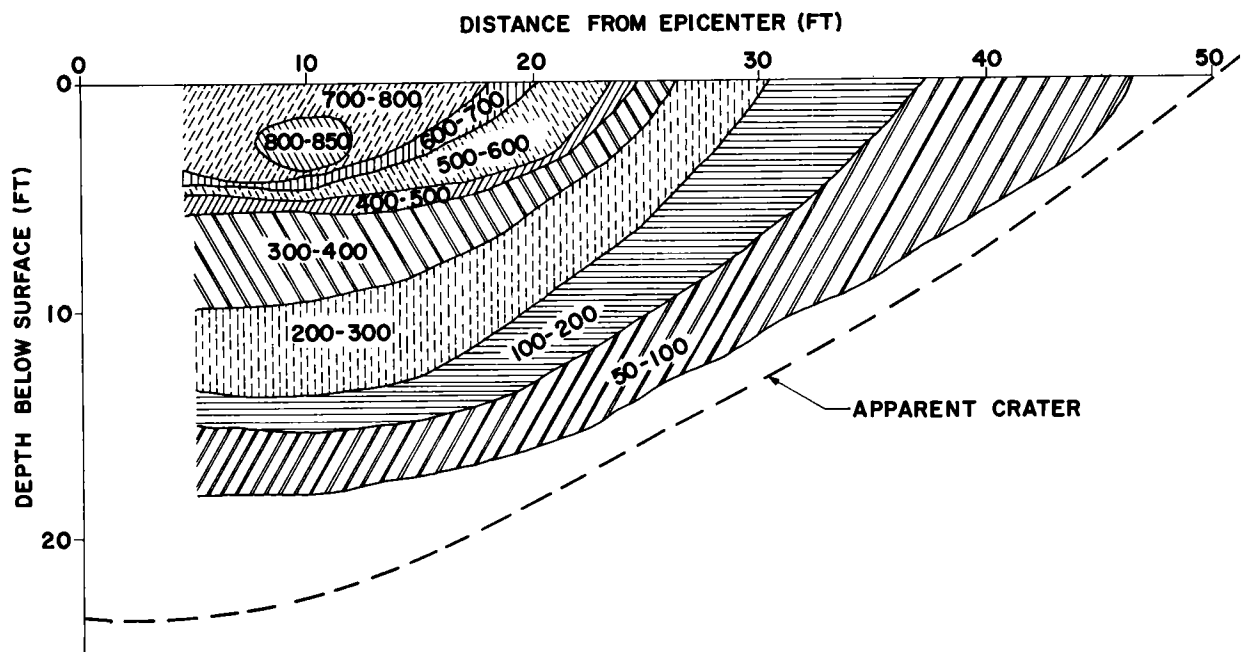
Fig. 5.4 Isorange contours determined from tracer data from the 20-ton shot at 17-foot burst depth.
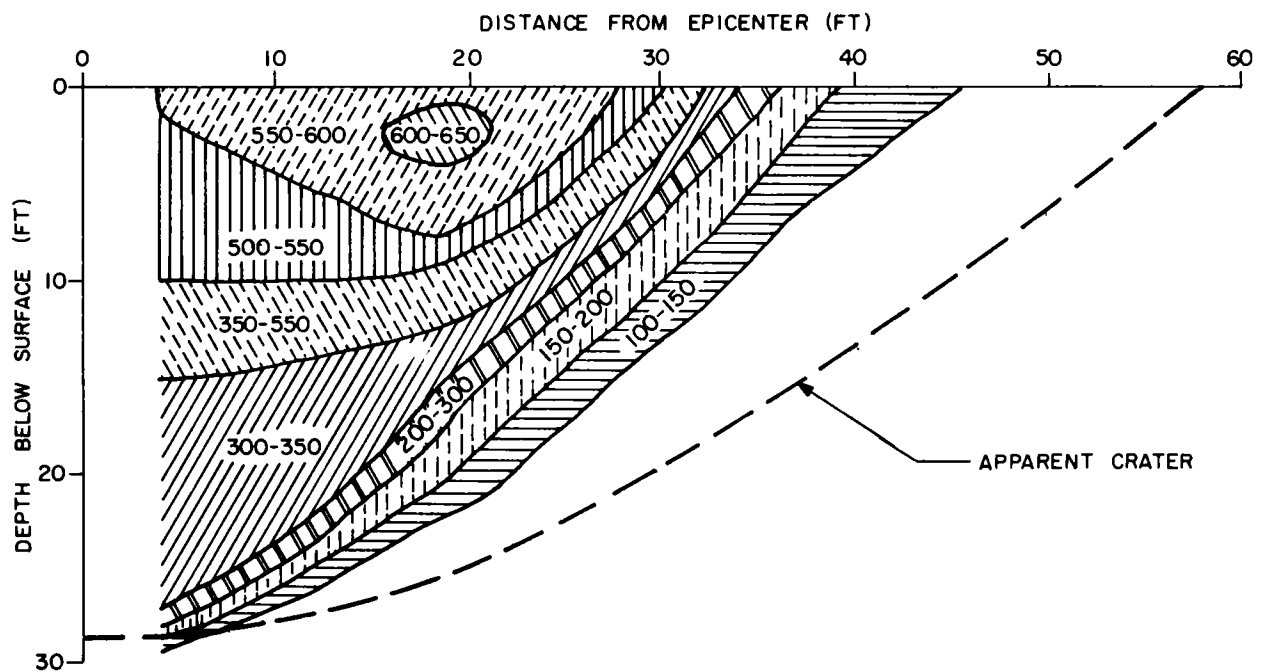
Fig. 5.5 Isorange contours determined from tracer data from the 20-ton shot at 34-foot burst depth.
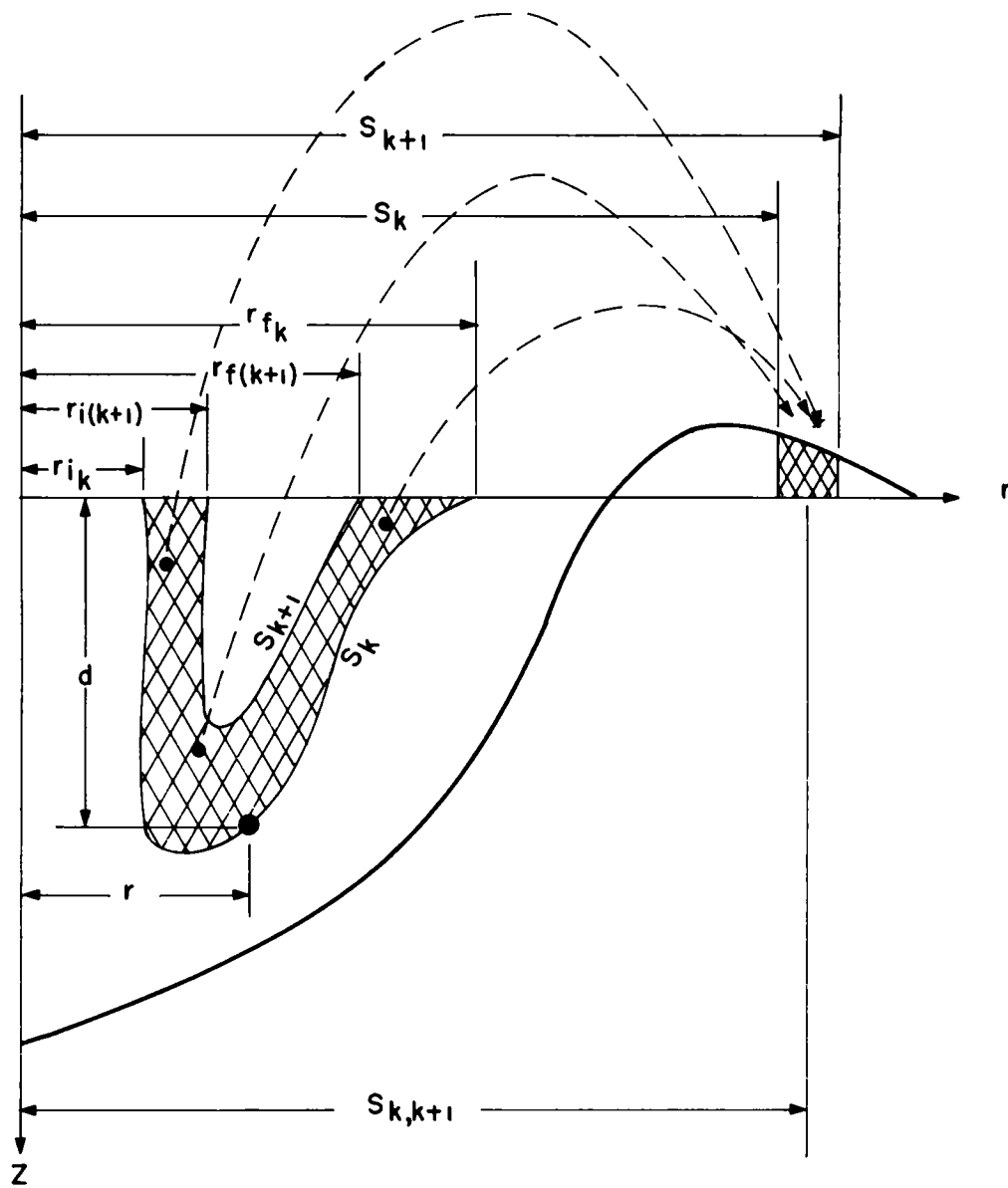
Fig. 5.6 Illustration of crater volume ballistically
deposited at radial distance $(S_k + S_{k+1})/2$.

TABLE 5.1 ANTIMONY 124 TRACER DATA, STAGECOACH 20-TON SHOT,
17-FOOT DEPTH

Pellet No.	Preshot Location		Postshot Location	
	Distance from epicenter (ft)	Depth below surface (ft)	Distance from epicenter (ft)	Bearing to epicenter
2	30	7.5	80.6	N30°W
4	10	16.0	59.9	N28°W
6	30	2.5	116.0	N47°W
9	10	11.5	222.5	N41°E
10	20	2.5	576.4	N34°W
12	40	2.5	85.2	N31°W
13	10	7.5	367.9	N30°W
15	40	5.0	55.5	N23°W
16	30	5.0	119.0	N32°W
17	20	12.5	347.2	N16°W
19	10	2.5	980.8	N28°W
20	20	7.5	23.2	N83°W

TABLE 5.2 ANTIMONY 124 TRACER DATA, STAGECOACH 20-TON SHOT,
34-FOOT DEPTH

Pellet No.	Preshot Location		Postshot Location	
	Distance from epicenter (ft)	Depth below surface (ft)	Distance from epicenter (ft)	Bearing to epicenter
1	20.5	17.5	189.5	N23°W
3	10.3	19.3	540.0	N46°W
5	20.5	2.5	490.9	N45°W
6	40.0	7.5	98.5	N32°W
7	30.0	8.5	103.6	N10°W
8	10.3	10.0	662.4	N37°W
9	40.0	2.5	102.9	N34°W
10	40.0	4.0	107.1	N35°W
11	10.3	15.0	336.7	N34°W
12	10.3	5.0	627.6	N37°W
13	10.3	24.3	322.1	N35°W
14	20.5	22.0	142.9	N45°W
16	30.0	5.0	193.9	N33°W
17	20.5	12.2	341.9	N40°W
18	20.5	7.5	513.4	N41°W
19	30.0	14.0	98.2	N35°W

contour, S_k, rotated about the vertical epicentral axis. The volumes, V_k, may be found from the integrals

$$V_k = \int_0^{2\pi} \int_0^{d(r)} \int_{r_{ik}}^{r_{fk}} r\,dr\,dz\,d\theta = 2\pi \int_{r_{ik}}^{r_{fk}} r\,d(r)\,dr$$

by means of numerical integration, using the contours of Figs. 5.4 and 5.5 as the functions, $d(r)$. Results of these calculations are shown in Figs. 5.7 through 5.10.

In Fig. 5.7 scaled areal density of ejecta as determined from radioactive pellet data is shown as a function of scaled distance from the charge epicenter. The scaling was arbitrarily chosen as 3/10, since most of the apparent crater data in desert alluvium are best scaled by this rule. It should be noted that the 34-foot Stagecoach explosion deposited more earth close to the crater edge than did the 17-foot explosion. As scaled depth of burial increases, ejecta are deposited closer to the crater rim, resulting in higher crater lips. For comparison with desert alluvium, some results[1] for loess and clay are shown in Fig. 5.8. Sakharov has stated[1] that the areal density of ejecta from explosions in loess is described to within a factor of 2 by the formula

$$\sigma(\text{lb/ft}^2) = 47d\ W^{3/4} \big/ r^{2.2}\ ,$$

$$r/W^{1/3} < 23\ ,\quad 0.6 < d/W^{1/3} < 1.9\ ,$$

where d is the burial depth of explosive in feet, r the epicentral distance in feet, and W the weight of (Ammonite No. 6) explosive in pounds. A comparison of Figs. 5.7 and 5.8 points out the differences in density of ejecta resulting from media differences as well as from different explosives.

In Figs. 5.9 and 5.10 are presented all data obtained on ejecta density from the Stagecoach experiments. Crater lip profiles, $h(r)$, are converted to areal density by taking $\sigma(r) = \rho_0 h(r)$, $\rho_0 = 100$ lb/ft^2. Lip profile data, antimony tracer data, and the fine particulate data together determine a
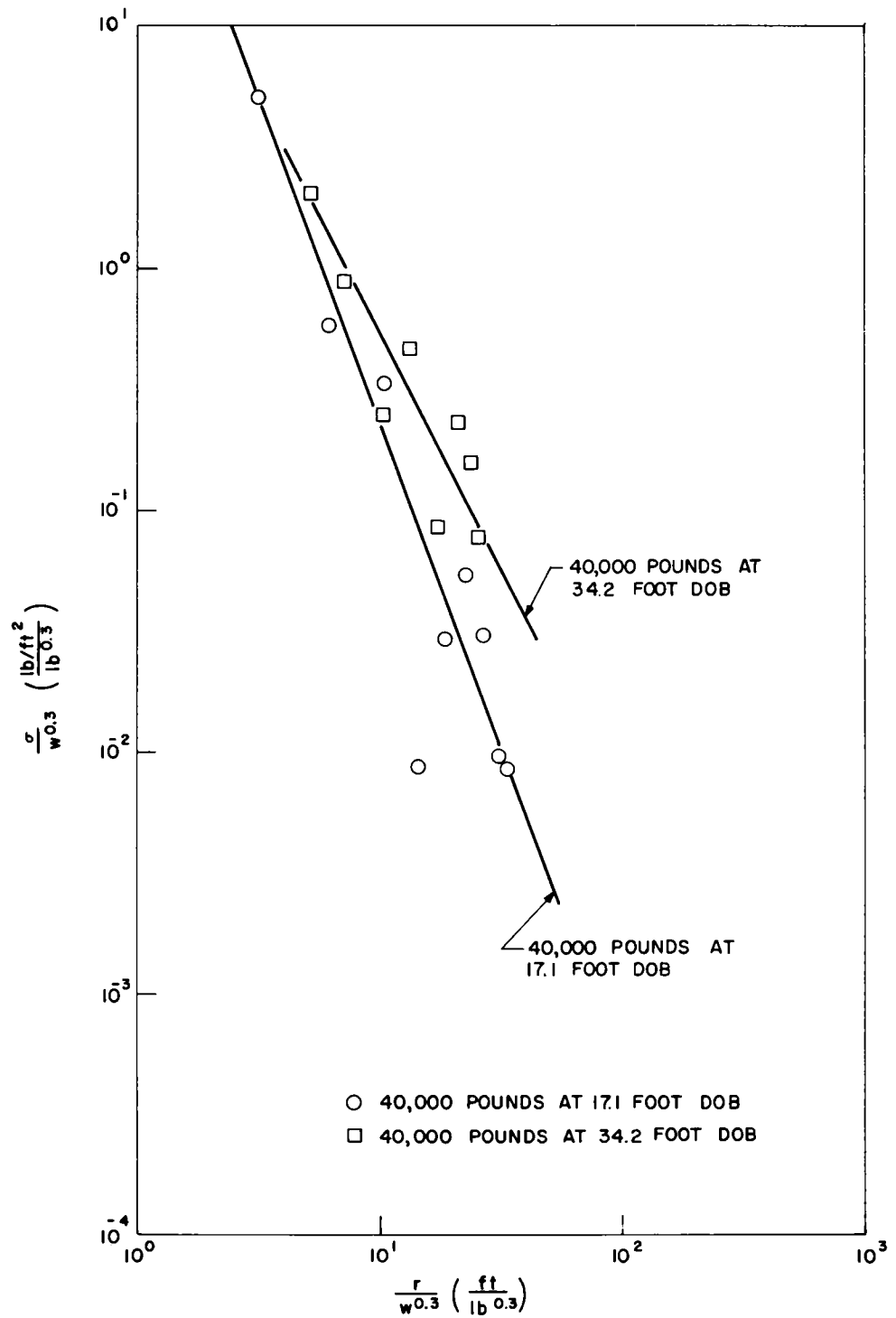
Fig. 5.7 Scaled ejecta density versus scaled epicentral distance for desert alluvium.
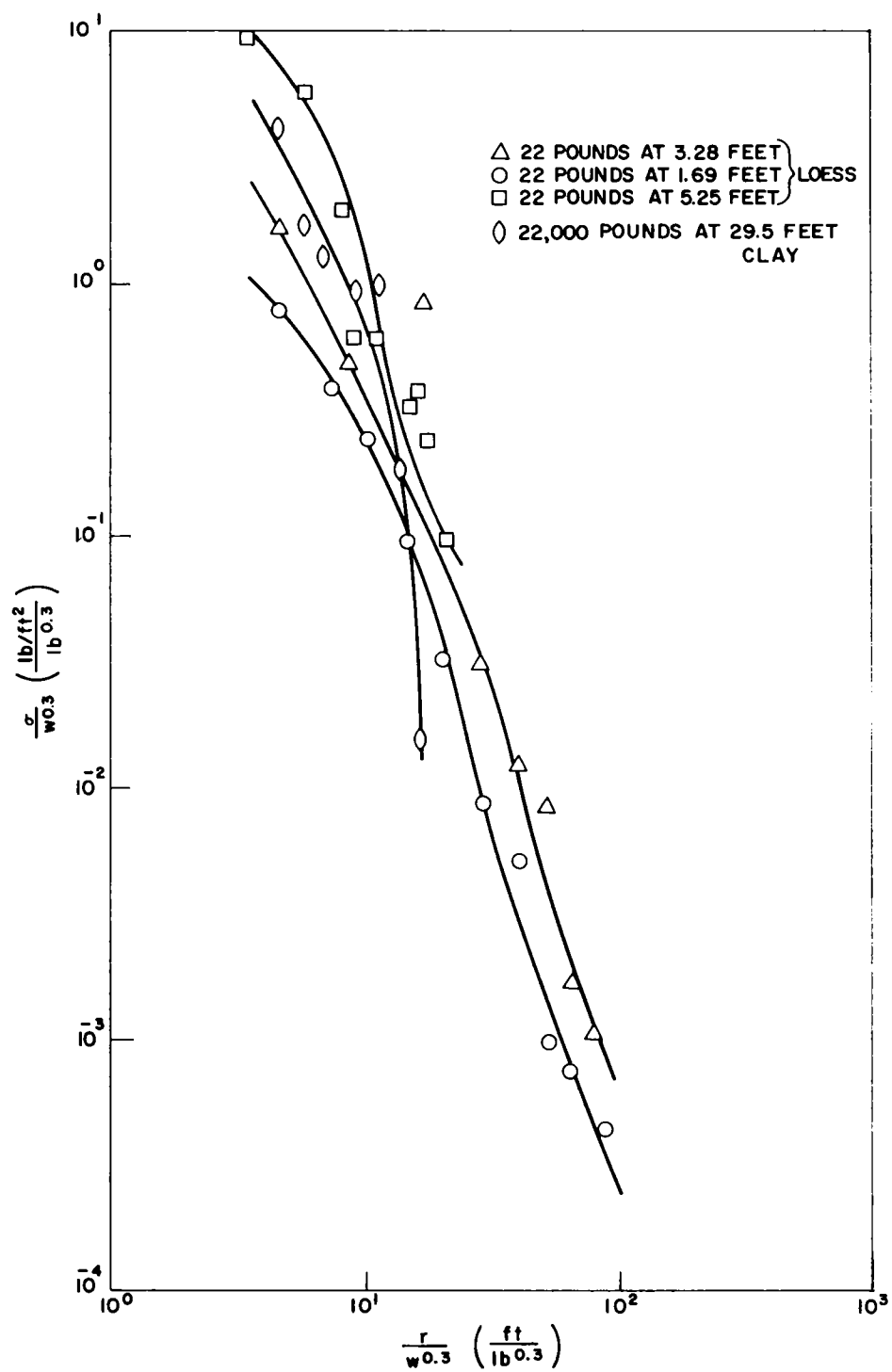
Fig. 5.8 Scaled ejecta density versus scaled epicentral distance for loess and clay.
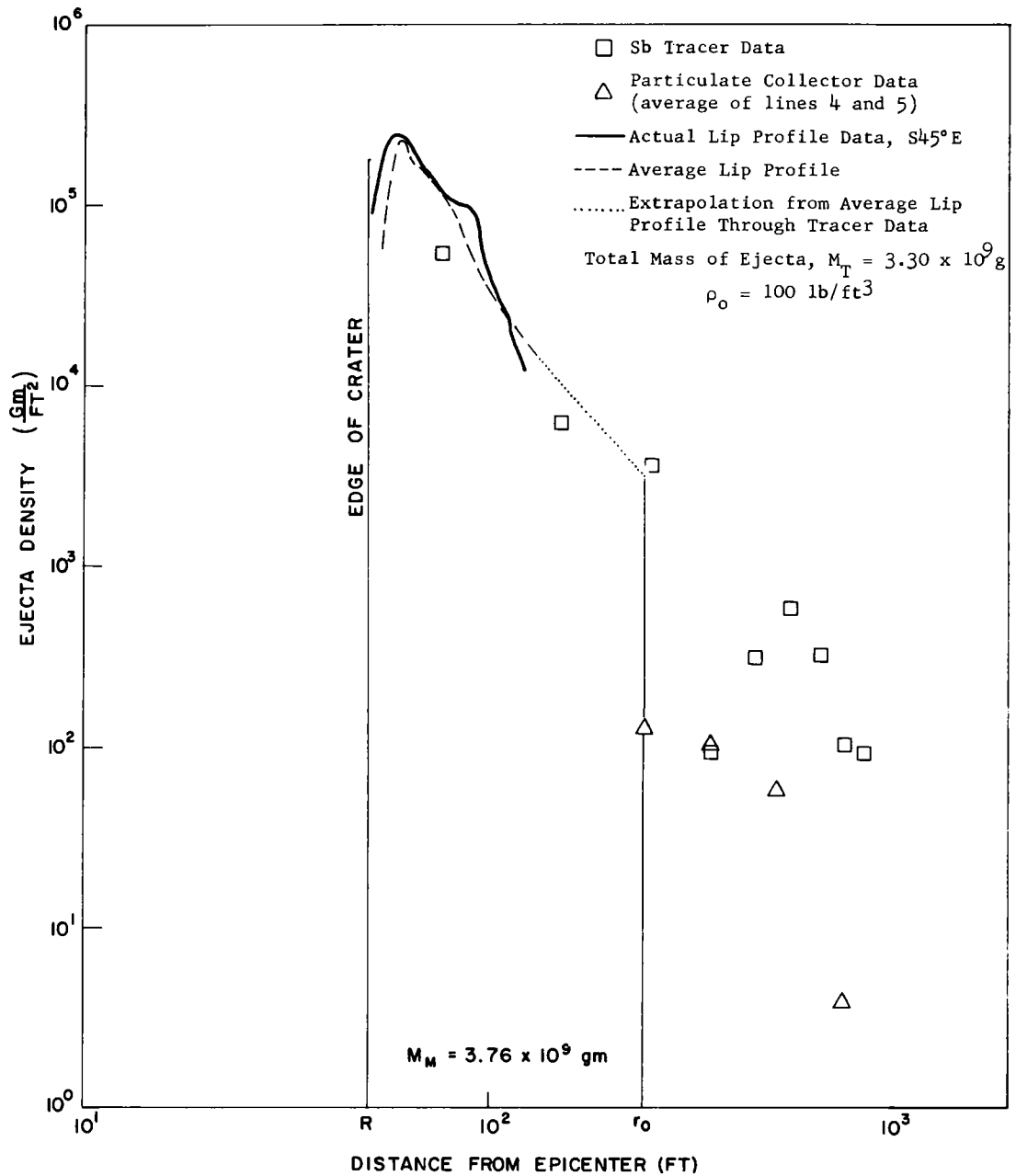
Fig. 5.9 Ejecta density versus epicentral distance for the 20-ton shot at 17-foot burst depth for desert alluvium.
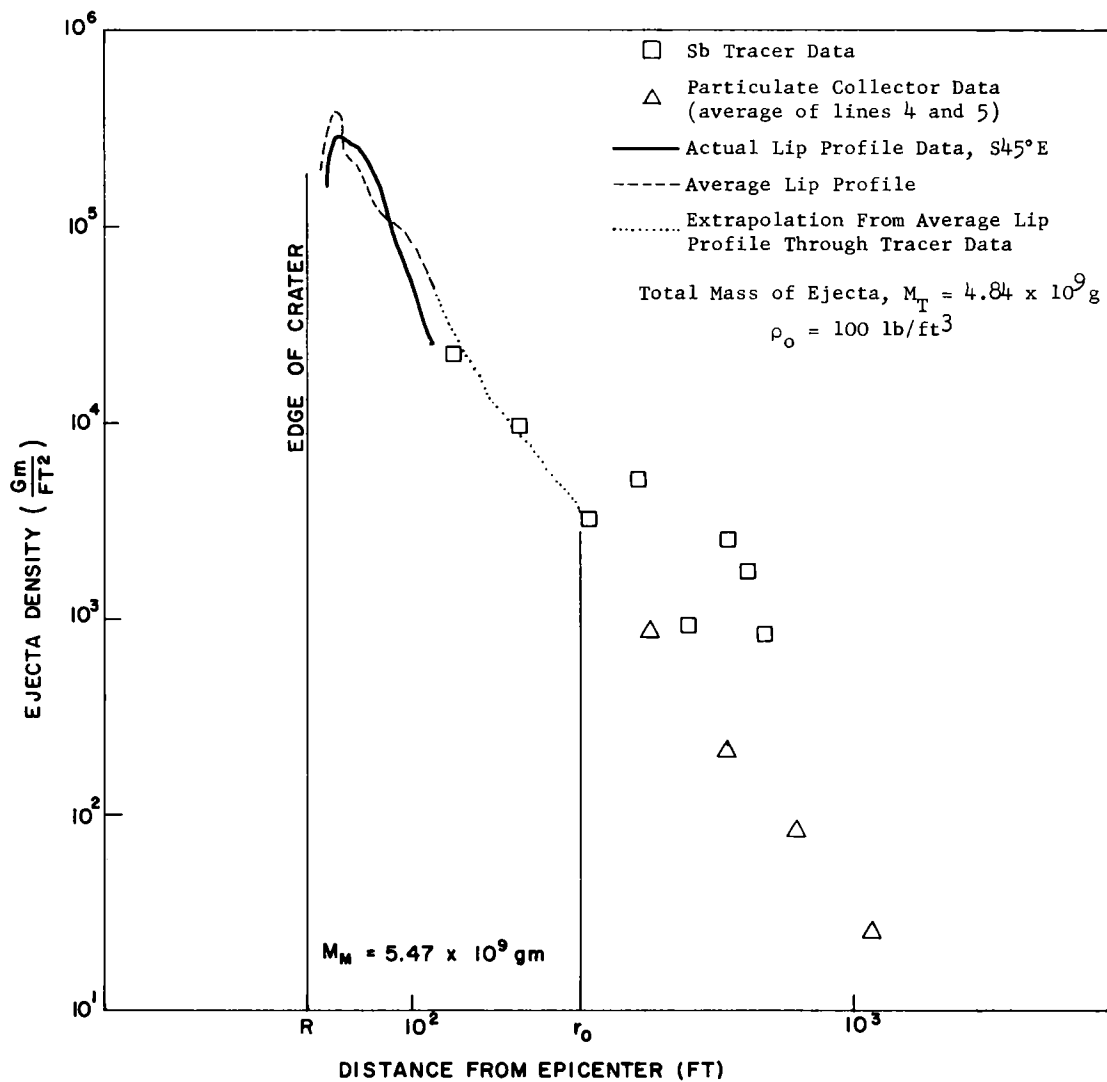
Fig. 5.10 Ejecta density versus epicentral distance for the
20-ton shot at 34-foot burst depth for desert alluvium.

fairly continuous curve for ejecta density as a function of epicentral distance. Density values obtained from particulate collectors at positions closest to the charge are unquestionably low, particularly for the explosion at the 17-foot depth; these collectors were destroyed by the air blast and samples were obtained from the collector mounting board (see Chapter 4).

Recalling from Section 5.2 how the areal density of ejecta was obtained from initial and final pellet position, one is impressed less by the fact that these data are higher (Figs. 5.9 and 5.10) than the particulate collector data than by the fact that they agree as well as they do.

Estimates of the total mass of ejecta may be made from antimony tracer data, particulate collector data, and from true and apparent lip profiles. The total mass of ejecta is defined as $M_T = M_m + M_p - M_{TL}$, where M_p is the value of the integral $2\pi \int_{r_0}^{\infty} \rho(r)rdr$ given in Chapter 4, M_{TL} is the mass of the true lip taken as the product of true lip volume (see Chapter 11), and the density $\rho_0 = 100$ lb/ft^3 and M_m is the value of the integral $2\pi \int_{R}^{r_0} \rho(r)rdr$ under the dashed-dotted curves in Figs. 5.9 and 5.10. Here R is crater radius and r_0 is the radius of circle A of the particulate collector array. Magnitudes of the various mass quantities described are listed in Table 5.3 for the Stagecoach experiments and also for Teapot Ess, the nuclear explosion of 1.2 kilotons buried at 67 feet. The total mass and mass of fine particulate deposited at distances greater than $7W(lb)^{1/3}$ are shown as functions of apparent crater volume in Fig. 5.11. M_T was 87 percent of the crater volume on the 17-foot and 73 percent on the 34-foot shot. A considerably smaller percentage was recovered from the Teapot ESS shot than from the 17-foot shot at the same scaled depth.

TABLE 5.3 MASS QUANTITIES IN GRAMS FOR BURIED EXPLOSIONS
IN DESERT ALLUVIUM

	Stagecoach		Teapot Ess
	20 tons, 17 ft	20 tons, 34 ft	1.2 kt, 67 ft
$M_o = \rho(r_o)\pi r_o^2$	0.87×10^8	0.51×10^9	1.49×10^9
$M_p = 2\pi \int_{r_o}^{\infty} \rho(r)r\,dr$	4.65×10^8	0.83×10^9	2.47×10^9
$M_F = M_o + M_p$	5.52×10^8	1.33×10^9	3.96×10^9
$M_m = 2\pi \int_{R}^{r_o} \rho(r)r\,dr$	37.6×10^8	5.47×10^9	67.7×10^9
M_{TL} (mass of true lip)	9.28×10^8	1.45×10^9	22.0×10^9
$M_T = M_m + M_p - M_{TL}$	32.96×10^8	4.8×10^9	48.2×10^9
M_c	38.0×10^8	6.56×10^9	118.0×10^9
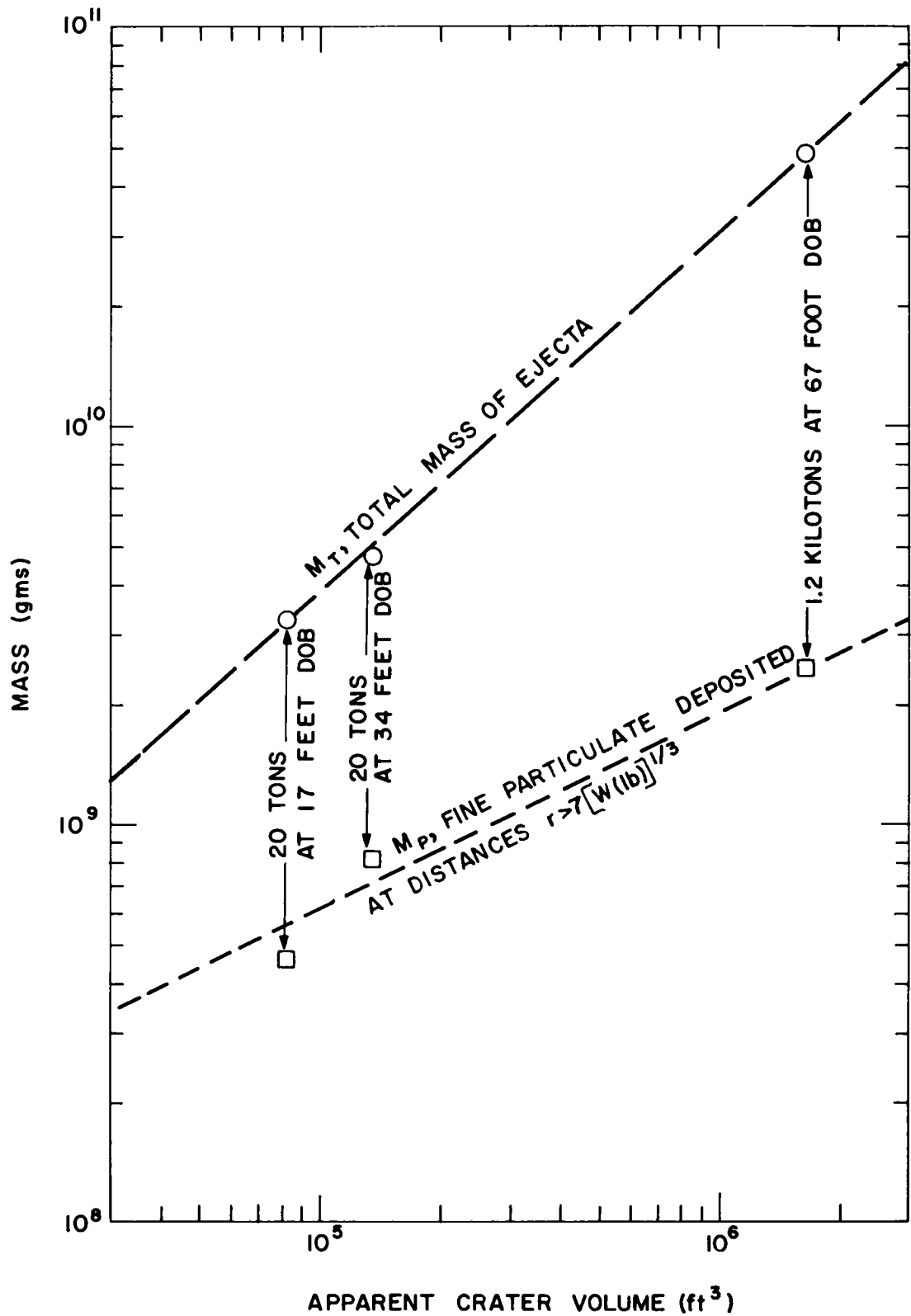
Fig. 5.11 Mass deposits from buried explosions in desert alluvium.

Photography of motion of targets placed on the earth surface above the explosive charge (see Chapter 3) allows values of surface particle velocities to be calculated. These measurements indicate that surface motion occurs in a radial direction along a line through the charge center and that velocities are less than one expects from the radiated shock or the stress wave. It is felt that the velocities observed result from expansion of high-pressure explosive gases released by the charge. If this is correct, one might expect that the particle velocity field in the region of soil about the upper hemisphere of the charge will be nearly radial, in spite of the fact that a compressive wave and a tensile wave reflected from the surface have passed through this region.

Assuming that the velocity field is radial and that this velocity field resulting from expansion of explosion gases determines trajectories of soil particles, an estimate of the velocity field may be obtained from observed ranges of the antimony tracers.

Neglecting air drag, the initial velocity of the jth tracer or soil particle is given by the ballistic formula

$$V_{oj} = R_j g^{1/2} \Big/ (R_j \sin 2\theta_j - 2y_j \cos^2 \theta_j)^{1/2} ,$$

where R_j is the range, y_j the initial depth below surface, θ_j the angle between a radial line through charge center and the horizontal for the jth tracer, and g the acceleration of gravity. Since the motion about the charge is assumed to be radial, and angles θ_j are known, and from knowledge of the initial positions, y_j, and the observed ranges, R_j, the initial velocity is found.

Values of effective initial velocities determined by the ballistic formula are shown in Figs. 5.12 and 5.13. Also shown are surface velocities obtained from photography of targets. The order of magnitude of ejecta velocities determined from motion picture photography (see Chapter 6, Figs. 6.5 and 6.6, high jet portion of curve) compare well with velocities calculated from tracer data.

REFERENCE

1. Sakharov, V. N., et al., Local Distribution of Earth Thrown Up by Underground Explosions, Doklady Akad. Nauk 124: 314-17, No. 2, January 1959.
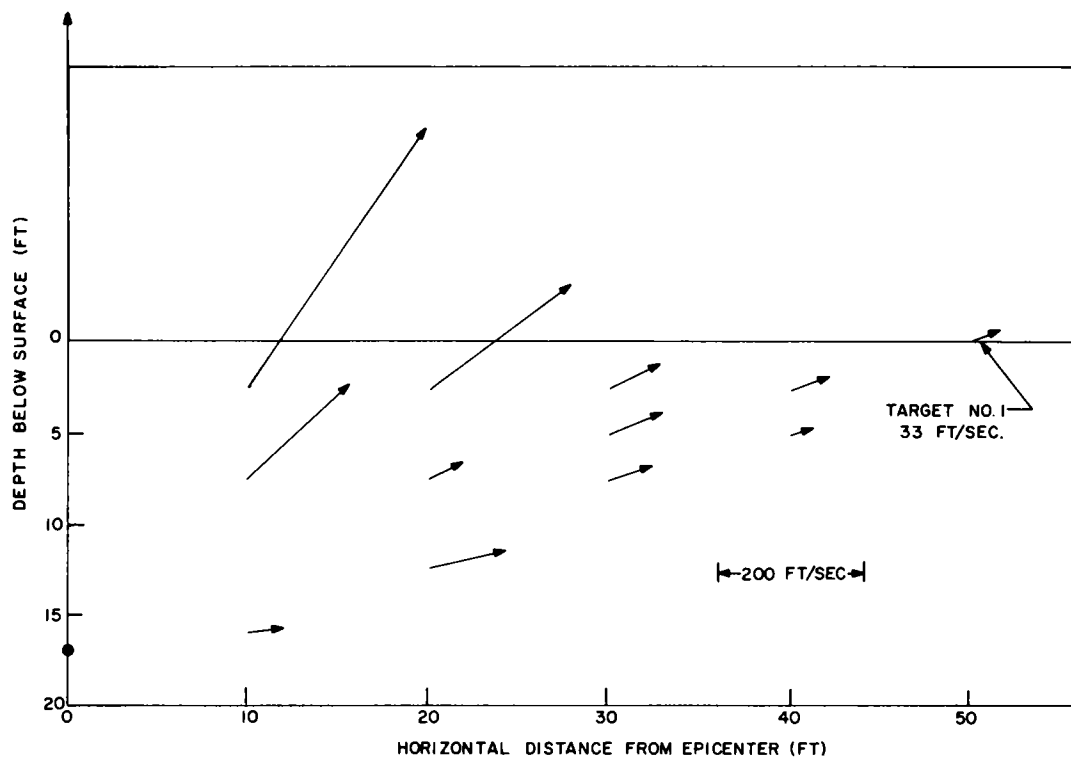
Fig. 5.12 Effective particle velocity field determined from tracer data from the 20-ton shot at 17-foot burst depth.
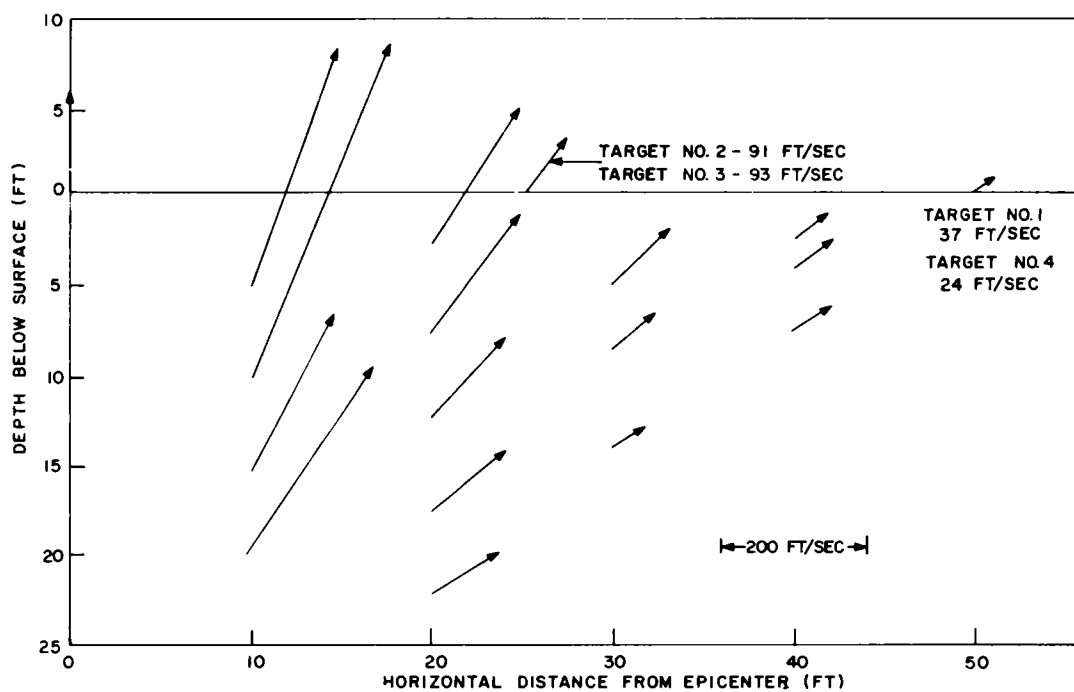
Fig. 5.13 Effective particle velocity field determined from tracer data from the 20-ton shot at 34-foot burst depth.

Chapter 6

CLOUD GROWTH by L. J. Vortman

6.1 INTRODUCTION

Cloud growth from underground high-explosive detonations has been described
in detail by Young.[1] It is the purpose here to present cloud growth information
in such a manner that it will be useful for development of a model which may be
used for prediction of fallout from underground detonations. It is also intended
to determine if information from Project Stagecoach is in agreement with that
reported by Young.

An underground detonation begins with mounding of the earth at the surface
of the ground. When the mound reaches a rupture height, explosive gases vent
through the top or near the top of the mound. The lower periphery of the mound
and the outer margin of the vented gas join to become the column of smoke and
dust that moves upward. As the cloud continues to grow, its crown rises grad-
ually. A jet of ejected material moves through the smoke crown and reaches
heights considerably greater in the case of a shallow burst than the height
of the crown itself. Then, as the material and the entrained air fall, a down-
ward motion of air and dust is generated which pulls material in the cloud
downward. As the direction of the downward flow is changed by the ground sur-
face, the base surge is formed.

6.2 DISPLACEMENTS

Figures 6.1, 6.2, and 6.3 show displacements versus time for the three
shots. The following displacements are presented where they are applicable:

(1) <u>Mound height</u> is measured along the vertical axis of the charge. (See
Fig. 6.4 in connection with this and following definitions.)

(2) <u>Smoke crown height</u>. Height of the smoke crown of venting gases is
measured along the vertical axis of the charge.

(3) <u>Jets</u>. These are the jets which break through the smoke crown and
reach to the greatest heights. Included are the vertical height of
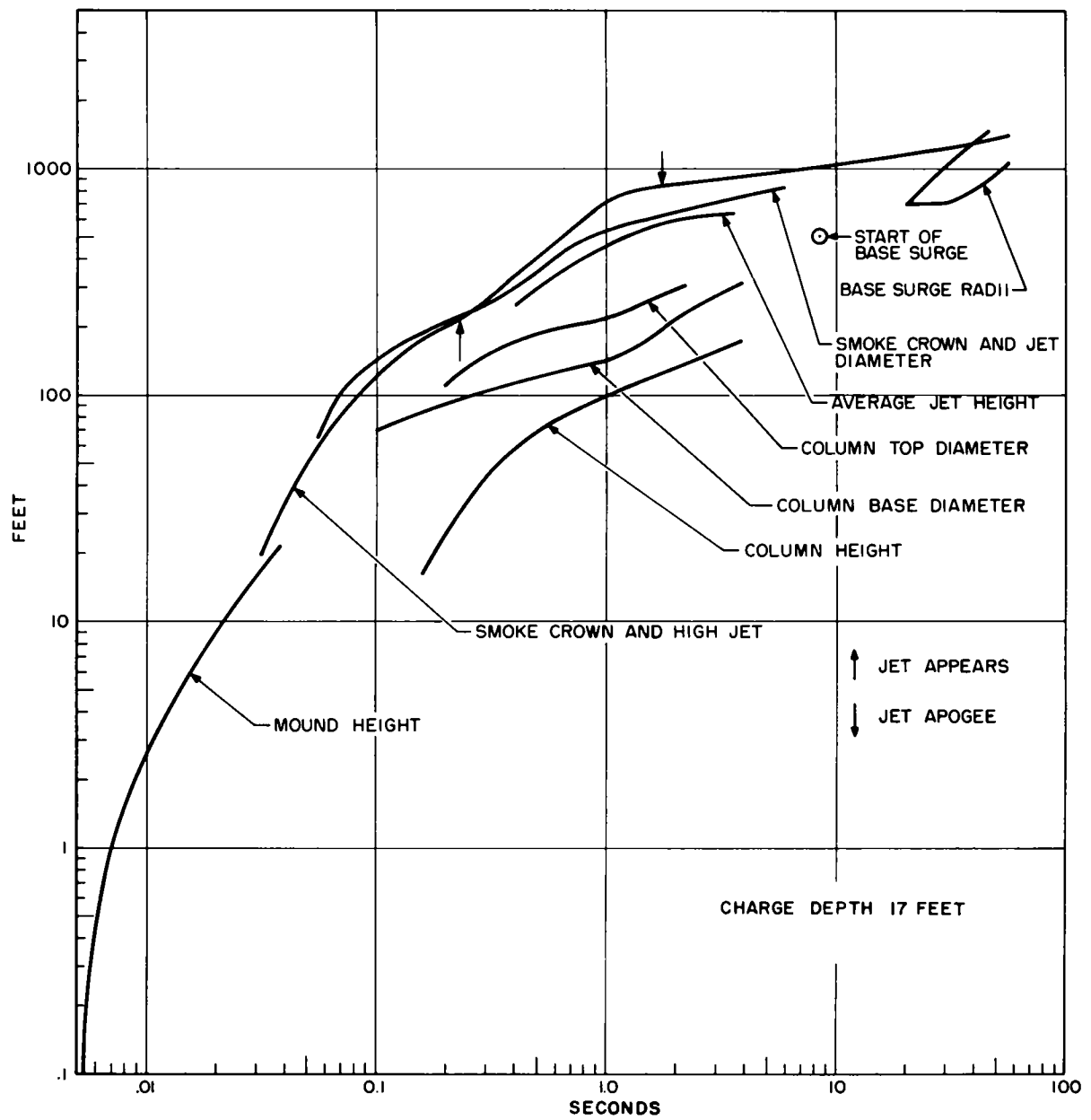
Fig. 6.1 Displacements as a function of time for the charge buried at 17 feet.
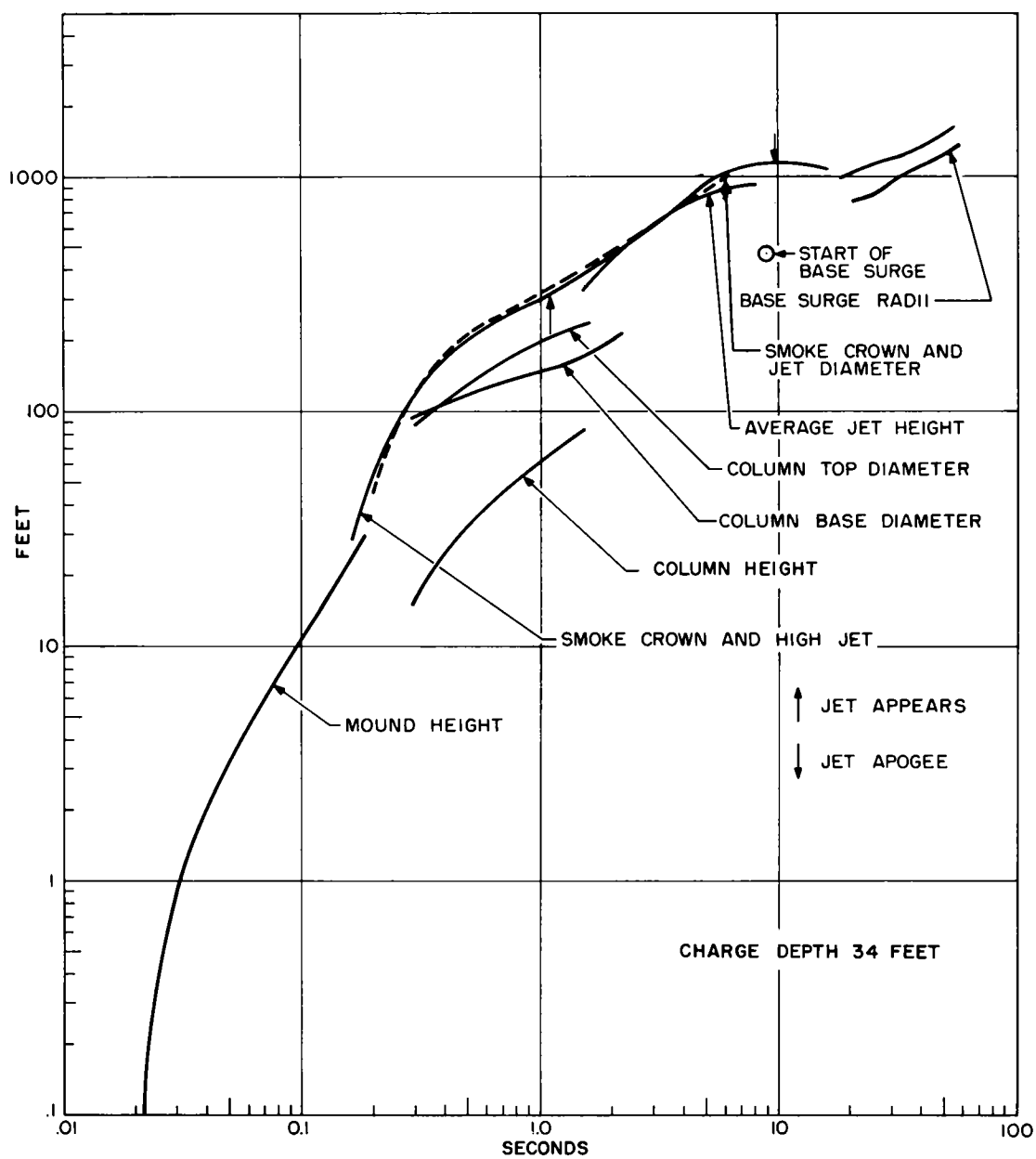
Fig. 6.2 Displacements as a function of time for the charge buried at 34 feet.
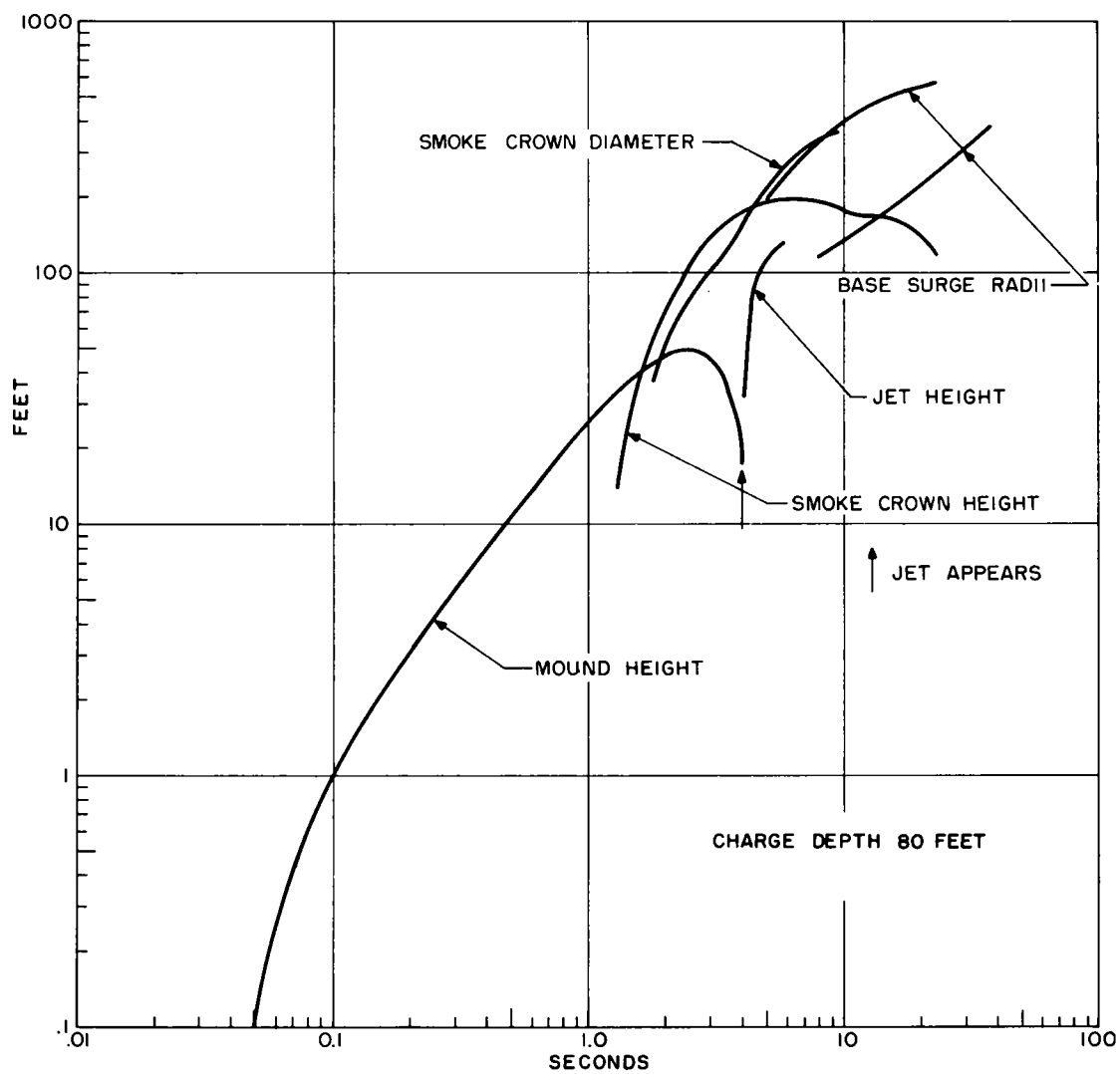
Fig. 6.3 Displacements as a function of time for the charge buried at 80 feet.
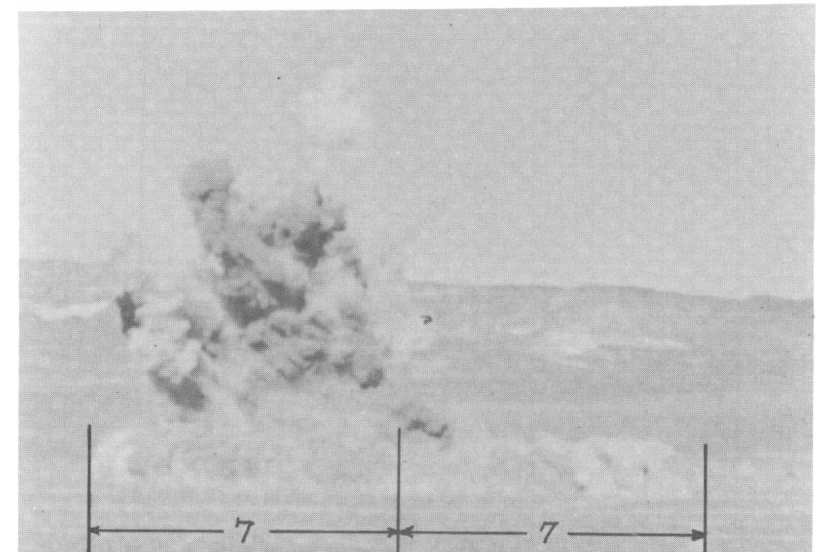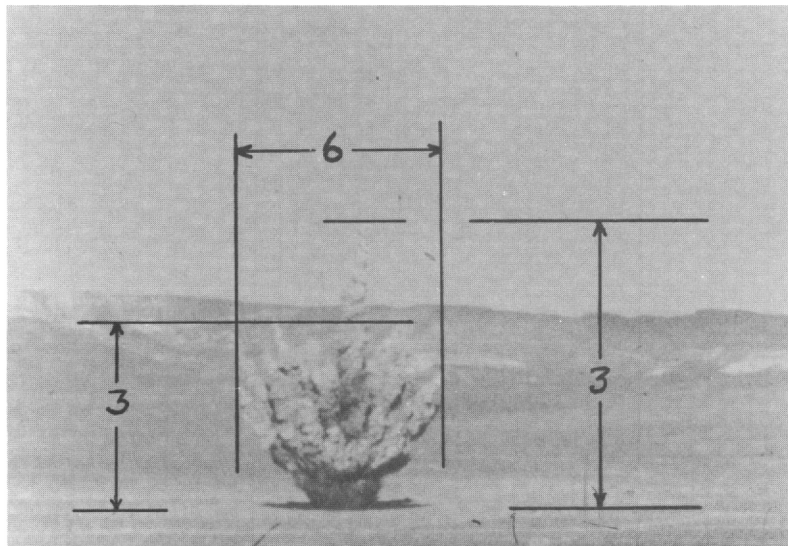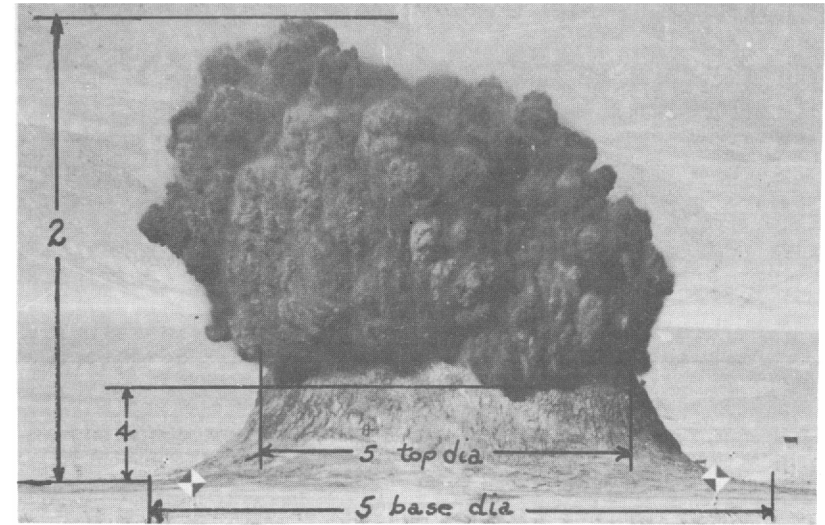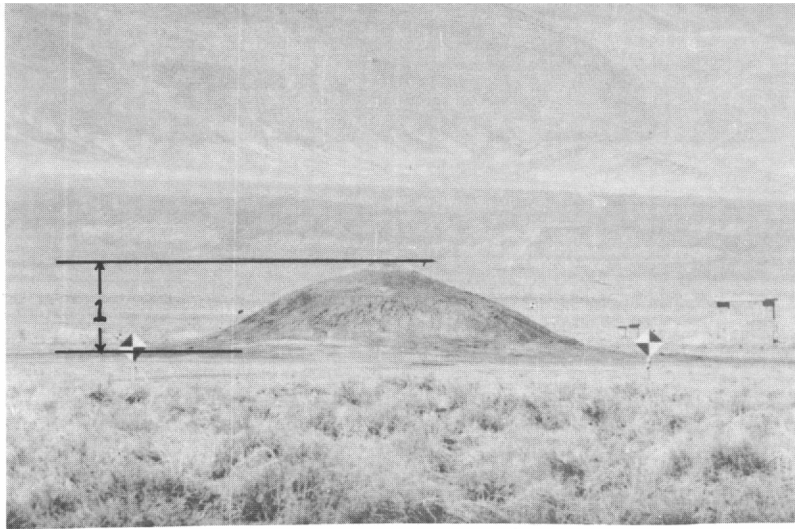
(Numbers refer to definitions in Chapter 6.2.)

Fig. 6.4 Illustrations of displacement definitions.

the center highest jet and the average height of two or three jets on either side. The highest jet in the center could be attributed to stemming material and, since it may be atypical, average height of adjacent jets was also determined.

(4) Vertical column height. Column height is defined by the margin between column and smoke crown.

(5) Column horizontal diameter. Column diameter is measured at both a point near the base and a point just below the intersection of column with smoke crown.

(6) Smoke crown and jet horizontal diameter. Horizontal diameter of the smoke crown and of the subsequent jet is measured at the widest point without reference to surface zero.

(7) Base surge horizontal radius. The horizontal radius of the base surge is measured at the widest point both to the right and left of surface zero.

6.3 VELOCITIES

Figures 6.5, 6.6, and 6.7 show vertical velocities as a function of time for mound, column, and smoke crown and jet. These plots aid in identifying the beginning of the jet phase. They are also valuable in pointing up the difference in smoke crown and jet with burst depth. If the mound and smoke crown and high jet curves are compared by shifting both axes, the similarities between those of the 17- and 34-foot shots are surprising (Fig. 6.8). Most noticeable differences are in the late velocities of the high jet and velocities of the mound rise.

It is interesting to see here differences reflected in the shapes of the velocity-time curves, since craters from the 17- and 34-foot shots are formed primarily by ejection of material both by initial acceleration (spalling), and by gas pressure (compression); the crater from the 80-foot shot is formed by material falling back into a cavity distended by the explosion (collapse).

6.4 MOUND HEIGHT

Information on mound height has been covered by B. F. Murphey in Chapter 3. Only a single additional item is in order here, other than the inclusion of mound rise in the illustrations: the fall of the mound of the deep shot shown
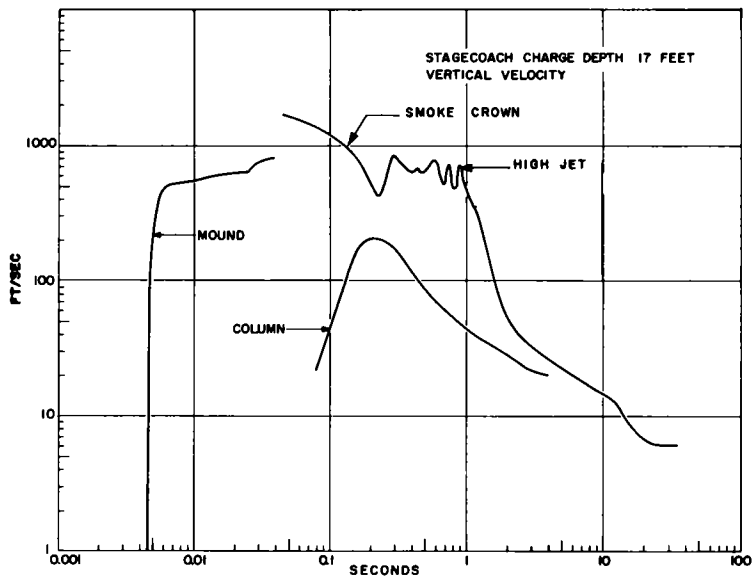
Fig. 6.5 Velocity versus time for charge buried at 17 feet.
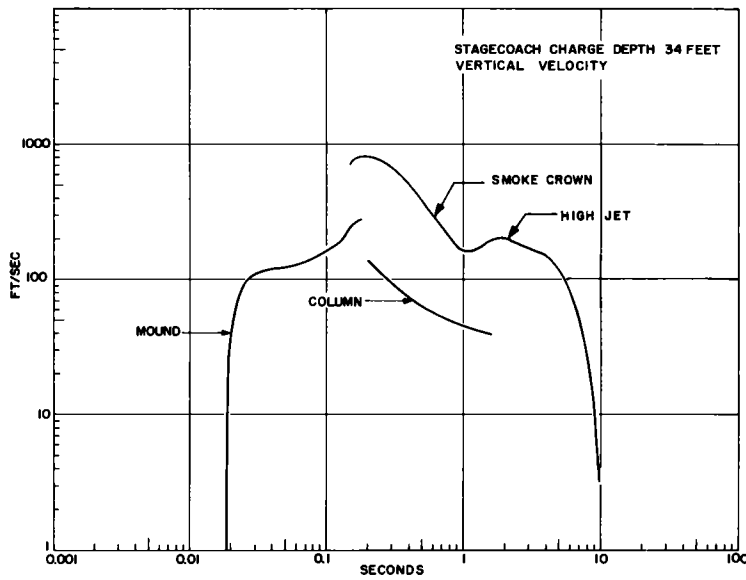
Fig. 6.6 Velocity versus time for charge buried at 34 feet.
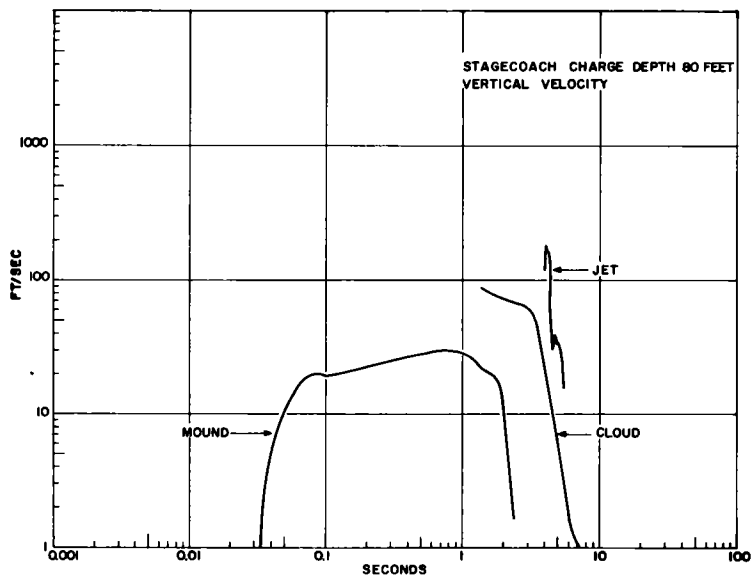
Fig. 6.7 Velocity versus time for charge buried at 80 feet.

in Fig. 6.9. As the fall terminates at 4 seconds, jets caused by gases compressed by the collapse of the mound into the cavity become visible. Also shown is a free-fall curve. It is surprising that the fall of the mound is so nearly free fall, indicating little resistance from residual gas pressure in the cavity or restraint from the distended earth. Also to be noted is the difference in velocity characteristics of the mound as shown in Fig. 6.8.

6.5 HEIGHT OF SMOKE CROWN

The smoke crown originates from initial venting of gases through the raised mound. Except at very deep burst depths, the smoke crown disappears as jets of ejected material pierce its outer boundary and quickly obscure it. Occasionally at late times, remnants of the smoke crown may be seen at the top of the cloud after heavier particles carried up by the jets have begun to fall.

Young[1] gives the time of break-through for charges fired in Dugway dry sand. Similar information is available[2] for two shots fired in NTS desert alluvium. Stagecoach shots have scaled times of break-through $(t_b/lb^{1/3})$ which agree with those of the Dugway dry sand and the alluvium (Fig. 6.10). On the deep Stagecoach shot the smoke broke through below the peak of the mound and continued upward to heights which were never reached by the material ejected (jets) as the mound collapsed into the cavity at a later time. Examination of results of 256-pound spherical charges fired in NTS desert alluvium[2] show that a charge fired at a scaled burst depth of 2 $ft/lb^{1/3}$ gave a very small vent which was quickly obscured by jetting material which seemed to come directly from the mound. This vent probably resulted from failure of the sand tamping and would not have occurred otherwise. A slightly deeper shot (2.5 $ft/lb^{1/3}$) gave no evidence of break-through of venting gases. In that case the rise of the mound gave way directly to jetting material. In the deep Stagecoach shot the only jetting material was that which materialized much later as a result of mound collapse, as also occurred in the two 256-pound charge shots just described. Thus it appears that there are nonscaling mechanisms changing with burst depth which prevent comparison of break-through times for 256-pound shots deeper than about 2 $ft/lb^{1/3}$ with break-through times of larger shots at comparable depths. The relationship between burst depth and break-through time of the Stagecoach shots and other shots shallower than

STAGECOACH
——— DOB = 17 FEET
— — — DOB = 34 FEET

MOUND

SMOKE CROWN AND
HIGH JET

LOG VELOCITY (LOG ft/sec)

LOG TIME (LOG SEC)
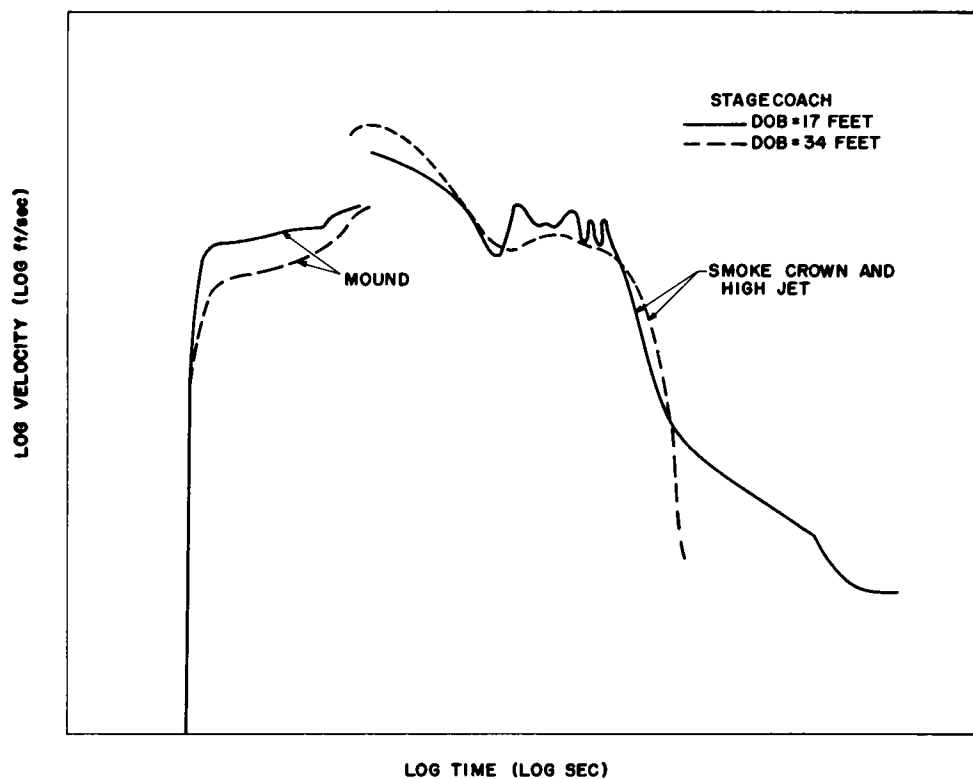
Fig. 6.8 Comparison of velocity-time curves for charges buried at 17 and 34 feet.

FEET

19
NO RESTRAINT
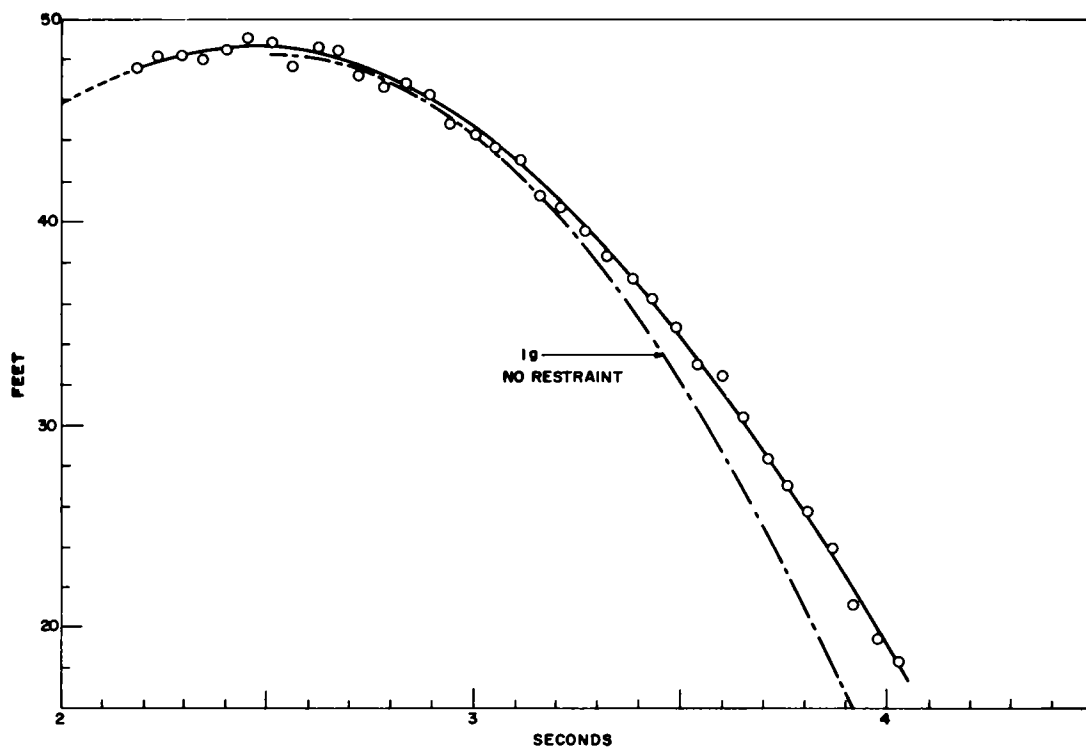
SECONDS

Fig. 6.9 Downward displacement of the mound from the charge buried at 80 feet.
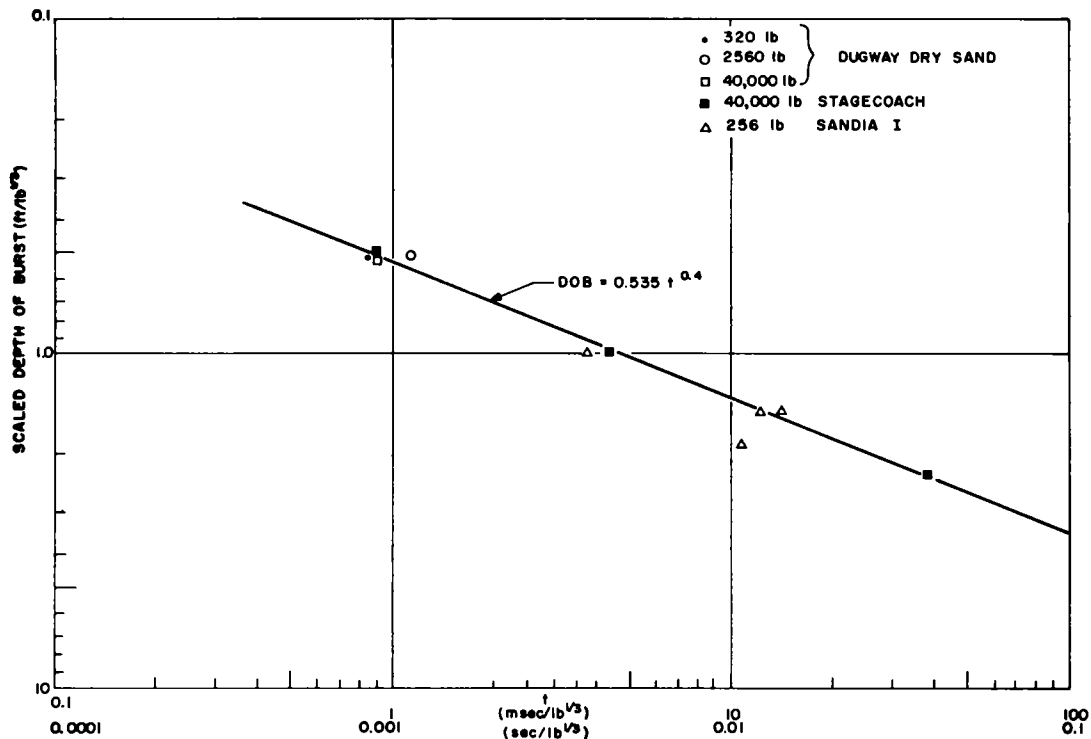
Fig. 6.10 Scaled times of break-through.

2 ft/lb$^{1/3}$ is dob = 0.534 t$^{0.4}$, where dob = the scaled burst depth in feet (ft/lb$^{1/3}$) and t = the scaled time in milliseconds (msec/lb$^{1/3}$).

Figure 6.11 shows detail of the vertical cloud rise as a function of time for the three Stagecoach shots. Also given are the times the jet appears, from which subsequent transitions from the smoke crown into the high jet are apparent.

6.6 JET

The definition of a jet as used here differs from that used by Young.[1] Young defines the center jet as being a combination of explosion gases and smoke which appears for charges fired at scaled depths less than 2 ft/lb$^{1/3}$.

As defined here, however, the jet refers to high-velocity ejected materials (soil and rocks) which pierce through the periphery of the turbulent black smoke crown after it has begun to slow down.

The distinction between the smoke crown and the high jet is quite marked for the two shallower Stagecoach shots. The times at which the jet phase

STAGECOACH 17-FOOT DEPTH
SMOKE CROWN AND JET HEIGHT

FEET (IN HUNDREDS)

JET APPEARS

SECONDS

STAGECOACH 34-FOOT DEPTH
SMOKE CROWN AND JET HEIGHT

FEET (IN HUNDREDS)

JET APPEARS

SECONDS

STAGECOACH 80-FOOT DEPTH
SMOKE CROWN AND JET HEIGHT

FEET (IN HUNDREDS)

JET APPEARS

SECONDS
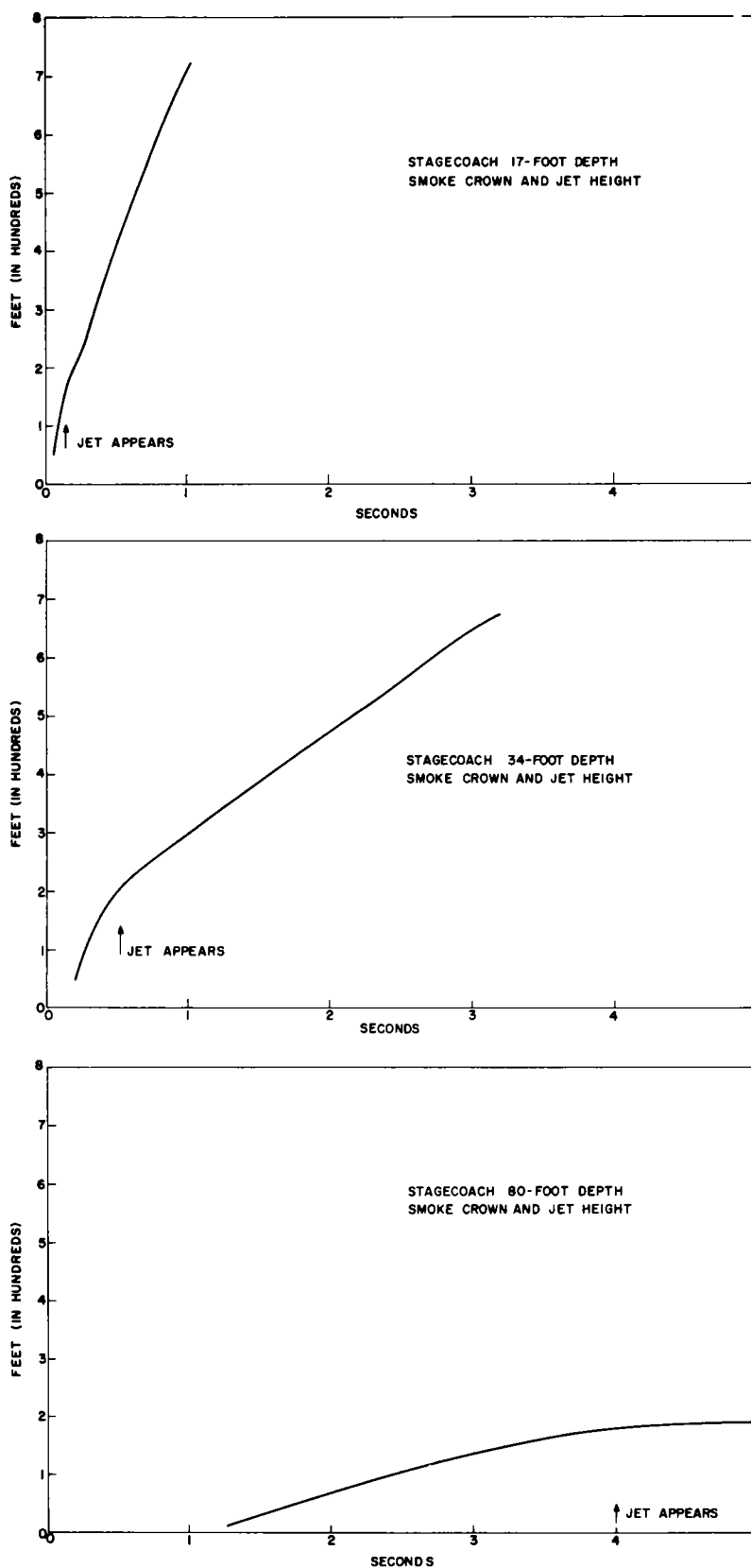
Fig. 6.11 Smoke crown and jet heights
for all Stagecoach shots.

begins, i.e., when the acceler-
ating ejecta break through the
decelerating smoke cloud, are
readily apparent from Figs. 6.5
and 6.6. This time is shown in
the illustrations and is related
to depth of burst within the re-
gion $0.5 < DOB/W^{1/3} < 1$ by the
approximate expression

$$t_j = 1.10 \left(\frac{DOB}{W^{1/3}} \right)^{2.25} ,$$

or

$$\frac{t_j}{W^{1/3}} = 0.032 \left(\frac{DOB}{W^{1/3}} \right)^{2.25} .$$

For these depths of burst
we are unable to see any evidence
of the smoke crown during the jet
phase, and it is assumed that the
gaseous products have been mixed
with the material being blown
from the crater. As the jet
reaches the highest point of its
trajectory and begins to fall, it
leaves behind a trail of ablated
dust as a lingering cloud. Where
gravity effects are ignored,
cloud dimensions and times are
proportional to the cube root of
the charge weight during the
explosion-produced motions and
until the jets reach apogee. Up
to that time moderate winds have

107

relatively little influence. Subsequently, the phenomena are essentially in-
dependent of the explosion and depend more and more upon local meteorological
conditions.

As the material and its entrained air fall back they generate a downward
motion of the air which, in the case of the Stagecoach shot at 34 feet, causes
the top of the lingering cloud to begin to fall at late times.

For deeper scaled burst depths the phenomena appear to be nonscaling.
For the deep Stagecoach shot there are no jets except those which develop late
as a result of mound collapse into the cavity below, which sends up jets caused
by compression of gases in the cavity (Fig. 6.12). These latter jets are in-
dicated in the photograph taken at about 5 seconds.

Since, for the shallower shots, maximum jet height invariably appears to
result from material directly over the charge, it is probable that material
used to stem the charge hole constitutes this highest trajectory material.
Therefore, average values of the adjacent two or three jets have been added.

Young has shown empirically that the maximum height of the jet for charges
at a scaled burst depth of about 0.5 $ft/lb^{1/3}$ may be expressed by the following:

$$J_{max} = 116 \ W^{0.224} \ ,$$

where J_{max} is the maximum height of the jet in feet, and W is equal to the
charge weight in pounds. A 915-foot-high jet from the Stagecoach 17-foot
shot is predicted. The high jet of the Stagecoach shot reached apogee at
about 850 feet. The difference is not sufficient to warrant a change of
Young's expression. After the ejecta of the jet reached apogee, ablated
dust continued to rise. Its effect is clearest when the continued positive
velocities of the shallower shot (Fig. 6.5) are compared with those of the
34-foot shot. The jet was too far above the main part of the cloud for the
subsequent rise to be attributed to bouyant lifting generated by hot explosive
gases. It was caused either by a local atmospheric rise or by the wake over-
run (as the dust following one's car overtakes the car when it is stopped) of
the mass transport of air generated by high velocity of ejecta in the jet.
The jet height of the Stagecoach shot at 34 feet was noticeably higher than
that of the shot at 17 feet, because the lower velocities of the 34-foot shot
act for longer times.
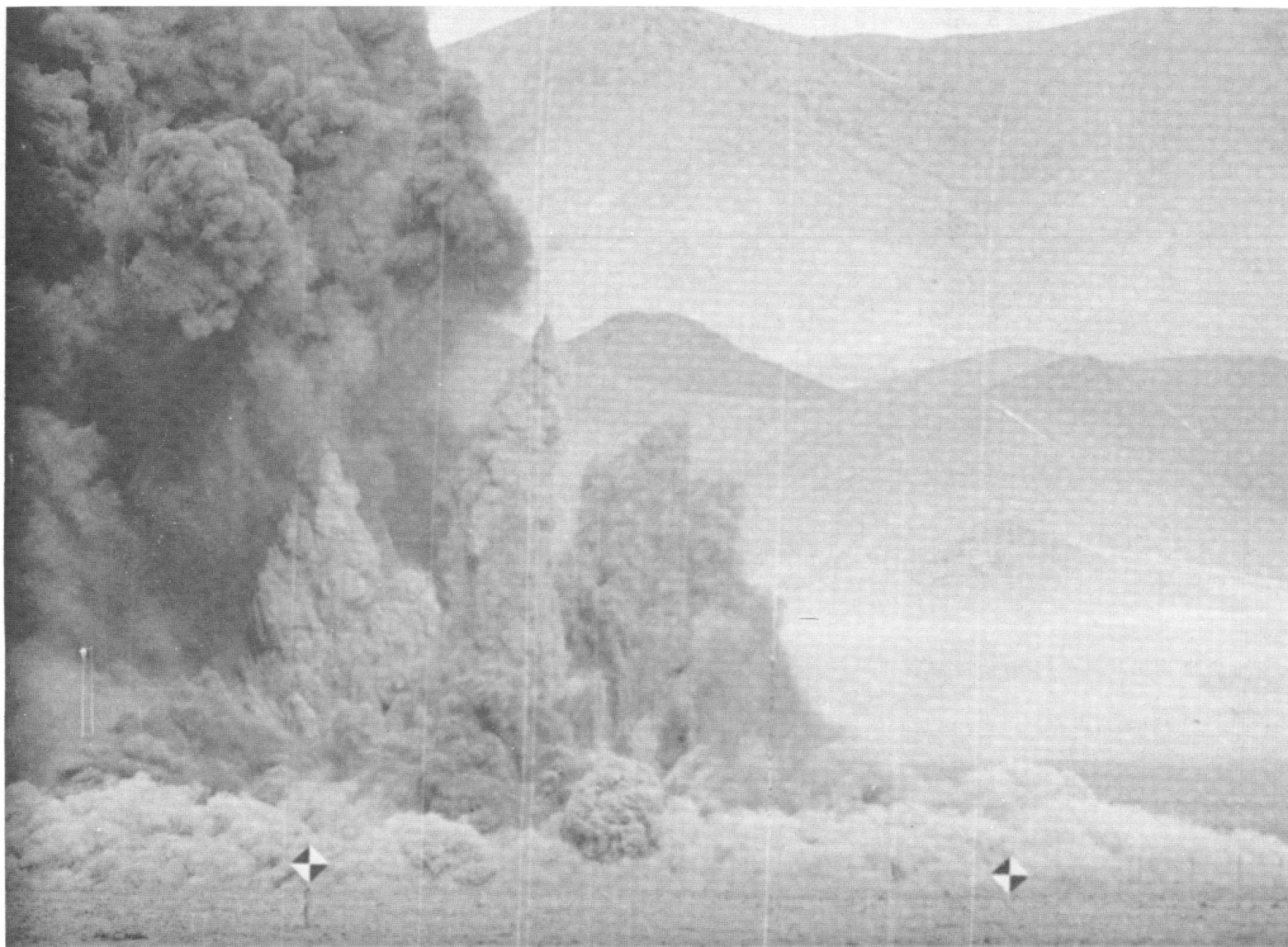
Fig. 6.12   Jets caused by compression of gases in the cavity of
the charge buried at 80 feet.

Young has also developed an expression for maximum over-all height of the cloud versus scaled charge depth. In this development he relies heavily upon four of the Dugway dry clay shots. His expression for 320-pound charges in dry clay, where scaled depth of burst is greater than 0.5 $ft/lb^{1/3}$ is:

$$\Omega_{max} = 774 \ e^{-1.13 \ dob} \ ,$$

where Ω_{max} is maximum over-all height in feet, and dob is scaled burst depth $(ft/lb^{1/3})$.

It has been impossible to reconcile the heights Young uses with those given for the same four shots in the basic reference.[3] Since maximum cloud height at such late times is greatly dependent upon atmospheric conditions, it would be surprising if as consistent a relationship could be developed for total cloud height as for maximum jet height. Scaled times $(t/W^{1/3})$ of observation of cloud heights for the four Dugway shots were between 5 and 40 times the scaled times at which jets of the Stagecoach shots at approximately the same scaled depths reached their maximum height.

Comparisons can be made at scaled times of 0.5 $sec/lb^{1/3}$ by making use of the earliest Dugway observations and the latest of the Stagecoach observations. Results, given in Fig. 6.13, indicate that maximum heights may be achieved for scaled burst depths between 0.75 and 1.0 $ft/lb^{1/3}$. The value for the largest Dugway shot falls below the other values, suggesting a possible inadequacy of cube-root scaling.

Armour Research Foundation found[4] the height of the cloud at about 20 seconds to be given by $(W - FW)^{1/3} = 0.00265 \ H^{1.34}$, where W is charge weight in pounds, F is depth factor, and H is cloud height. The expression gives heights which agree exactly with experimental results for the Stagecoach 34-foot shot, which are lower than experimental results for the Stagecoach 17-foot shot and which break down for the Stagecoach 80-foot shot, at which scaled depth the depth factor becomes zero.

6.7 COLUMN HEIGHT

The column (or stem) develops below the smoke crown from material in the mound. Height has been measured to the average height of the boundary between mound and smoke crown.
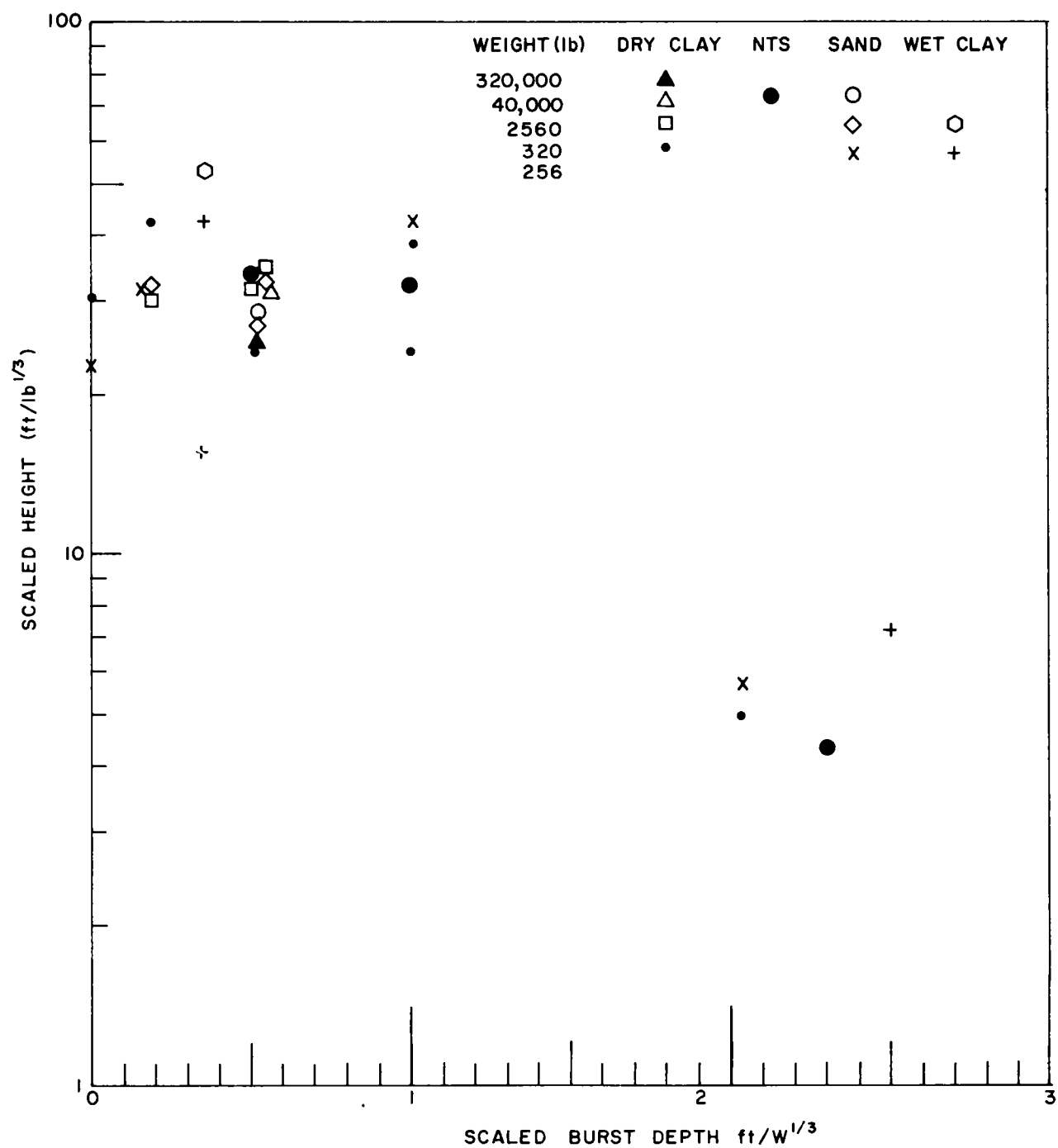
Fig. 6.13 Scaled cloud heights at a scaled time of 0.5 sec/lb$^{1/3}$.

Young has given expressions, developed from Dugway data, for maximum column height for scaled burst depths of 0.512 and 0.135 ft/lb$^{1/3}$. That for the former would predict a height of about 280 feet for the shallowest Stagecoach shot. We were able to follow the maximum height only to about

175 feet, after which time the boundary became quite indistinct. Column height was quite distinct at early times. It did not cease abruptly as an identifiable feature, but faded as the ejecta of the jet broke through the column and crown. Thus, maximum column height was not a uniquely identifiable feature.

Young indicates maximum column heights occur for scaled burst depths of $1 \text{ ft/lb}^{1/3}$, but we were able to follow the column height of the $0.5 \text{ ft/lb}^{1/3}$ Stagecoach shot higher than that for the $1.0 \text{ ft/lb}^{1/3}$ Stagecoach shot.

There was no column on the deeper Stagecoach shot.

6.8 COLUMN HORIZONTAL DIAMETERS

Column diameter for both shallower Stagecoach shots was greater at the top than at the bottom except for a very brief period at the beginning of the column on the 34-foot Stagecoach shot. Young notes that maximum column diameter increases with increasing depth of burst to a maximum at $1 \text{ ft/lb}^{1/3}$, yet we were able to follow the diameter of the Stagecoach 17-foot shot much farther than that of the 34-foot shot $(1 \text{ ft/lb}^{1/3})$. As with maximum column height, maximum column diameter is not uniquely identifiable. Young's expression for maximum diameter at a shot burst of $0.5 \text{ ft/lb}^{1/3}$ gives a result (272 feet) within 10 percent of our experimental value (300 feet) and is considered adequate: $D_{max} = 10.9 \ W^{0.304}$, where D_{max} is maximum column diameter and W is charge weight in pounds (TNT). For $0.01 < t/lb^{1/3} < 0.1$, the base diameter of the column of both the 17- and 34-foot Stagecoach shots agree within ± 5 percent with the following expression: $D_b = W^{1/3}(2.25 + 1.90 \ t)$ where D_b is the base diameter in feet, W is charge weight in pounds (TNT), and t is time in seconds.

The top diameters of the two Stagecoach shots were quite different, that for the shallower shot being the larger.

6.9 SMOKE CROWN AND JET DIAMETER

Diameters of the smoke crown and jet are measured at the altitude of their widest point. Diameter of the crown and jet on the Stagecoach 34-foot shot almost exactly equaled height. On the 17-foot shot the smoke crown diameter was greater initially but smaller later, due to the higher velocity of the vertical portion of the jets.

6.10 BASE SURGE

Base surge dimensions were read from Bell and Howell camera film running at 64 frames per second (see Appendix A, Table A.1). Its growth to the left and and right of the plume was measured perpendicular to the camera line of sight. Its point of origin was read along the line of site from a Mitchell camera film and is included in Figs. 6.1, 6.2, and 6.3. By the time the base surge of the Stagecoach shots became identifiable on the Bell and Howell film, it was an expanding cloud of turbulent eddies from which the heaviest particles had already settled out. The remaining aerosol contained particles so small that the local surface-wind conditions quickly destroyed the symmetry of the propagation. Local wind conditions were:

Shot depth (ft)	Average wind velocity* (ft/sec)	Wind angle with perpendicular-to-camera line of sight (degrees)
17	15	23
34	12	8
80	3	88

Since winds were not steady, neither average wind velocity nor direction accounts for cloud behavior. Only on the 17-foot shot is the wind effect clearly defined by surge growth as about 15 ft/sec perpendicular to the camera line of sight. At any given time the two base surge radii of the Stagecoach 17-foot shot are larger than those of the Dugway shot at the same depth and size.

Young reports successful efforts to scale base surge dimensions by maximum diameter of the column and the times by its square root. While the scaling requires an equivalence of Froud numbers, choice of maximum diameter of the column as the characteristic length seems a poor one, since the maximum diameter of the column was so difficult to identify. However, it is difficult to suggest a better one. Using maximum column diameters, we were able to obtain values for the two shallower Stagecoach shots. (The deep shot could not be scaled in the same manner, since no column developed.) Results for the 17-foot shot agree (slightly higher) with Young's scaling of Dugway and NTS results, but those of the 34-foot shot are higher by a factor of two.

---

*See Appendix B for more complete weather data.

REFERENCES

1. Young, George A., Base Surge Analysis--HE Tests, Operation Jangle, WT-339, U. S. Naval Ordnance Laboratory, May 20, 1952.

2. Murphey, Byron F., High Explosive Crater Studies: Desert Alluvium, SC-4614(RR), Sandia Corporation, May 1961.

3. Engineering Research Associates, Inc., Instrumentation for Underground Explosion Test Program, Supplement to Interim Technical Report, Vol. I, June 1, 1952.

4. Engineering Research Associates, Underground Explosion Test Program, Final Report, Vol. I, Soil, August 30, 1952.

Chapter 7

MISSILE HAZARD FROM PARTLY CONTAINED EXPLOSIONS by R. H. Bishop

7.1 INTRODUCTION

Two cratering shots of the Stagecoach series at 17- and 34-foot burial depths have furnished data concerning range and quantity of material thrown out by 20 tons of TNT. Results from 8 pounds of TNT at the same scaled burial depths are also presented. Comparison of the two sets of data gives a good basis for predicting the amount of material thrown out at various distances by TNT explosions of intermediate yields.

7.2 THROWOUT COLLECTION STATIONS

Coordinates of the collection stations are defined by intersections of a series of circles and radii (Table 7.1). Azimuth is indicated by numbers from 1 to 12 which designate equally spaced radii 30 degrees apart. Due north corresponds to number 12 and due south to number 6. Letters designate the circles, with A the inner circle (see Figure 4.1).

TABLE 7.1 40,000 POUNDS OF TNT AT 17-FOOT DEPTH OF BURST
$$(dob = 0.5 \text{ ft/lb}^{1/3})$$

Scaled distance $(\text{ft/lb}^{1/3})$	Radial distance (ft)	Circle	Throwout concentration (lb/ft^2) Azimuth		
			1	7	10*
7	240	A	0.73	0.18	4.37
10	345	B	--	--	0.49
15	510	C	0.03	0.10	0.38
22	750	D	--	--	0.12
32	1095	E	0	0	0.07
47	1590	F	--	--	0.02
68	2325	G	0	0	0.0

*Data for azimuth 10 obtained from measurements by J. A. Blaylock and W. A. Roberts, Boeing Airplane Company.

Throwout material was collected on canvas sheets, each 10 by 10 feet, placed flat on the ground at various distances along selected radii.

7.3 THROWOUT CONCENTRATION

Throwout weight per square foot as a function of radial distance at various azimuth directions corresponding to the numbering systems just described is shown in Tables 7.1 and 7.2. Figure 7.1 shows the same data averaged for the various azimuth directions.

TABLE 7.2 40,000 POUNDS OF TNT AT 34-FOOT DEPTH OF BURST

$$(dob = 1.0 \ ft/lb^{1/3})$$

Scaled distance $(ft/lb^{1/3})$	Radial distance (ft)	Circle	Throwout concentration (lb/ft^2) Azimuth			
			1	4*	7	10*
7	240	A	--	1.9	7.0	3.74
10	345	B	--	0.93	--	2.86
15	510	C	0.23	0.42	1.5	1.23
22	750	D	--	0.23	--	0.17
32	1095	E	--	0.06	0.05	--
68	2325	G	0	0	0	0

*Data for azimuths 4 and 10 obtained from measurements by J. A. Blaylock and W. A. Roberts, Boeing Airplane Company.

Figure 7.1 gives throwout concentration values from Tables 7.1 and 7.2 which have been averaged over all available azimuth directions around each circumference at any given radial distance from the explosion epicenter. Fallback data obtained at Coyote Test Field (Sandia Laboratory) from the explosion of 8-pound spheres of TNT at the same scaled depths of burst $(dob = 0.5 \ ft/lb^{1/3}$ and $dob = 1.0 \ ft/lb^{1/3})$ are also shown in Fig. 7.1 for comparison.

It is evident from Fig. 7.1 that throwout concentration at the same scaled distance is not very dependent on the size of the explosion. In going from 8 pounds yield to 40,000 pounds yield, throwout concentration shown in Fig. 7.1 at a scaled distance equal to 20 goes only from 0.05 lb/ft^2 to 0.11 lb/ft^2, which is about a factor of 2. (Scaled depth of burst in both
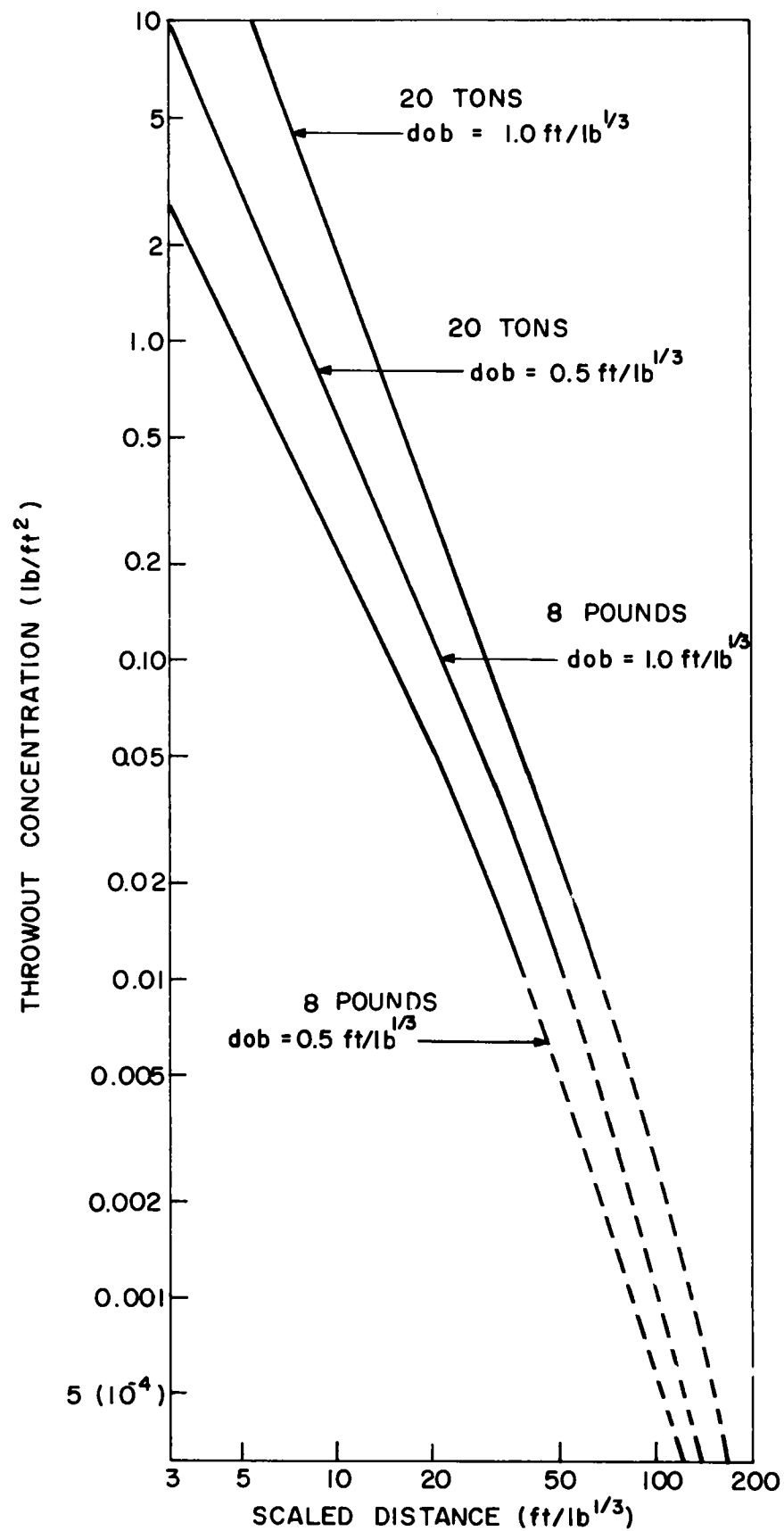
Fig. 7.1 Throwout concentration versus scaled radial distance.

cases is 0.5 ft/lb$^{1/3}$.) In changing scaled depths of burst of the 40,000-pound shot from dob = 0.5 ft/lb$^{1/3}$ to dob = 1.0 ft/lb$^{1/3}$, throwout concentration at a scaled distance of 20 (same as previous figure) changed from 0.11 lb/ft^2 to 0.29 lb/ft^2, i.e., by a factor of 2.6; this is larger than the factor of 2.0 resulting from a change in yield by a factor of 40,000/8 (5000 to 1).

At first glance, Figure 7.1 may seem to disagree with the information contained in Chapter 4. Figure 7.1 is the best fit to data such as that of Table 7.2, and the data have a wide variation with azimuth, although (since the sample is large) the variation with azimuth is less than in the data reported in Chapter 4. There the sample was small, and the addition of a single rock or clod increased weight by many times. By averaging samples from all azimuths, a relatively consistent value was determined for each range; this value agrees with Figure 7.1 within a factor of about four.

7.4 SIZE DISTRIBUTION

Figure 7.1 shows concentration of throwout material irrespective of particle size. In order to find a more accurate basis for actual hazard from individual missiles, it is necessary to know what percentage of throwout weight consists of particles exceeding any given mass (per particle). Evidently, when large rocks land at a considerable radial distance, the concept of throwout weight per unit area becomes statistical, since the probability is much less than 1.0 that any given square foot of area will have even one rock of large size. For this reason, "large" rocks are not included in Tables 7.3 and 7.4, and their occurrence is treated separately. Note that the throwout material consisted almost entirely of fine powder at scaled distances greater than 22 (actual radial distances greater than 750 feet).

From the 34-foot-depth explosion, five individual rocks landed near the F-circle (1590 feet) as indicated below. Directions were near azimuth 12.

118

Weight of rock (lb)	Radial distance (ft)
32	1440
8.5	1501
8	1730
7.5	1793
7	1646

From the 17-foot-depth explosion the largest individual rock which could be found weighed only 1 pound 10 ounces. It landed on the "azimuth 1" canvas at a distance of 510 feet. The difference between the 17-foot and 34-foot depths is probably related to absence of appreciable boulder content except near the depth of 34 feet. According to the drilling log of hole number 1

TABLE 7.3   FALLBACK SIZE DISTRIBUTION FOR 40,000 POUNDS OF TNT AT 17-FOOT DEPTH OF BURST[*]

Scaled distance $(ft/lb^{1/3})$	Circle	Radial distance (ft) azimuth = 10	Percent of total particles by weight		
			Smaller than 0.03 inch	0.03 inch to 0.26 inch	Larger than 0.26 inch
7	A	240	50.4	32.9	13.8
10	B	345	60	13.8	26.5
15	C	510	75	7.2	16.8
22	D	750	80	6.2	12.5
32	E	1095	100	0	0
47	F	1590	100	0	0
68	G	2325	0	0	0

TABLE 7.4 FALLBACK SIZE DISTRIBUTION FOR 40,000 POUNDS OF TNT
AT 34-FOOT DEPTH OF BURST[*]

Scaled distance $(ft/lb^{1/3})$	Circle	Radial distance (ft) azimuth = 10	Percent of total particles by weight		
			Smaller than 0.03 inch	0.03 inch to 0.26 inch	Larger than 0.26 inch
7	A	240	44.2	33.4	22.6
10	B	345	30.7	43	25.8
15	C	510	63	18.8	18.2
22	D	750	91	1.8	7.1
32	E	1095	100	0	0
47	F	1590	0	0	0
68	G	2325	0	0	0

[*]Data obtained from measurements by J. A. Blaylock and W. A. Roberts, Boeing Airplane Company.

(Area 10, NTS, 80-foot Stagecoach shot), boulders were noticed only at a depth from 33.3 to 34.2 feet.

7.5 ROCK MISSILE VELOCITIES FROM STAGECOACH 34-FOOT EXPLOSION

As shown in the above table, several rock missiles of approximately 8 pounds each landed at horizontal ranges from 1500 to 1800 feet. Using reasonable assumptions concerning rock fragment density and shape, it has been calculated that initial velocities of these missiles must have been in the vicinity of 1000 feet per second. Note that the velocity calculated is 6 to 10 times the velocity of the ground surface motion (see Chapter 3). Thus, material coming out at later times must have had velocities considerably greater than those of the ground surface (see Chapter 5).

Since zenith angle of initial velocity is unknown, only a lower limit for its magnitude, assuming a 45° angle, can be deduced (see Reference 1) from the observed range of any rock missile of known weight, shape, and density.

Choosing a single representative rock from the 34-foot, 20-ton Stagecoach explosion which weighed 8.0 pounds and traveled 1730 feet, it has been deduced that the initial rock missile velocity was 1030 ft/sec. This velocity, in order of magnitude, agrees with those cited in Chapters 5 and 6.

REFERENCE

1. Bishop, R. H., Maximum Missile Ranges from Cased Explosive Charges, SC-4205(TR), Sandia Corporation, July 1958, p. 18.

Chapter 8

CLOSE AIR BLAST SUPPRESSION BY CHARGE BURIAL by L. J. Vortman

8.1 INTRODUCTION

Air blast along the ground surface at NTS, Area 10, has been measured on three series of below-surface HE shots,[1-4] and on the Jangle Underground[5] and Teapot Ess[6] subsurface nuclear shots. A few measurements were made on underground HE shots in other media,[3] specifically, Utah dry clay, California wet sand, and California moist clay. Blast measurements from earlier HE subsurface shots fired at NTS were generally from charges of 256 pounds of TNT. However, three charges weighing 2560 pounds and a single charge of 40,000 pounds were fired at relatively shallow depths of burst. One of the 2560-pound charges was fired at 0.5 $ft/W^{1/3}$; the other two, in addition to the 40,000-pound charge, were fired at 0.15 $ft/W^{1/3}$. (Throughout Chapter 8, W is the weight of the explosive charge in pounds.)

From the foregoing it is clear that Project Stagecoach offered an opportunity to extend blast pressure information to deeper depths of burst with larger HE charges than had been used heretofore. One could thus look for possible departures from cube-root scaling, or verify that scaling over a wider range of HE yields and burst depths. Differences between blasts from HE and NE could then be considered with greater confidence.

A thorough examination demands consideration of peak overpressure (p_+), positive phase impulse (I_+), positive phase duration (t_+), and wave shape. Figure 8.1 shows a typical wave shape for shots at 0.5 and 1.0 $ft/W^{1/3}$ and the terminology used.

Stagecoach air blast results are summarized in Tables 8.1 and 8.2. Throughout this chapter ambient conditions for NTS, Area 10, $(p_o \approx 12.6$ psi) have been used. No values have been adjusted to sea level conditions. Where other comparisons are indicated, they have been scaled to NTS altitude.
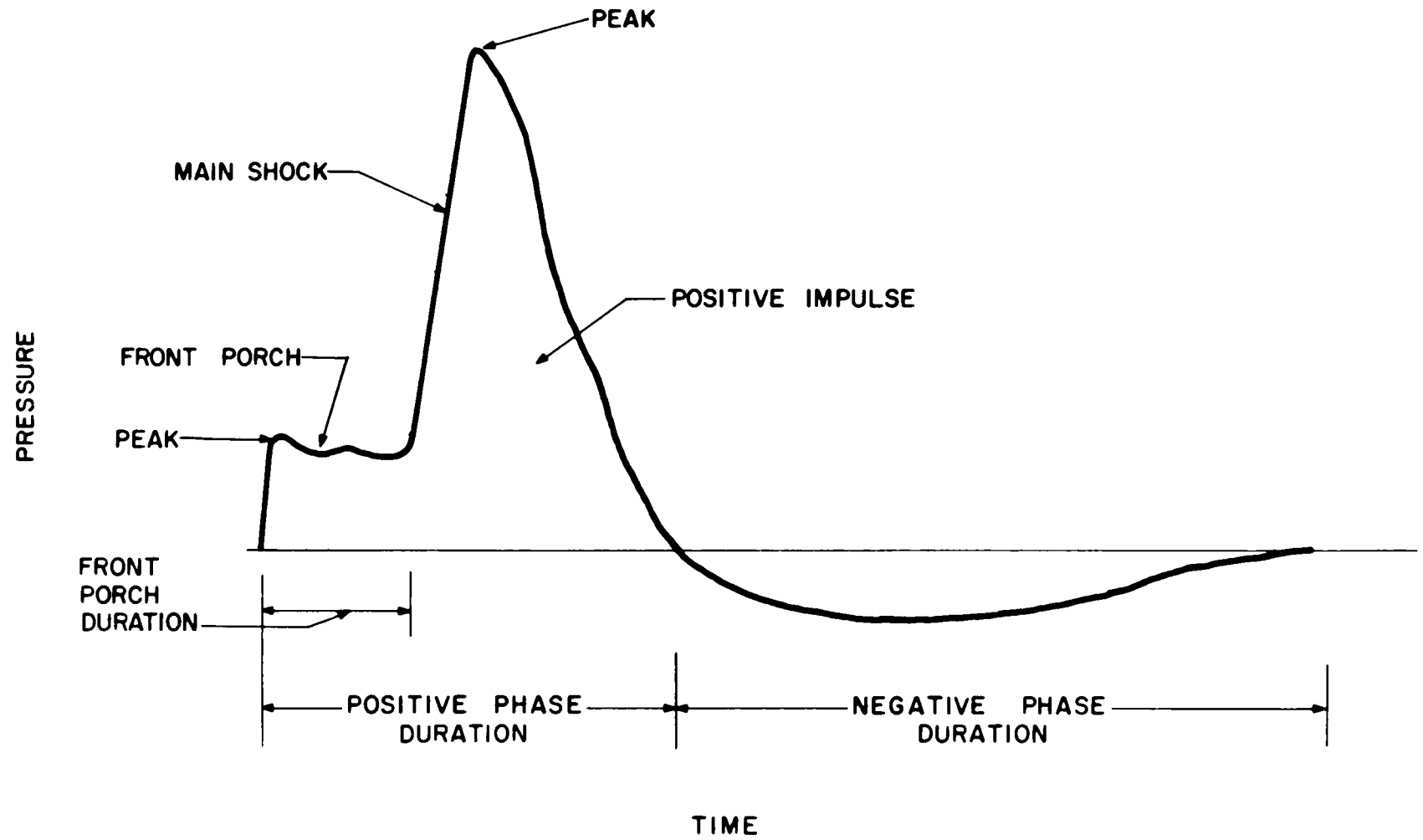
Fig. 8.1 Shape of a typical blast wave.

TABLE 8.1 STAGECOACH AIR BLAST RESULTS[*]

Shot	Station	Distance (ft)	Scaled distance $(ft/W^{1/3})$	Peak overpressure (psi) Front porch	Main shock	Arrival times (sec) To front porch	To main shock	Duration (sec) Front porch	Positive phase (total)	Negative phase	Positive impulse (psi-sec)	Scaled impulse (psi-sec) $(ft/W^{1/3})$
Stagecoach 2 DOB = 17 feet	32	110	3.216	0.68	4.65	0.097	0.112	0.018	0.068	0.352	0.133	0.00389
		110	3.216									
	33	160	4.678	0.43	4.10	0.137	0.148	0.012	0.076	0.331	0.110	0.00322
		160	4.678	0.40	4.00	0.136	0.148	0.011	0.072		0.100	0.00292
		160	4.678									
	34	270	7.895	2.58	3.05	0.234	0.242	0.008	0.080	0.333	0.073	0.00213
		270	7.895									
	35	430	12.573	--	1.65	--	0.380	--	0.085	0.327	0.057	0.00167
		430	12.573	--	1.68	--	0.376	--	0.085	0.337	0.063	0.00184
		430	12.573									
	36	700	20.468	--	0.91	--	0.604	--	0.092	0.312	0.034	0.000994
		700	20.468	--	0.90	--	0.603	--	0.093	--	0.035	0.00102
	37	1600	46.783	--	0.29	--	1.393	--	0.110	0.297	0.016	0.000468
		1600	46.783	--	0.34	--	1.392	--	0.113	0.258	0.017	0.000497
	38	3000	87.719	--	0.173	--	2.633	--	0.120	0.277	0.008	0.000234
		3000	87.719	--	0.176	--	2.630	--	0.120	0.265	0.009	0.000263
Stagecoach 3 DOB = 34 feet	22	110	3.216	0.29	0.68	0.092	0.261	0.173	0.285	--	0.056	0.00164
		110	3.216									
	23	160	4.678	0.19	0.57	0.135	0.304	0.173	0.291	0.841	0.064	0.00187
		160	4.678	0.19	0.58	0.132	0.305	0.171	0.291	0.679	0.046	0.00134
		160	4.678									
	24	270	7.895	0.08	0.34	0.229	0.396	0.169	0.294	0.570	0.028	0.000819
		270	7.895									
	25	430	12.573	0.07	0.26	0.372	0.540	0.169	0.303	0.464	0.009	0.000263
		430	12.573	0.06	0.27	0.374	0.539	0.169	0.292	0.555	0.021	0.000614
		430	12.573									
	26	750	21.930	0.04	0.155	0.657	0.819	0.168	0.309	0.419	0.013	0.000380
		750	21.930	0.03	0.150	0.654	0.823	0.166	0.299	0.480	0.012	0.000351
	27	1100	32.164	0.02	0.100	0.965	1.125	0.167	0.314	0.438	0.008	0.000234
		1100	32.164	0.02	0.090	0.962	1.128	0.166	0.302	0.530	0.012	0.000351
	28	1600	46.783	0.015	0.073	1.410	1.577	0.166	0.306	0.489	0.008	0.000233
Stagecoach 1 DOB = 80 feet	11	80	2.339	0.09	--	0.054	--				0.00960	0.000281
		80	2.339	0.09	--	0.053	--				0.00862	0.000252
	12	110	3.216	0.056	--	0.056	--				0.00619	0.000181
		110	3.216	0.056	--	0.055	--				0.00559	0.000163
	13	160	4.678	0.028	--	0.090	--				0.00361	0.000106
		160	4.678	0.030	--	0.094	--				0.00494	0.000144
	14	270	7.895	0.027	--	0.112					0.00250	0.0000731
		270	7.895	0.026	--	0.126					0.00242	0.0000708
	15	430	12.573	0.015	--	0.184					0.00194	0.0000567
		430	12.573	0.014	--	0.189					0.00145	0.0000424

[*]Naval Ordnance Laboratory records.

125

TABLE 8.2 STAGECOACH AIR BLAST RESULTS[*]

	Station	Distance (ft)	Scaled distance $(ft/W^{1/3})$	Peak over-pressure (psi) front porch	Peak over-pressure (psi) Main shock	Arrival times (sec) To front porch	Duration (sec) Positive phase (total)	Duration (sec) Negative phase	Positive impulse (psi-sec)	Scaled impulse (psi-sec) $(ft/W^{1/3})$
Stagecoach 2 DOB = 17 feet	32	110	3.216		5.65	0.065	0.067	0.313	0.116	0.00339
		110	3.216		5.66	0.200	0.067	0.355	0.116	0.00339
	33	160	4.678		4.64	0.220	0.070	0.345	0.100	0.00292
	34	270	7.895		2.58	--	0.067	0.247	0.070	0.00205
	35	430	12.573		1.80	0.475	0.081	0.311	0.052	0.00152
	36	700	20.468		0.99	0.730	0.094	0.304	0.037	0.00108
	37	1600	46.783		0.35	1.340	0.104	0.298	0.017	0.000497
	38	3000	87.719		0.19	2.710	0.112	0.283	0.009	0.000263
		3000	87.719		0.18	2.740	0.114	0.282	0.009	0.000263
		3000	87.719		0.22	2.710	0.115	0.293	0.009	0.000263
	39	4700	137.426		0.13	--	0.122	0.282	0.007	0.000205
Stagecoach 3 DOB = 34 feet	22	110	3.216		0.71	0.115	0.336	0.543	0.072	0.00210
	23	160	4.678		0.58	0.140	0.360	0.600	0.051	0.00149
	24	270	7.895		0.38	0.310	0.304	0.551	0.033	0.000965
	25	430	12.573		0.25	0.270	0.341	0.481	0.022	0.000643
	26	750	21.930		0.16	0.700	0.308	0.490	0.014	0.000409
		750	21.930		0.16	0.690	0.310	0.489	0.014	0.000409
		750	21.930		0.15	0.6501	0.306	0.515	0.013	0.000380
		750	21.930		0.16	1.020	0.494	0.490	0.014	0.000409
		750	21.930		0.15	0.620	0.497	0.503	0.014	0.000409
		750	21.930		--	--	--	--	--	--
		750	21.930		0:16	0.680	0.491	0.497	0.014	0.000409
	27	1100	32.164		0.11	0.770	0.313	0.457	0.010	0.000292
	28	1600	46.783		0.073	1.370	0.369	0.476	0.007	0.000205
	29	5020	146.783		0.021	--	0.312	0.468	0.022	0.0000585
Stagecoach 1 DOB = 80 feet	11	80	2.339	0.096	--	--	--		0.0079	0.000231
		80	2.339	0.093	--	< 0.005	0.166		0.0078	0.000228
	12	110	3.216	0.057	--	0.005	0.168		0.0053	0.000155
	13	160	4.678	0.024	--	0.025	0.249		0.0034	0.0000994
	14	270	7.895	0.029	--	0.160	0.251		0.0020	0.0000585
	15	430	12.573	0.014	--	0.175	0.345		0.0015	0.0000438

[*]Ballistic Research Laboratories records.

8.2 WAVE FORMS

Wave forms of the blast waves are shown in Figs. 8.2 through 8.16. Those records labeled NOL (Naval Ordnance Laboratory) in Tables 8.1 and 8.2 were obtained with Ultradyne strain-diaphragm gages, and those identified as BRL (Ballistic Research Laboratories) with BRL self-recording diaphragm-type gages. The peak value is not shown in the first record of Fig. 8.2 because of limitations in the playback system.

Figure 8.17 shows graphically the changes which occur in the shape of the blast wave as charge depth of burial is increased. The information used comes from Stagecoach and Mole high-explosive experiments and from three nuclear shots. The wave form for a surface burst is a typical shock wave with a fast rise and a sharp peak. As the depth of burst is increased, the sharp peak gives way to a rounded one. The change to rounded peak occurs at greater radial distances for the deeper depths of burst. The roundness is more pronounced with increased depth and nearness to surface zero. In some cases the roundness is sufficiently small that the wave has a chance to shock up by the time it reaches the more distant ranges. As burst depth is increased, the pressure rise rate continues to decrease.

The "front porch" begins to appear as burst depth is increased below the surface. The front-porch wave originates when the ground shock, arriving at the surface, acts as a piston to induce a shock wave in the air.[*] This wave was observed photographically on the Stagecoach shots at 0.5 and 1.0 $ft/W^{1/3}$.

---

[*] The front porch has been attributed[1] to the earth piston action of the rising earth mound. It should be made clear that this implies that the air shock results from a velocity transfer to the air when the ground shock reaches the surface. It is not due to the subsequent rise of the mound. The clearest explanation comes from the Stagecoach shot at 1 $ft/W^{1/3}$. The front porch decays from peak to a value between 1/4 and 1/2 peak in 20 to 50 msec and pressure thereafter remains sustained (Figs. 8.5, 8.6, and 8.7) until the main shock arrives. Extrapolation of front porch peak values back to the vicinity of the epicenter would give peak porch values of approximately 2 psi. This leads one to expect initial surface velocities such as 120 ft/sec, which agree well with values in Fig. 3.2. The pressure decays during the 20 to 50 msec following the peak, during which time the mound velocity continues to increase. Thus, although subsequent mound rise does not account for the shock front of the front porch, it may well account for the sustained positive pressure between the front porch shock and the main shock.
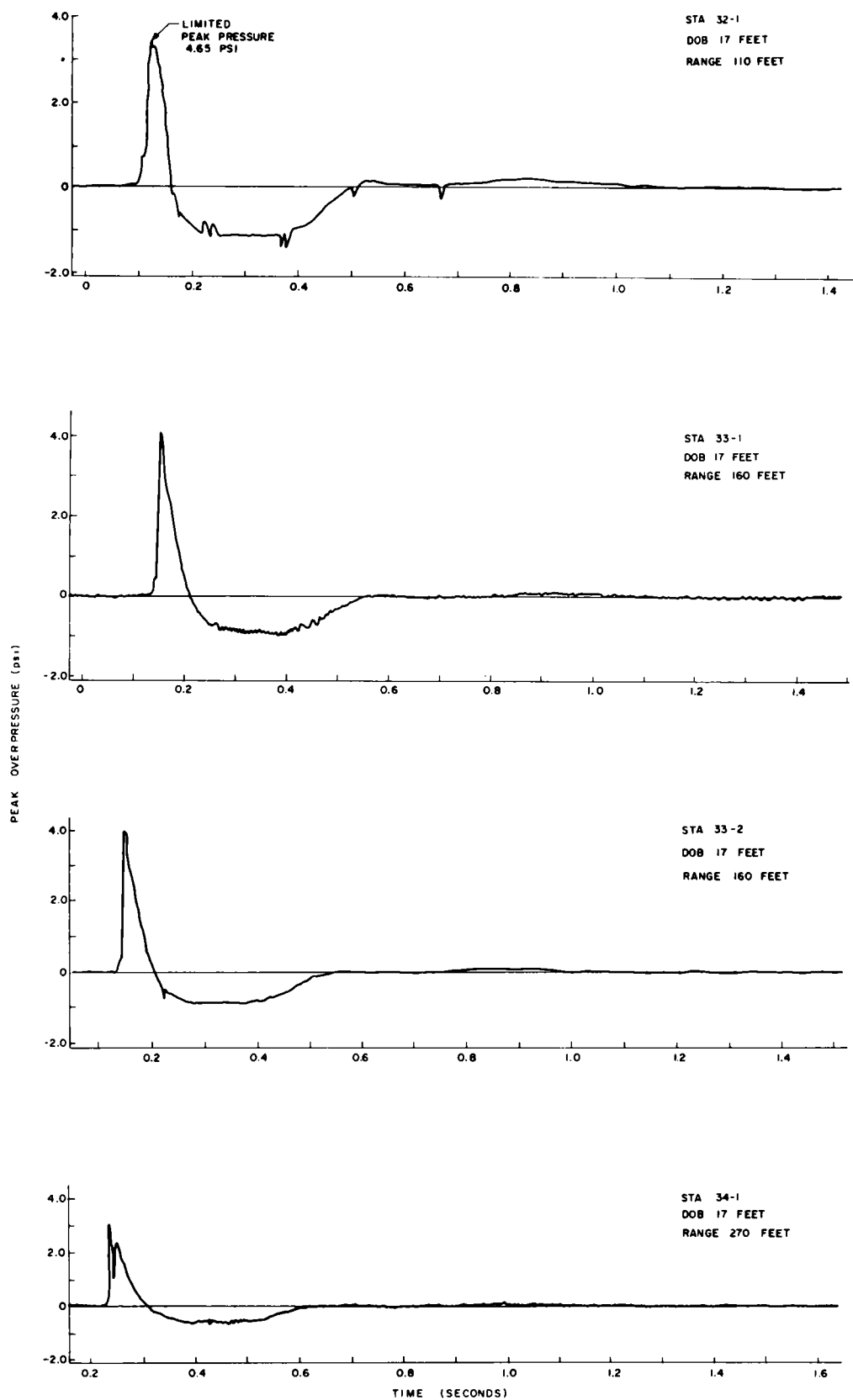
Fig. 8.2   Pressure records, NOL.
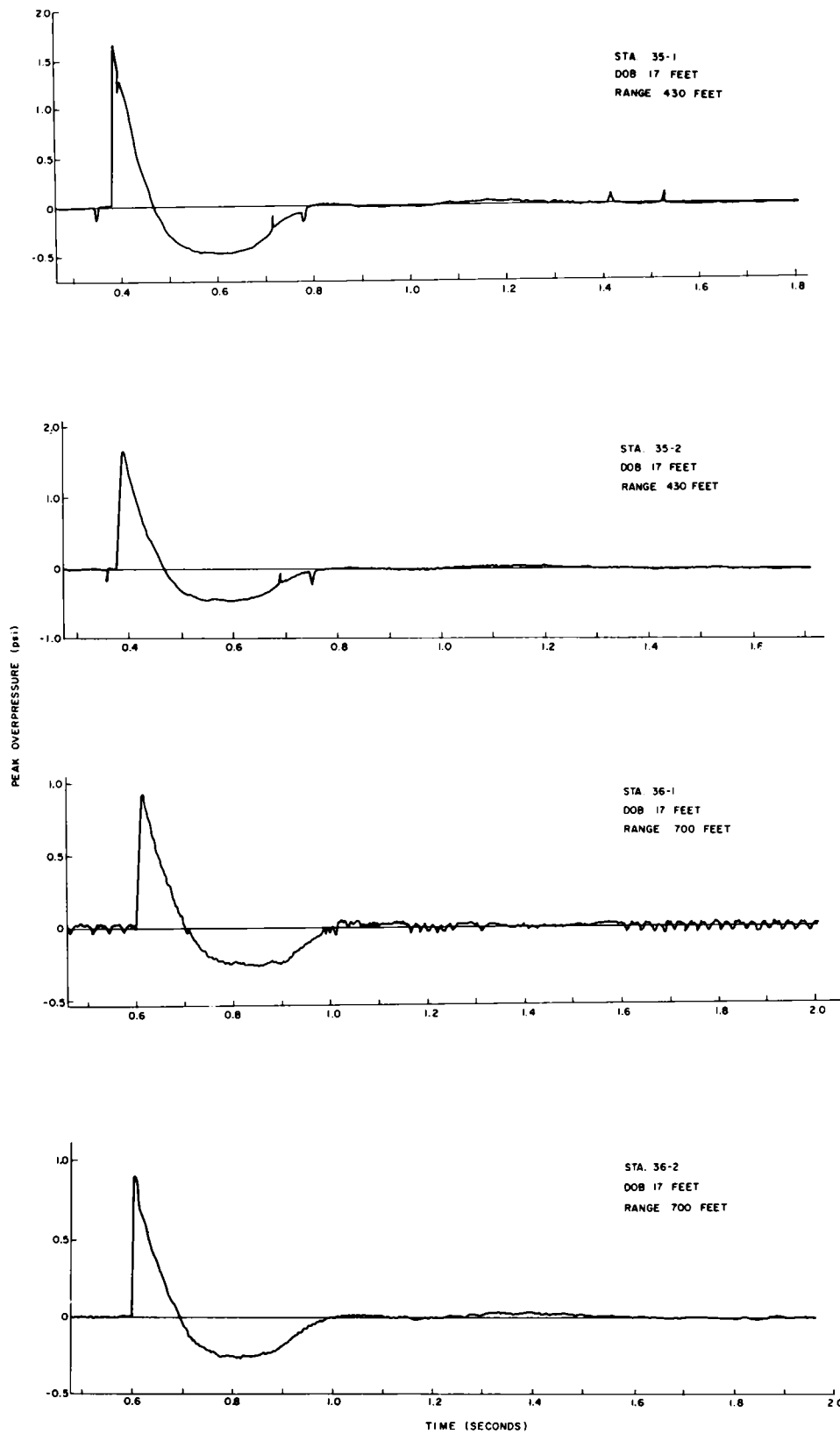
Fig. 8.3 Pressure records, NOL.
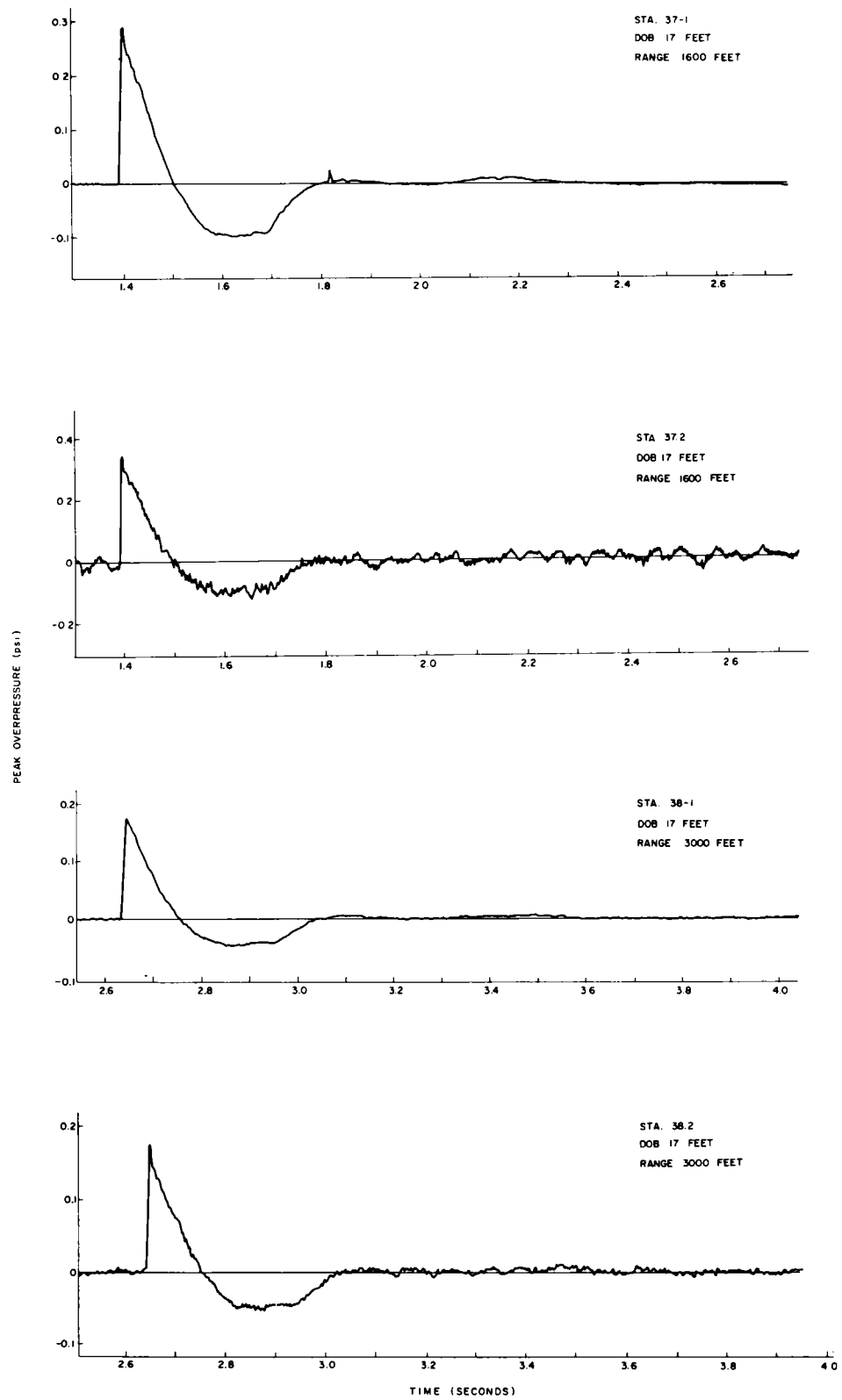
Fig. 8.4 Pressure records, NOL.
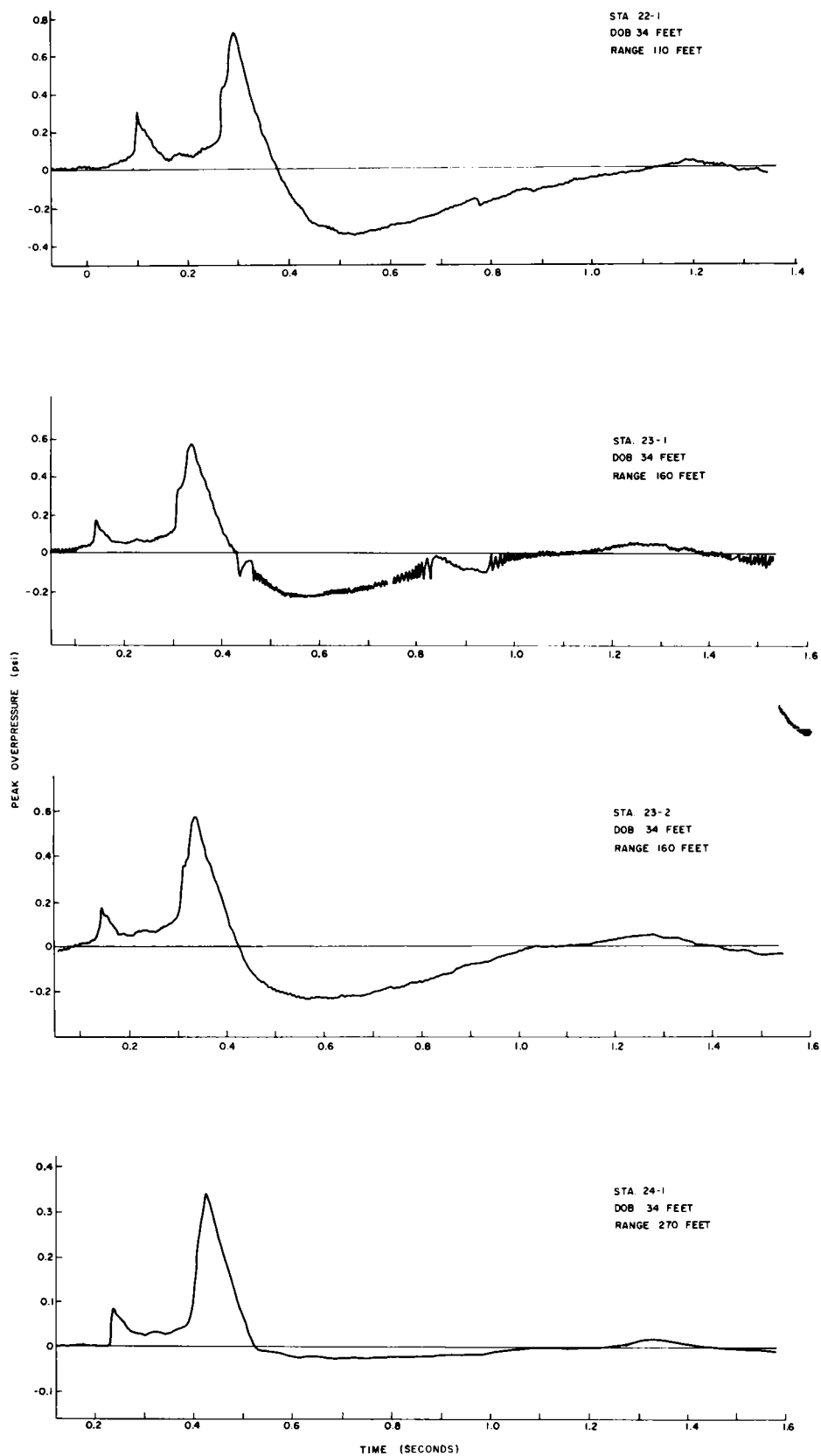
Fig. 8.5 Pressure records, NOL.
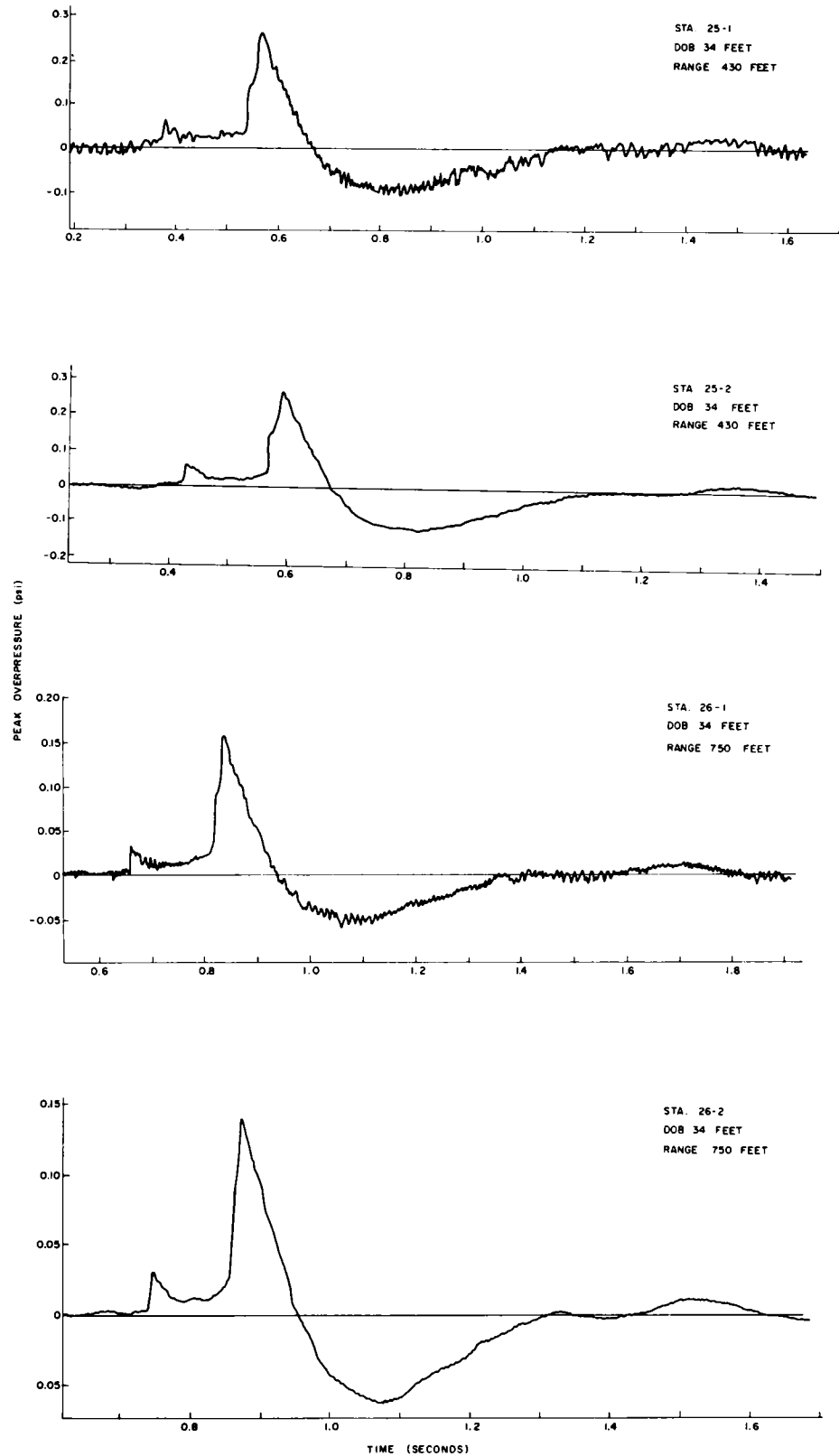
Fig. 8.6 Pressure records, NOL.
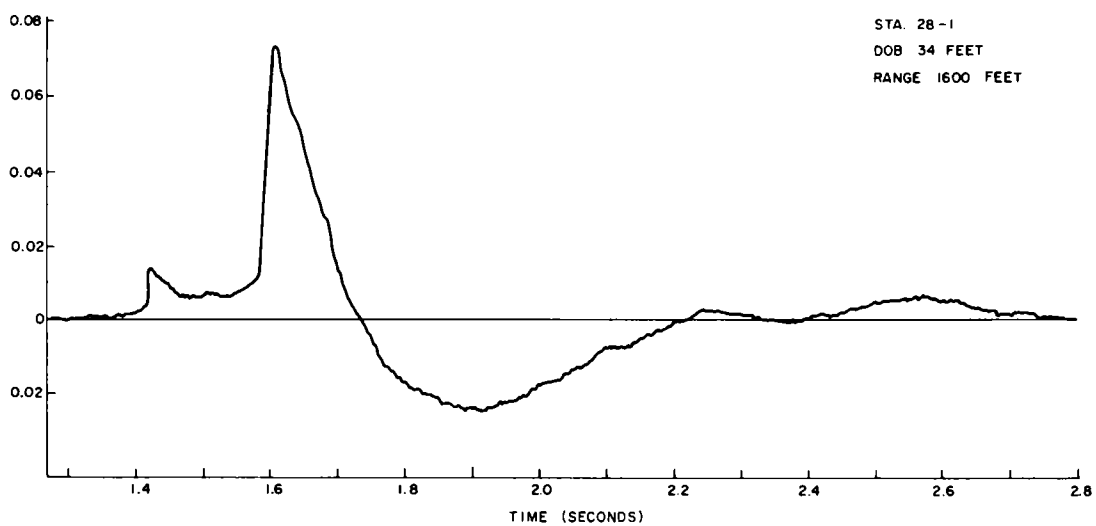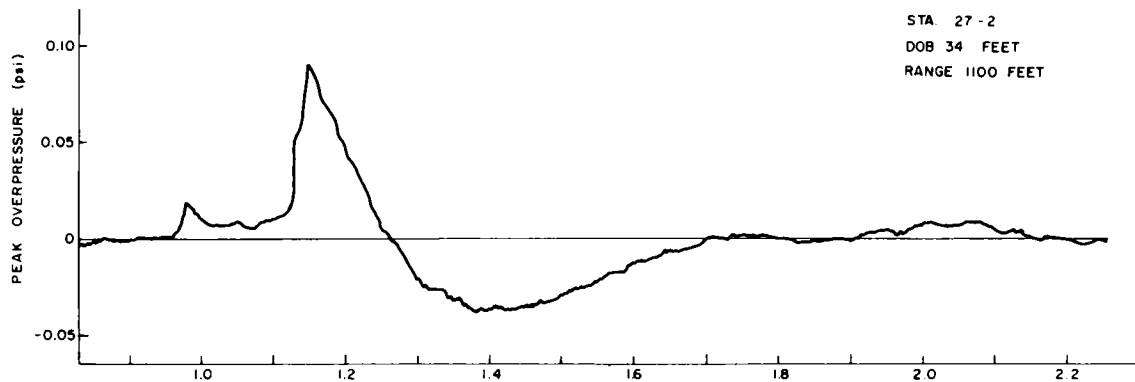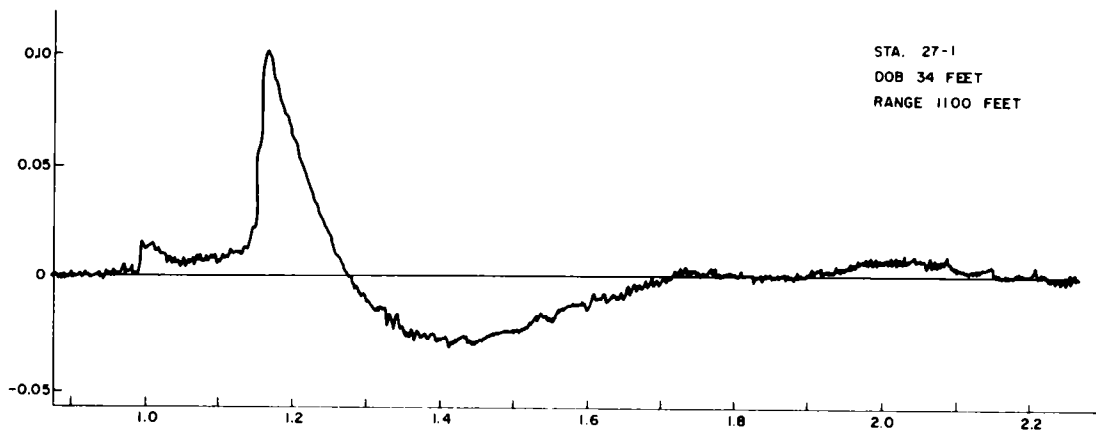
Fig. 8.7 Pressure records, NOL.
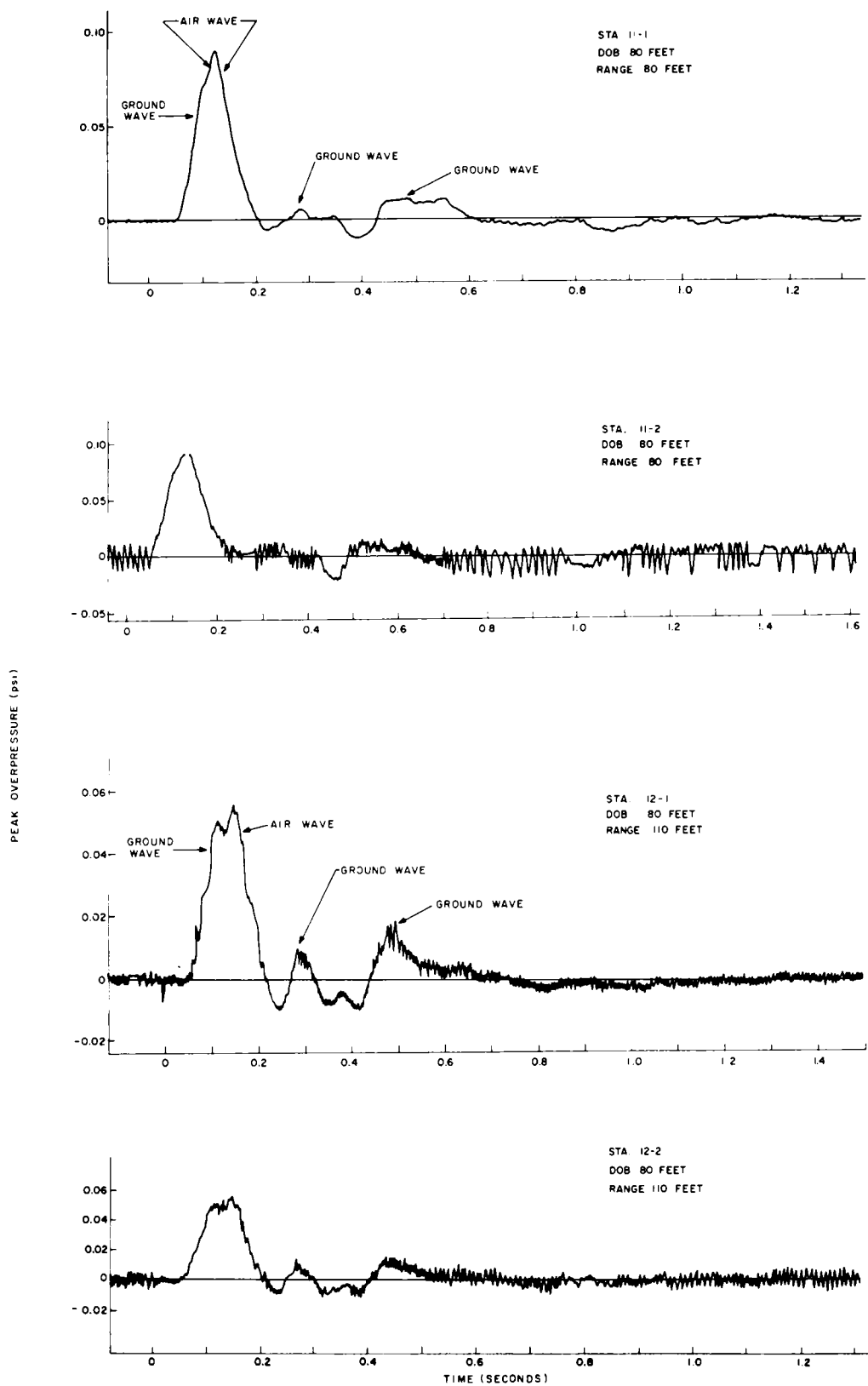
Fig. 8.8 Pressure records, NOL.
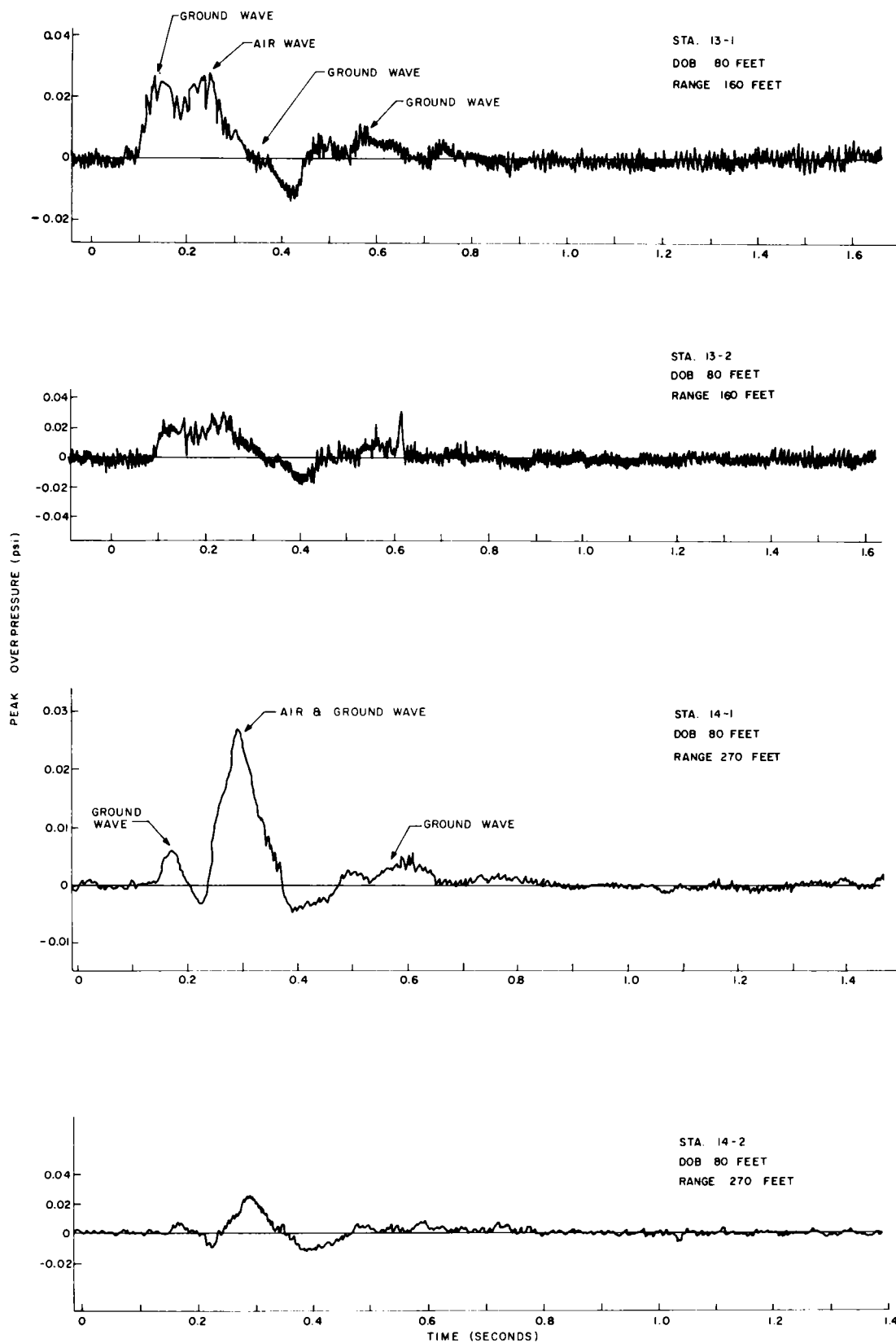
Fig. 8.9 Pressure records, NOL.

135
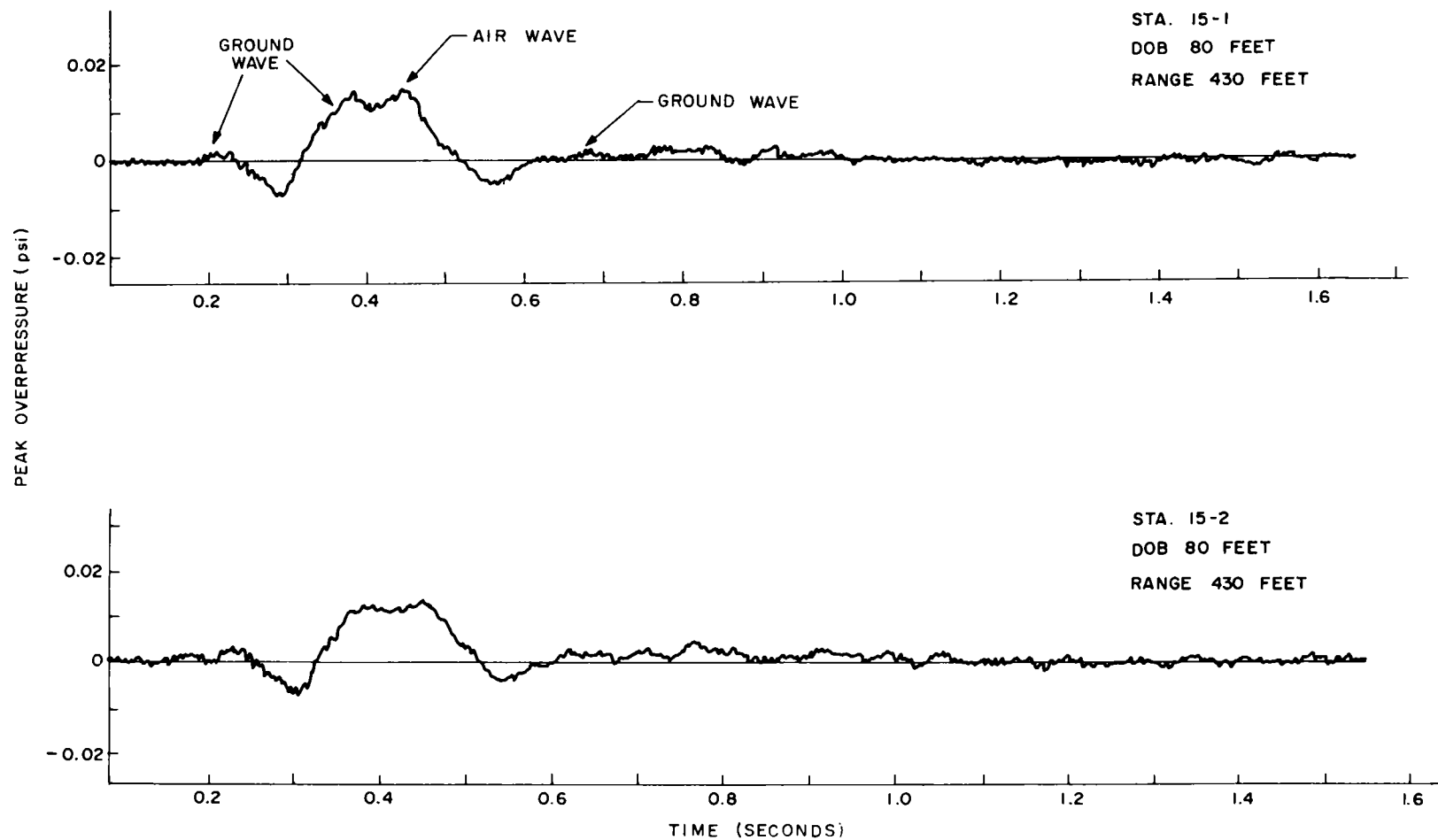
Fig. 8.10 Pressure records, NOL.
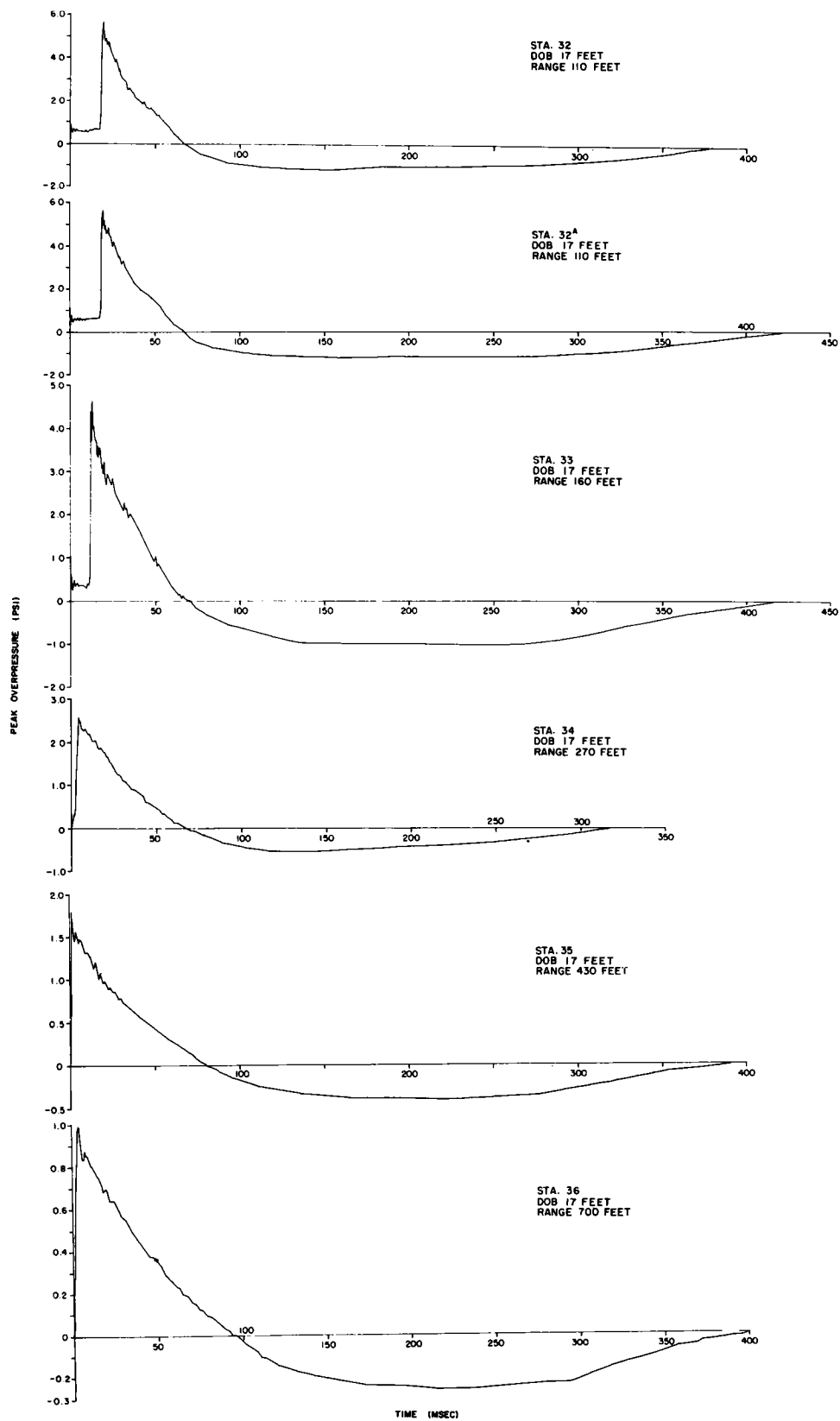
Fig. 8.11 Pressure records, BRL.
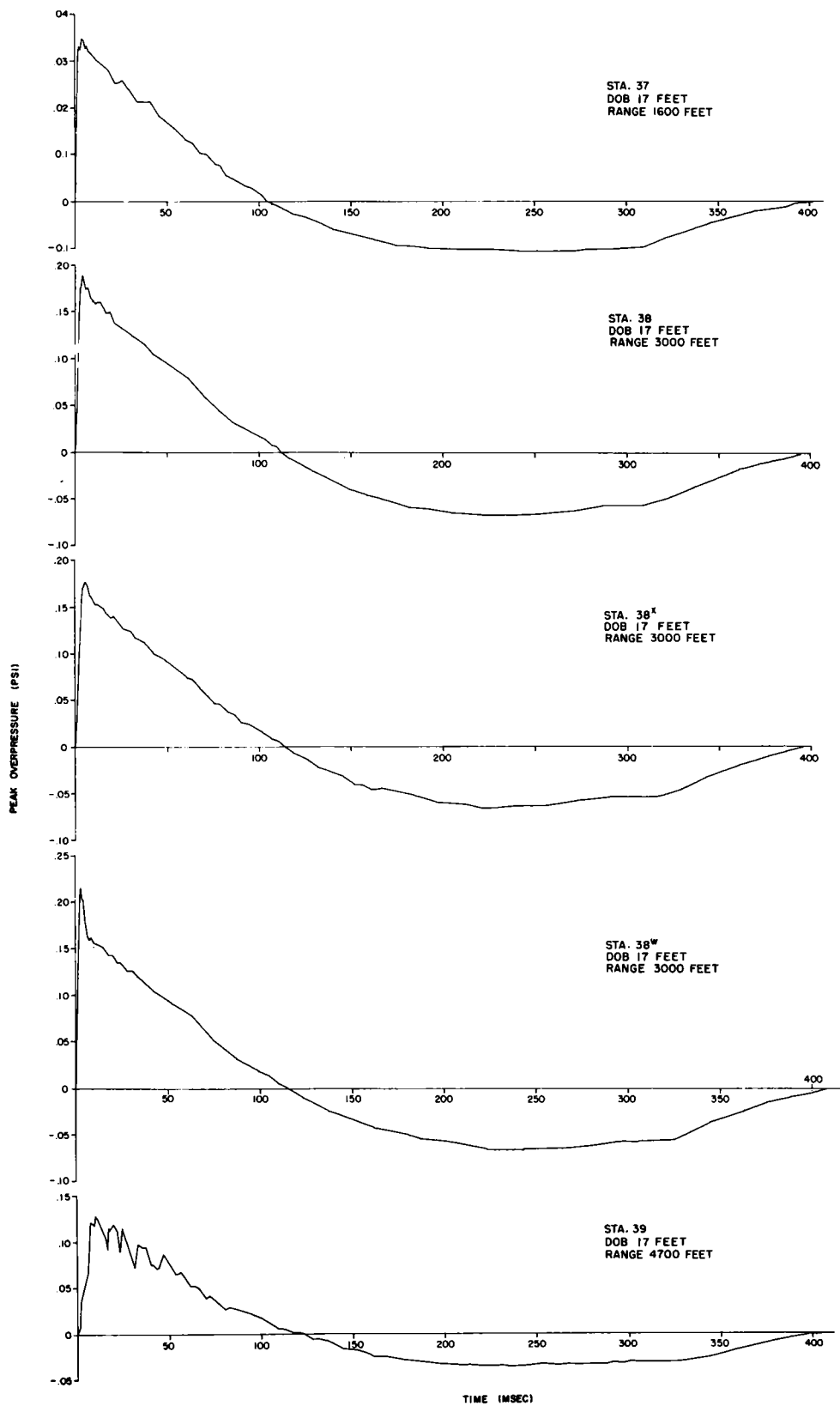
Fig. 8.12   Pressure records, BRL.
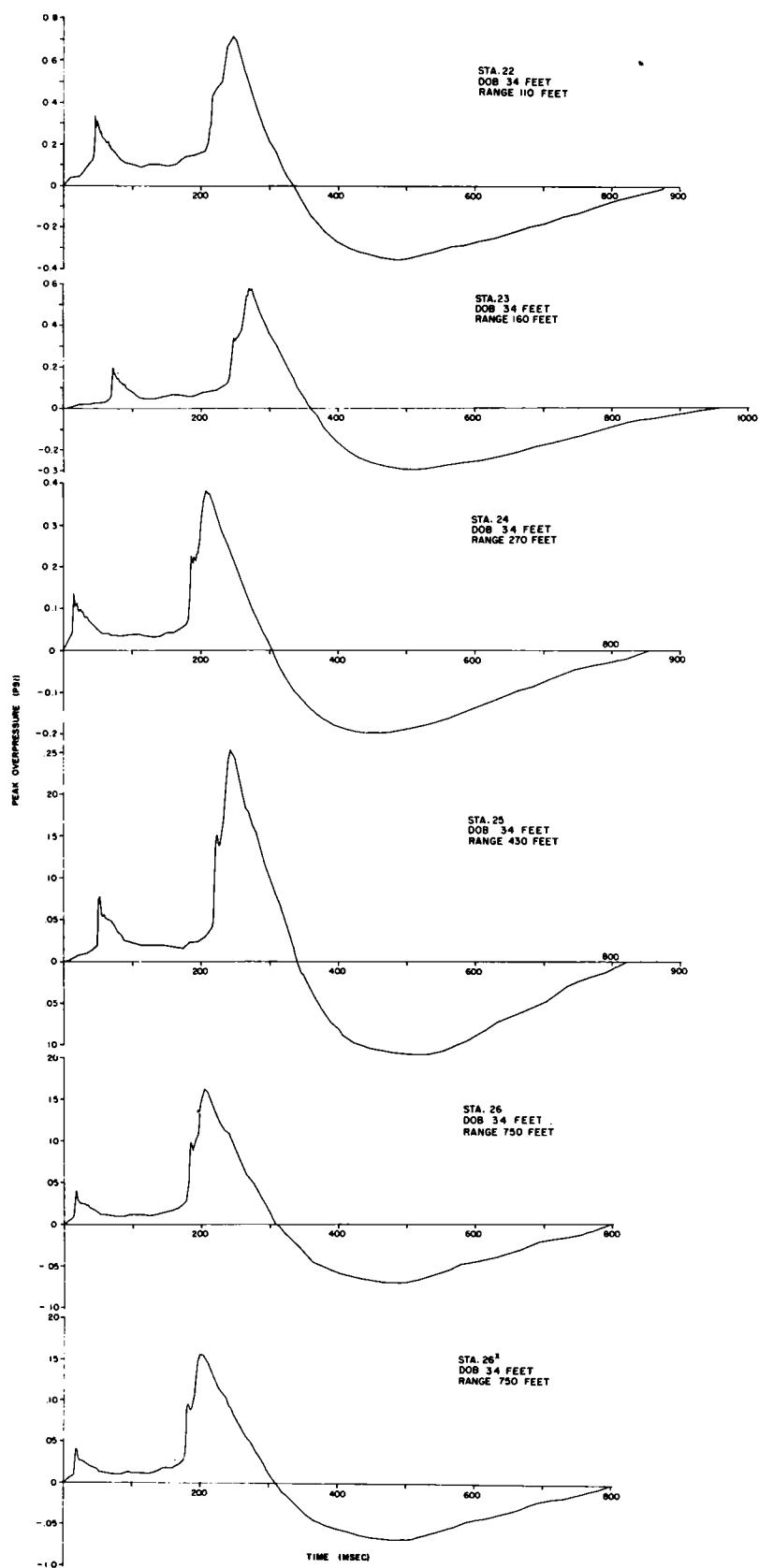
Fig. 8.13 Pressure records, BRL.

139
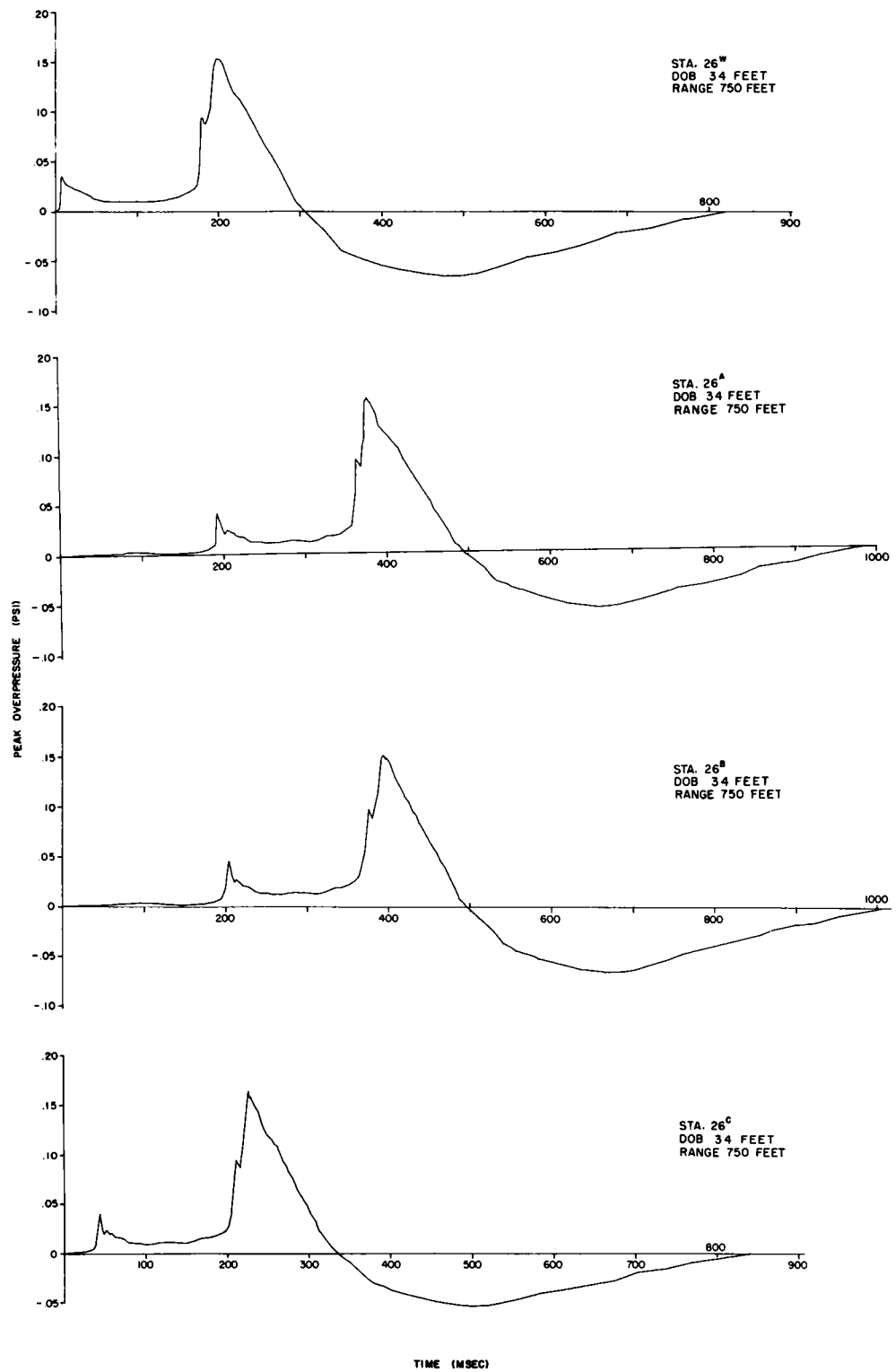
Fig. 8.14 Pressure records, BRL.
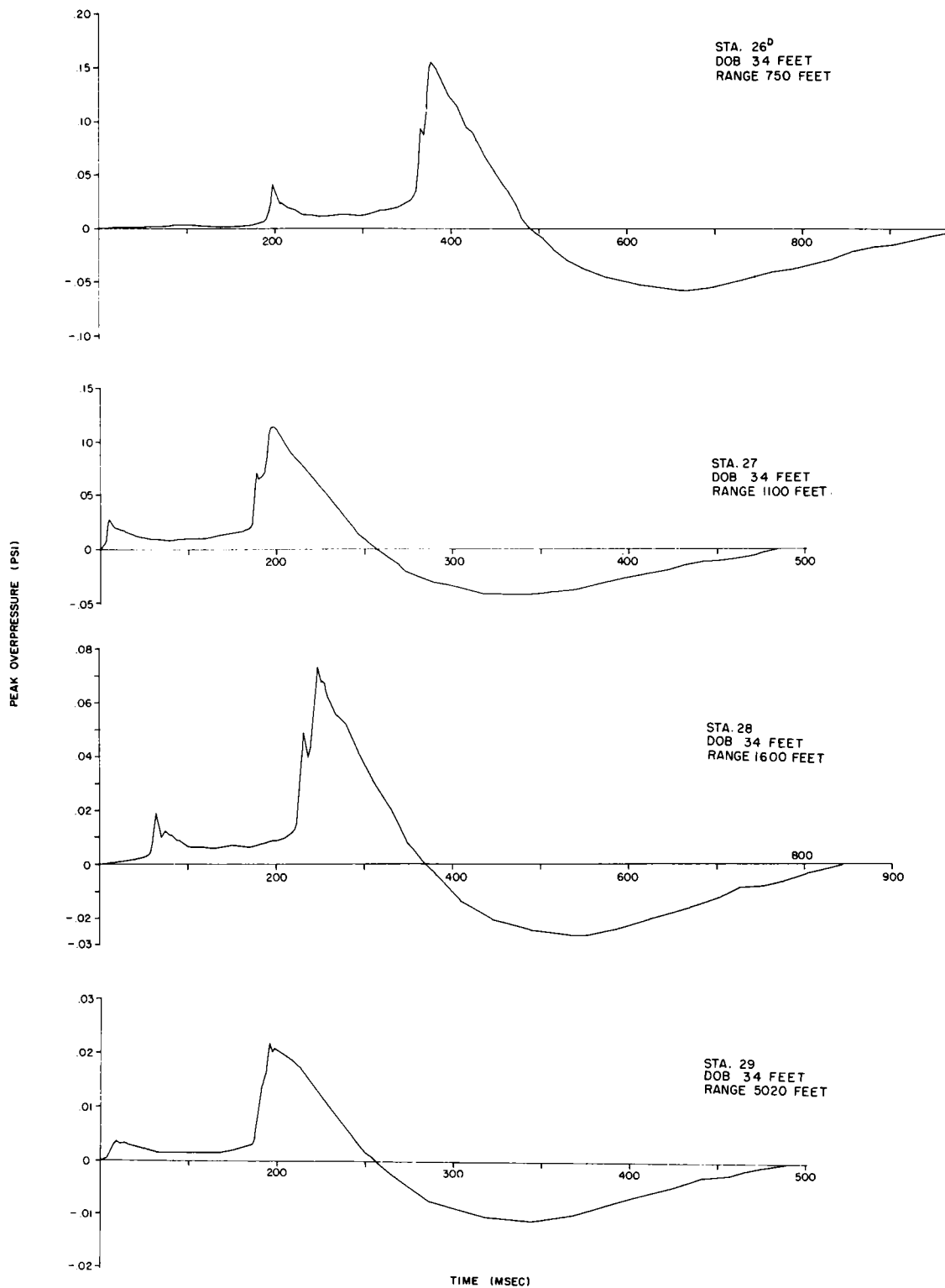
Fig. 8.15 Pressure records, BRL.
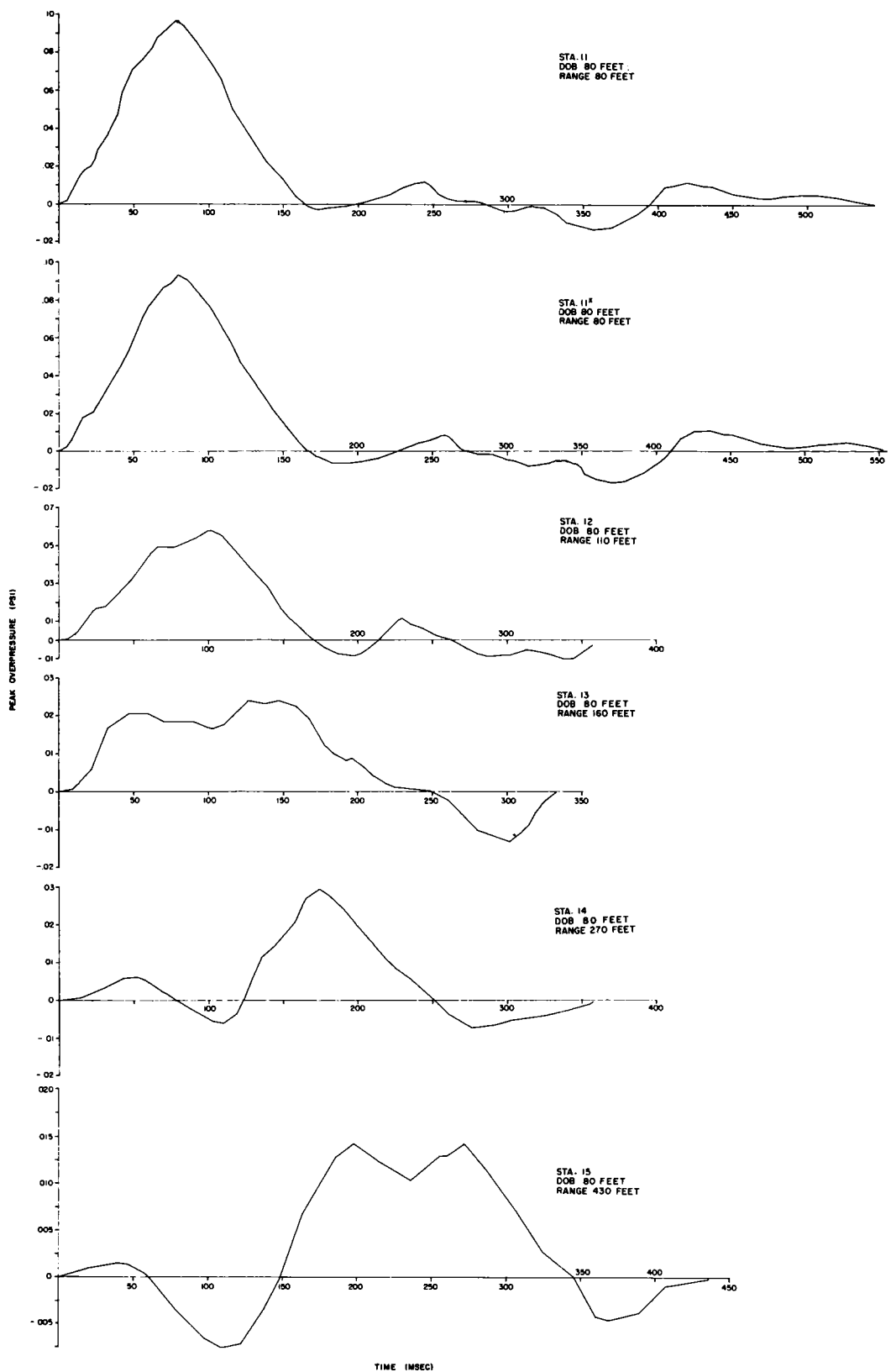
Fig. 8.16   Pressure records, BRL.
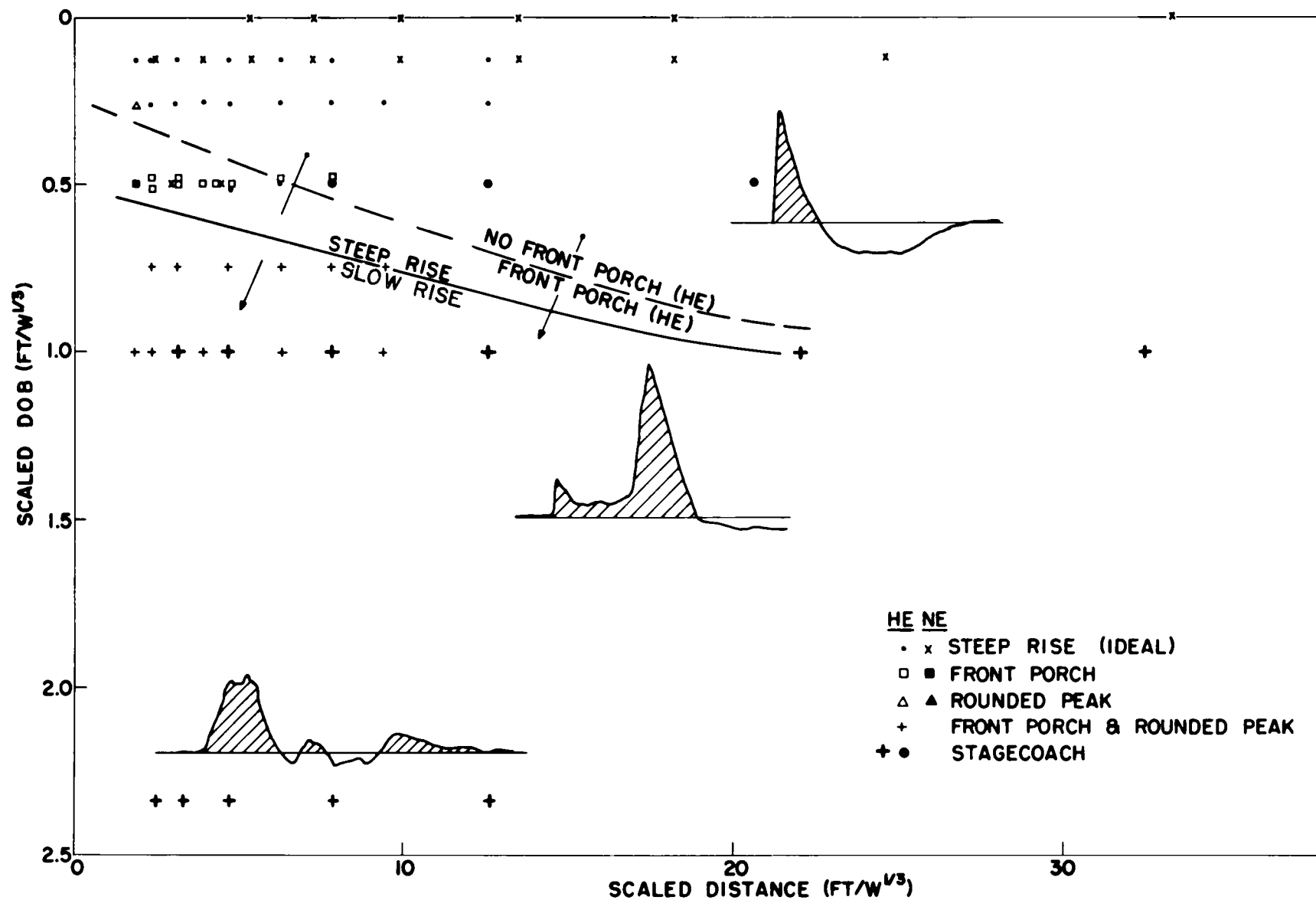
Fig. 8.17 Changes in blast wave shape with change of burial depth and radial distance.

Since the wave is not detectable close to the ground but becomes visible only when it is well above the ground (6 or 8 feet), one suspects that close to the ground the wave does not have a steep rise and that it shocks up after it breaks away from the ground surface. The appearance of the front porch is also a function of burst depth, and the time interval separating the ground shock-induced front porch from the main gas-vented shock increases with depth. At the shallow depths, where the interval is short, the main shock overtakes the first shock at a range which increases with burst depth as shown in Fig. 8.17. The scaled distance at which catch-up occurs for bursts at 0.5 $ft/W^{1/3}$ is at the lower limit of the range reported earlier.[1] For a burst depth of 1 $ft/W^{1/3}$ there is no evidence of the main wave overtaking the front porch. Although the nuclear data are sparse (Teapot Ess only), it appears that there the main shock overtakes the front porch at a range between 2 and 3 $ft/W^{1/3}$. This would be true if either the main shock followed more closely the ground shock-induced air shock, or if the ratio of peak overpressure in the main shock to that in the front porch shock were higher than that of the high-explosive case. As depth of burst is increased, both waves become weaker. By a burst depth of 2.3 $ft/W^{1/3}$, the main wave disappears.

For either of the shallower depths of burst, it is interesting to note that the wave shape following the main peak remains relatively unchanged throughout the range of radial distances over which measurements were made. At 0.5 $ft/W^{1/3}$ the decay with time immediately following the peak was more rapid than for an ideal wave (one with the same peak pressure, positive phase duration, positive phase impulse, and a smooth decay), and a decay slower than ideal was maintained throughout the balance of the positive phase. These features were the same as those of the Teapot Ess shot,[6] but less pronounced. A late positive pulse follows the negative phase on the records from the shot at 1.0 $ft/W^{1/3}$ (Figs. 8.5, 8.6, and 8.7). The pulse occurs at nearly 1 second after the gas venting pulse. The only phenomenon occurring at about 1 second after gas venting which could contribute to such a pulse is the jetting of the ejecta through the smoke crown (see Fig. 6.6). A higher velocity jet was observed on the shot at 0.5 $ft/W^{1/3}$, but no late pulse occurred on that shot.

A significant feature of wave form, more obvious on the BRL records, is the appearance of a discontinuity on the rise of the main shock wave of the 0.5 $ft/W^{1/3}$ shot (Figs. 8.13 and 8.14). At closer stations the discontinuity is preceded by a fast rise and followed by a slower one. Examination of the

motion picture records shows separate plumes of the vent breaking through at different times (see Fig. A.14 in Appendix A). The arrivals of the two shocks are separated by 6 to 12 msec. A second major plume of vents appears at 12 msec after the first.

8.3 ARRIVAL TIMES

At the 2.3 ft/$W^{1/3}$ depth, the main shock wave produced by venting of the gaseous products had completely disappeared. Motion pictures show that venting took place at about 1-1/2 seconds, and no signal was detectable on the pressure records at or following that time. The front-porch signals were measured at each of the five stations. The peak overpressure versus distance plots which are presented later show a higher pressure at 270 feet than at the next station closer or farther. An examination of arrival times as shown in Fig. 8.18 shows that the first signal in each case is a direct ground shock-induced air shock, which originates when ground surface motion pulses the air upon arrival of the ground wave along a direct radial path from the charge. This wave was traveling along the ground surface at an average velocity of about 2650 feet per second. Seismic velocities for the Area 10 alluvium were found by Rugg[7] to be in the range from 2750 feet to 3300 feet per second. Thus the observed arrival times give velocities that are reasonable for Area 10 desert alluvium.

There is observational evidence of the separate existence of two ground-shock-induced air shocks even though they would not be predicted from theoretical considerations. They may be explained as follows: When the direct shock wave hits the surface immediately over the charge, an earth piston effect over the charge generates a relatively strong pressure wave. That wave originates when the earth shock reaches the surface. This wave propagates through the air up-ward and outward from surface zero. Since the wave is air-transported after it leaves the vicinity of surface zero, it will move at a lower velocity than does the wave discussed in the paragraph above. When arrival times of this airborne wave are separated from those of the direct-path ground-shock-induced air shock, results indicate a velocity of about 1130 feet per second for the former (Fig. 8.18). This compares well with 1110 feet per second sonic velocity, calculated for atmospheric conditions at shot time. Only at Stations 14-1 and 14-2, located 270 feet from surface zero (Fig. 8.9), was the airborne shock separated sufficiently from the ground-shock-induced air shock that the arrival times of the airborne shock were clearly definable. Elsewhere their arrival times
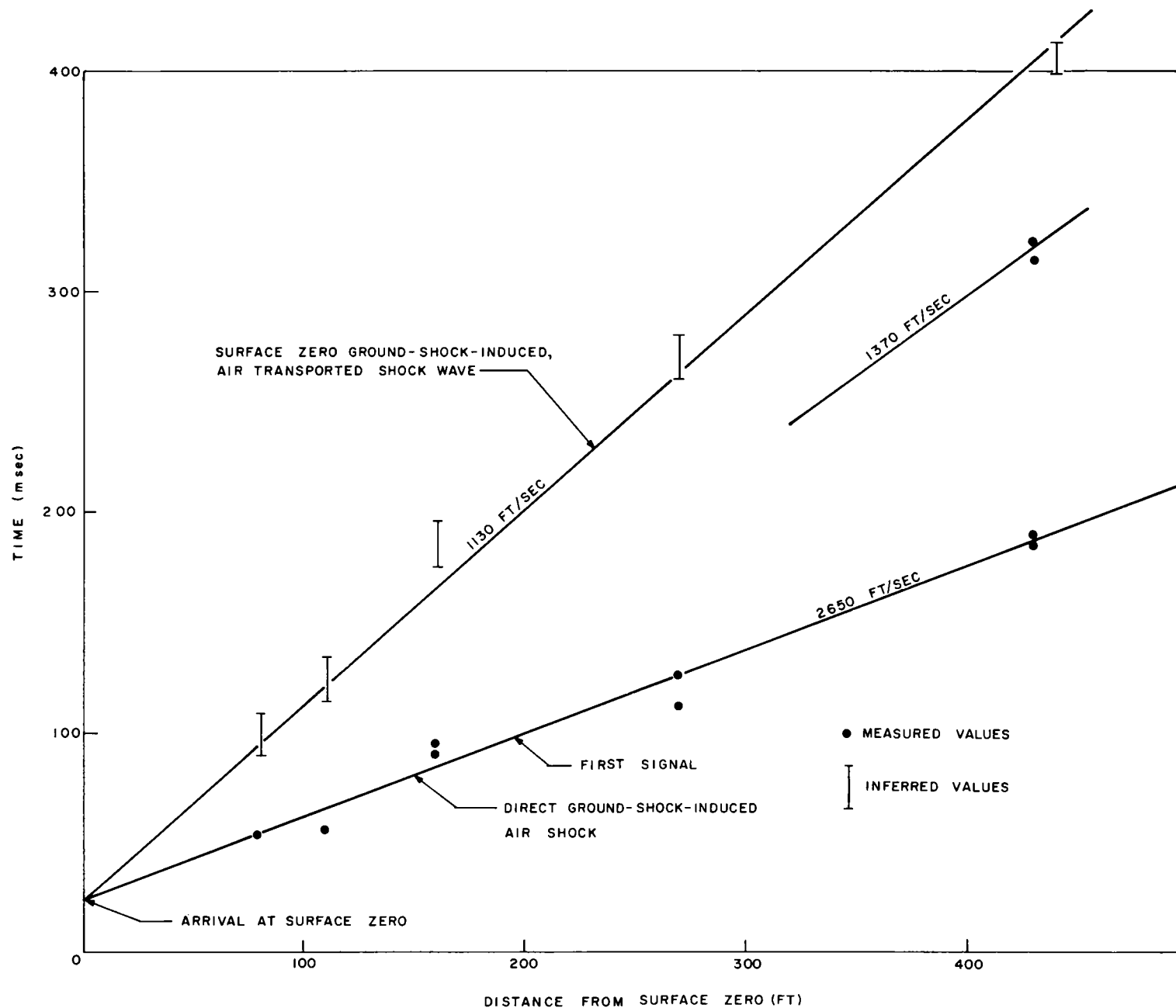
Fig. 8.18 Measured and inferred values of shock wave and arrival times.

have been inferred from pressure records by an approximate separation of the direct ground-shock-induced air shock from the airborne shock. The former is identified as a ground wave, the latter as an air wave in Figs. 8.8, 8.9, and 8.10. The arrival time of what appears to be the major portion of the wave at Station 15-1 (Fig. 8.10) would indicate an air shock velocity of 1370 feet per second. Clearly, this is too fast for so weak a shock wave, indicating that the arrival is that of the second ground wave and that the airborne wave follows at a later time and its arrival is obscured by the second ground wave. Similar interferences can be noted at the three closer stations (Stations 11-1, 11-2, and 11-3, shown in Fig. 8.8).

Figure 8.8 shows that at Station 11-1 a major pulse is followed by two smaller pulses of positive pressure. The first pulse is a combination of the direct ground-shock-induced air shock and the surface-zero ground-shock-induced airborne shock wave. The two pulses following are believed to be caused by second and third dilatational cycles (bubble oscillations) of the direct ground shock. These appear to have a frequency of about five cycles per second, which is not unreasonable for a 40,000-pound burst located 80 feet below the surface.

The shock arrival times for the two shallower Stagecoach shots are shown in Figs. 8.19 and 8.20. The first signal seen on records from the closer gages on both shots is a slow rise which occurs before the arrival of the front porch. Only those from Stations 22 and 23 (Fig. 8.5) can positively be attributed to a ground-shock-induced air shock. It is followed quickly by the front porch. The front-porch peak occurs 3 to 7 milliseconds after arrival of the wave, but the delay is logically attributable to response of the gages. The front porch is followed by arrival of the main shock: quickly in the case of the shallower shot, later for the shot at 1.0 $ft/W^{1/3}$.

8.4 PEAK OVERPRESSURE

Figure 8.21 shows Stagecoach peak overpressure versus scaled distance from surface zero. Data from NOL and BRL have been combined, and the front porch peaks have been separated from those of the main shock wave from the venting gases. It should be noted that the unusual shape of the pressure-distance curve for the shot at 2.3 $ft/W^{1/3}$ is caused by interaction of the airborne wave with the direct ground-shock-induced air shock. At a scaled distance of 7.95 $ft/W^{1/3}$, the two waves are added together to give a higher
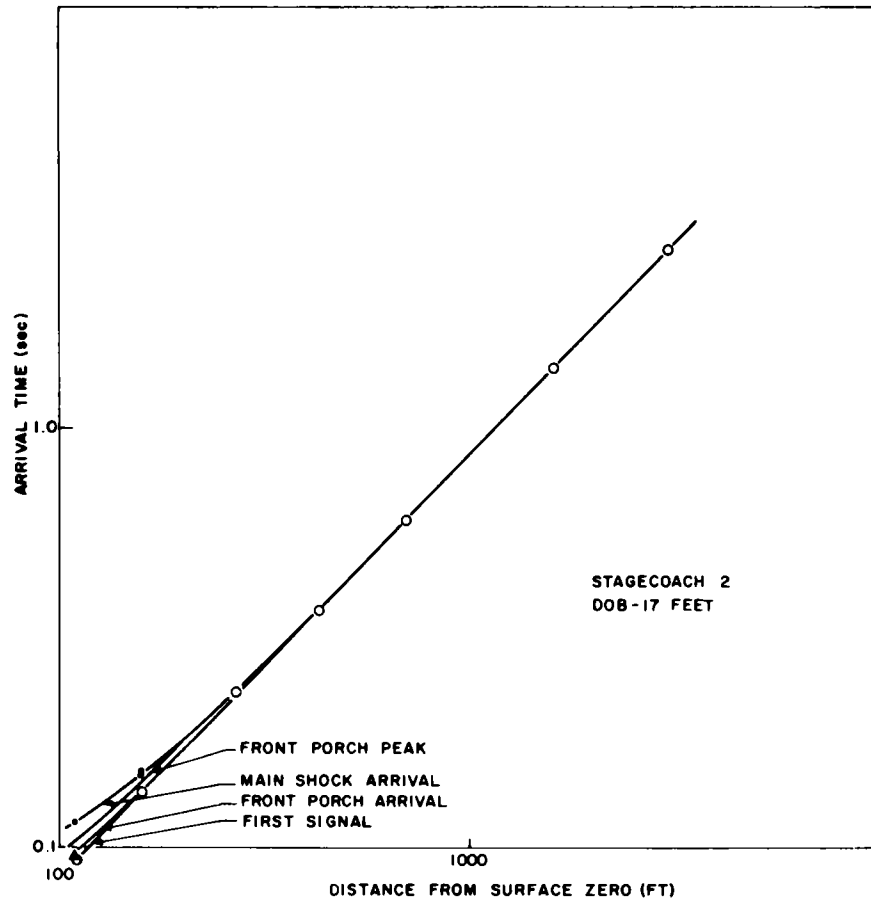
Fig. 8.19 Shock arrival times for the shot at 0.5 ft/W$^{1/3}$.
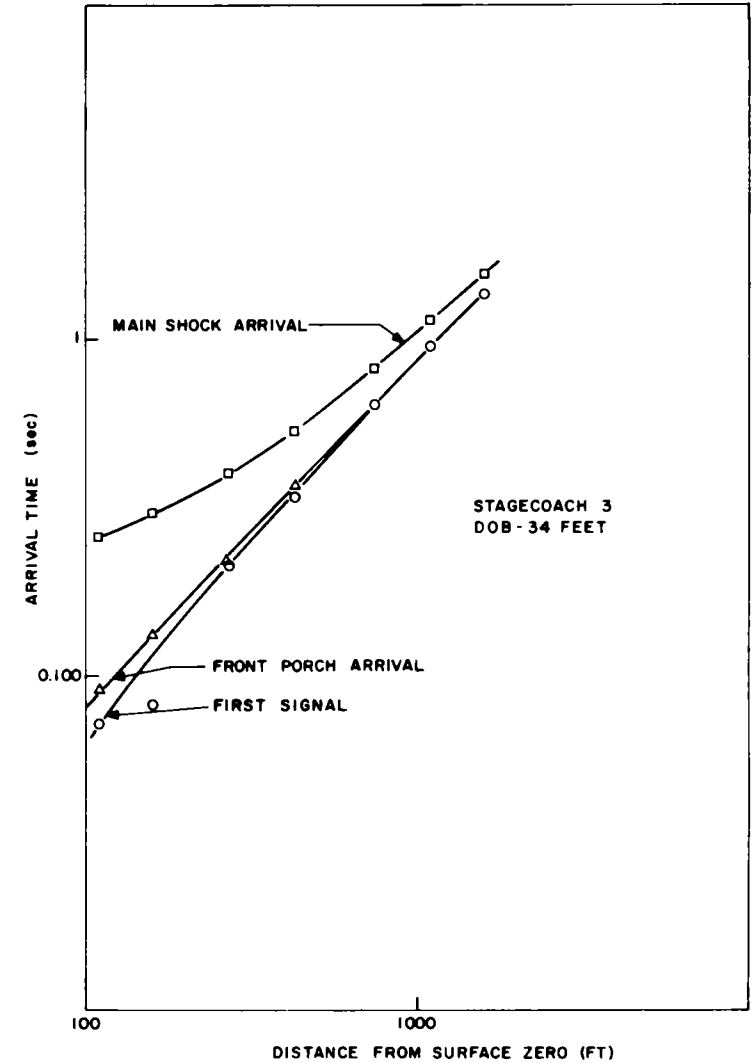
Fig. 8.20 Shock arrival times for the shot at 1.0 ft/W$^{1/3}$.
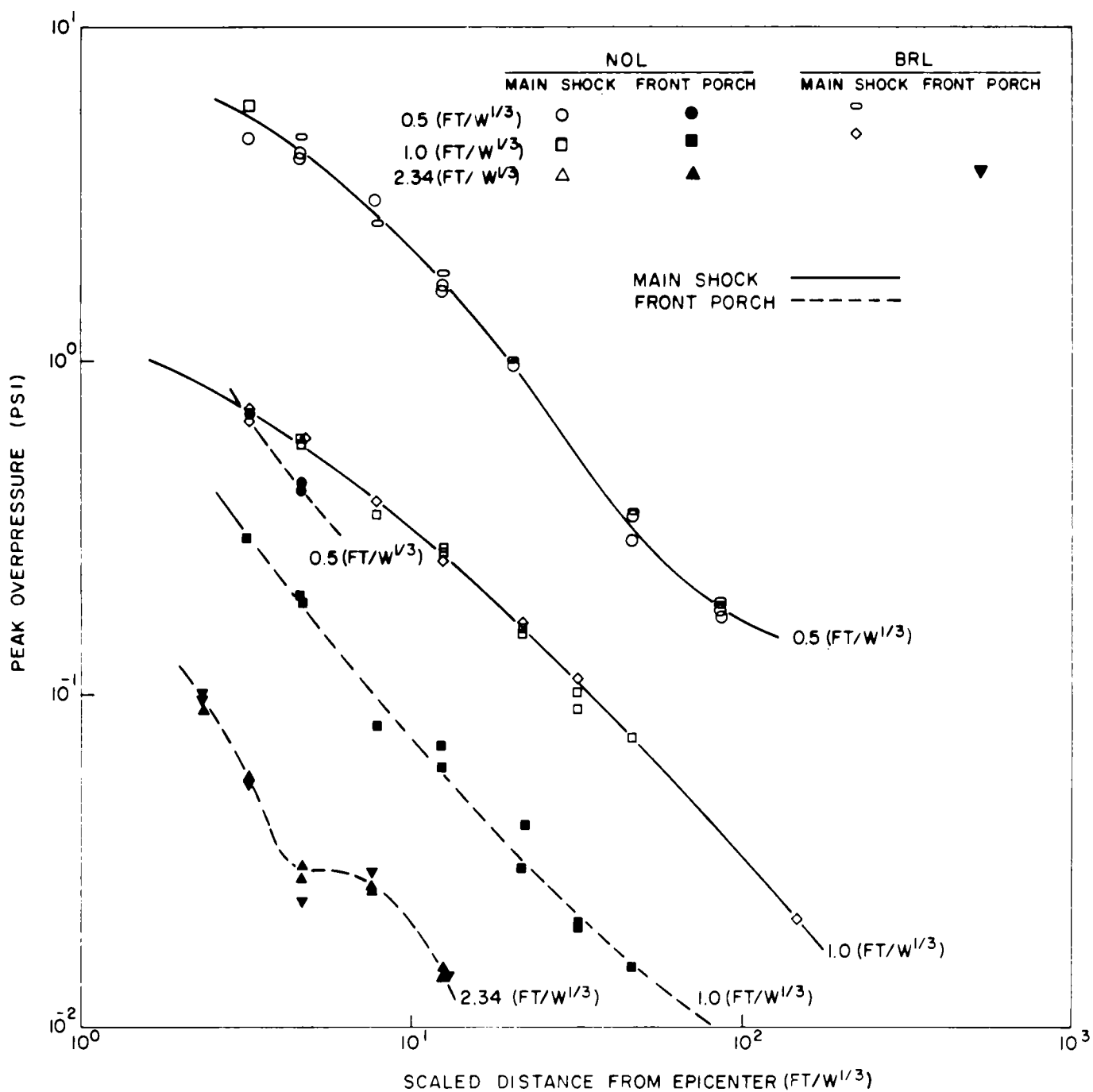
Fig. 8.21 Peak overpressure versus scaled distance from surface zero for Stagecoach shots.

value than would ordinarily be expected. The depth of burst at which the main gas-vented overpressure wave disappears has not been determined.

In Fig. 8.22, Stagecoach overpressure data have been added to those from all available high-explosive series in NTS desert alluvium, together with nuclear data from Jangle Surface, Underground Jangle, and Teapot Ess. The curves shown are "eye-ball" fit to the data, and no attempt has been made to fit the data with any analytical curve. Stagecoach air blast peak overpressure values are consistent with those from earlier high-explosive series in NTS desert alluvium. The Kirkwood-Brinkley[8] theoretical curve for cast TNT in free air has been added (to all but the surface burst data which it would have obscured) so that for depth of burst, departures from free air values are readily apparent. These data confirm observations by Shreve[9] that surface burst values agree well with free air values without the usual 2 W correction for surface bursts. Nuclear data have been scaled here using the full radio-chemical yield, rather than the 50-percent blast yield customarily used for comparison.[10] These data agree well with the 1.6 W curves for surface nuclear bursts[11] when scaled to 1 pound, where 2,000,000 pounds per kiloton (100 per-cent efficiency) are assumed. Thus, the increase in apparent yield due to the reflecting plane must be directly offset by the lower blast yield of the nuclear explosive. Nuclear explosive data are both so sparse and so scattered as to preclude determination of relative blast efficiencies of nuclear and chemical explosives. Although 100-percent efficiency fits the experimental data and has been used for underground detonations in the past,[12] it is dif-ficult to see how a 47 (approximately 50) percent efficiency for above-ground bursts can increase to 100 percent for below ground bursts when the nuclear radiation part of the total energy cannot be converted to mechanical energy. Only in the case of Teapot Ess (at $0.5 \text{ ft/W}^{1/3}$) does the peak overpressure and impulse depart significantly from those of the HE shots. The departure in the 5- to 15-psi region is such as to indicate an efficiency even greater than 1.

The experimental data of Fig. 8.22 agree well with NAVORD data,[13] in spite of medium differences.

Figure 8.23 shows Sandia scaled height-of-burst curves.[14] These have been extended below the ground surface, using the composite overpressure-versus-scaled distance curves of Fig. 8.22.
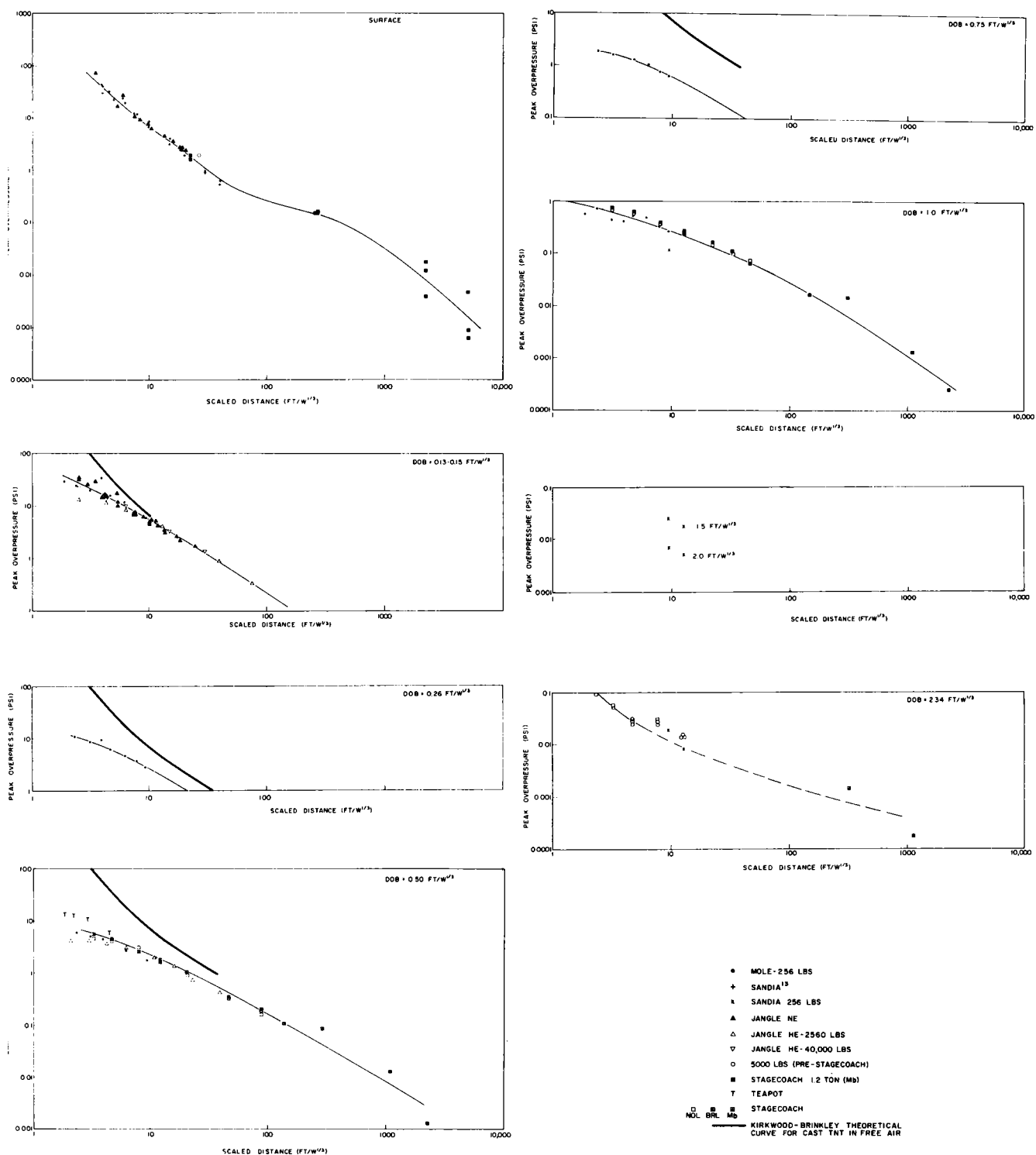
Fig. 8.22   Peak overpressure versus scaled distance from surface zero
for all charges buried in NTS desert alluvium.
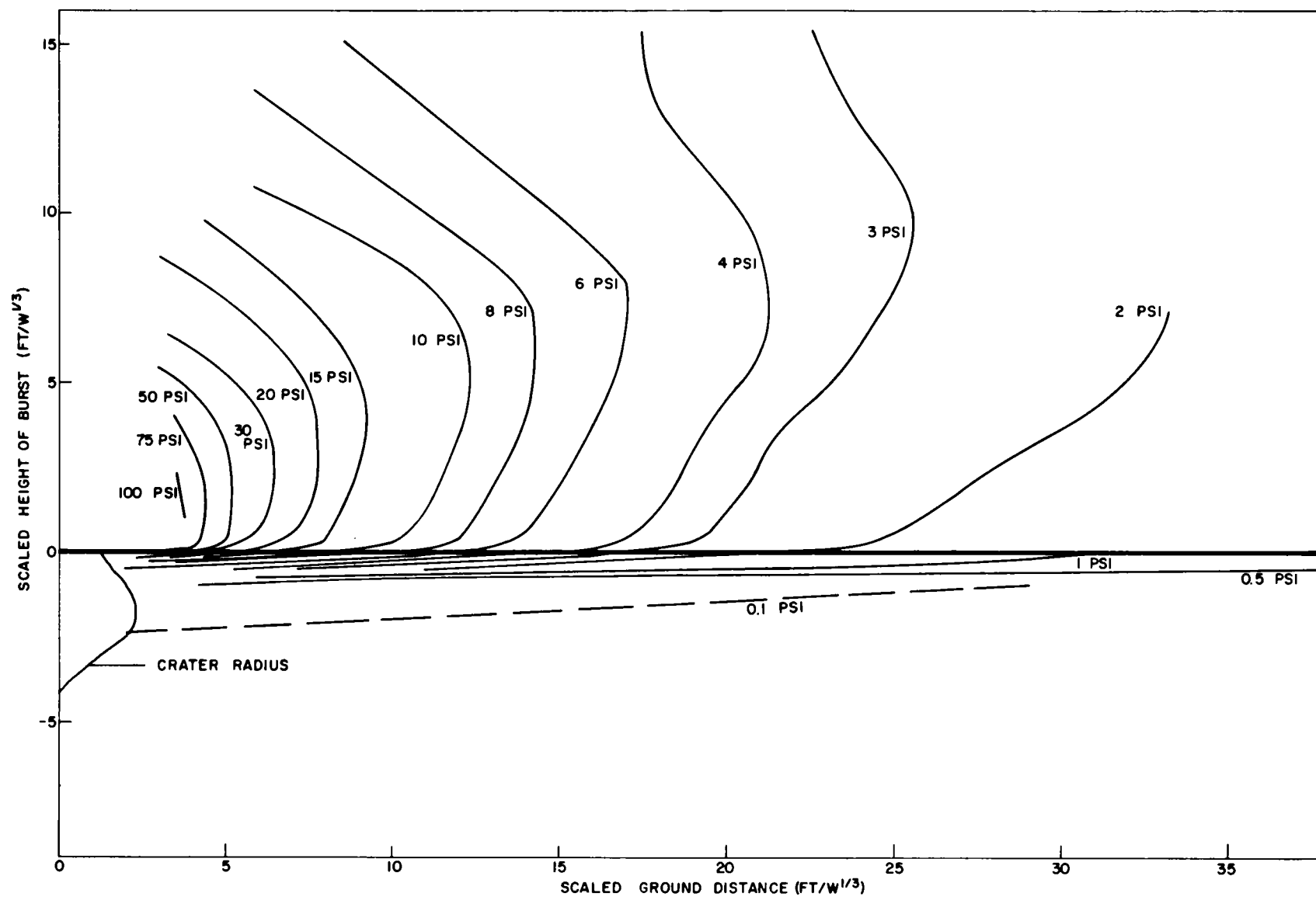
Fig. 8.23 Overpressure height of burst curves.

The composite information from underground bursts thus defines the extent of peak overpressure suppression as a function of burst depth of the charge. This information has been summarized in Fig. 8.24, but a range of $\pm$ 70 percent would include most of the data.

8.5   IMPULSE

Figure 8.25 shows scaled impulse versus scaled distance for the combined NOL-BRL Stagecoach data. In each case the impulse is that of the positive phase and includes both the front porch and the main shock wave. At the deeper depth of burst (80 feet), where the entire wave was a front-porch wave, the positive phase has been interpreted as the positive portion of each of the waves in the wave train, rather than that of either the first wave or the dominant wave alone.

The Stagecoach impulses have been combined with those from other high explosive experiments in NTS desert alluvium and from the Teapot Ess, Jangle Surface, and Jangle Underground nuclear explosions. These are shown in Fig. 8.26. The scaled impulse-distance curve for the deeper shot is not given in Fig. 8.26, since it is the same as that shown in Fig. 8.25.

From the composite impulse-distance curves, Sandia impulse height-of-burst curves[13] have been extended below ground. These are shown in Fig. 8.27. All values shown here are from the main shock wave except the lower two (0.2 and 0.4 psi-msec), which are from both the main (airborne) wave and the ground-shock-induced wave, or from the latter alone.

The extent to which blast impulse is suppressed by charge burial is summarized in Fig. 8.28. The suppression of blast impulse can be approximated by the empirical expression

$$\log I = - 1.44 - 0.89 \log r - 0.816 \text{ dob},$$

where I = scaled impulse in psi-sec/$W^{1/3}$

r = scaled range ($ft/W^{1/3}$)

dob   = scaled burst depth ($ft/W^{1/3}$).

Since wave shape changes with distance and burst depth, the impulse suppression curves portray the effect of charge burial somewhat better than do the peak
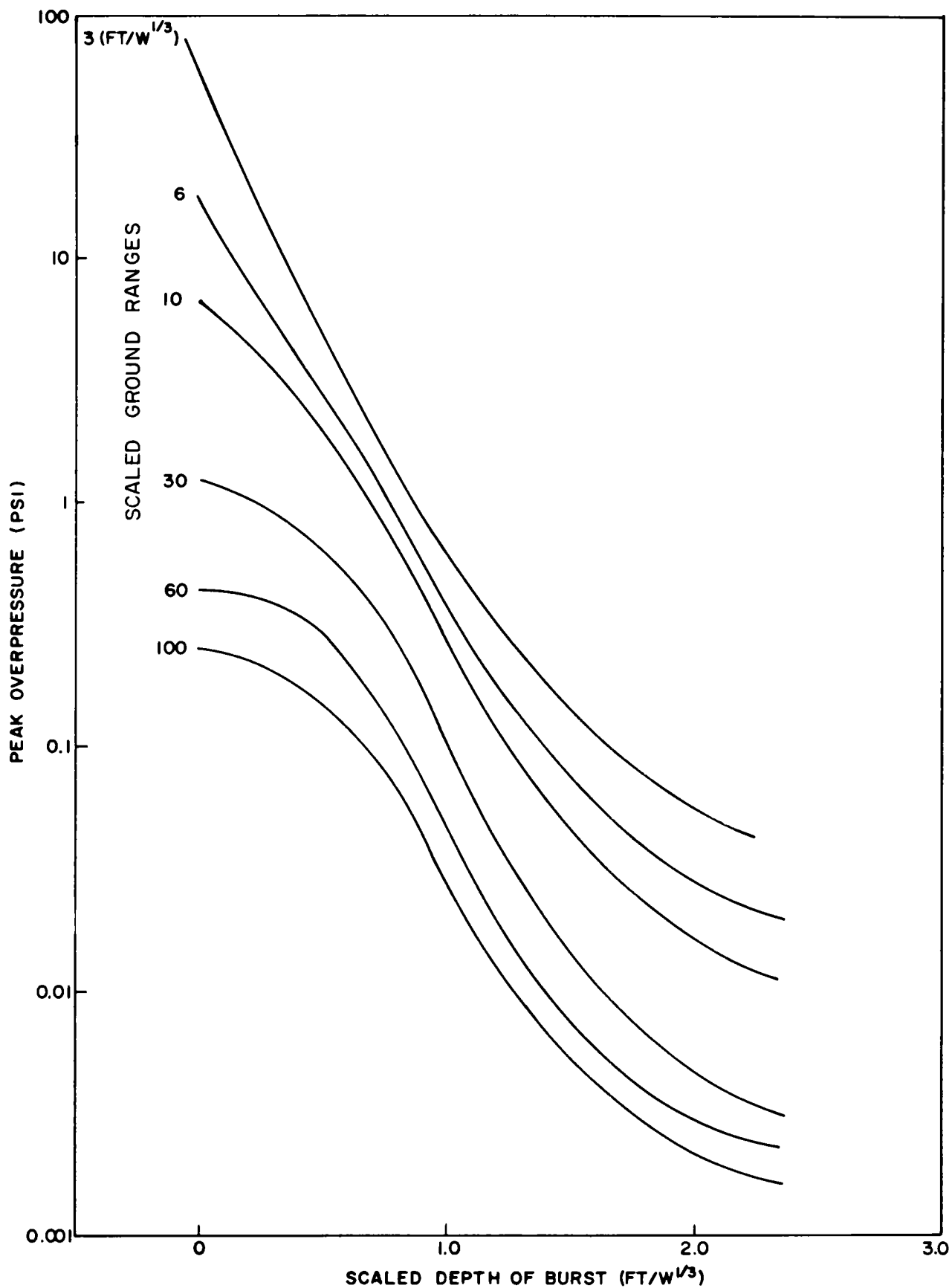
Fig. 8.24 Peak overpressure suppression as a function of burst depth.

154
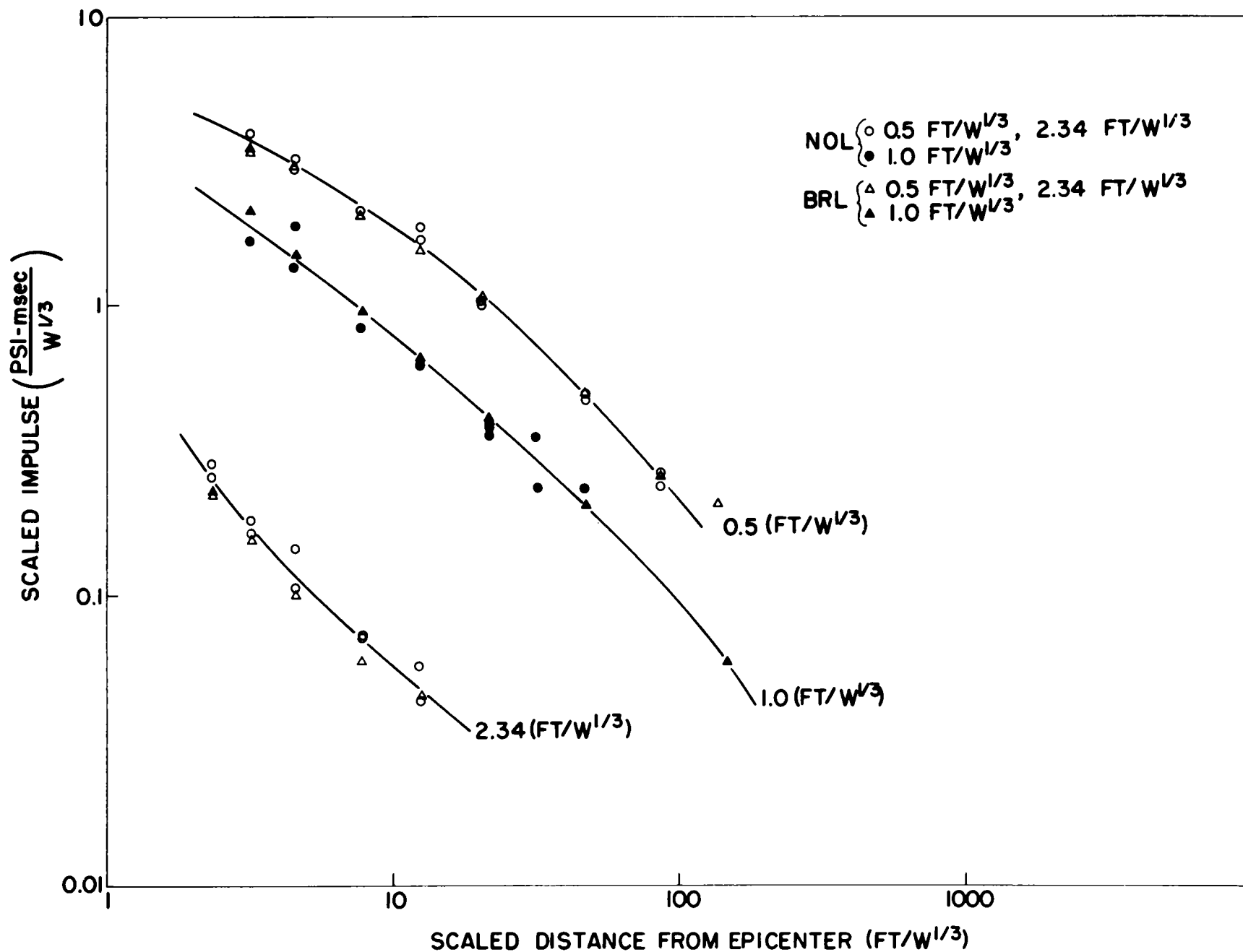
Fig. 8.25 Scaled impulse versus scaled distance from surface zero for the Stagecoach shots.
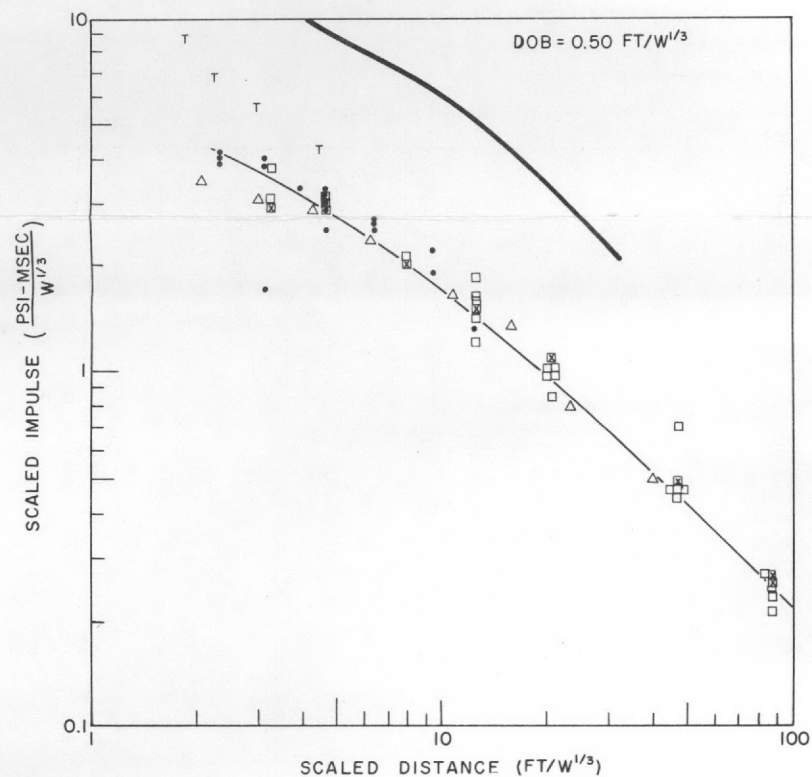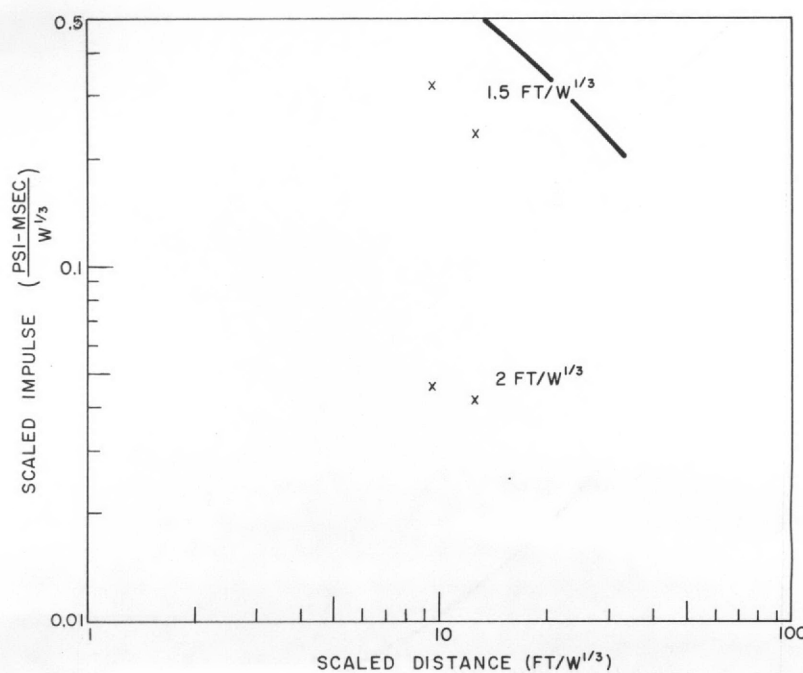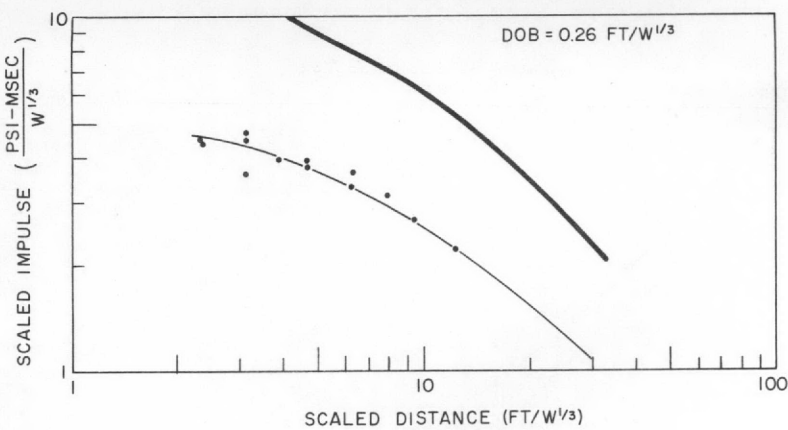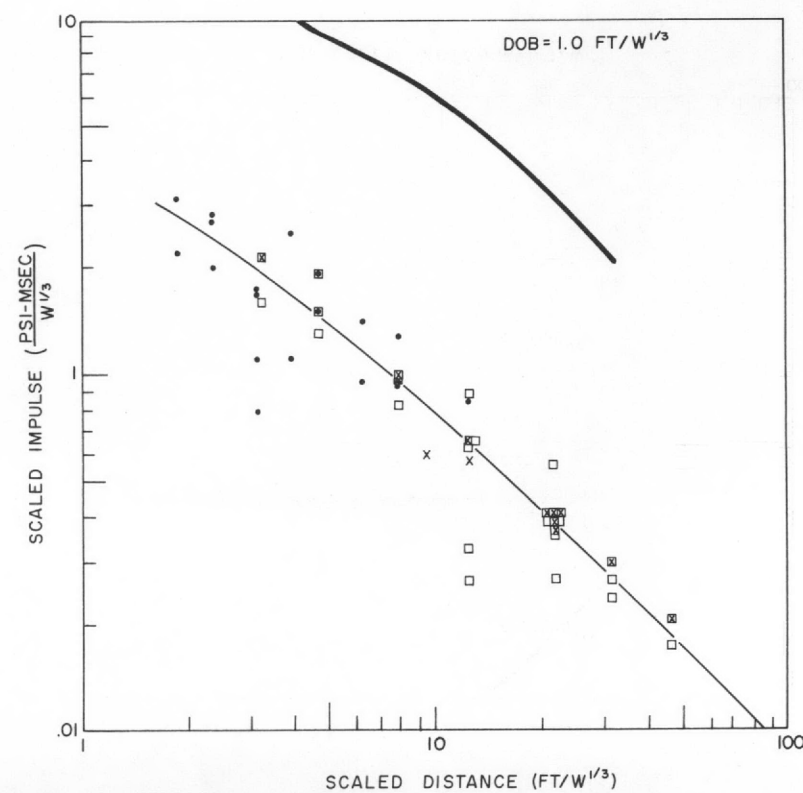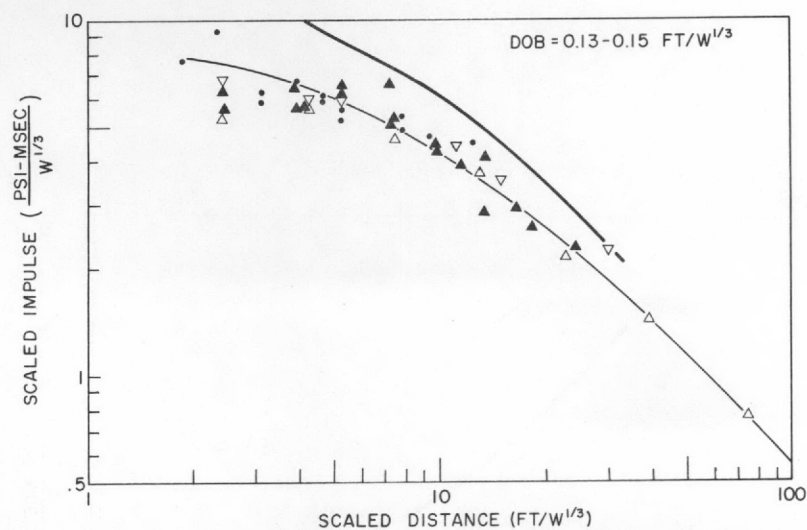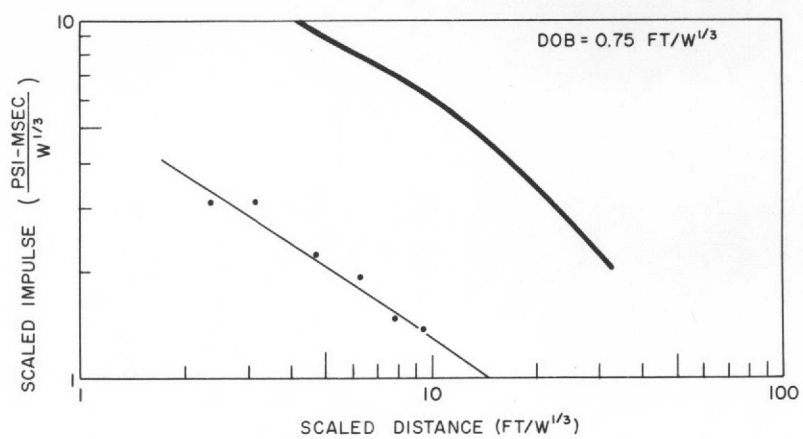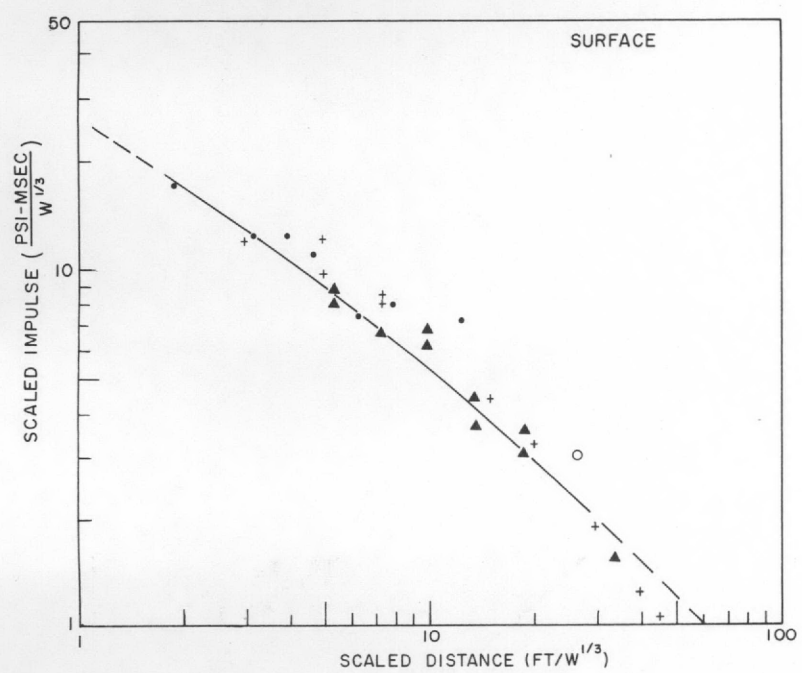
Fig. 8.26 Scaled impulses versus scaled distance from surface zero for all
charges fired in NTS desert alluvium.
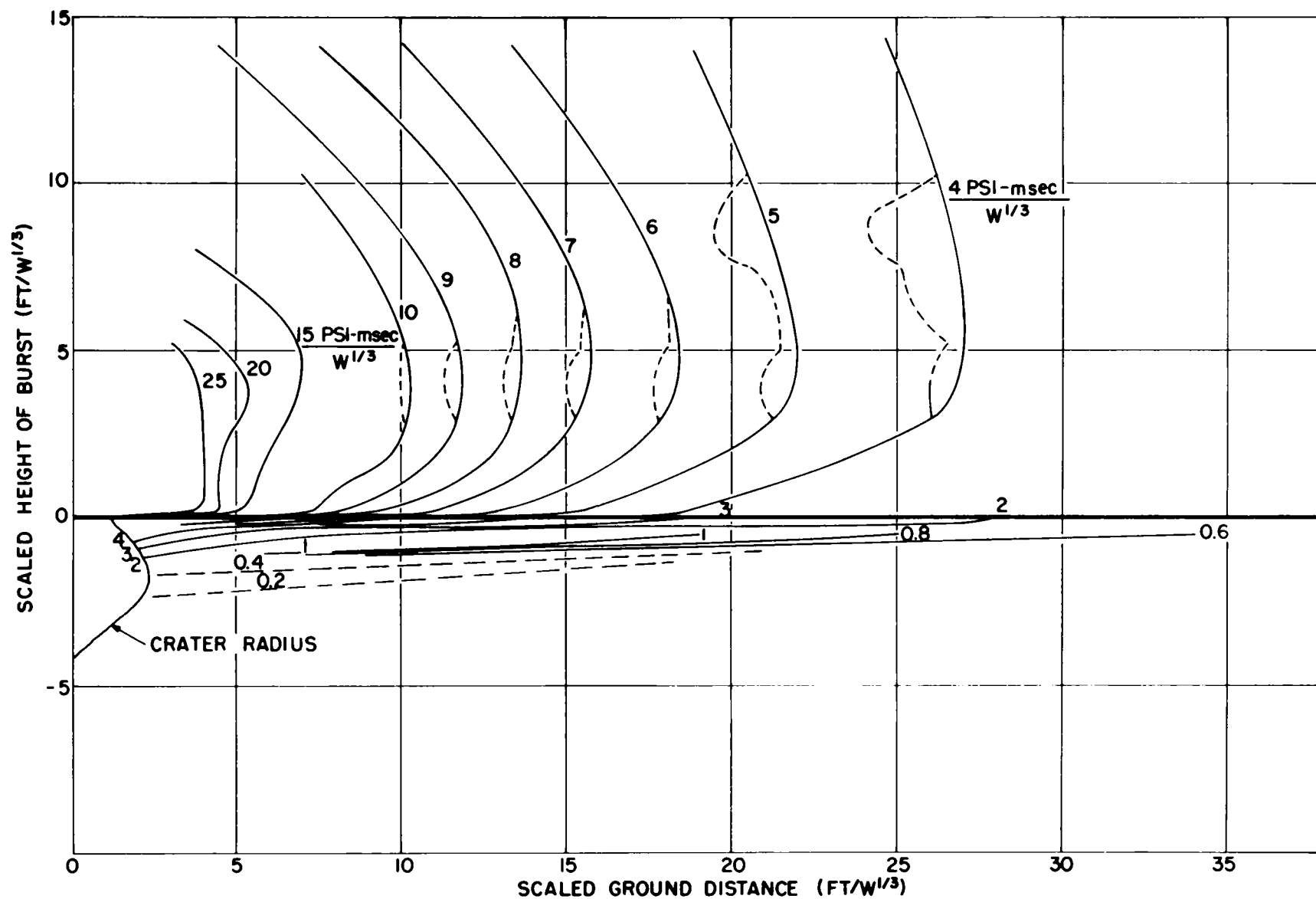
Fig. 8.27 Impulse height of burst curves.

overpressure suppression curves of Fig. 8.24. Accuracy, too, is better, and ± 25 percent would include most of the scatter.

8.6 POSITIVE PHASE DURATION

Duration data are notorious for their scatter, primarily brought about by the fact that a small difference in gage damping can make a significant difference in crossover, where pressure differential is small. Stagecoach results were no exception in this respect.

Figure 8.29 shows scaled positive-phase duration versus scaled distance from surface zero for the 17- and 34-foot shots. A combination of BRL and NOL pressure data has been used. Duration of the main wave has been separated from the total duration to give that for the front porch. The front porch duration of the shallow shot goes to zero at about 12 $ft/W^{1/3}$ as the main shock catches up with it. At the 34-foot depth, however, the front porch duration appears to be decreasing slowly enough to indicate that the main wave is unlikely to catch up with the front porch. Positive-phase durations for the shot at 2.3 $ft/W^{1/3}$ have been omitted from Fig. 8.29, since it is not clear whether one should use the sum of the positive-phase durations of each of the three waves observed, or of the major pulse alone.

Figure 8.30 is a composite of the scaled durations versus scaled distance for all high-explosive data from shots in NTS desert alluvium. Included is nuclear information from Jangle Surface, Jangle Underground, and Teapot Ess shots.

The lower portion of duration height-of-burst curves, taken from an earlier Sandia report,[14] has been extended below ground, using the composite curves of Fig. 8.29, and are given in Fig. 8.31.

Figure 8.32 shows the change which takes place in positive-phase duration as charge burial depth is increased. Information for the deeper shots comes from a series of 256-pound shots, where only two gages were used on the blast line. Because of the manner in which they were obtained, as well as the small number of gages used, values obtained should be used with caution. Durations for the Stagecoach deep shot have been included with reservation, and are the sum of the positive portion of all the waves. Even so, ± 25 percent would include most of the scatter.
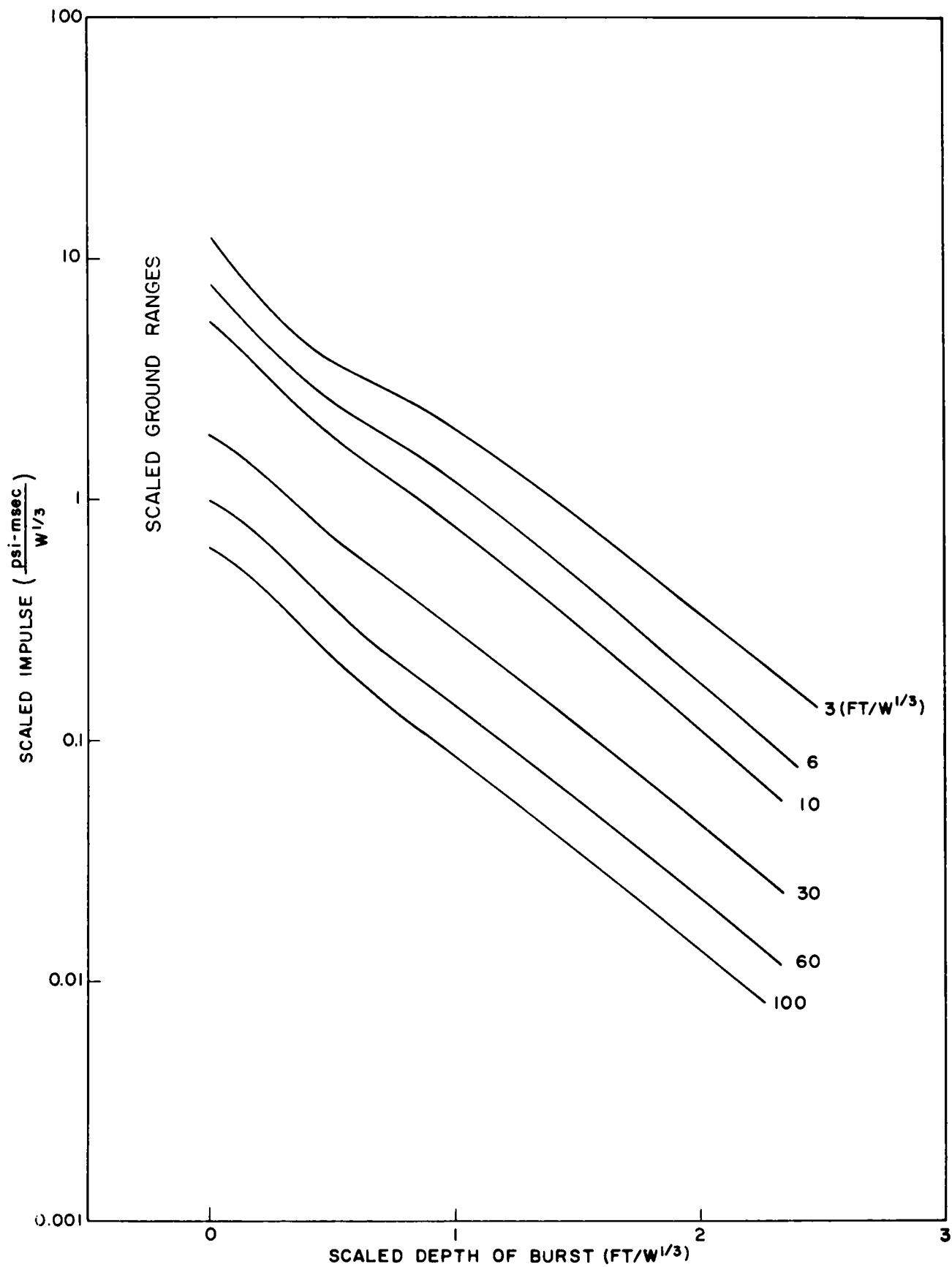
Fig. 8.28 Suppression of blast impulse by charge burial.
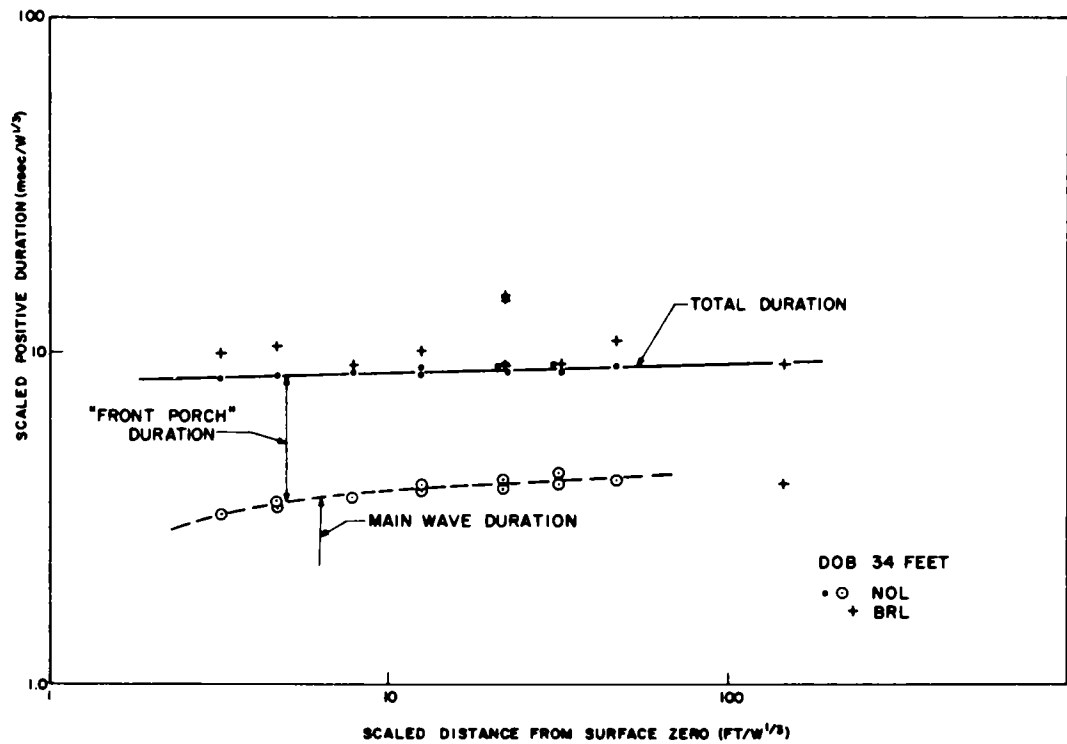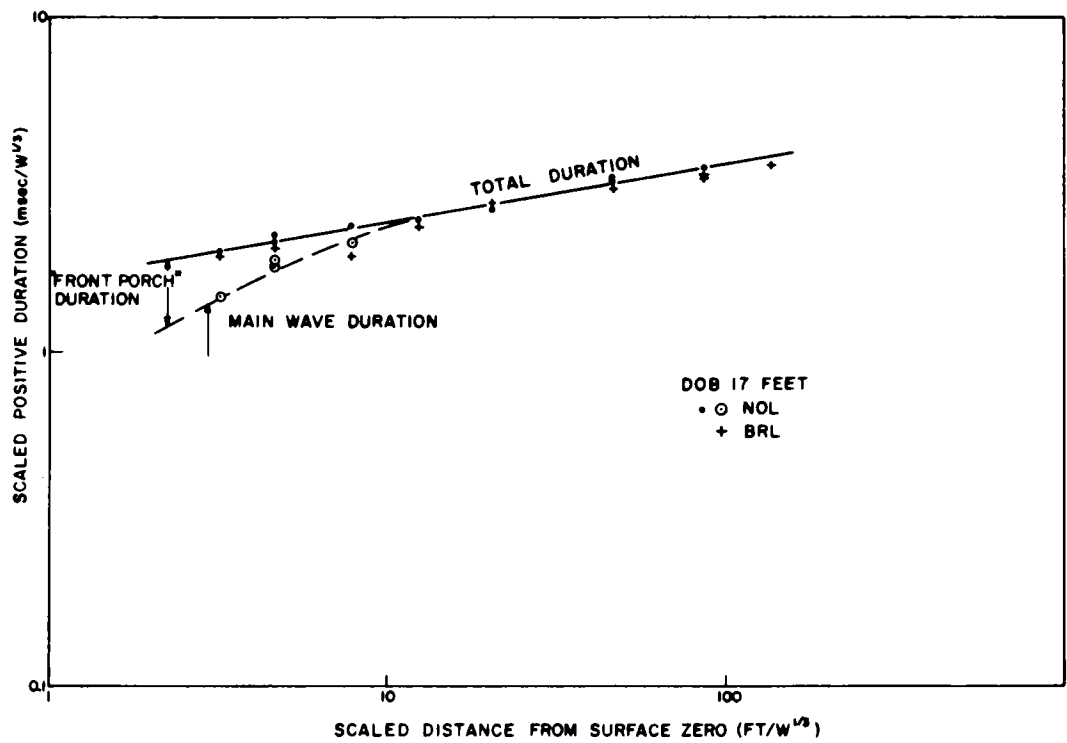
Fig. 8.29 Scaled positive phase duration versus scaled distance from surface zero for two Stagecoach shots.
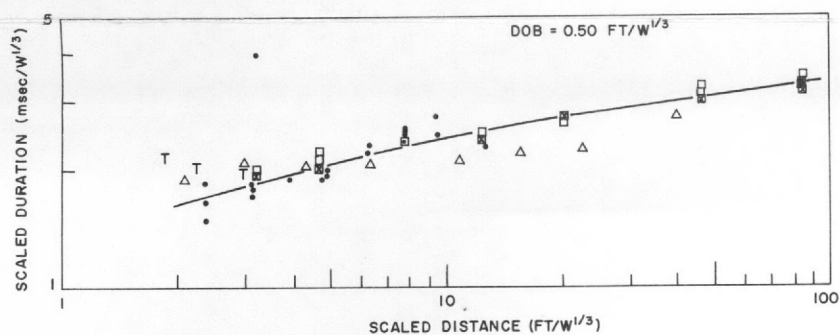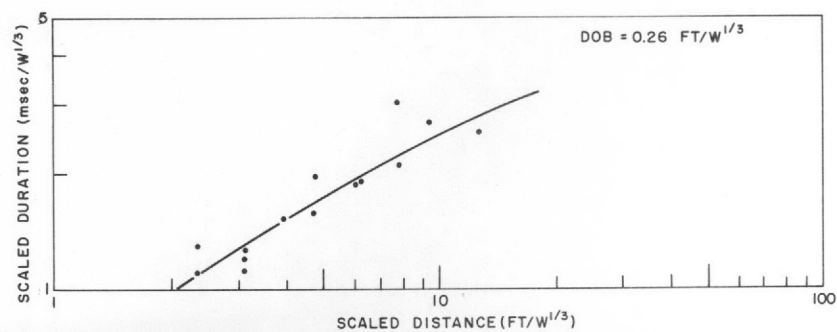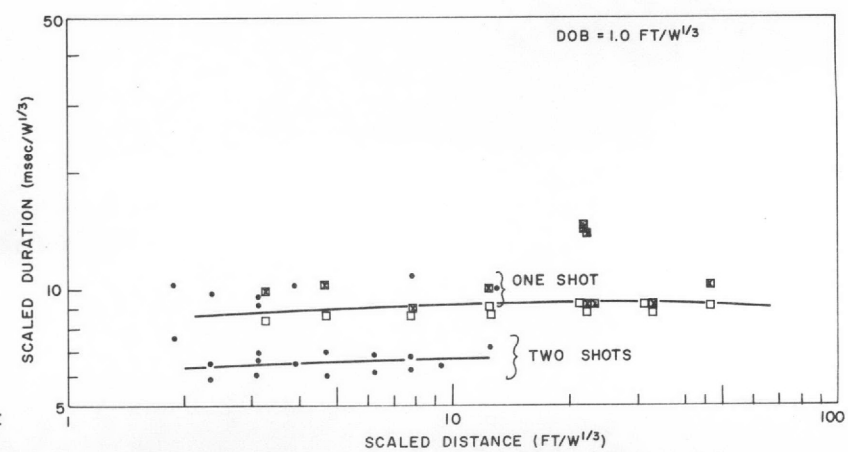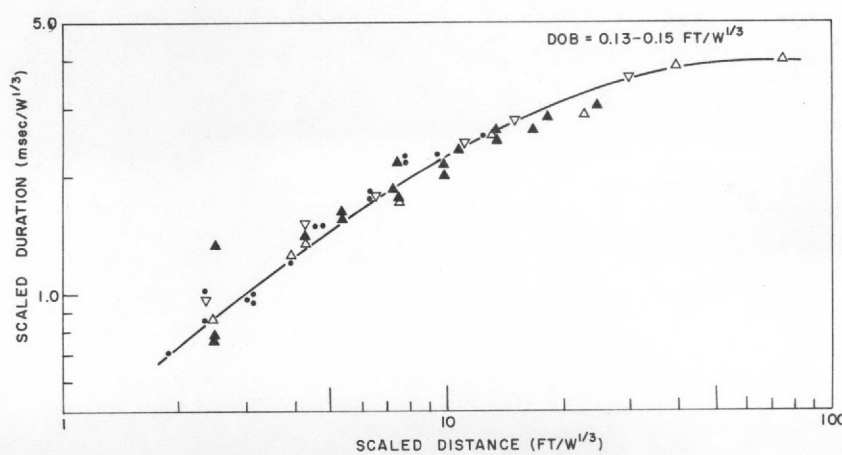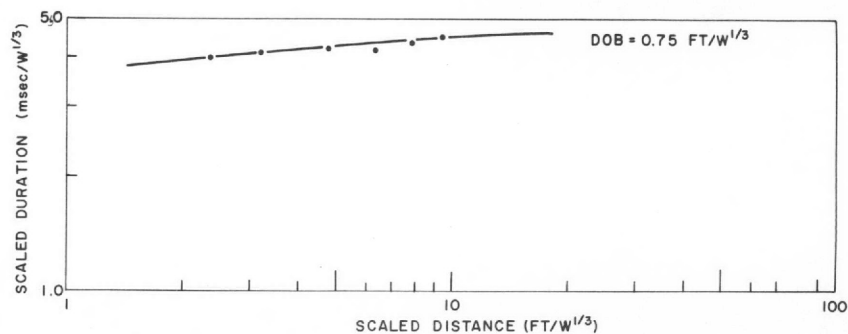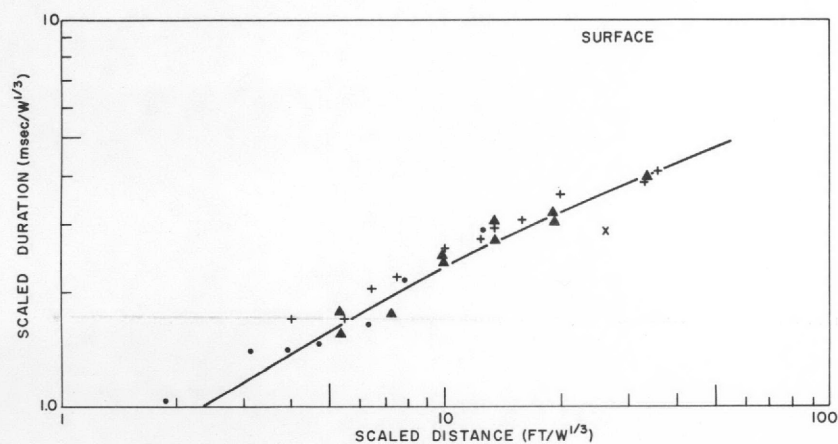
Fig. 8.30 Scaled positive phase duration versus scaled distance from surface zero for all high explosives fired in NTS desert alluvium.
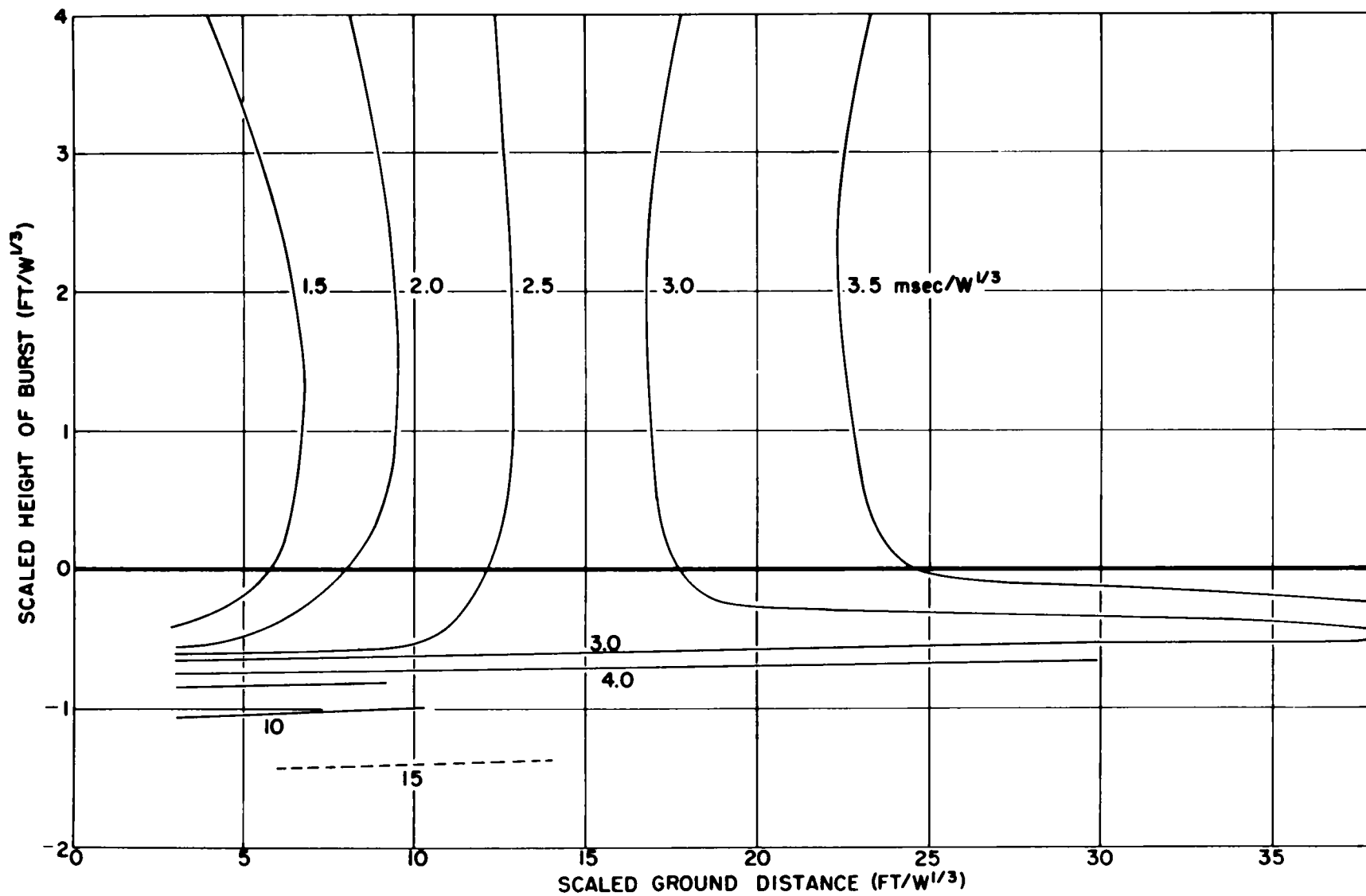
Fig. 8.31 Duration height of burst curves.
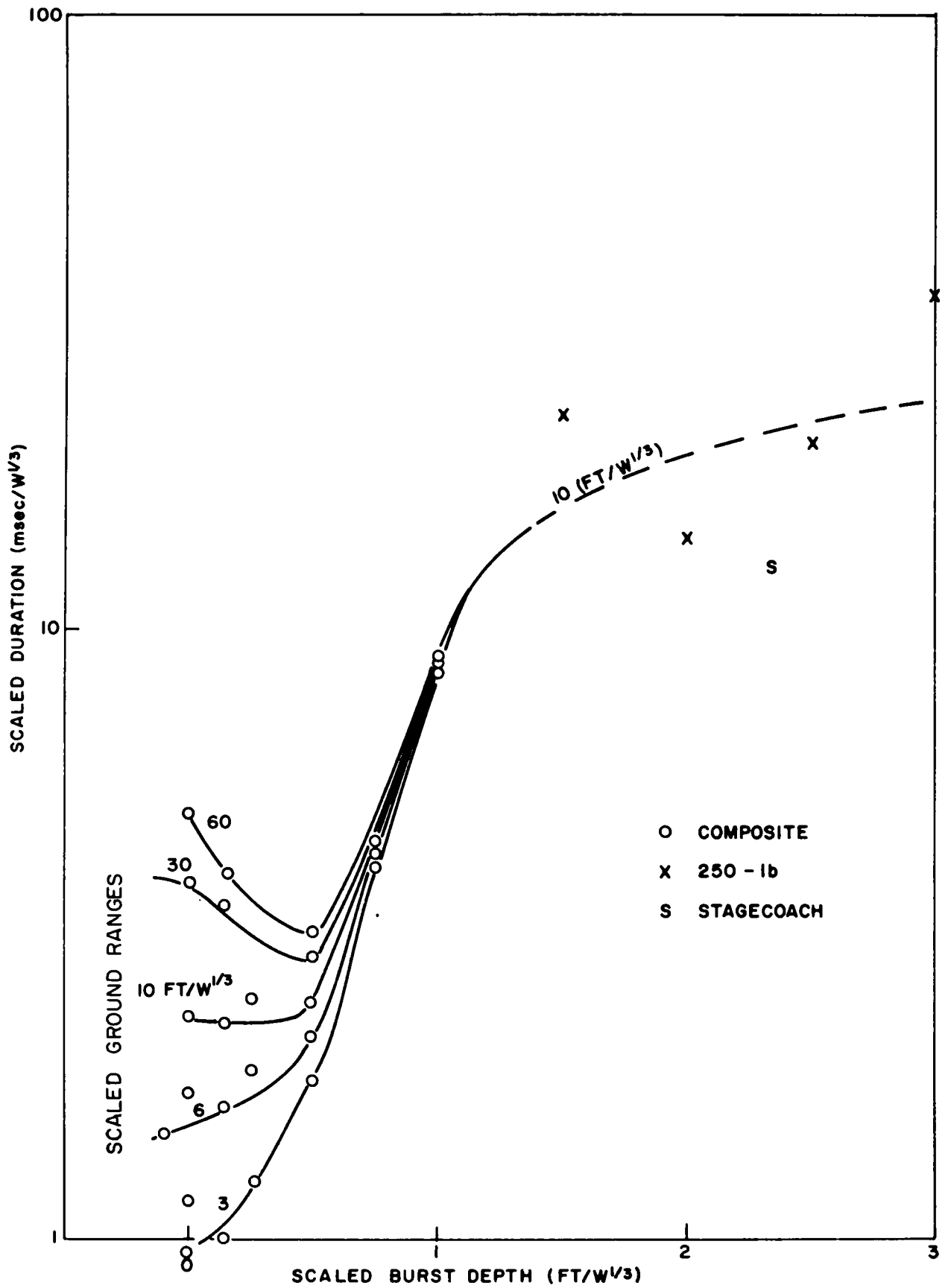
Fig. 8.32 Effect of charge burial on positive phase duration.

The most interesting feature about Fig. 8.32 is that, at the greater distances, it is possible to have a duration which decreases with burst depth to the 0.5 $ft/W^{1/3}$ depth of burst and which increases as burst depth is further increased. Increasing duration with burst depth is characteristic of durations at all stations closer than 10 $ft/W^{1/3}$. Actually, the decrease at the greater distance is an underground manifestation of the knee which occurs in the above-ground duration curves in the region from the surface to 6 or 7 $ft/W^{1/3}$.[8]

Perhaps it is more significant to say that for burst heights between -0.5 and +7.0 the observed durations as evidenced by the knee are less than one might expect. Experiments by OSRD[8] indicate that the British found the cutback at the knee to be even more pronounced than has been demonstrated by work in this country.

8.7 CONCLUSIONS

Project Stagecoach provided the opportunity to observe blast overpressures from larger charges buried at deeper depths in a single medium than had existed before. Suppression of close air blast with charge burial has been defined for peak overpressure, positive-phase impulse, and positive-phase duration. Cube-root scaling was used throughout and no evidence of departure from cube-root scaling was observed within the range of burst depths and charge weights considered.

The main shock wave from venting gas from the Stagecoach shots disappeared between 1 and 2.3 $ft/W^{1/3}$. Wave forms of earlier smaller shots at depths between 1.5 and 3 $ft/W^{1/3}$ are similar to those from venting gas rather than to those from ground-shock-induced air shock but arrival-time information is not sufficiently accurate for proof.

At the deepest Stagecoach shot, one wave was ground-shock induced by earth piston action when the earth shock reached the surface. This airborne wave moved radially outward from surface zero at air shock velocities. Another wave was generated by direct radial propagation of the earth shock; this wave traveled across the surface at near ground-shock velocities. There is an inconclusive suggestion that a train of three waves was so generated.

REFERENCES

1. Doll, E. B., and Salmon, V., Scaled HE Tests, Operation Jangle, WT-377, Project 1(9)-1, Stanford Research Institute, April 1952.

2. Eberhard, R. D., Kingery, C. N., and Molesky, W. F., Peak Air Blast Pressures from Shock Velocity Measurements Along the Ground, Operation Jangle, WT-32, Ballistic Research Laboratories, July 1952.

3. Sachs, D. C., and Swift, L. M., Small Explosion Tests, Project Mole, Vols. I and II, AFSWP-291, Stanford Research Institute, December 1955.

4. Murphey, B. F., and Ames, E. S., Air Pressure versus Depth of Burst, SCTM 42-59(51), Sandia Corporation, February 20, 1959.

5. Howard, W. J., and Jones, R. D., Free Air Pressure Measurements, Operation Jangle, WT-306, Project 1.21, Sandia Corporation, February 19, 1952.

6. Sachs, D. C., and Swift, L. M., Underground Explosion Effects, WT-1106, Stanford Research Institute, March 23, 1958.

7. Rugg, H. M., Seismic Refraction Survey for Nye County, Nevada, WT-327, United Geophysical Company, Inc., July 27, 1951.

8. Kirkwood, J. G., and Brinkley, S. R., Jr., Theoretical Blast-Wave Curves for Cast TNT, OSRD-5481, Office of Scientific Research and Development, August 23, 1945.

9. Shreve, J. D., Pressure-Distance-Height Study of 256-lb TNT Spheres, WT-520, Sandia Corporation, March 13, 1953.

10. The Effects of Nuclear Weapons, S. Glasstone, Ed., DOD/AEC, Washington 25, D. C., June 1957.

11. Belliveau, L. J., Rodgers, W. C., Jr., and Lehto, D. L., The Prediction of Shock Overpressures from Surface-Burst Nuclear Weapons Along the Surface, NAVORD-6240, Naval Ordnance Laboratory, January 21, 1959.

12. Rudlin, L., Airblast from Surface and Underground HE and Nuclear Explosions, NAVORD-5709, Naval Ordnance Laboratory, September 2, 1958.

13. Stephens, G., The Behavior of the Shock Wave in Air from Small Underground Explosions, NAVORD-5709, Naval Ordnance Laboratory, September 2, 1958.

14. Vortman, L. J., and Shreve, J. D., The Effect of Height of Explosion on Blast Parameters, SC-3858(TR), Sandia Corporation, June 20, 1956.

Chapter 9

MICROBAROGRAPHY by J. W. Reed

9.1 INTRODUCTION

Air blast is attenuated by charge burial. The few previous recordings from buried shots do not show just how attenuation factors vary with depth of burst (DOB) or distance. Sandia Laboratory operated fifteen microbarographs at ranges from 2 to 140 miles from the three Project Stagecoach shots. It was hoped that recordings from these stations would aid in the understanding of air-blast wave formation and scaling for DOB and range.

Coincident high-altitude rocket wind measurements were made at Tonopah Test Range to allow comparison between computed and observed long-range sound propagation patterns. These are shown together with rawinsonde upper air measurements by the U. S. Weather Bureau in Appendix C.

9.2 BACKGROUND

Teapot Ess close-in pressure records, reported by Sachs and Swift,[1] showed 27 percent of Jangle Surface shot amplitude at 600-foot range. Closer to ground zero, even more attenuation was found. Ess was shot at a 67-foot depth, which is equivalent to 0.5 $ft/lb^{1/3}$ if it is assumed that buried nuclear and high-explosive yields are equal in blast production (half of air-burst nuclear yield goes out in radiation, etc.). Microbarograph records at near 100-mile ranges showed Ess pressure amplitudes were not much different from those forecast for a surface burst.[2]

A few pressure recordings[3] at 6 and 7 miles range from 256-pound HE shots in August 1959 at depths to 4.5 $ft/lb^{1/3}$ hinted that p ~ exp(-5 DOB/3), for DOB in $ft/lb^{1/3}$. Weather and sound ducting conditions were poor during this test, so these results have limited usefulness.

A diagram of early air shock conditions from a buried charge is shown in Fig. 9.1. Most of the blast energy is shot upward through a conical region
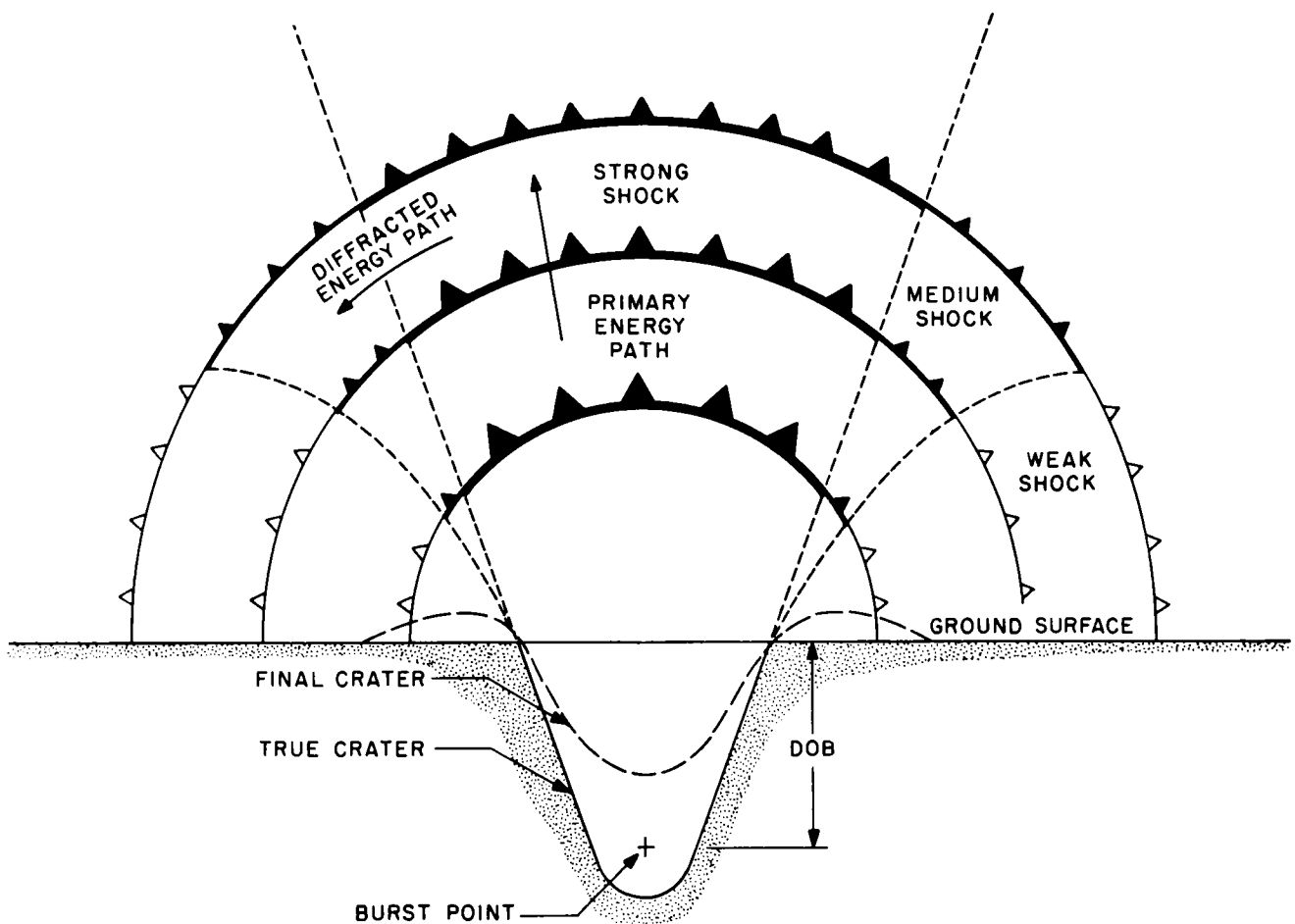
Fig. 9.1 Air shock from buried explosion.

defined by the true crater slope. Some of this energy is then diffracted
tangentially to the front, maintaining a continuous front down to ground
level. As time goes on, diffraction tends to make a uniform energy-density
wave front. It is questionable whether this uniformity is reached in finite
ranges. Close to ground zero (GZ), crater lip shadowing causes much lower
than surface burst pressures. Farther away, where diffraction has more time
to act, larger and larger proportions of surface burst pressures will be felt.

At these longer ranges, atmospheric propagation conditions become impor-
tant, causing refraction and sometimes ducting to further confuse pressure-
distance curve predictions. Initial blast rays which may be ducted by the
atmosphere are shown in Fig. 9.2. Rays emanating from GZ below 10- or 15-
degree elevation angles may be trapped under a surface temperature inversion
or wind condition. This effect may double blast isobar ranges beyond the 2-
psi region. High-speed winds aloft, in jet streams at 25,000 to 40,000-foot

altitudes, may duct blast and give sound rings at ranges to nearly 100 miles. Initial rays to about 20-degree elevation angles may thus be ducted. Sound rays elevated to about 30 degrees are ducted by high temperatures in the ozonosphere between 100,000 and 150,000 feet and land at 60- to 150-mile ranges. Some recordings have been made of even 45-degree rays returned to ground from ionosphere heights to 400,000 feet, but pressure amplitudes for these signals are small. Large megaton sources have caused audible waves which returned to ground at 500-mile ranges from over 10^6-foot heights at 70-degree elevation angles.

BLAST WAVE

BLAST RAYS

GROUND ZERO

10°-15° DUCTED BY SURFACE INVERSION

15°-20° DUCTED BY JET STREAM WIND

20°-30° DUCTED BY OZONOSPHERE

45° DUCTED BY IONOSPHERE
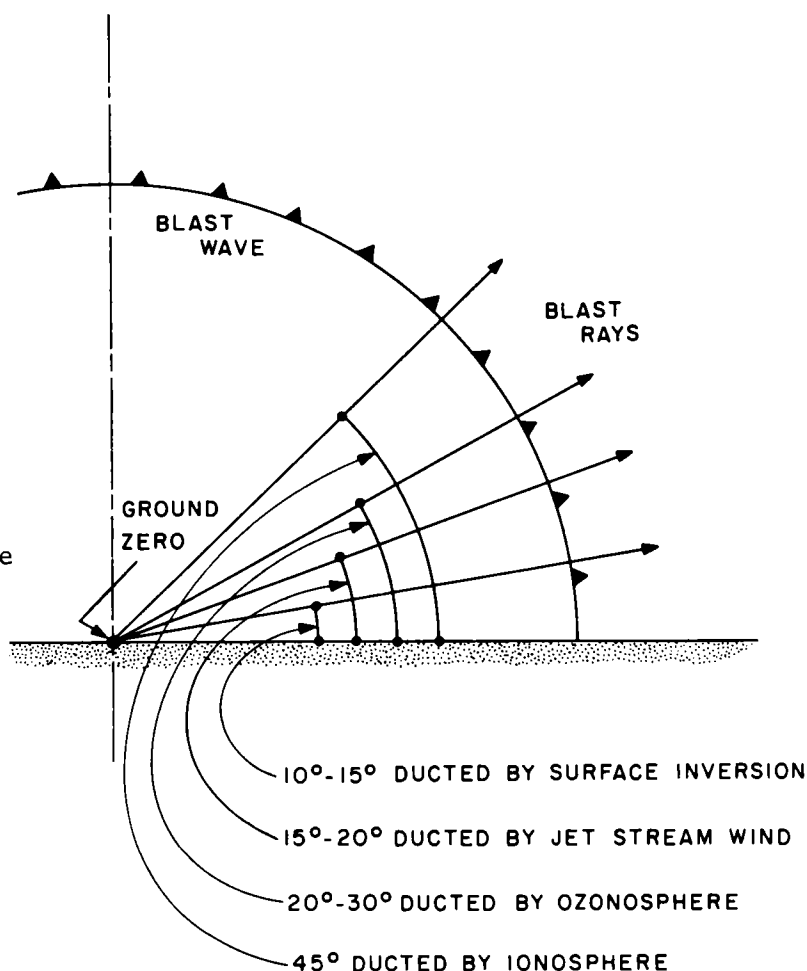
Fig. 9.2 Atmospheric sound ducting.

Calibration shots, at ground-surface level, at near buried shot times show atmospheric ducted sounds on microbarographs. Four 600-pound depth charges should give pressure amplitudes $(1.2/20)^{1/3}$ = 0.391 times as large as 20-ton surface shots at long ranges in almost constant weather. Recordings of 20-ton buried shots thus should show how DOB affects attenuation. Varied muffling for different elevation angle bands may show on records at distance ranges affected by various atmosphere ducts. If diffraction works very fast, however, a uniform blast-energy density may appear.

A few instances of blast damage have been claimed at ozonosphere sound ring ranges. During full-scale test operations, 1.2-ton HE surface shots were fired just before atomic blasts. Microbarograph recordings from these shots were yield-scaled to predict long distance effects to avoid damages. This system was found not to be fully satisfactory. There was no means then for observing high-altitude conditions (above 100,000 feet) so that a refracted ray path

calculation could be made and a predicted sound pattern drawn. In 1958, a Deacon-Arrow two-stage rocket system shown in Figs. 9.3 and 9.4 was developed at Sandia Laboratory to dump a load of radar-reflecting chaff near 300,000 feet altitude.[4] As it fell, a radar track plan showed wind motions. Since then, rocket-chaff wind measurement has been developed to an operational system at Tonopah Test Range (60 miles northwest of Yucca Flat). Rocket wind reports, added to an assumed upper temperature structure, allow refracted-ray tracing and sound-pattern prediction at over 100-mile ranges. Comparison with observed sound patterns would show whether scaling shots could be replaced and improved upon by forecasts computed from direct weather reports. Also, a blast pattern climatology for long ranges from a new shot site could be made with rocket soundings rather than a more costly blasting-microbarograph program. Furthermore, there is a large difference between sound-ranging and rocket-measured temperature-height structures at ozonosphere heights[5] which may be resolved with direct local wind data. Observed sound signals around explosions indicate that temperatures range from +4 degrees C at 100,000 feet to +45 degrees C at 150,000 feet MSL. Rocket-measured temperatures at these heights range from -40 degrees C to +6 degrees C.[6]

9.3 EXPERIMENTAL PROCEDURE

Project Stagecoach air-blast-pressure measurements were made by the Naval Ordnance Laboratory (NOL) out to about one-mile range, as described in the preceding chapter. Results and details of these measurements from balloon-borne gages will be reported separately by NOL. Sandia Laboratory operated three on-site microbarographs at 2-, 7-, and 12-mile ranges, as shown in Fig. 9.5, which recorded blast waves trapped in shallow atmospheric surface ducts. Detailed surface inversion temperatures and winds were recorded from 500-foot weather towers near Yucca Weather Station and the BJY road junction. A tower and instrument arm are shown in Figs. 9.6 and 9.7. Surface-burst 1.2-ton calibration shots were fired at site F-5 ten minutes before each Stagecoach event. Blast-pressure gages were placed 300 feet from calibration shots.

Six microbarographs were placed along Highway 95 to Las Vegas at points shown in Fig. 9.8. These points had been fixed for an earlier project to record ducted and focused blast waves refracted by jet-stream winds. It was hoped that some Stagecoach shots could be fired when wind jets were overhead.

Fig. 9.3 Deacon-Arrow chaff rocket and launcher at Tonopah Test Range.
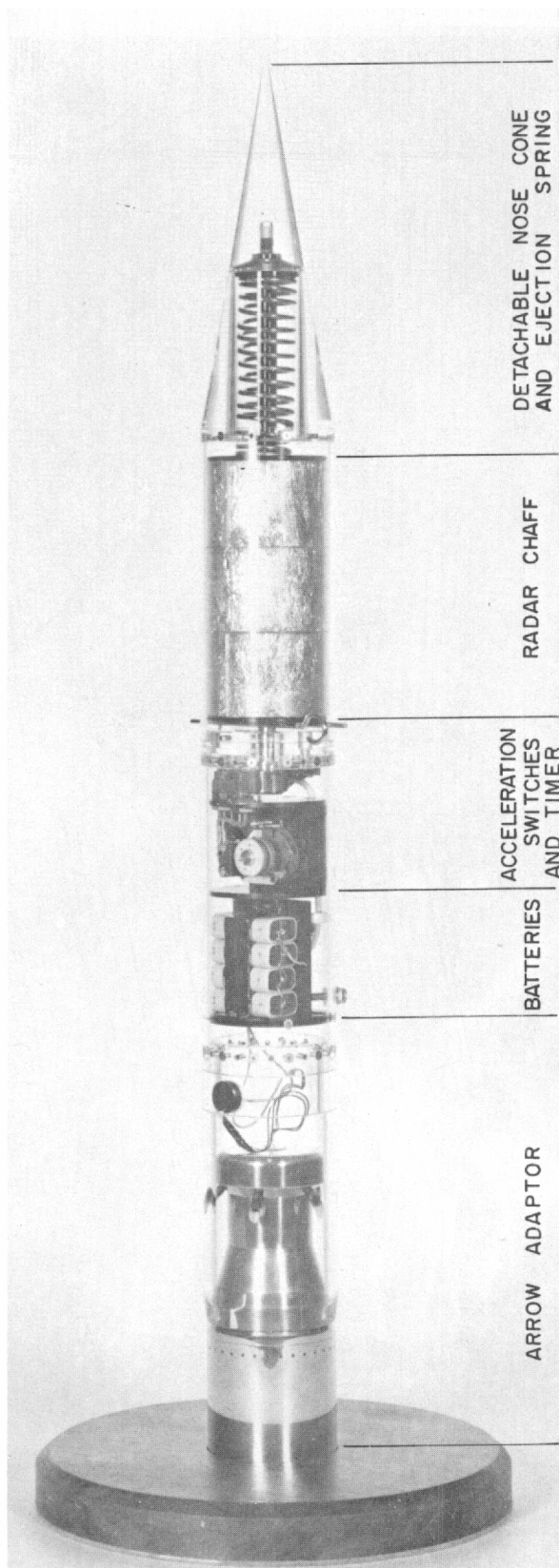
Fig. 9.4 Dart nose section model.
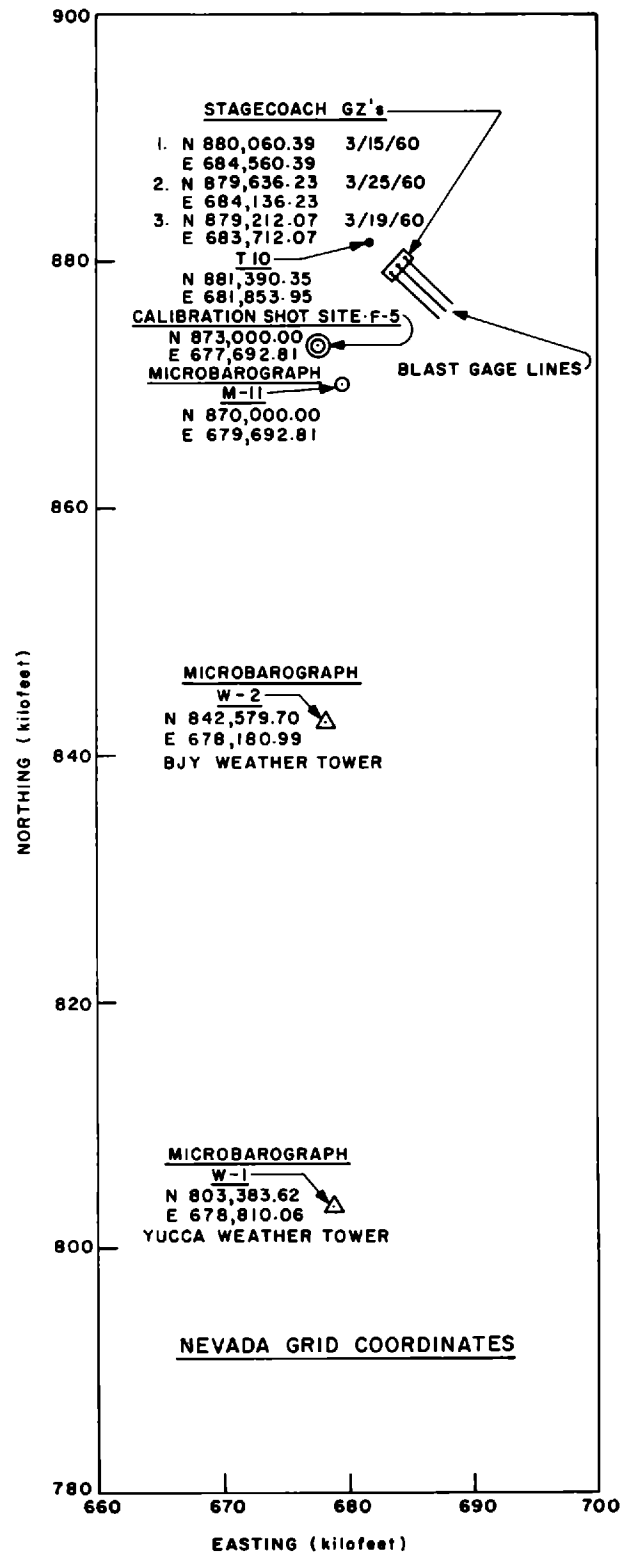
Fig. 9.5 Yucca Flat microbarograph locations.
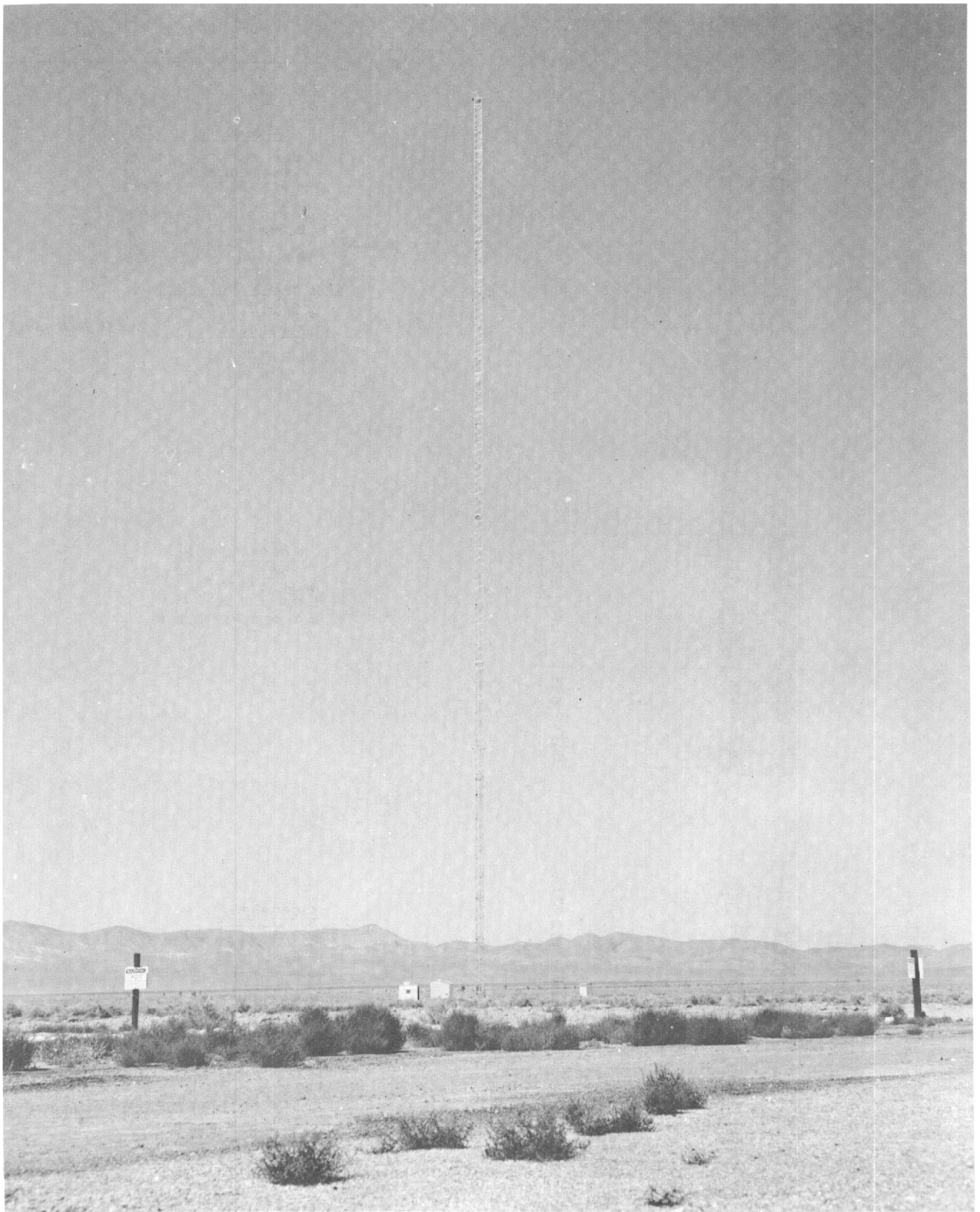
Fig. 9.6 Weather tower on Yucca Flat.
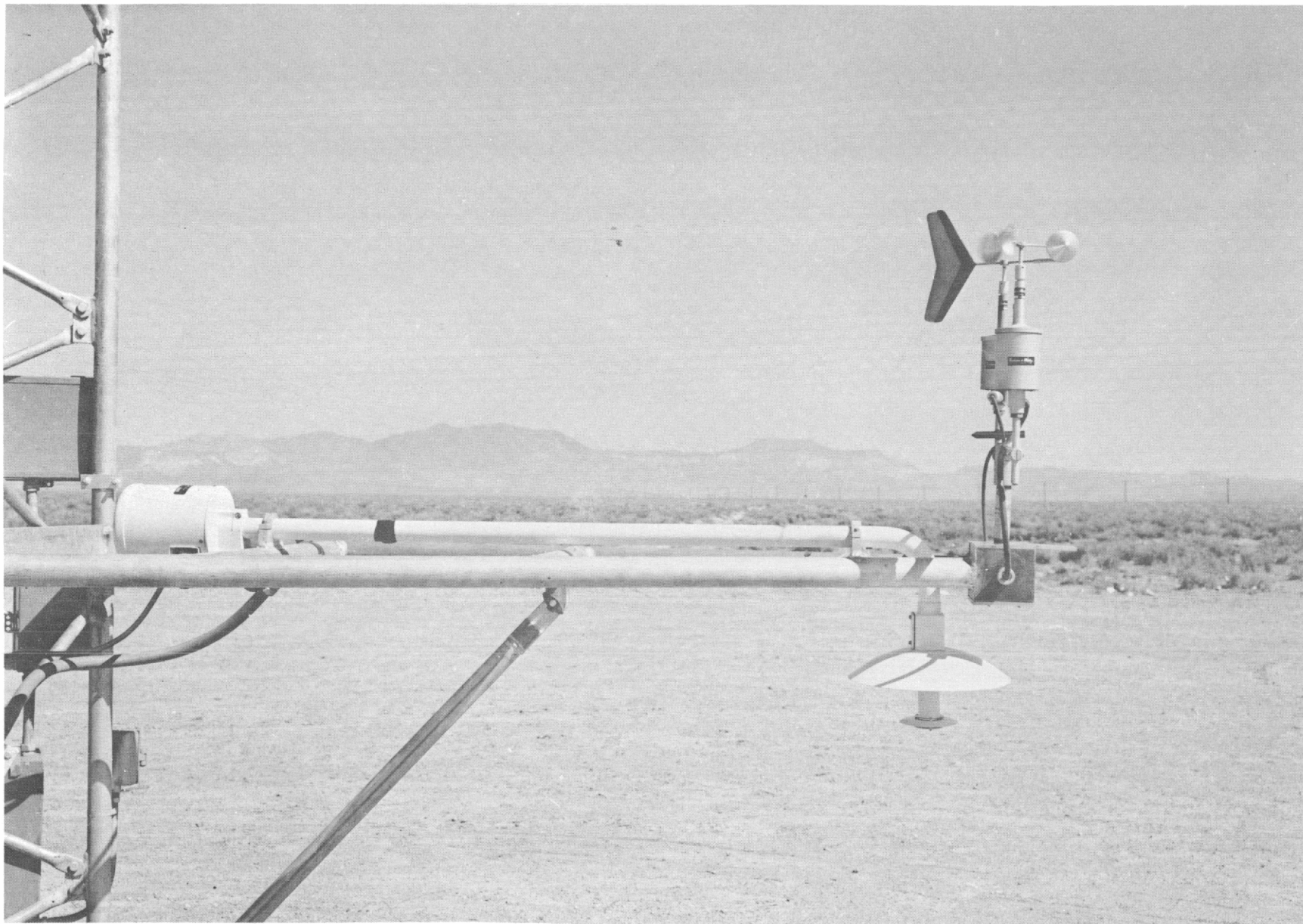
Fig. 9.7 Weather tower instrument arm.

N

N47°20'55"W

TO MERCURY

U.S. HIGHWAY 95

TO LAS VEGAS →

LEE CANYON ROAD

M-11
M-12
M-13
M-15
M-16
M-17

N 630,000

N 605,000

E 825,000

E 850,000

E 875,000

	NEVADA STATE GRID COORDINATES	
	CENTRAL ZONE	
	NORTHING	EASTING
M-11	637,485.46	837,448.20
M-12	633,908.59	841,331.01
M-13	630,331.72	845,213.82
M-15	623,177.97	852,979.44
M-16	619,589.08	856,875.29
M-17	615,985.11	860,787.52
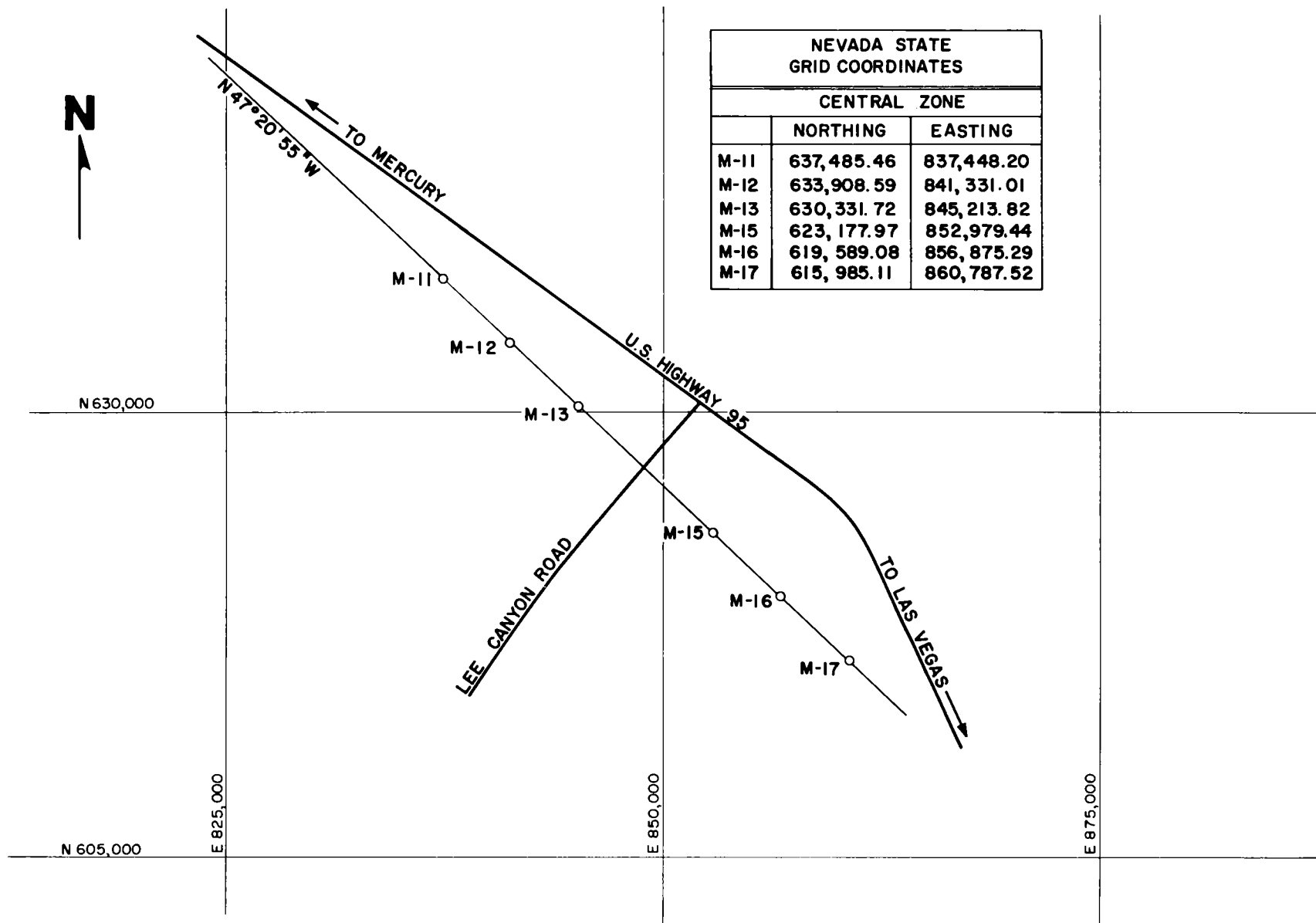
Fig. 9.8 Highway 95 microbarographs.

Maximum ozonosphere blast signals land near St. George, Utah, in winter.[5]
Amplitudes, incidence angles, and possible caustics were recorded on six micro-
barographs in that region at locations shown in Fig. 9.9. These signals are
also used to calculate sound velocities and altitudes necessary to give ob-
served ray-path times and distances.[2]

Distance and bearing from each microbarograph to each shot point have been
calculated and are shown in Table 9.1. Oblate spheroid earth dimensions, from
St. George SM-4F to NTS shot point T-10, were computed from first-order surveys
for Operation Teapot. Approximate corrections for Stagecoach shots were made
around this base line. St. George stations, other than 4C,F and Las Vegas
highway stations, were located by third-order triangulation.

Radiosonde reports of upper air temperatures and winds from the U. S.
Weather Bureau Yucca Flat Station were entered in the Raypac blast computer
at the NTS control point. Also, Raypac patterns were made from assumed ozono-
sphere temperatures and rocket winds observed at Tonopah.

9.4 RESULTS OF ATTENUATION EXPERIMENTS

Pressure records from on-site microbarographs on the Stagecoach shot at
80 feet, March 15, 1960, are reproduced in Fig. 9.10. Radio contact with
Station W-1 was lost shortly before firing, so there was no zero time; a cali-
bration signal was mixed with the scaling signal and is not shown. The buried
shot signal could not be separated from ambient noise without accurate timing.
The buried shot was attenuated much more than was expected; insensitive set
ranges allowed only a barely visible ripple on M-11 and W-2 traces.

Better records were made of the 17-foot-depth shot, March 19, 1960, as
shown in Fig. 9.11. A typical pattern for blast, ducted under a surface in-
version, occurred, with maximum amplitude drifting from the first positive
phase into a second positive cycle at over ten miles. This same effect was
demonstrated several times by the Blast Unit Research Project (BURP) in late
summer, 1959.[7]

On March 25, an extra 1.2-ton surface shot was fired at 0515 PST, ahead
of the Stagecoach shot at 34 feet, to show time variability of ozonosphere
propagation. On-site pressure records from three shots for this data are
shown in Fig. 9.12. Several cycles of noise developed by a nighttime tem-
perature inversion were heard.
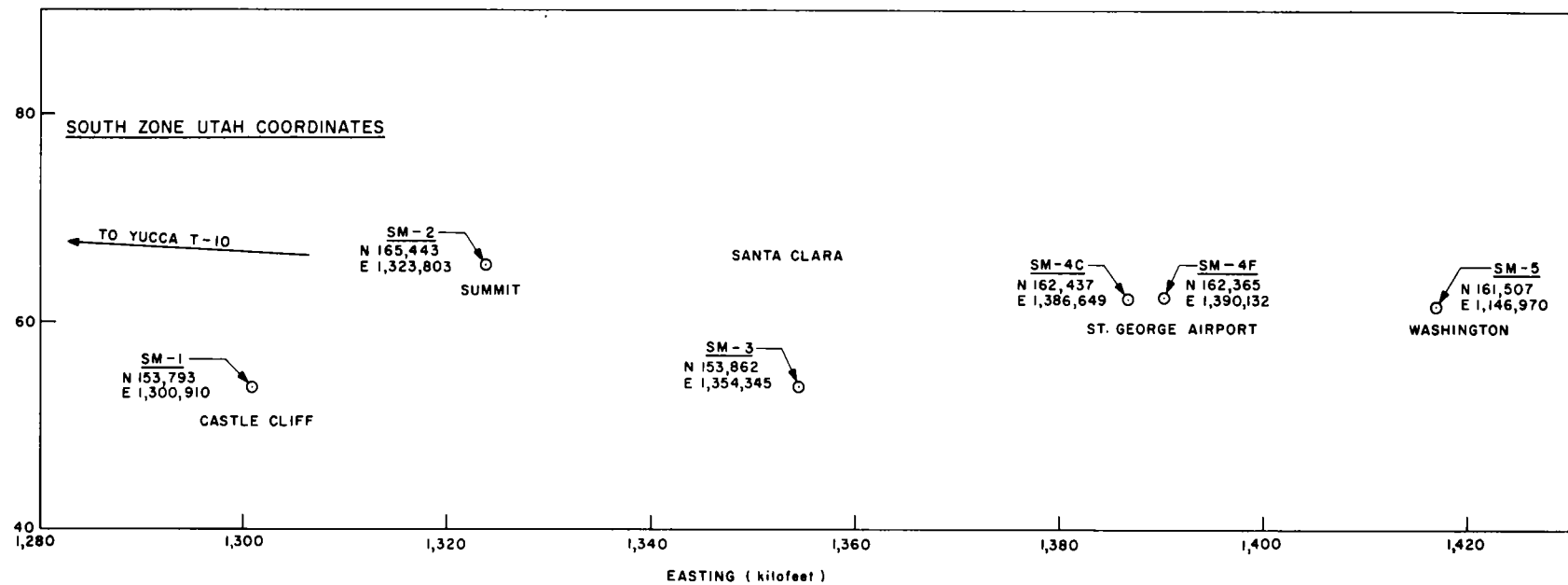
Fig. 9.9 St. George microbarographs.

TABLE 9.1 STAGECOACH MICROBAROGRAPHS

Firing point	S-1	S-3	S-2	F-5
St. George, Utah				
SM-1	623,998*	624,392	624,786	630,544
	274°3.5461'†	274°1.0487'	273°58.5522'	273°22.8349'
SM-2	646,139	646,541	646,945	652,836
	272°52.8634'	272°50.5004'	272°48.1315'	272°14.2625'
SM-3	677,299	677,695	678,091	683,886
	273°43.7737'	273°41.4900'	273°39.2048'	273°6.4729'
SM-4C	709,057	709,460	709,864	715,753
	272°52.1151'	272°49.9625'	272°47.8039'	272°16.9246'
SM-4F	712,539	712,942	713.345	719,233
	272°51.6220'	272°49.4797'	272°47.3315'	272°16.6039'
SM-5	739,389	739,793	740,196	746,084
	272°49.3737'	272°47.3107'	272°45.1591'	272°15.6374'
On Site				
M-11	11,176	10,611	10,051	3,605.6
	25°49.1556'	24°45.3029'	23°34.3059'	326°18.6024'
W-2	38,020	37,532	37.048	30,424
	9°39.5690'	9°7.7900'	8°35.1633'	359°4.8345'
W-1	76,892	76,439	75,987	69,625
	4°18.0483'	3°59.7300'	3°41.9172'	359°4.8310'
Las Vegas Highway				
M-11	286,736	286,603	286,473	284,586
	327°46.6829'	327°39.6683'	327°32.6293'	325°50.9884'
M-12	291.835	291,706	291,578	289,728
	327°30.4205'	327°23.5585'	327°16.6415'	325°36.6976'
M-13	296,941	296,814	296,689	294,875
	327°14.7756'	327°07.9810'	327°01.1878'	325°22.8860'
M-15	307,170	307,049	306,929	305,183
	326°45.0071'	326°38.4268'	326°31.8500'	324°56.6837'
M-16	312,311	312,192	312,074	310,361
	326°30.8095'	326°24.3310'	326°17.8571'	324°44.1977'
M-17	317,480	317,362	317,246	315,564
	326°17.0071'	326°10.6214'	326°4.2558'	324°32.0682'

*Distances in feet.
†Bearings clockwise from north.

180
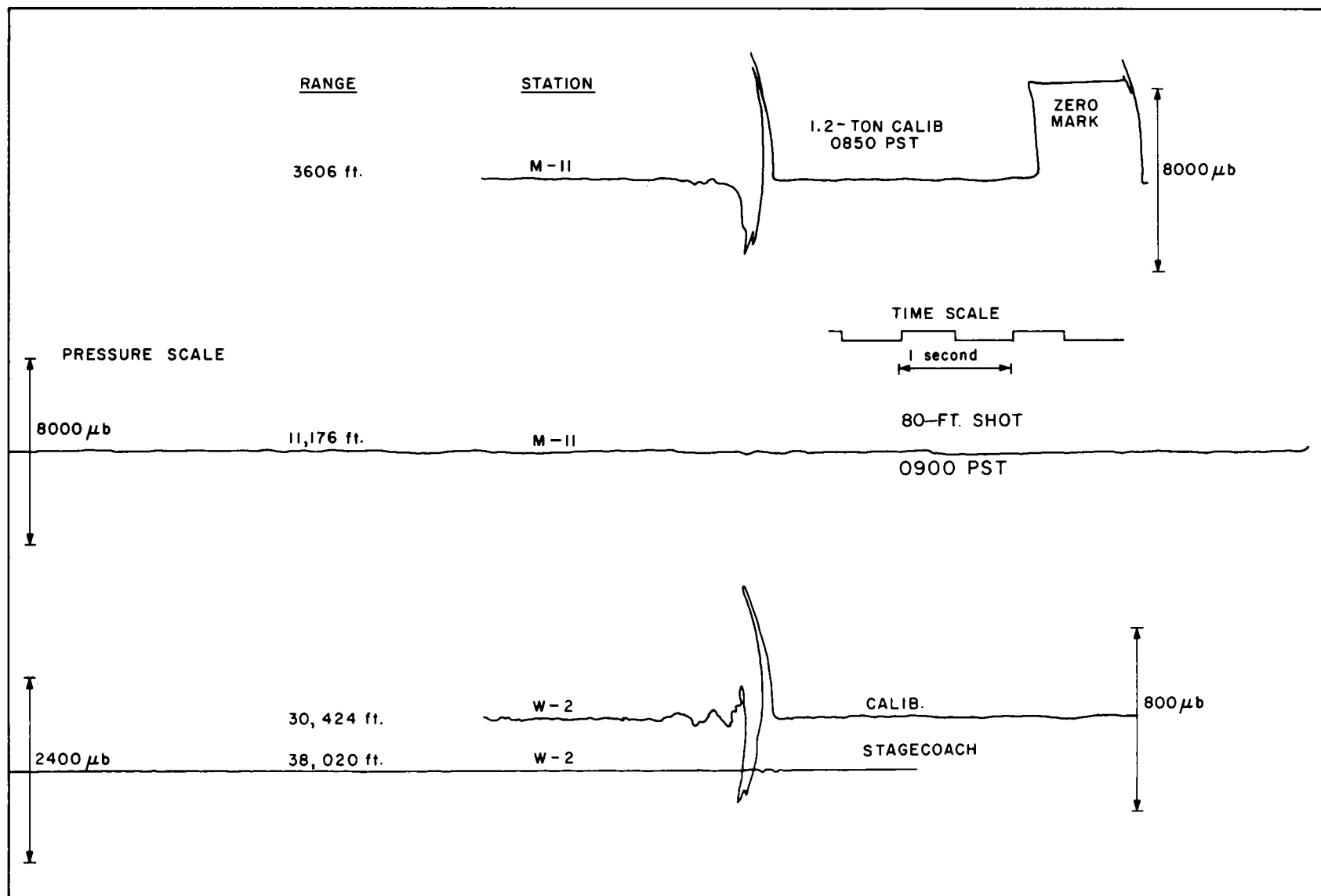
Fig. 9.10 Stagecoach shot at 80 feet, on-site microbarograph records, March 15, 1960.

STATION   SHOT   RANGE

1.2-TON
M-11   CALIB.   3606 ft.
0750 PST

ZERO
MARK

24000

PRESSURE SCALES

TIME SCALE

1 second

17-FT SHOT

24000

M-11   10,051 ft.
0800 PST

W-2   CALIB.   30,424 ft.

2400

2400   W-2   ST.   37,048 ft.

W-1   CALIB.   69,625 ft.
W-1   ST.   800

800   75,987 ft.
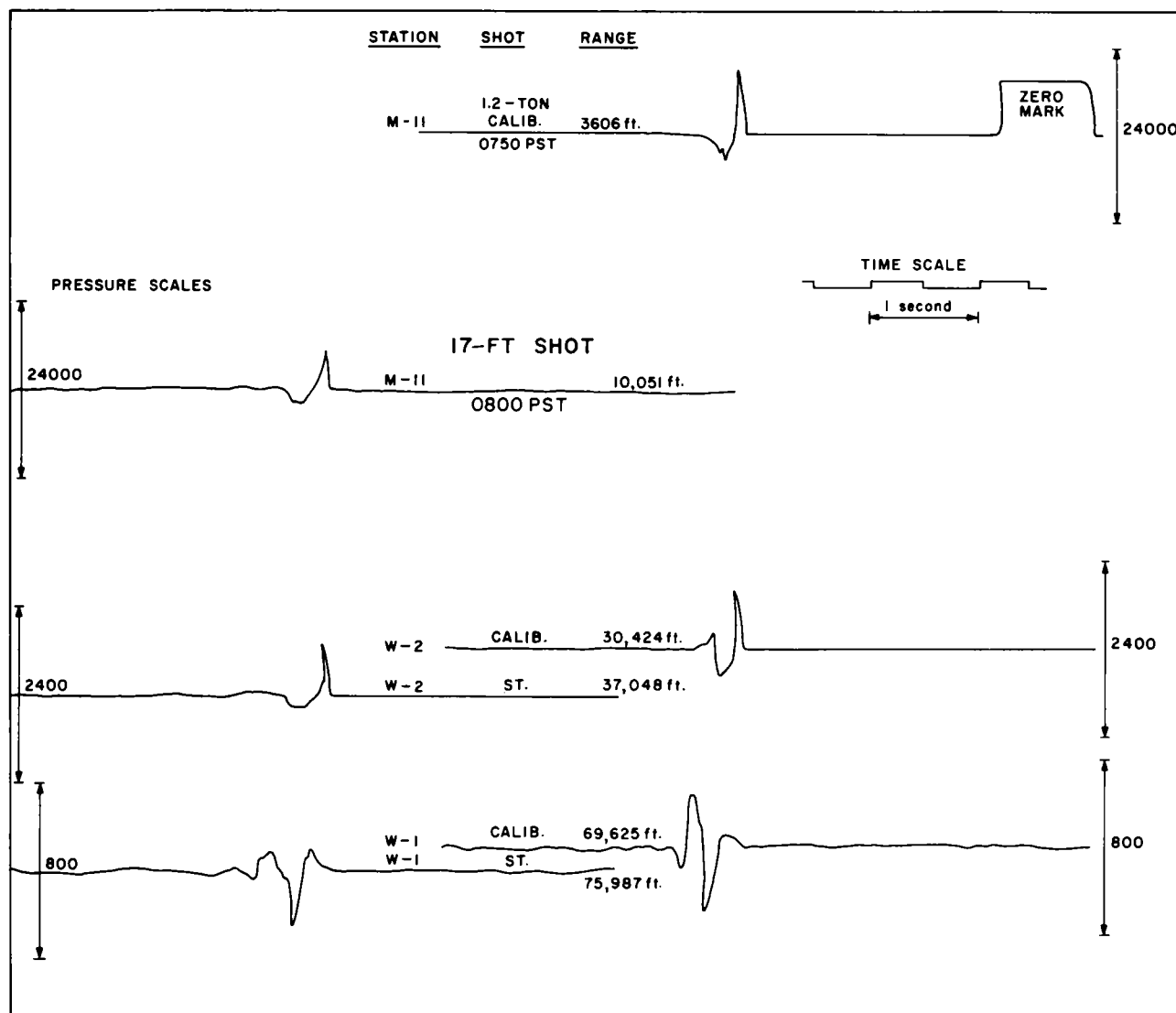
Fig. 9.11 Stagecoach shot at 17 feet, on-site microbarograph records,
March 19, 1960.
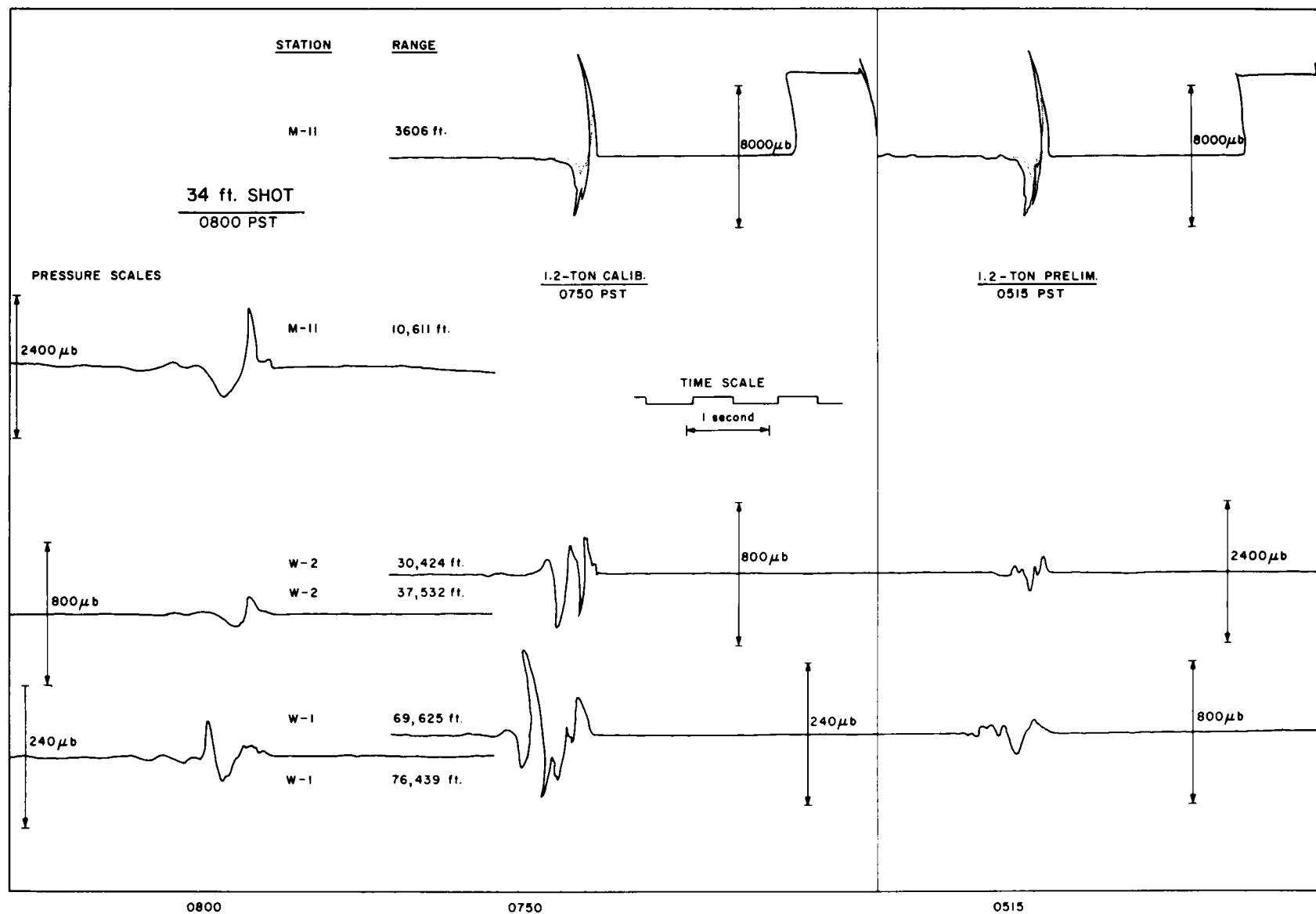
Fig. 9.12 Stagecoach shot at 34 feet, on-site microbarograph records,
March 25, 1960.

Results of several detailed calculations of Yucca Flat sound-velocity-versus-height patterns are shown in Fig. 9.13 for each operational date and time. South-directed velocity curves toward the Sandia microbarograph line were computed from U. S. Weather Bureau balloon radiosonde temperatures in addition to (a) Area 10 pibal winds, (b) and (c) tower W-2 wind recordings for H minus 10 minutes (scaling shot time) and H-hour, respectively, and (d) and (e) tower W-1 winds at H minus 10 minutes and at H-hour.

On March 15, many large wind eddies confused sound velocity and propagation patterns at low altitudes. Strong northwesterly winds aloft caused south-directed sound velocity generally to increase with altitude to 25,000 feet MSL. Lacking a strong surface inversion duct, which would soon spread a blast pulse out to several cycles of noise, the scaling shot first and main pulse retained relatively high strength in traveling through Yucca Flat, as shown by its on-site pressure-distance curve in Fig. 9.14.

A moderately strong temperature inversion and associated light wind speeds on March 19 gave a fairly uniform sound velocity-height structure throughout the shot basin. Similarly, on March 25, an even stronger inversion showed only small-scale turbulent variations in sound velocity between wind measurement stations. Pressure-distance curves for shots on these dates are graphed in Figs. 9.15 and 9.16. Since peak overpressure for only the first positive-phase signal is used for scaling--and at long range, blast energy is more concentrated in later cycles, depending in a complex manner upon yield and inversion characteristics--there is an abrupt drop, shown plotted in pressure-distance curves for inversion shots. In scaled curves this slope-change distance has been conserved. Usually, when a maximum peak-to-peak amplitude for the whole signal is plotted, a slower decay of pressure with distance results, as is shown in Fig. 9.17. Further study of inversion blast ducting is planned in order to refine predictions for these intermediate ranges. Byatt and DeVault[8] have recently derived a theoretical expression for inversion propagation which should be compared to Stagecoach and other data from NTS shots.

A standard pressure-distance curve for 1.2-ton surface bursts is given for reference in Figs. 9.14 through 9.17. This curve was scaled from results of IBM Problem M calculations made at Los Alamos, as graphed by Broyles.[9] Scaling was computed from 1000-mb sea-level, free-air, 1-kt nuclear shot parameters
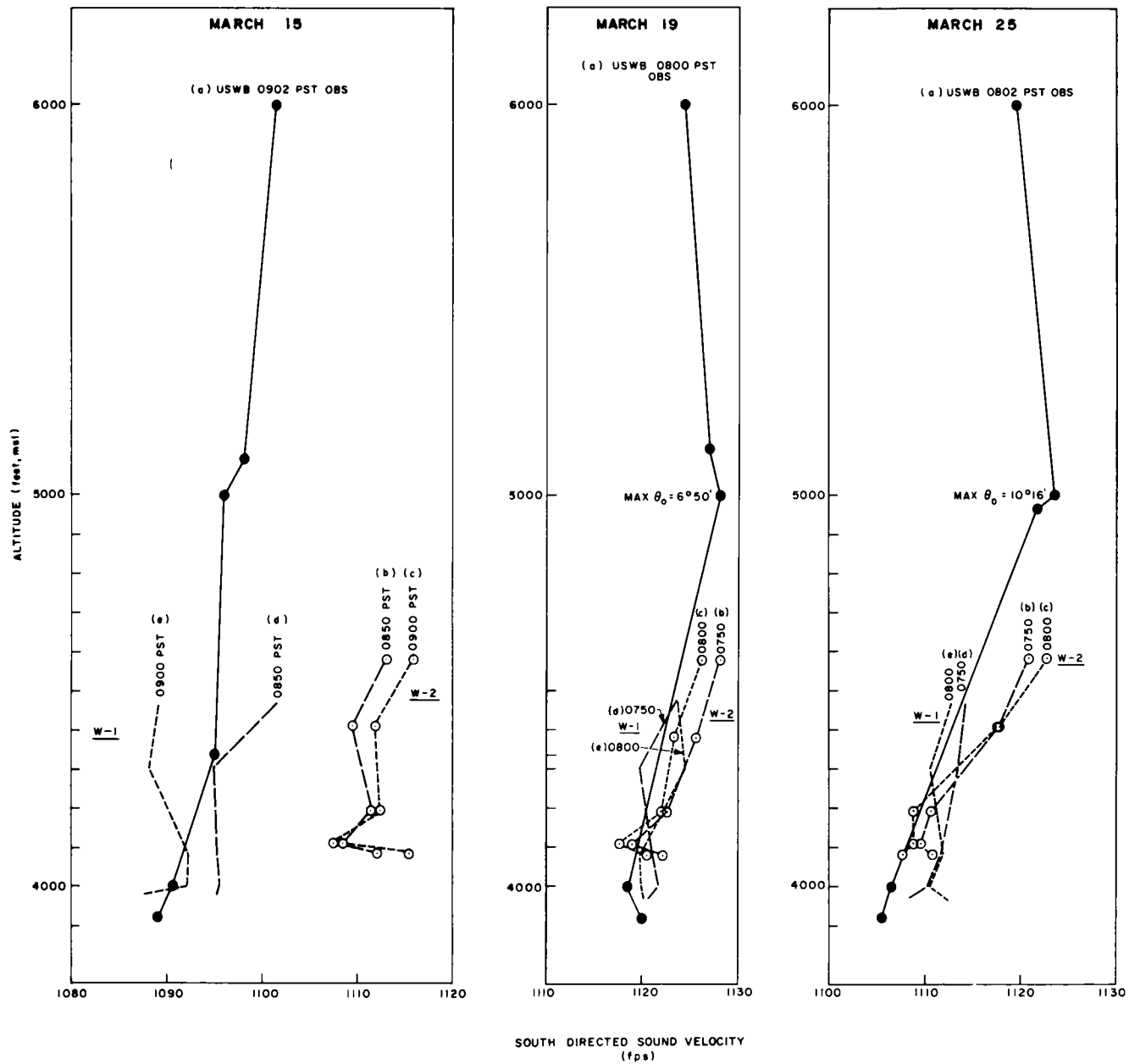
Fig. 9.13   Sound velocity versus altitude measurements.
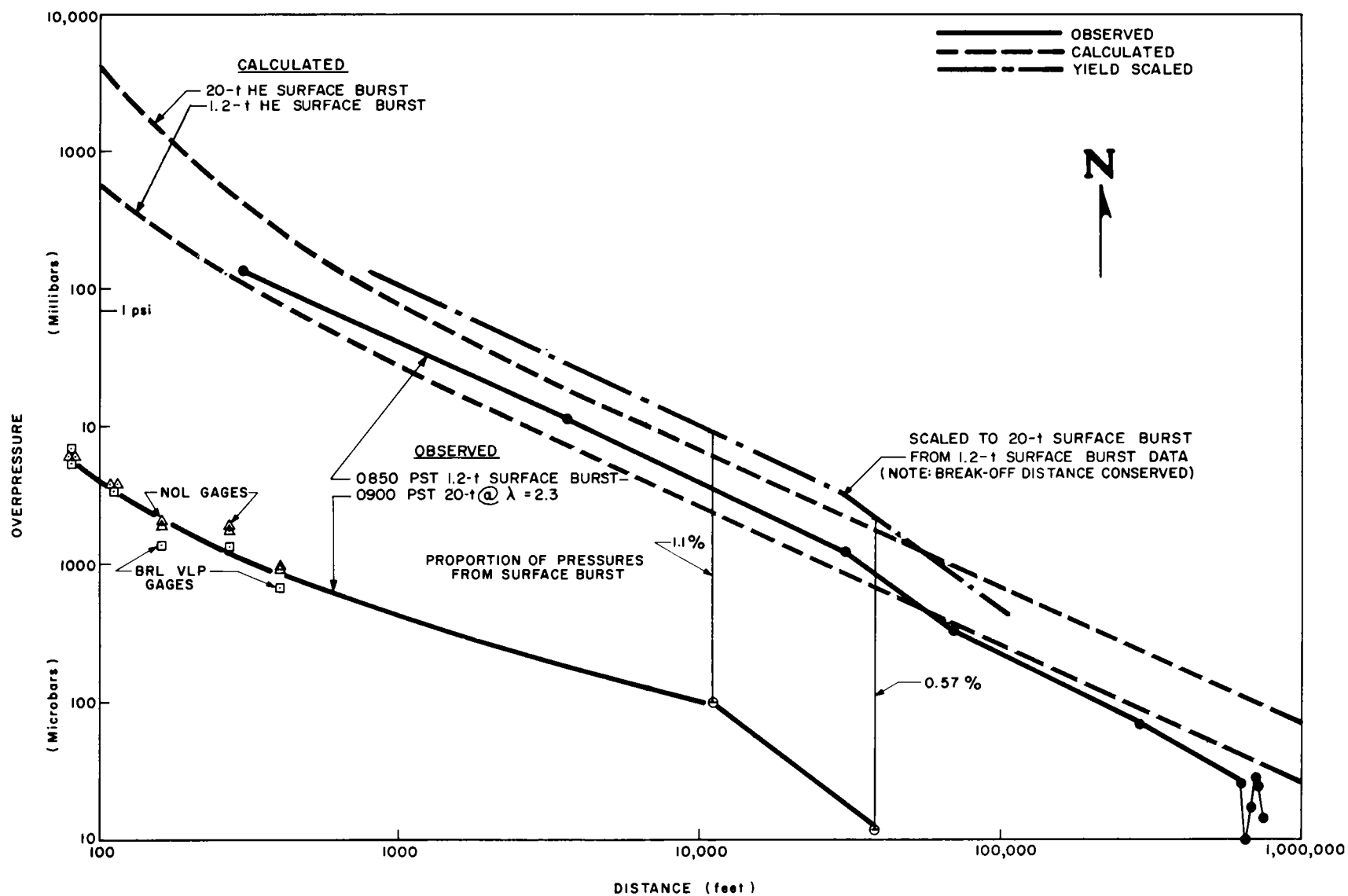
Fig. 9.14 Pressure-distance curves, Stagecoach 80-ft shot.
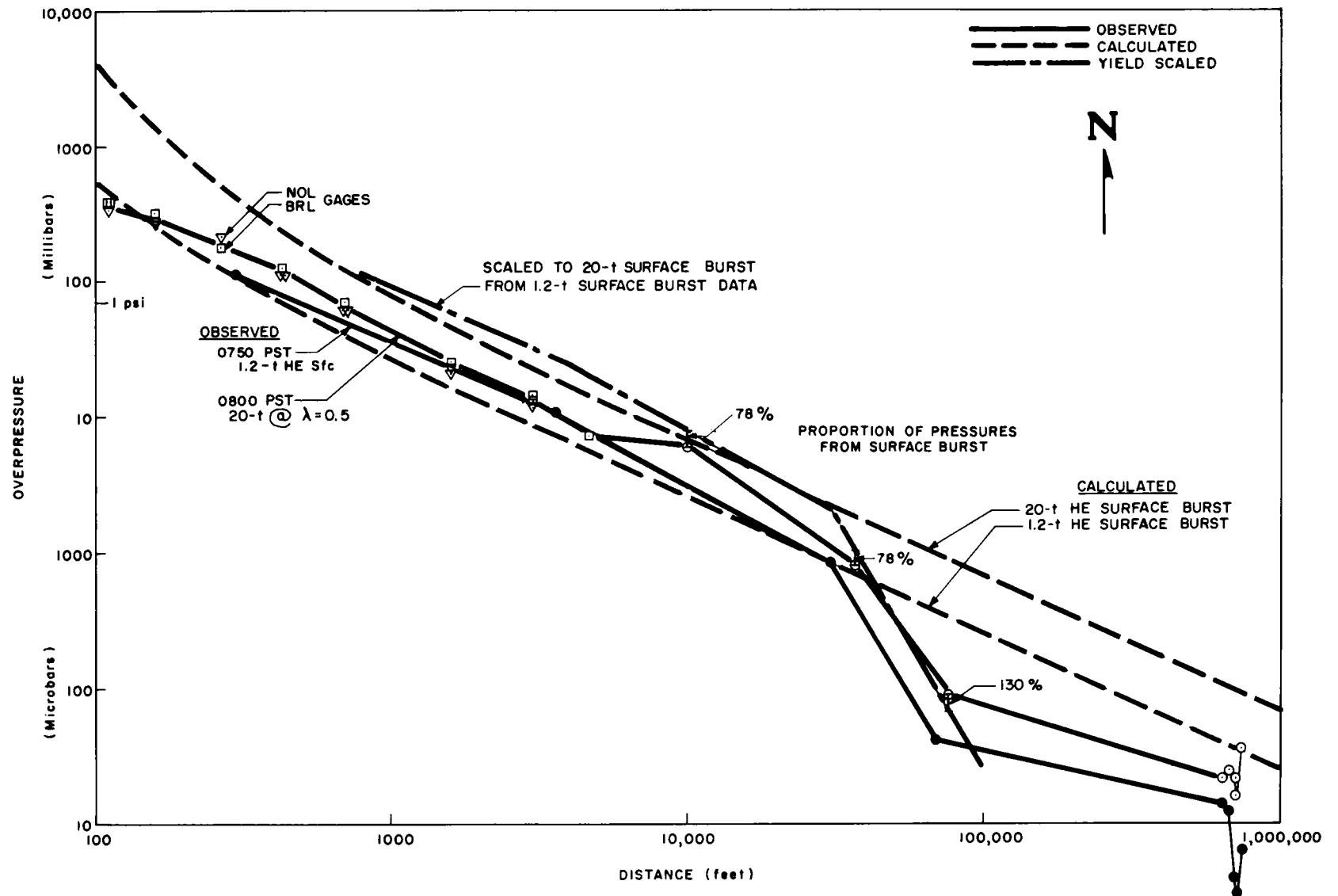
Fig. 9.15 Pressure-distance curves, Stagecoach 17-ft shot.
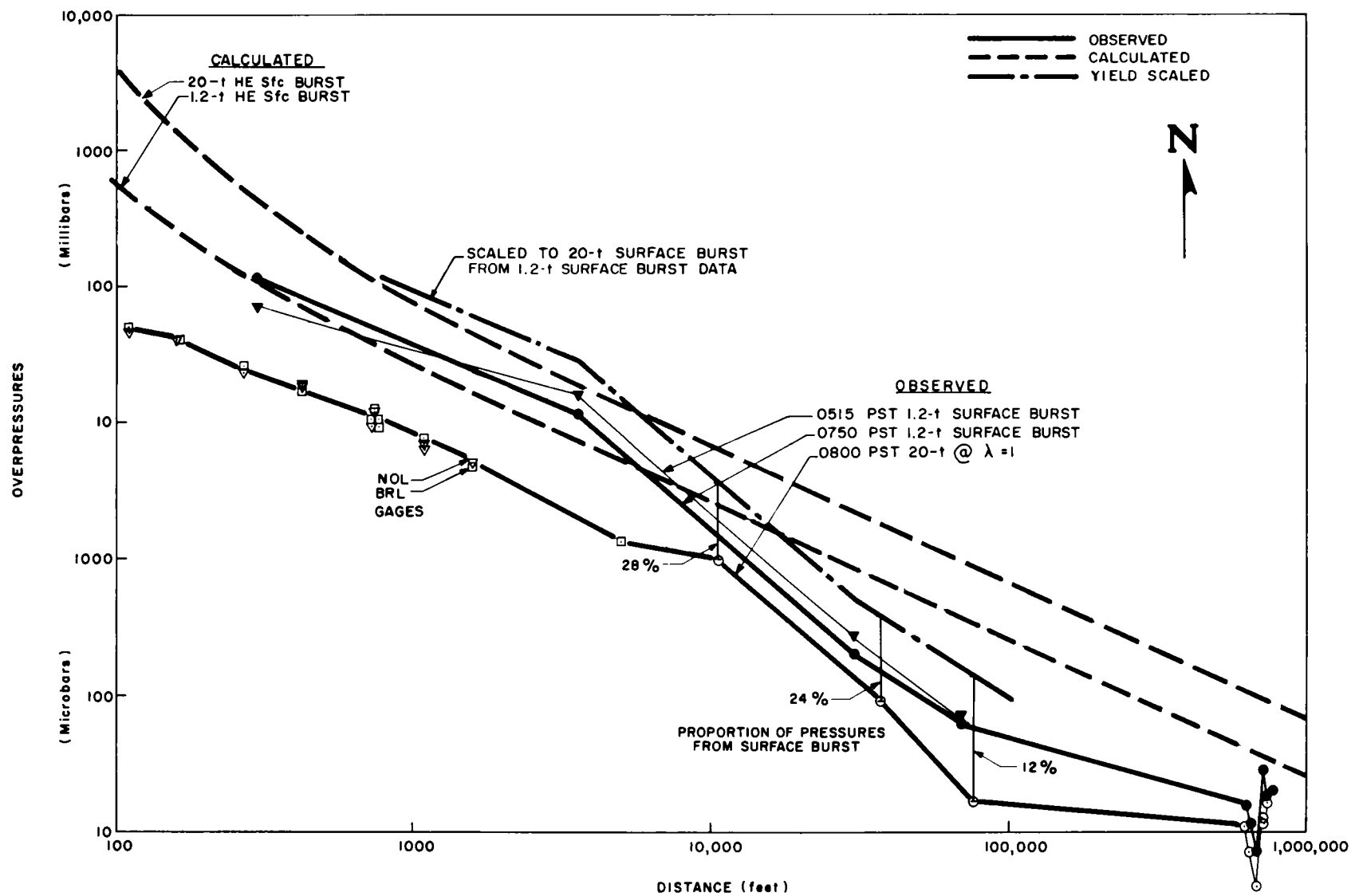
Fig. 9.16 Pressure distance curves, Stagecoach 34-ft shot.
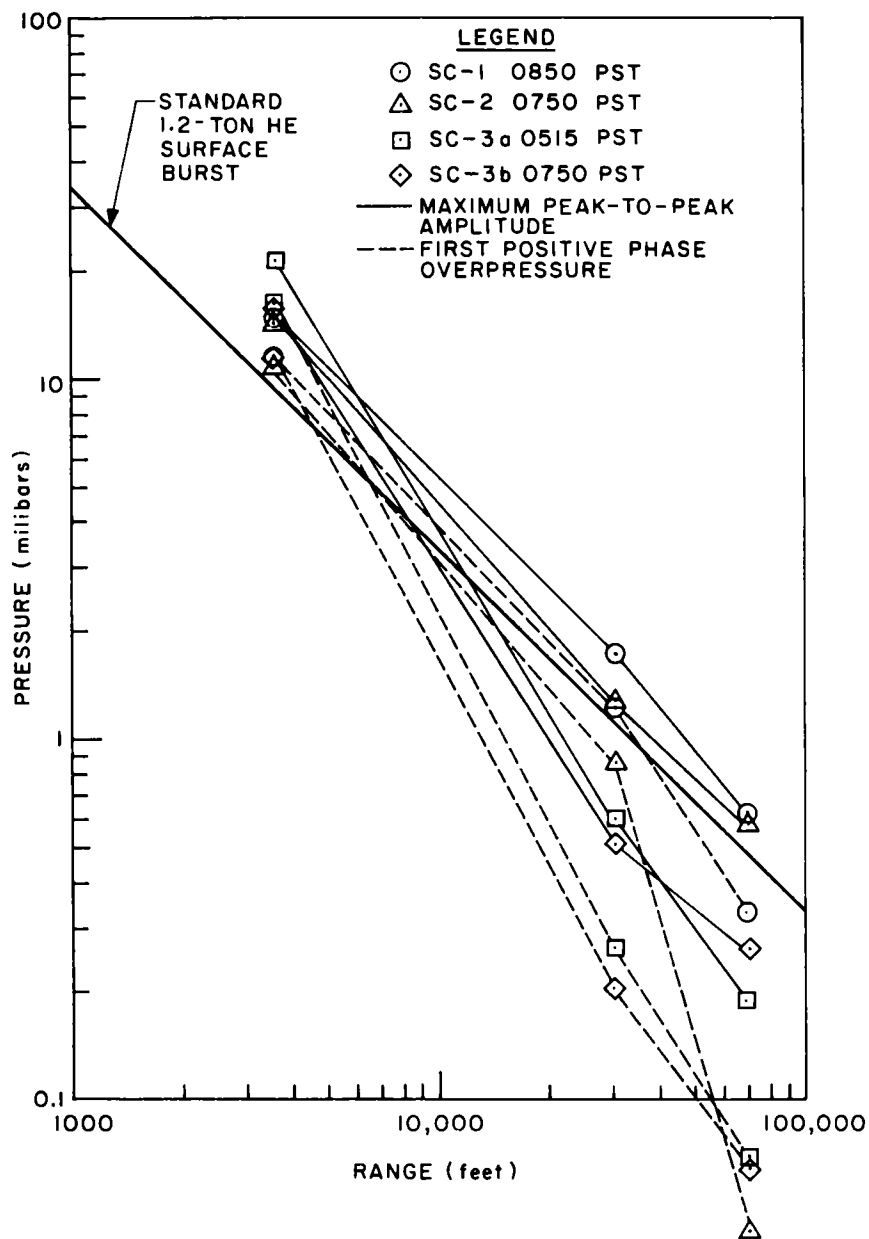
Fig. 9.17 On-site pressure-distance measurements.

189

to 1.2-ton high-explosives (blast from 1 ton HE is equivalent to blast from 2 tons nuclear), at 888-mb ambient pressure at NTS, and apparent blast yield for a surface burst equivalent to blast from a free-air burst of 55 percent as large a yield, as shown by Shreve.[10] No correction for nonspherical charge shape (four 600-pound, war surplus, ash-can depth charges) was made. Similarly, a standard reference curve for 20-ton HE surface bursts is shown in Figs. 9.14 through 9.16.

Actual recorded overpressures from 1.2-ton scaling shots have been scaled to show pressure-distance for 20 tons, surface-burst under the same weather conditions. This last curve is to be compared to observed pressures from buried shots to give burial attenuation factors. Ratios between observed pressures from buried shots to expected blasts from equal weight surface shots for all measurements, including close-in data furnished by NOL, are shown in Fig. 9.18.

Pressure values plotted for off-site stations in Figs. 9.15 through 9.17 are all peak-to-peak amplitudes of maximum amplitude cycles. Only on March 15 was there the strong tropospheric ducting necessary to give recorded signals at Las Vegas highway stations. After that date, very light upper winds prevailed throughout the Stagecoach operation. The shot at 80 feet allowed little air blast, and no signals were recorded off-site for comparison with the scaling shot. Ozonosphere signal scaling comparisons for the shots at 17 and 34 feet were made only where a good signal-arrival-time correlation was observed. Several signal cycles were recorded on only one of the 10-minute spaced shot pairs. (Apparently, even short-time wind variations are effective in shifting sound patterns.) Time variability was further demonstrated on March 25 by an additional scaling shot at H minus 2-3/4 hours. Individual signal or station comparison of ozonosphere signal amplitudes gives erratic results, and for each shot, all comparable signals recorded by the six microbarographs were averaged to give burial effect factors for ozonosphere signals shown in Fig. 9.18.

Pressure, ratio, range, and DOB patterns verify patterns of nonuniform blast intensity postulated earlier in Figs. 9.1 and 9.2. Around a buried shot, blast attenuation factors decrease with distance as diffraction has more time to act. Ratios level off at a range probably determined by inversion, yield, and DOB parameters and continue at a constant value as far as inversion ducting carries recorded waves. Throughout this range, inversion strength determines the maximum initial elevation angle rays carried in the duct, as shown in Fig. 9.13.
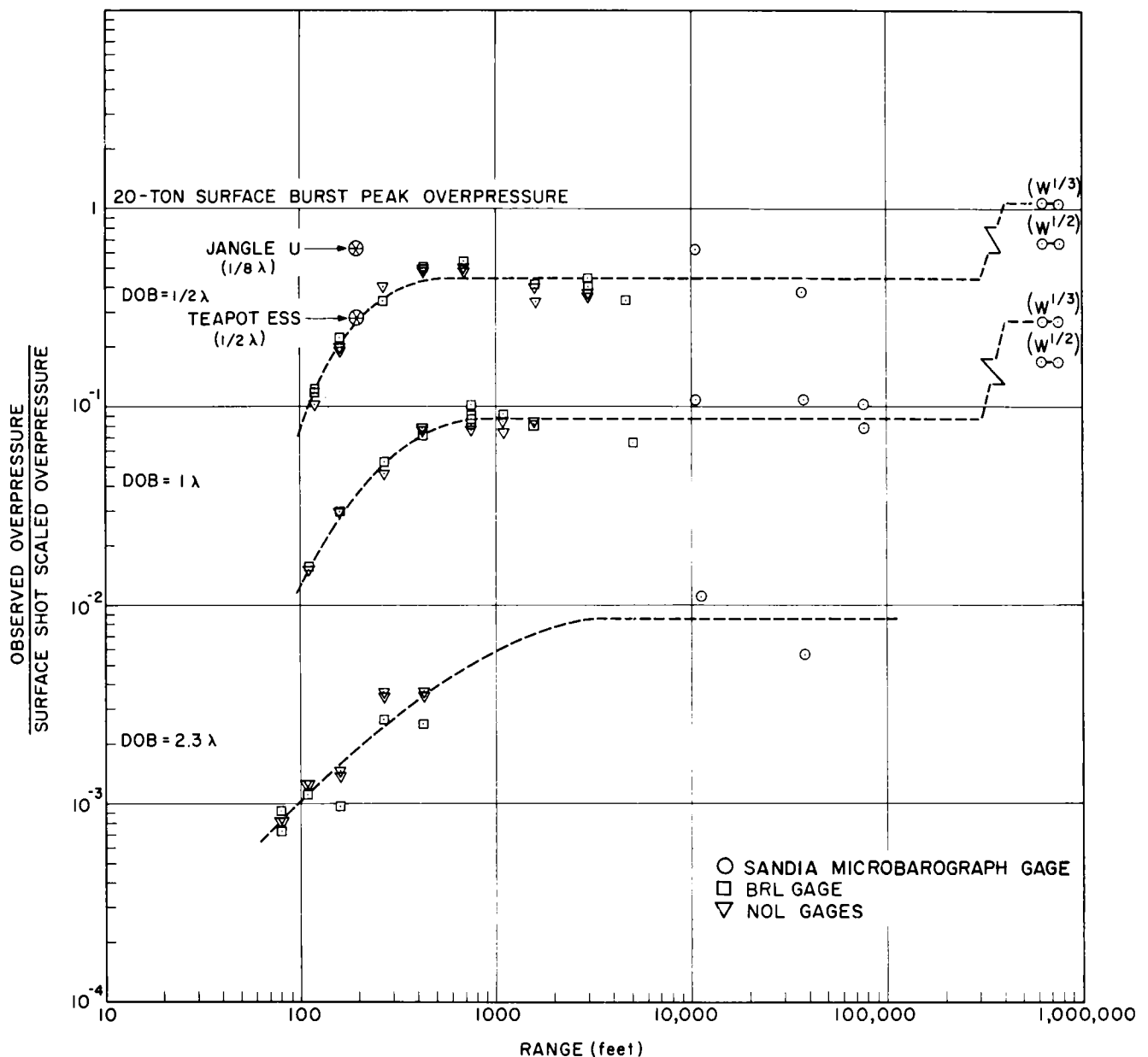
Fig. 9.18 Effects of charge burial on blast overpressures.

Close-in pressure measurements by NOL at ground level and from gages suspended from balloons do not clearly indicate this overpressure dependence on elevation angle from source. No data were obtained above ground from the 80-foot shot. The 17-foot shot data to 480-feet above ground at 430- and 700-foot pound ranges give only a very weak hint that pressures at elevation angles above 45 degrees may be larger than pressure along lower angle rays. On the

shot at 34 feet, above ground data scattered so much because of instrument errors that no pattern could be seen.*

Ozonosphere signals break out of the lower inversion duct before a uniform blast hemisphere has been developed through diffraction. Thus, when refracted back to ground level near St. George, their pressure ratios are higher than lower elevated ray waves because their origin was in a stronger blast-wave region of the initial sphere. That ozonosphere signal ratios should be two and one-half to three times larger than on-site ratios is indeed surprising, but repeatability between the shots at 17 and 34 feet is convincing.

In Fig. 9.18 ozonosphere ratios are also shown for $W^{1/2}$ scaling laws. So far, there is no strong rational argument for this anomalous scaling which has been observed in atomic test operations.[2,5] If this scaling is real, it may be caused by constructive interference of signal waves. There are, however, possible alternative explanations. There may be a false factor resulting from comparison of true surface HE scaling burst with finite height-of-burst conditions of nearly all full-scale tests. Furthermore, even surface nuclear shots do not suffer blast reduction as found in HE tests (Fig. 8.23). This, as yet, has not been fully verified. Selective absorption at high altitudes of high-frequency components of small shot signals may also cause scaling anomalies.

The 17-foot shot at 0.5 $ft/lb^{1/3}$ DOB gave pressure ratios at St. George slightly larger than 1. There is nothing in principle against this, since it may show that blast channeling by the crater cone gives larger blast pressures above a buried shot than at the same range over a surface burst having a hemispheric expanding blast wave.

A coordinate transformation of Fig. 9.18 is shown in Fig. 9.19 for comparison with data previously obtained from 256-pound HE sphere experiments.[3] This clearly shows a more complicated reaction to burial than was shown by the limited data and accuracy of the previous measurements. Much lower apparent pressure ratios at 2.3 $ft/lb^{1/3}$ from Stagecoach may result from confused sound propagation patterns which obtained both on March 15, 1960 and on August 19, 1959, the latter of which dates the 256-pound experiment was fired. It is

---

*Similar data collected later on Project Scooter (500-ton HE burst at 1.25 $ft/lb^{1/3}$, October 13, 1960) showed that a nearly uniform intensity wave propagated outward below 30 degrees elevation; pressures increased above 30 degrees by 50 percent near 45 degrees.
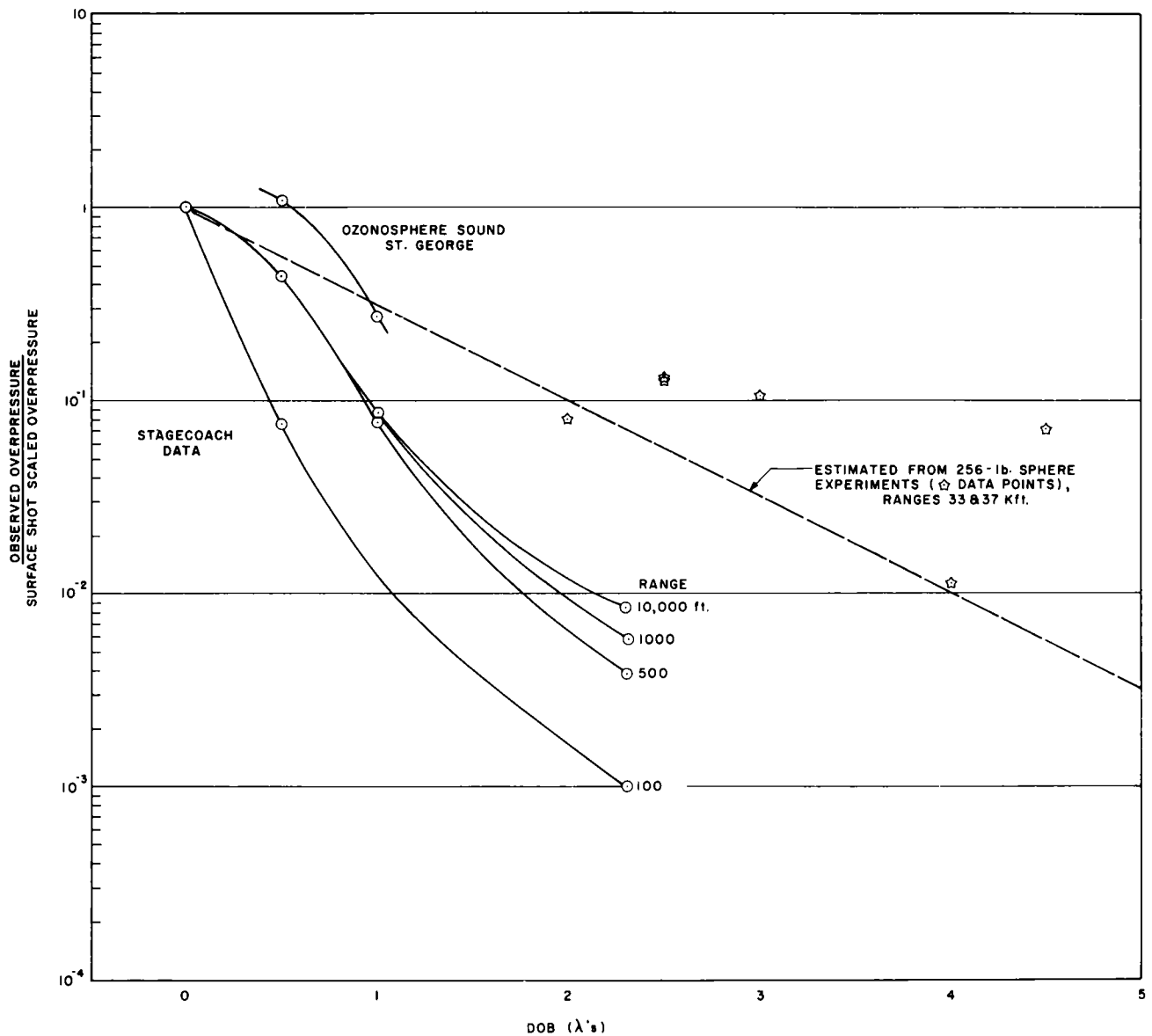
Fig. 9.19 Effects of charge burial on blast overpressures.

possible that weather conditions changed enough between surface and buried shot times to wipe out any real correlations. But by comparison with Stagecoach shots at 17 and 34 feet, with known weather stability, it seems that the 256-pound data are most likely to be in error.

At the present state of prediction capability, amplitude reduction by burial for ozonosphere signals, applied to cube-root-scaled 20-mt bursts for various directions referred to ozonosphere winds, gives pressures shown in Fig. 9.20. A sine-wave direction dependence has been assumed, with amplitude scaled from St. George recordings of full-scale tests.[5] This experience showed
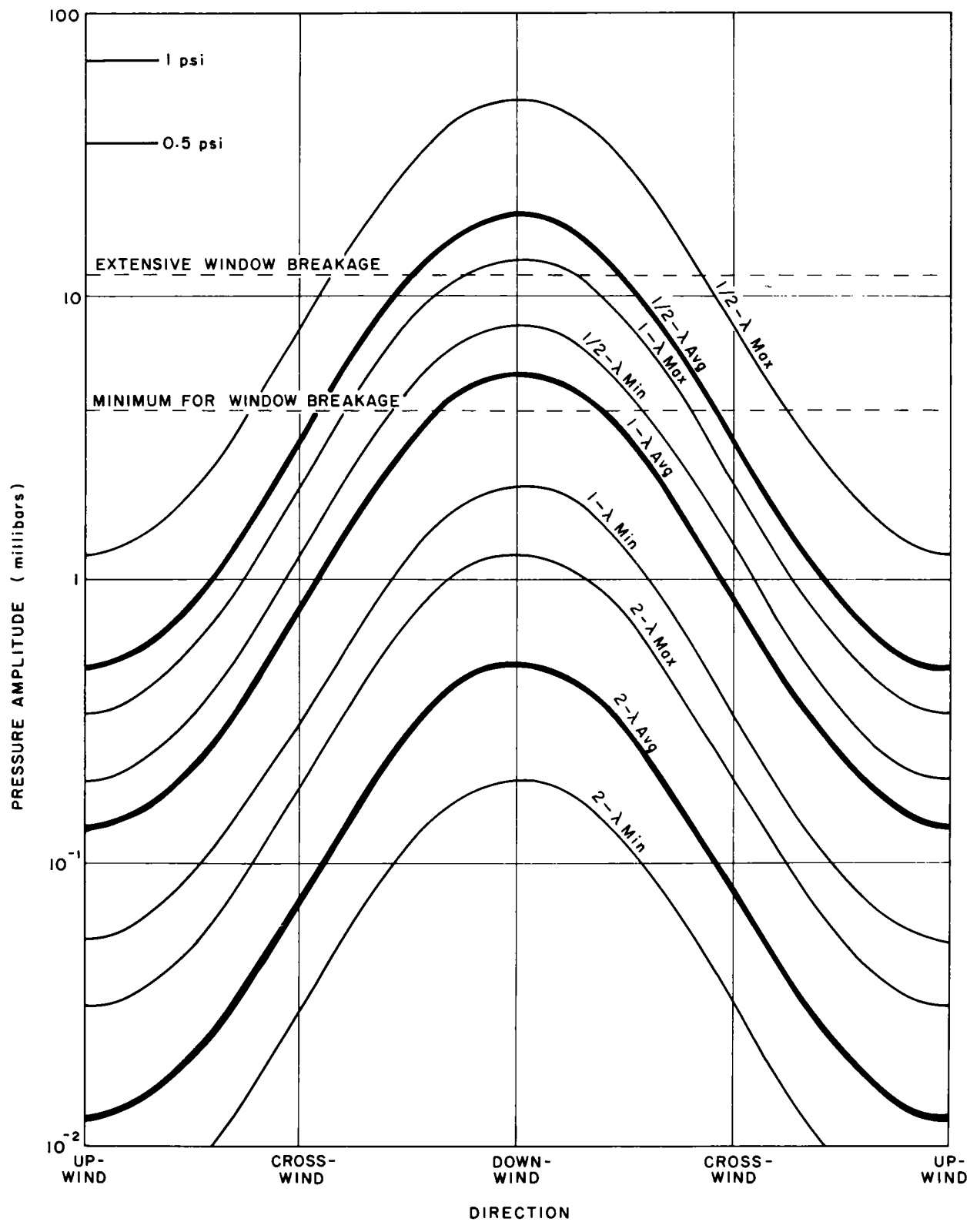
Fig. 9.20 Ozonosphere pressure amplitudes from buried 20-mt bursts.

that 20 kt would cause a 2-mb average amplitude downwind, 50-μb upwind, and a scatter range over factors from 0.4 to 2.5 times the average value. Thus 20 mt, burst on the surface or 0.5 ft/lb$^{1/3}$, would give a 20-mb average amplitude downwind on the first strike near 100 to 150 miles. This burst could break windows at up to 110 degrees bearing from downwind. At 1 ft/lb$^{1/3}$ DOB, 20 mt could break windows 70 degrees from downwind. Depth of burst at 2 ft/lb$^{1/3}$ should always be safe at any bearing. This pattern would vary in places where ozonosphere-level seasonal wind speeds are different from those in Nevada. Before this can be used for design-yield limitations, actual winds should be studied at an excavation site. Wind measurements are also necessary to show seasonal rotation or direction shifts which occur generally all over the world, on dates depending mainly on latitude.

9.5 ADDITIONAL ANALYSES OF OZONOSPHERE SIGNALS

A sound wave which has been turned over at high altitude by refraction returns to and strikes the ground at an incidence angle. Thus, multiple ground-level recordings make the wave appear to travel along the ground at a speed greater than local sound velocity. Following Snell's law for refraction,

$$\frac{V_i}{\cos \theta_i} = V_p = \text{constant,}$$

where V is sound velocity,[*] θ is elevation angle for a ray, and i subscripts define conditions at an altitude. The constant V_p is the horizontal projection of the wave motion vector. Apparently velocity of a wave between two spaced sound recordings on a radial from a shot equals this characteristic velocity. Sound velocity at maximum path altitude, where θ equals zero degrees, also equals V_p. Several methods can be used to find turnover height for a signal; the simplest seems to be shown by an empirical formula[2] for height:

$$h = D\left(0.865 - 0.789 \frac{D\Delta t}{t\Delta D}\right) .$$

---

[*]Sound velocity is sound speed, a function of temperature, plus the directed wind component.

For dual stations, D is shot-to-station distance, t is sound-arrival time, and Δ indicates interval in time or space between sensing heads. Thus each recorded sound from this project, which can be correlated between two stations on the St. George line, gives a point value for altitude and east-directed sound velocity.

Ozonosphere signal recordings for March 25 firings are reproduced in Figs. 9.21, 9.22, and 9.23. Apparent or characteristic velocities for the various signals on the three Stagecoach dates were measured to give sound velocity-height points shown in Figs. 9.24, 9.25, and 9.26. An approximate average curve is drawn through each data group. Rocket winds from Tonopah Test Range are shown on the left margin for the two dates of successful firings. East components of wind subtracted from east-directed sound-velocity curves leave a sound speed-height curve for comparison with standard atmosphere values.[6] Also, standard sound speeds plus east wind components give east-directed sound velocity for comparison with acoustic curves.

These curves show that temperatures and sound speeds are much closer to standard values than were found in previous acoustic experiments.[2,5] In past operations, several dual stations were operated in various directions from the test site. Atomic tests above ground always gave signals upwind. As a result, when mean velocity over all directions was taken for sound speed, it forced a considerably larger value than at ground level. Now it appears that, if standard upper temperatures are correct, upwind sound velocity must be much lower in the ozonosphere than at ground level, and it follows that refraction cannot cause observed sound propagation. Diffraction must have spread signals to ground, and our arguments against this explanation must have been in error. In fact, a brief review of NTS full-scale test data shows that upwind sound intensity does generally decrease, rather than increase, with distance, as it appeared from comparing Las Vegas with Boulder City records of Operation Plumbbob. It also appears that there may well have been strong northerly wind components giving real refracted signals at those two stations on dates when it was thought east winds were blowing to give upwind propagation toward southeast.

A complete recalculation of upper atmosphere conditions inferred from test blasts, using only downwind data points, is necessary. A refined analysis of upwind signals will allow better calculation of diffraction effects.
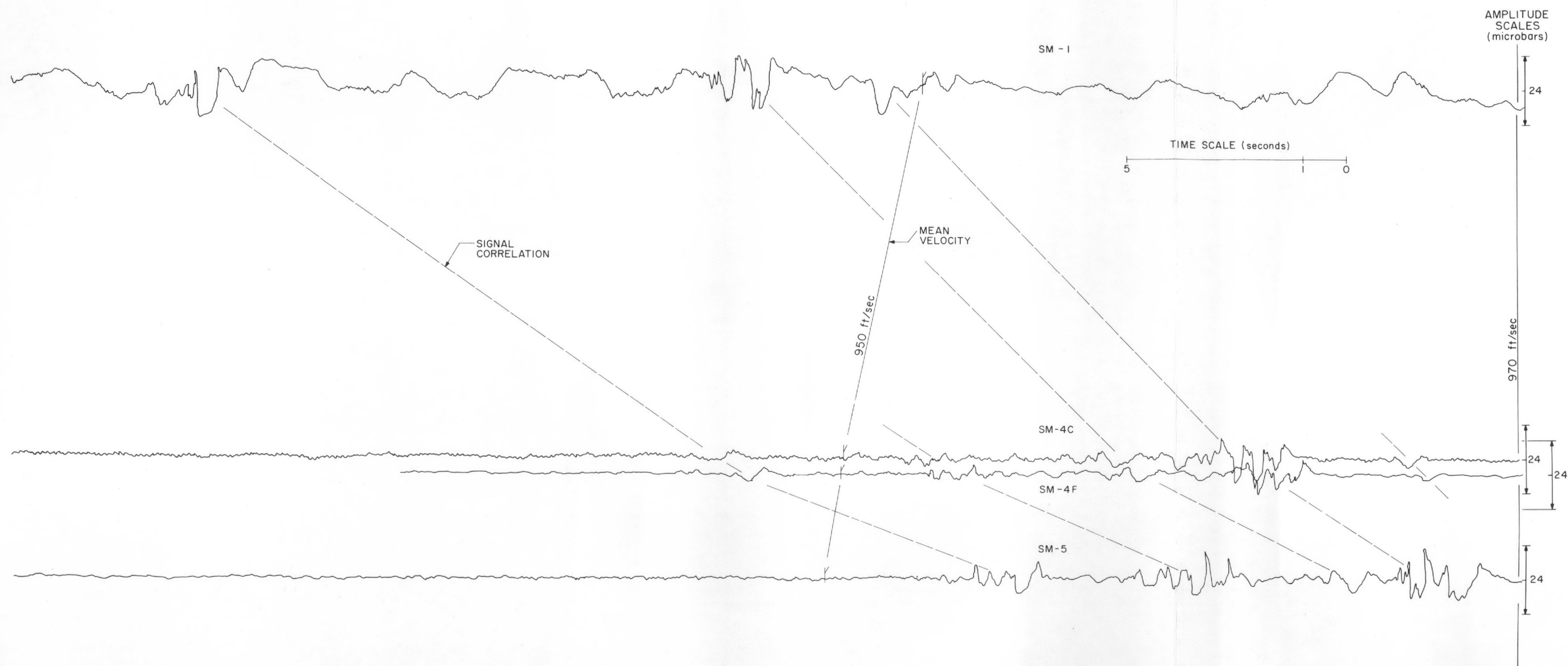
Fig. 9.21 St. George microbarograph recordings, 1.2-ton HE scaling shot, March 15, 1960.
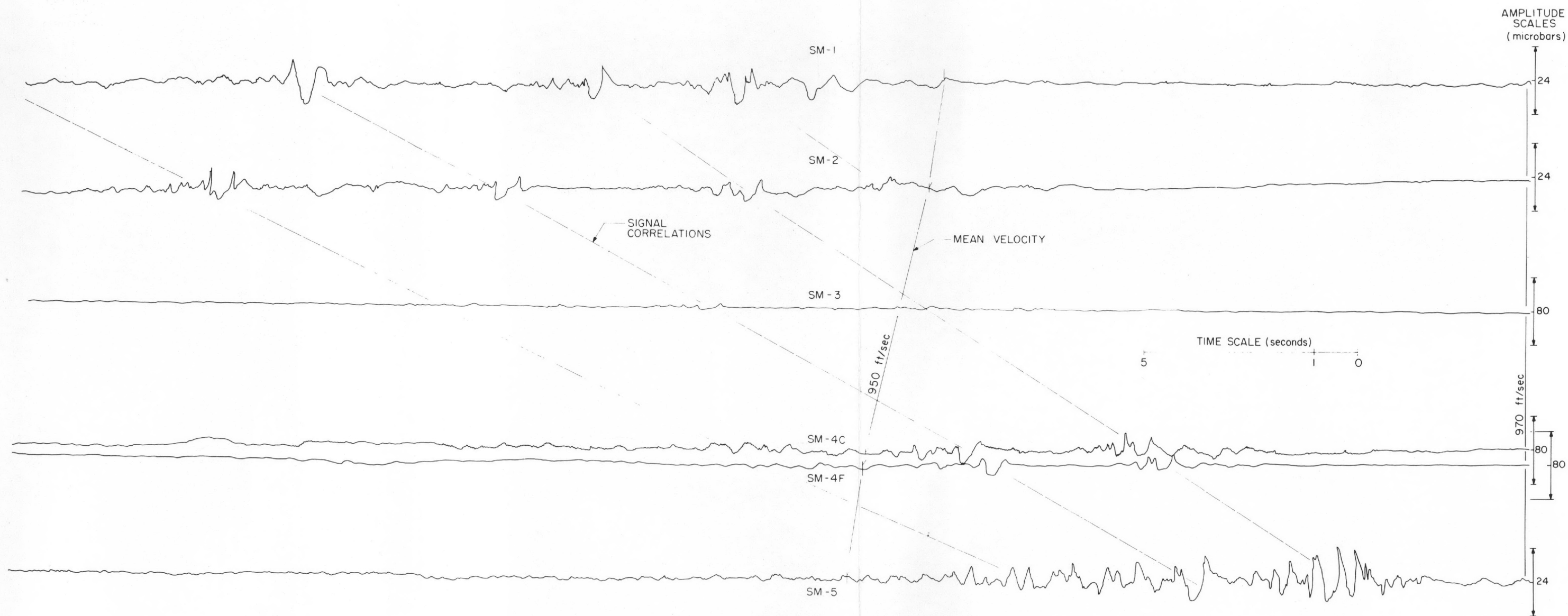
Fig. 9.22 St. George microbarograph recordings, 1.2-ton HE scaling shot, March 19, 1960.
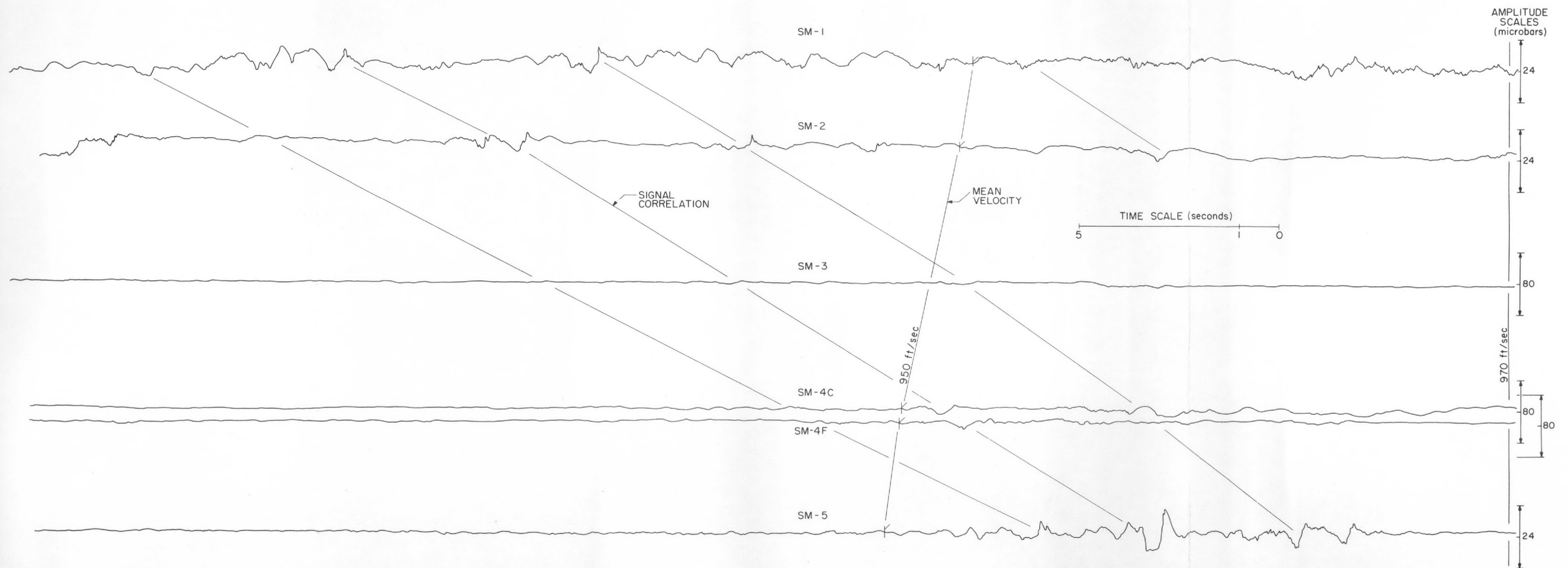
Fig. 9.23 St. George microbarograph recordings, 1.2-ton HE scaling shot, March 25, 1960.
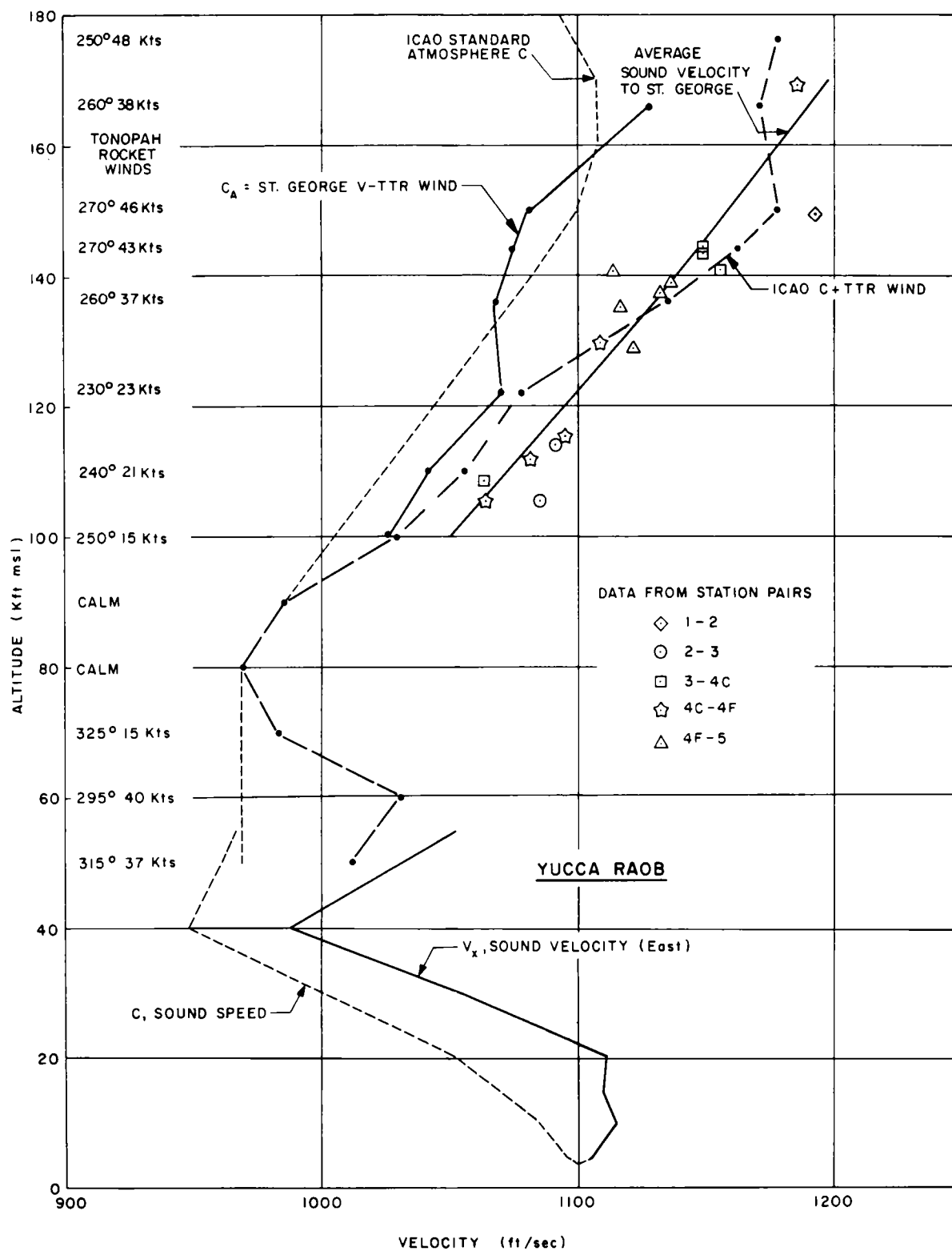
Fig. 9.24   Sound velocity-altitude measurements, March 15, 1960.
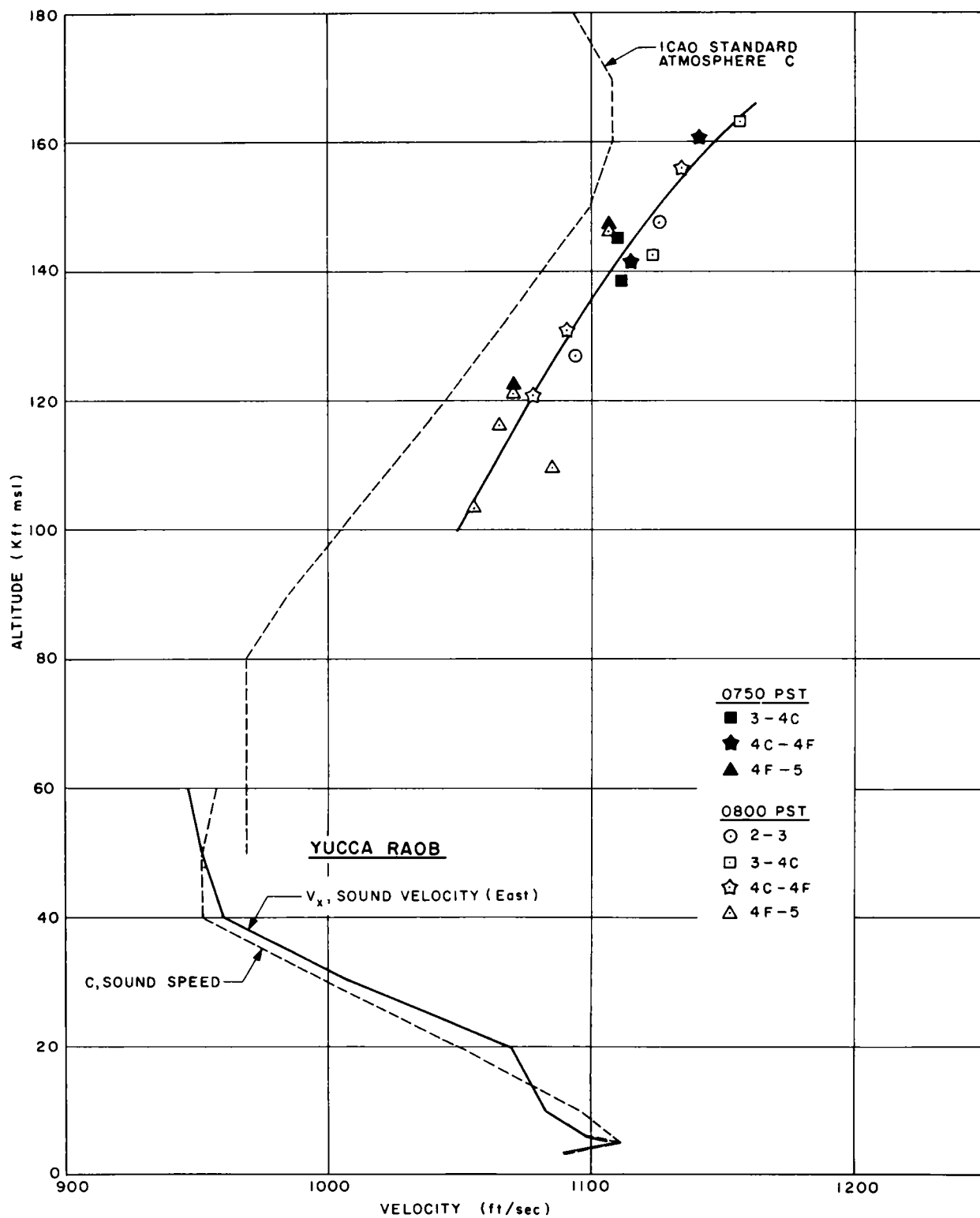
Fig. 9.25 Sound velocity-altitude measurements, March 19, 1960.
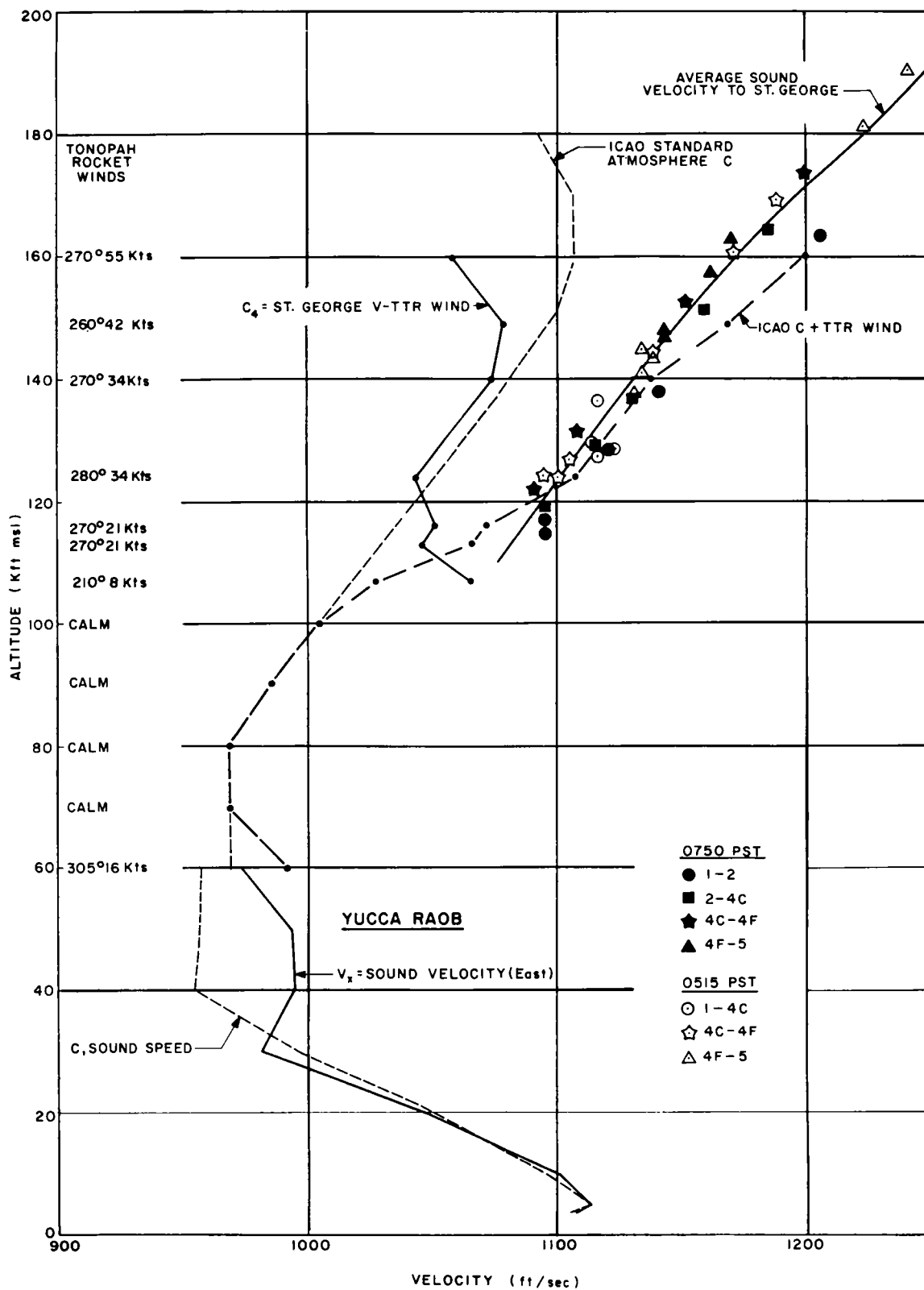
Fig. 9.26 Sound velocity-altitude measurements, March 25, 1960.

An IBM-704 program for calculating ray paths, times, and pressure ampli-
tudes has been used to make predictions for the St. George area from observed
weather data. Pressure-distance calculations for the 1.2-ton calibration shot
of the Stagecoach 80-foot shot, compared with observed signal amplitudes, are
shown in Fig. 9.27. The same comparisons for the Stagecoach shot at 34 feet
are shown in Fig. 9.28. (No rocket wind measurements were made on SC-2.)
Within limits of accuracy and weather variability, signal incidence angles and
arrival times agree with calculations.

There are generally smaller sound amplitudes landing than calculations
show, even with a high-altitude atmospheric attenuation factor of about one-
half having been applied. The main discrepancy is that several, often discon-
nected, waves are recorded, while usually only one wave and path are calculated
to land on each recorder. It thus appears that fine structure in the atmosphere
has broken the wave front into several segments. Each segment spread and landed
on the recording array, but at slightly different times and with reduced in-
tensity. This fine structure is also likely to be quite variable with time;
thus detailed pressure signatures are not repeated exactly, even with 10-minute
spaced shots. These small variations may not be so important in reducing am-
plitudes from large shots having long time durations and wavelengths. Also,
atmospheric attenuation, as calculated, has little effect in reducing amplitudes
from even 1-kt shots. In general then, it should be possible with rocket wind
data to make even more accurate ozonosphere blast predictions for atomic shots
than for 1.2-ton shots, with errors expressible in percent rather than as fac-
tors as previously given.

9.6 CONCLUSIONS

Nonuniform blast-energy distribution over early-time blast waves from
buried charges is maintained at great distances. Acoustic-level blast-pressure
amplitudes to 12 miles range are reduced from expected surface burst values of
44 percent for 0.5 $ft/lb^{1/3}$ DOB, 8.6 percent for 1.0 $ft/lb^{1/3}$, and 0.85 percent
for 2.3 $ft/lb^{1/3}$. At long range, in the ozonosphere sound ring, amplitudes
are raised to 108 percent for 0.5 $ft/lb^{1/3}$ DOB and reduced 28 percent for
1.0 $ft/lb^{1/3}$. However, 20-mt excavation bursts at 2 $ft/lb^{1/3}$ DOB should never
break windows where there is ozonosphere ducting. Burial at 1.0 $ft/lb^{1/3}$ will
allow window breakage only in directions with a downwind component in high-
altitude flow.
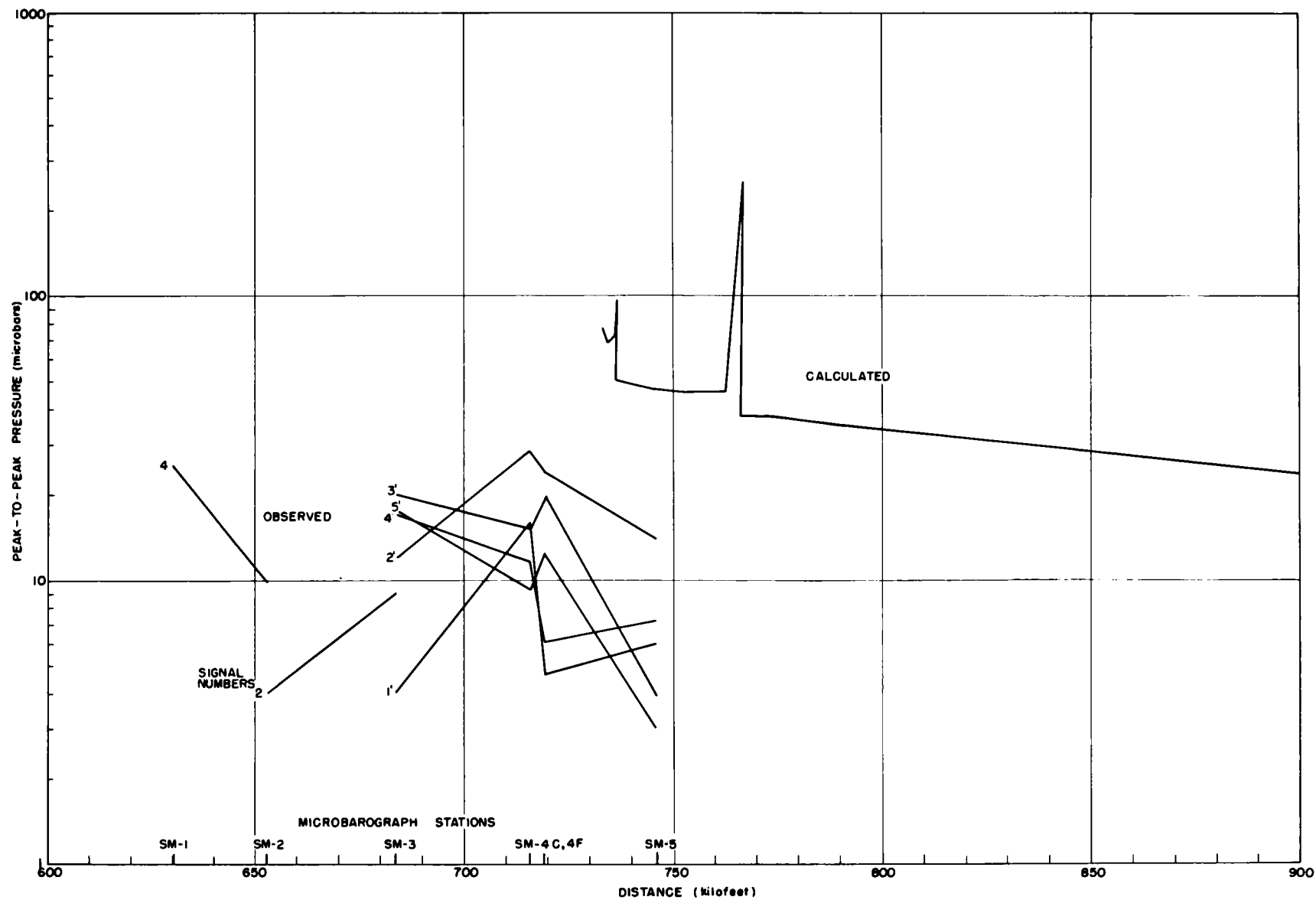
Fig. 9.27 Ozonosphere signal pressures, March 15, 1960.
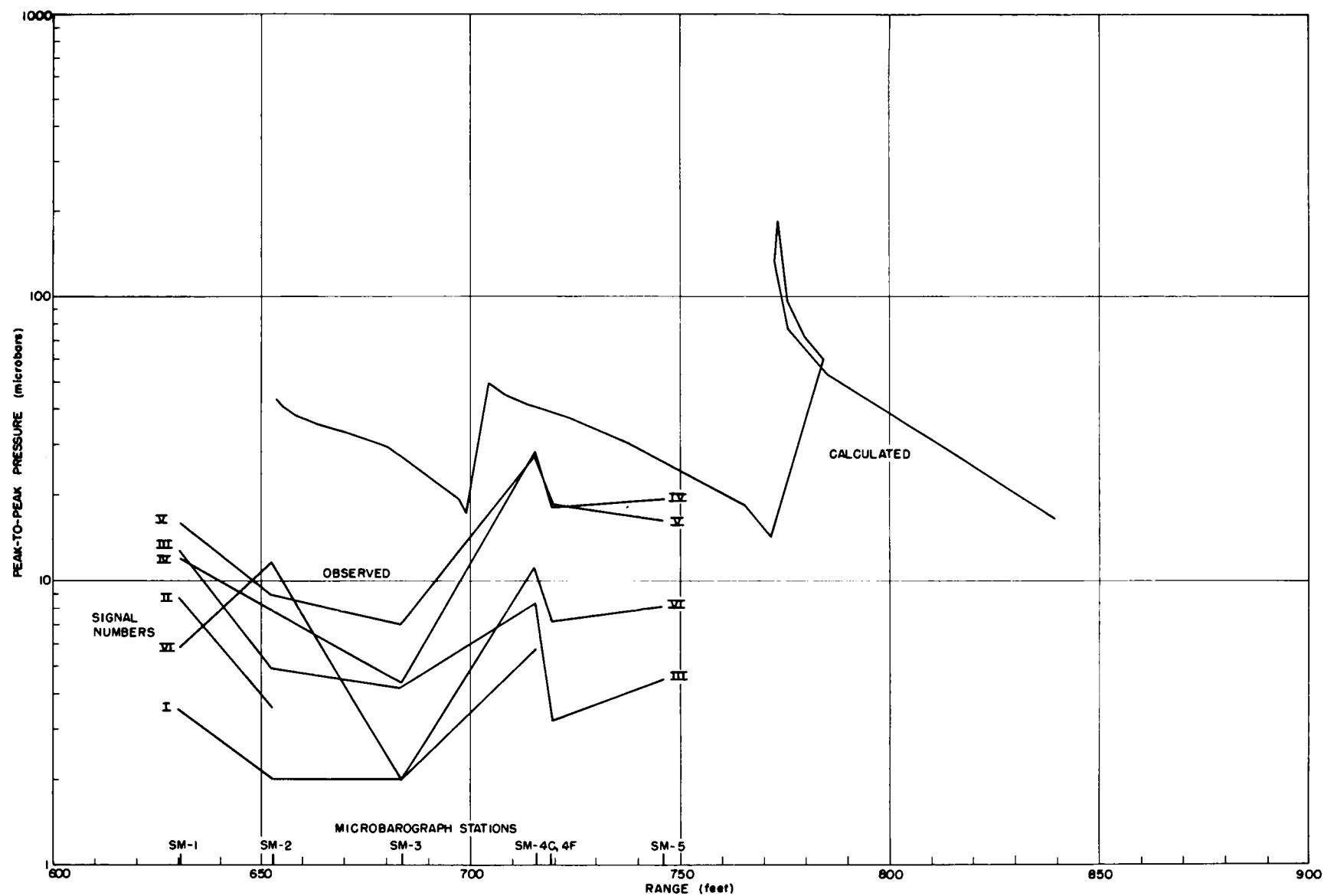
Fig. 9.28 Ozonosphere signal pressures, March 25, 1960.

Acoustic method upper-air sound-velocity data, used with rocket wind reports, show that ozonosphere temperatures agree fairly well with ICAO Standard Atmosphere values. Thus, sound-ranging upper-air data from past atomic tests was confused by diffracted signals recorded upwind from shot points.

Ray calculations for ozonosphere signal amplitude predictions can be satisfactorily made in Nevada from rocket upper-wind measurements and standard atmosphere temperatures.

9.7 RECOMMENDATIONS

(a) Microbarograph measurements should be made at similar ranges, from 2 to 150 miles, from more large buried explosions to refine burial attenuation coefficients as functions of both scaled depth of burst and burial material.

(b) Air blast measurements over the wave hemisphere from smaller HE crater shots should be made to define the early pressure field at more manageable distance ranges. Data to 50 feet from 1-pound HE's and 100 feet from 5-pound HE's should be gathered from above and around bursts with different depths of burst.

(c) Rocket wind measurements should be made in association with future blast microbarography to further check validity of ICAO Model temperatures in the ozonosphere, especially for different times of year and locations.

(d) Dual-station sound recordings of past NTS and PPG atomic tests should be reanalyzed to give upper-air temperatures and winds, correcting errors caused by upwind sound diffraction in past analyses.

(e) Fundamental blast propagation and absorption laws for truly great distances and small pressures should be investigated to find whether finite overpressure and yield or frequency effects are large enough to change assumed acoustic scaling rules for large shots.

REFERENCES

1. Sachs, D. C., and Swift, L. M., Underground Explosion Effects, Proj. 1.7, Operation Teapot, WT-1106, Stanford Research Institute, Menlo Park, Calif., March 1958.
2. Cox, E. F., and Reed, J. W., Long Distance Blast Predictions, etc., General Report on Weapon Tests, WT-9003, Sandia Corporation, Albuquerque, N. M., September 20, 1957 (SRD).

3. Reed, J. W., Long-Distance Blast Wave Attenuation by High-Explosive Charge Burial, Sandia Corporation, SCTM 312-59(51), September 21, 1959.

4. Smith, L. B., The Measurement of Winds Between 100,000 and 300,000 Feet by Use of Chaff Rockets, Journal of Meteorology, Vol. 17, No. 3, June 1960.

5. Reed, J. W., and Church, H. W., Observation and Analysis of Sounds Refracted from the Ozonosphere, General Report on Weapons Tests, WT-9005, Sandia Corporation, October 1959 (SRD).

6. Minzner, R. A., Ripley, W. S., and Condron, T. P., U. S. Extension to the ICAO Standard Atmosphere, ARDC-AFCRC-GRD, and U. S. Weather Bureau, Washington, D. C., 1958.

7. Reed, J. W. and Church, H. W., Preliminary Report on the Blast Unit Research Project, SCTM 33-60(51), Sandia Corporation, April 1960.

8. Byatt, W. J., and DeVault, G. P., An Iteration-Variation Method for Wave Propagation Problems, (SCDC-2225X), J. Geophys. Res., Vol. 66, No. 6, June 1961.

9. Broyles, C. D., IBM Problem M Curves, SCTM 268-56(51), Sandia Corporation, December 1, 1956.

10. Shreve, J. D., Jr., Pressure-Distance-Height Study of 250-Pound TNT Spheres, Operation Tumbler, WT-520, Sandia Corporation, March 13, 1953 (Conf).

Chapter 10

OFFSITE SEISMIC MEASUREMENTS by D. M. Hankins

No special instrumentation was provided for teleseismic data from the Stagecoach shots; however, signals were recorded at the U. S. Coast and Geodetic Survey station at Boulder City at an epicentral distance of about 170 kilometers. The USC&GS provided eight-power prints of these seismograms which were recorded on 35 mm film. Thus, the prints give ground-motion magnifications of 100,000 and 50,000, respectively, for the vertical and horizontal components. Analysis of the records was limited by relatively small signal-to-noise ratio and a broad trace width on most of the prints. Nevertheless, the records were digitized by means of a photoreader, after which Tukey power estimations were run on the IBM 704. For spectral analysis the record was divided into two time increments: (1) from the beginning of the P-wave to the beginning of the S-wave, and (2) from the beginning of the S-wave to the end of the discernible signal.

The time of arrival of the first discernible signal is about 30 to 31 seconds after shot time. Signal-to-noise ratio is too small to identify this time as a true travel time, but it does fix the first readable signal as belonging to the early part of the P-wave group.

All seismograms show maximum amplitude in the S- and surface-wave group to be larger than that in the P-wave group. Maximum peak-to-peak amplitudes in the P-wave group ranged from 20 to 50 mμ, while those in the S- and surface-wave groups ranged from 35 to 100 mμ.

Since the seismogram of vertical motion from the shot 2.3 ft/lb$^{1/3}$ allowed reasonably good resolution, the spectra from this shot are presented for illustration of the frequency content of the signals. Power spectra obtained by means of the Tukey Spectrum Estimation program have been multiplied by the length of record analyzed so that the ordinate in Fig. 10.1 essentially represents the sum of the square of amplitudes at a given frequency and is plotted against frequency. As plotted, the ratio of the S- and surface-wave curve to
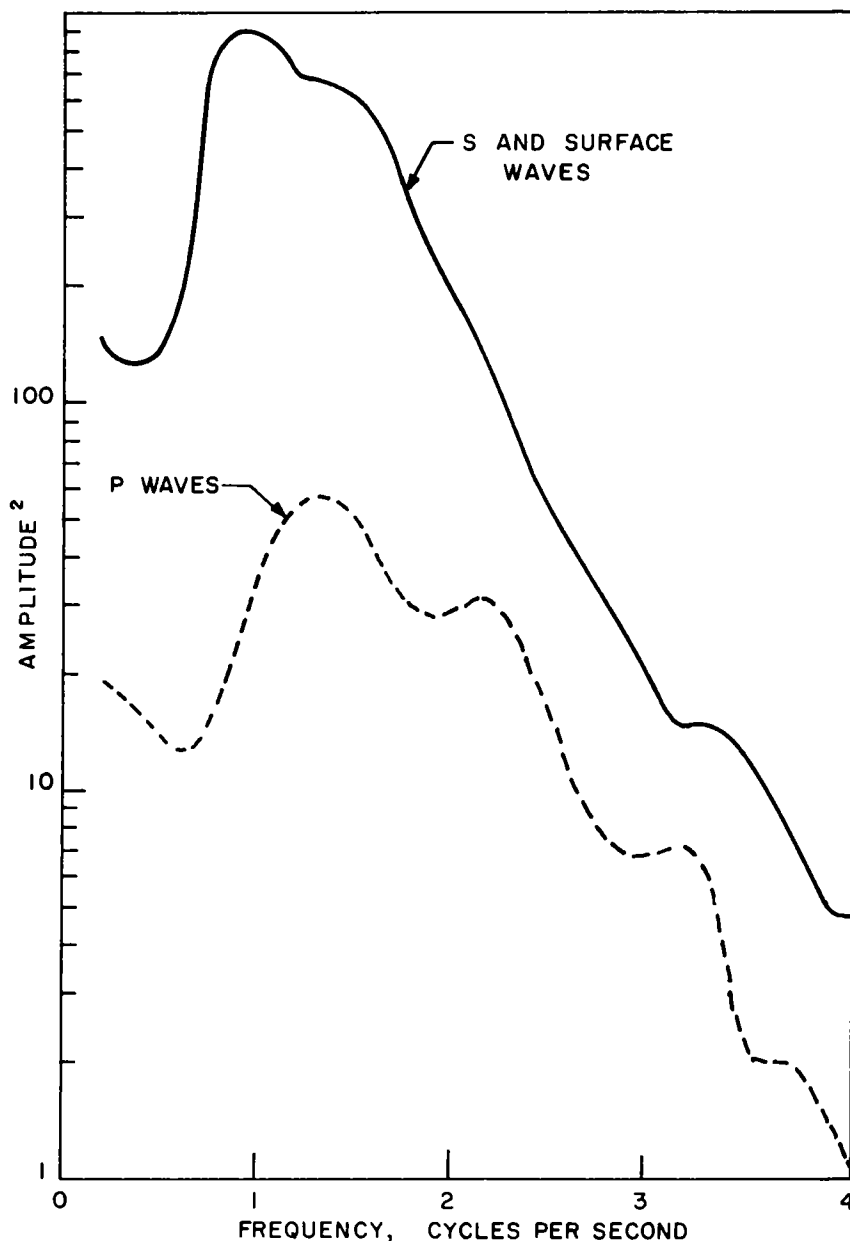
Fig. 10.1 Power spectrum times time for P-wave
group and S- and surface-wave group for vertical
component.

the P-wave curve represents the ratio of the sum of the squares of signals obtained before the arrival of the S-wave to those obtained after its arrival. Spectra from other components and other shots have the same character as those in Fig. 10.1. The spectral peak and total power in the signal from the shot at 2.3 $ft/lb^{1/3}$ were about 10 times those from the shot at 0.5 $ft/lb^{1/3}$ for the vertical component; however, the horizontal components do not show as much difference. The ratio of the maximum peak-to-peak amplitude for the vertical signal from the shot at 2.3 $ft/lb^{1/3}$ to that at 0.5 $ft/lb^{1/3}$ was 2.

Data are not sufficient to determine quantitatively the variation of seismic energy with depth of burst. It can only be concluded that an increase in scaled depth from 0.5 to 2.3 $ft/lb^{1/3}$ increases the seismic energy received at a distance of 170 km.

Chapter 11

MISCELLANEOUS CRATER OBSERVATIONS by L. J. Vortman

11.1 CRATER PROFILES

Figures 11.1, 11.2, and 11.3 show apparent crater profiles together with
profiles of the mounds and columns of the three Stagecoach shots. These pro-
files are made along an axis through the three shots from a viewpoint of 135
degrees azimuth. The axis is oriented 45 degrees east of north. The left
half of the profile as viewed thus (225-degree line) is folded over and plotted
with the right half of the profile (45-degree line). Target trajectories of
Figs. 3.6, 3.7, and 3.8 have been superimposed.

Although the field in which the Stagecoach shots were fired was not level,
the profiles have been corrected to a level terrain. The illustrations show
the mound at the time of venting and the growth of the mound into the column
base at given later intervals of time. Those times shown are 0.06, 0.1, 0.3,
0.6, and 1.0 second. The growth into the column is shown only for the 17- and
34-foot depth shots; no column developed on the deep shot. The profile shown
for that shot is at near the maximum height of the mound. For the 17-foot-
depth shot the radius of the mound at time of venting was much smaller than
the apparent crater radius. At the time of venting, the mound radius of the
34-foot shot was about equal to the apparent crater radius, and that of the
80-foot shot was considerably greater than the final apparent crater radius.

It is especially interesting to note in Figs. 11.1 and 11.2 that at any
given time the edge of the column is nearly the same for both shots in spite
of the differences in burst depths. Column profiles were not read beyond 1
second, since after that time material ejected out through the column surface
leaves a margin which can be only poorly defined.

11.2 CRATER CROSS SECTIONS

Fourteen months after the Stagecoach shots were fired, two trenches were
excavated through portions of each of the Stagecoach craters. Prior to shot
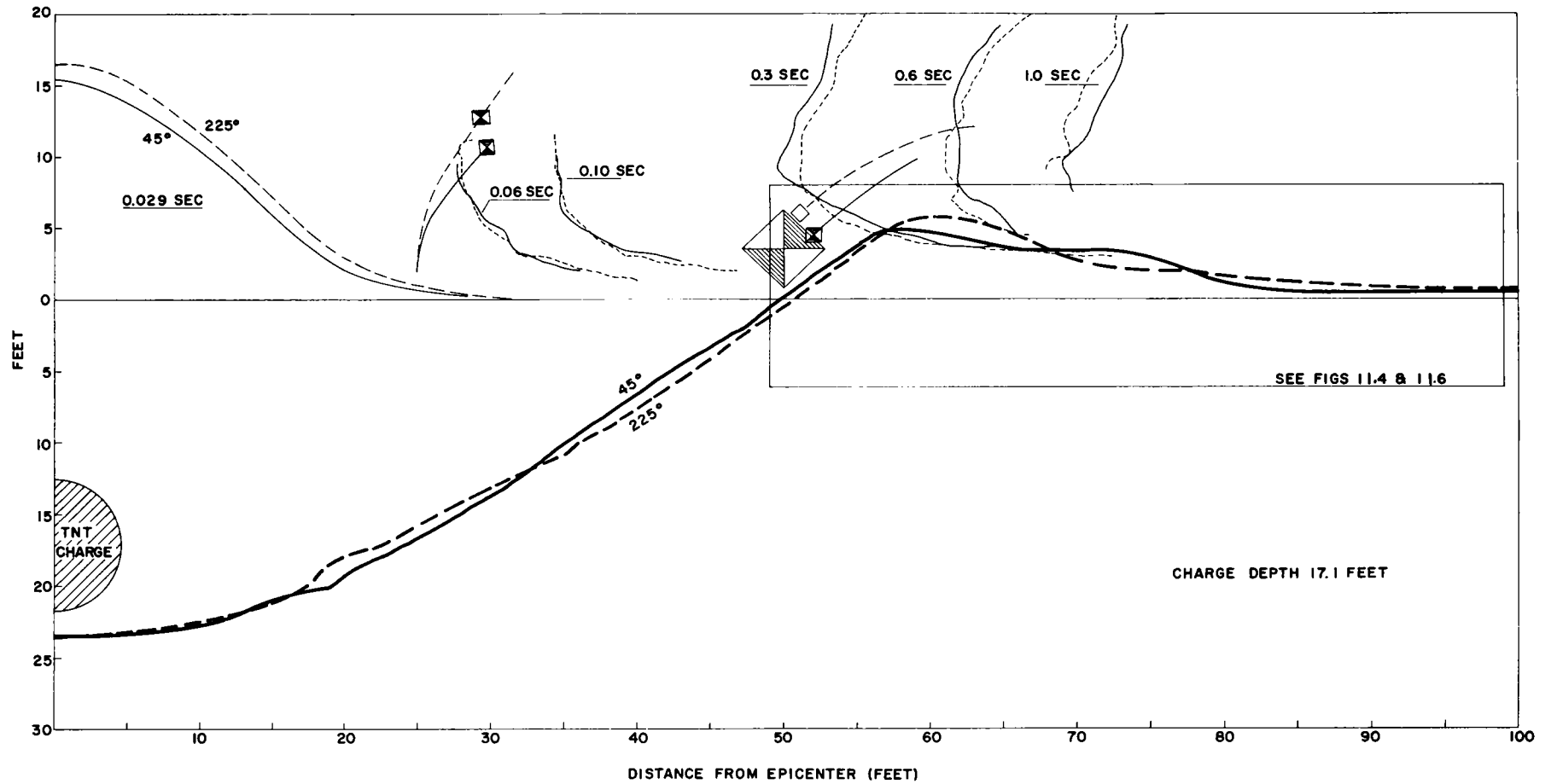
Fig. 11.1 Profile of the crater from a charge buried at 17.1 feet.
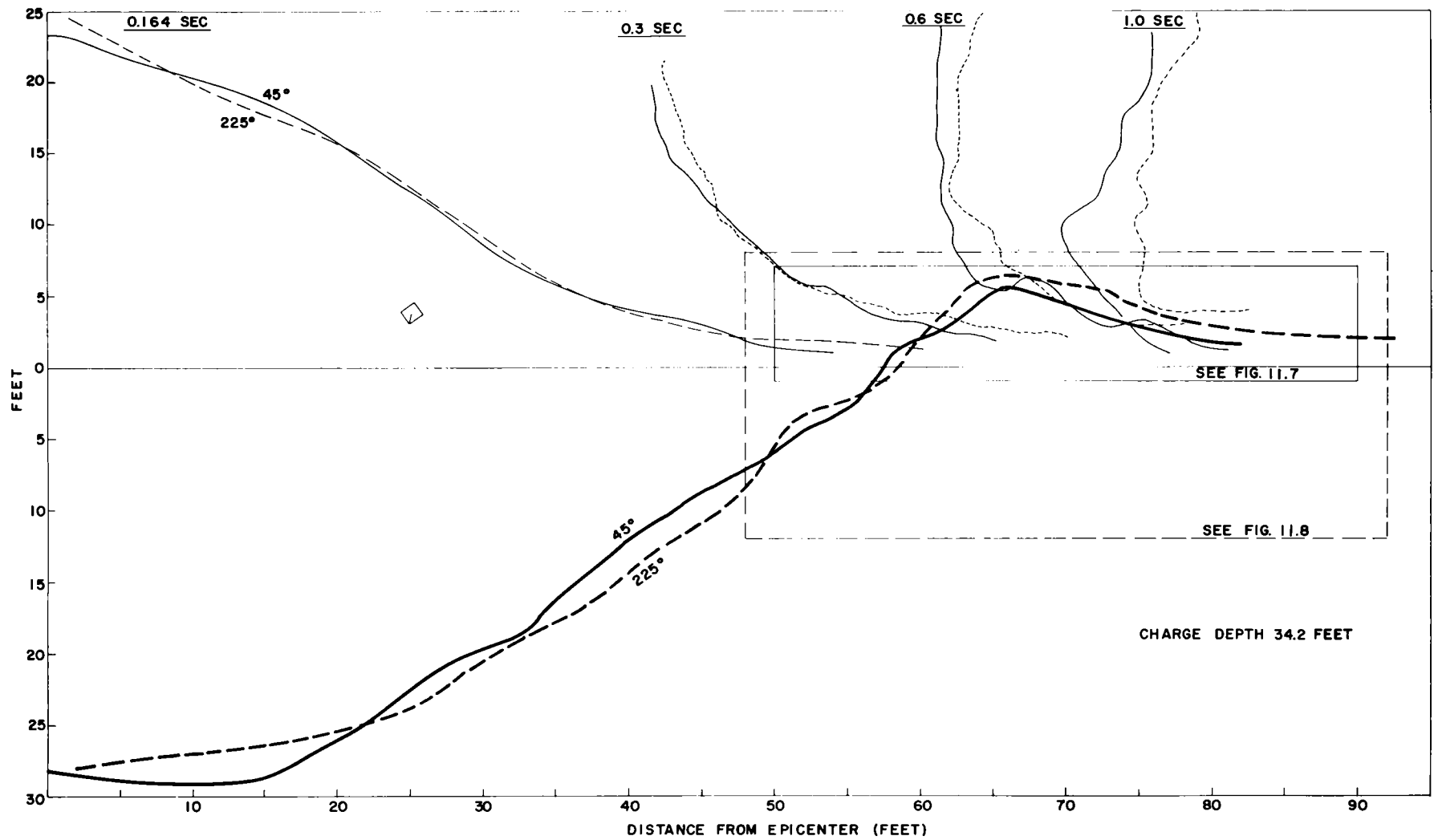
Fig. 11.2 Profile of the crater from a charge buried at 34.2 feet.
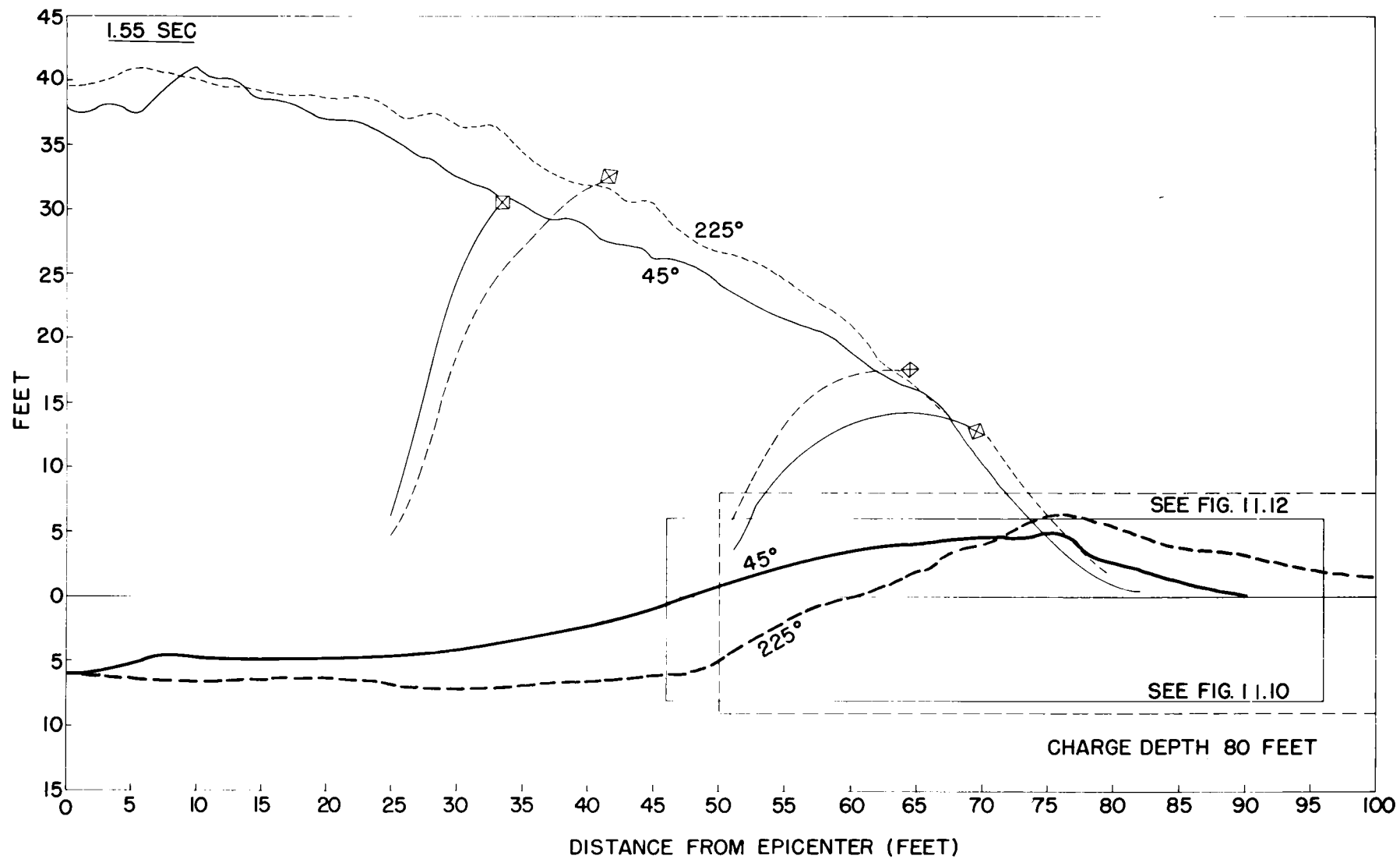
Fig. 11.3 Profile of the crater from a charge buried at 80 feet.

time, an oiled strip had been placed on the 45-degree azimuth radius of each crater. Wooden posts were placed in a row in the center of the oiled strip. (See photographs, Figs. A-2 through A-7, Appendix A.) One ditch was dug parallel to the oiled strip, cutting through the strip, thus permitting the oil to be used to identify the original ground surface. The other ditch was dug on the opposite side of the crater. The center line of the latter ditch was the 225-degree azimuth radius of the crater. Depths of the trenches varied to as much as 15 feet below the original ground surface within the crater, sloping up to only a 4-foot depth at the greatest distance from the center of the crater. The trench was nominally 10 to 12 feet wide. The top edges of the excavation at the greatest distance from the crater remained about 10 or 12 feet apart because of the stability of the material. The amount of caving of the side of the trench increased as the crater was approached, and the widest part of the trench usually occurred at the high point of the crater lip where the top of the excavation might be three times as wide as where the material was stable.

As regions of the crater were identified, their locations of specific points were determined in three dimensions. Though a point was located several feet along the circumference of the crater from the axis at 45 or 225 degrees, the locations have been plotted as though they were located along the axis.

Two distinct regions were readily identifiable. The first of these was the ground surface. Along the 45-degree trench, the ground surface on one side of the trench was readily identified as the oil strip. On the opposite side of the trench, and on both sides of the 225-degree trench, the ground surface was readily identifiable from vegetable fibers which had originally grown downward from the ground surface. The second identifiable feature was the layers of caliche which had been deposited in such a way that they were approximately planar. While their original position was not precisely known, excavations out to nearly two crater radii reached a region where the material had been essentially undisturbed. The principal layer of caliche was located at depths varying from 3.3 to 8 feet below the original ground surface. In only one trench was a deeper caliche layer found at 13 to 13-1/2 feet. This layer was observed only once, since the bottom of the excavation usually was filled rather quickly with loose material from the sides. Results of the excavation are shown below.

Charge Depth: 17.1 Feet

45° Line (Fig. 11.4). The excavation showed that fallback material at
a depth of 16 to 18 feet below the ground surface along the apparent crater
boundary was an extremely fine dust.

Caliche was noted at the edge of the crater only. Talus from the sides
of the trench prevented its identification elsewhere in the trench and a de-
termination of its _in situ_ depth. It is this upturned layer of caliche rising
above the original ground level from its deeper position and frequently pierc-
ing the surface of the apparent crater which appears in the vertical photos
(Figs. A-2 and A-3, Appendix A) as a ring below the crater lip. Thus, while
the ring within the crater lip as shown in the photographs is an indication
of true crater, it does not represent the original ground surface but, rather,
a layer which probably lies between 3 and 3-1/2 feet below the surface.

Surface profiles are nearly the same for both sides of the trench. There
is an interesting overthrust at between 64 and 65 feet which is shown in detail
in Fig. 11.6. The overthrust results from compression of the material at the
ground surface when the caliche layers were folded upward and back.

225° Line (Fig. 11.6). A most interesting feature is the foldover of the
caliche on the southeast side of the trench. It is of interest that the origi-
nal ground surface was identified at 61 feet in spite of the nearby foldback of
the caliche, whereas, on the opposite side of the trench, it was identified
only in to 67 feet. On the southeast side, however, it was impossible to iden-
tify the original ground surface between 68 and 78 feet, and the material in
that region appeared crushed.

Charge Depth: 34.2 Feet

45° Line (Fig. 11.7). Here again the natural depth of caliche layer was
not determined, but across the crater, along the 225-degree line, it was be-
tween 3-1/2 and 4 feet deep, and therefore must have been near that depth along
the 45-degree line.

An overthrust appears at between 69 and 72 feet, similar to that described
for the preceding crater. In this case, both layers of the oil strip were
clearly definable. The gaps shown between 60 and 75 feet represent regions
where the surface could not be positively identified or where the region
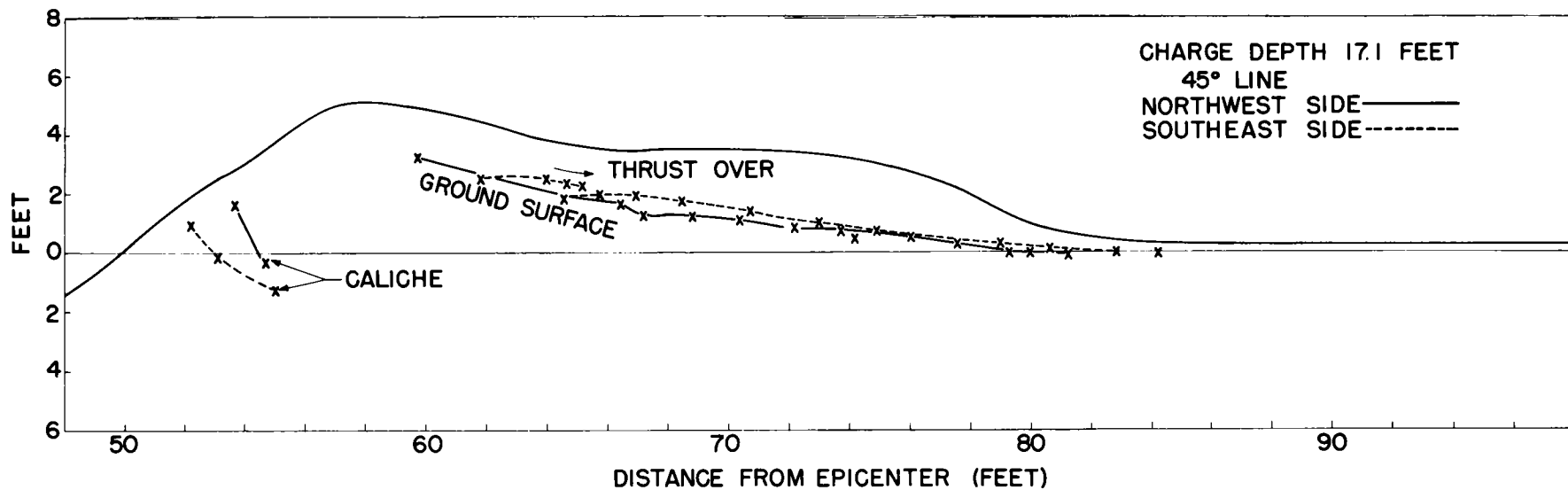
Fig. 11.4 Profile through the crater lip from a charge buried at 17.1 feet, 45° line.
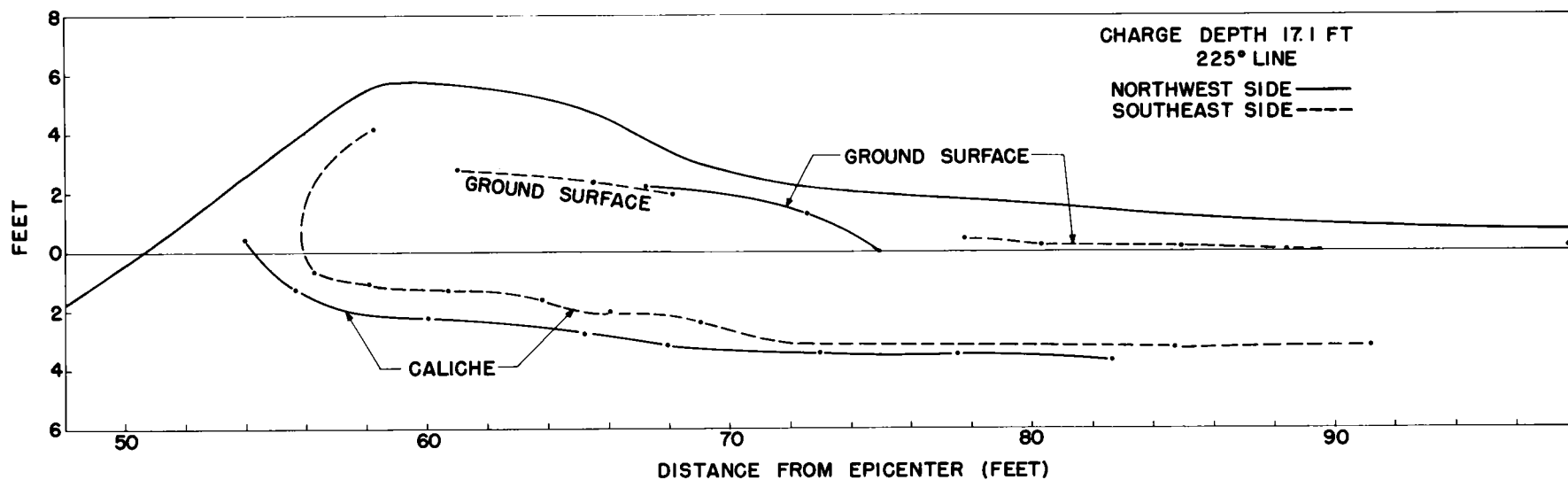
Fig. 11.5 Crater lip profile from a charge buried at 17.1 feet, 225° line.

Fig. 11.6 Detail of overthrust.

CHARGE DEPTH 34.2 FEET
45° LINE
SOUTHEAST SIDE ——
NORTHWEST SIDE ----

OVERTHRUST

GROUND SURFACE

CALICHE

DISTANCE FROM EPICENTER (FEET)
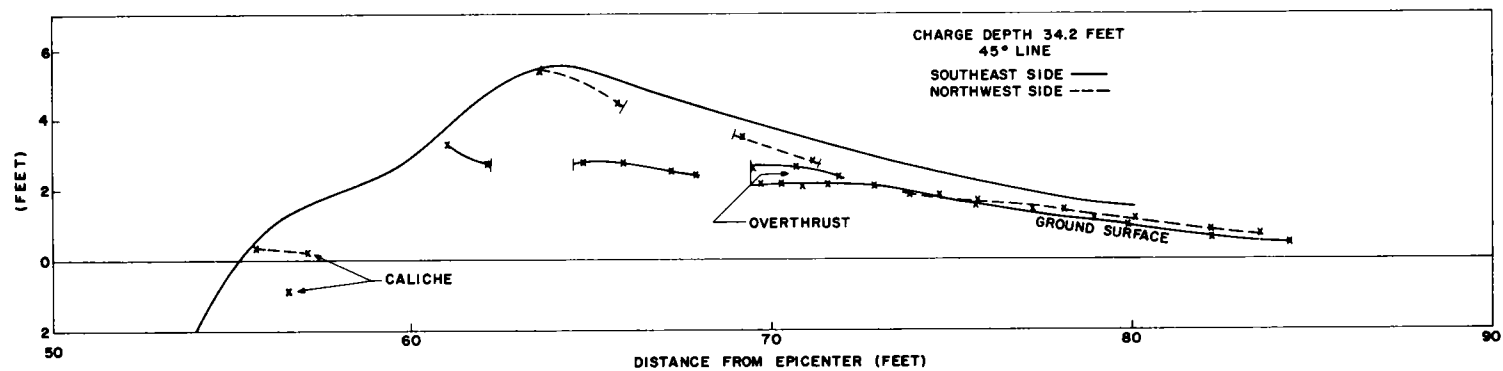
Fig. 11.7   Crater lip profile from a charge buried at 34.2 feet, 45° line.

CHARGE DEPTH 34.2 FEET
225° LINE
SOUTHEAST SIDE --------
NORTHWEST SIDE ————

GROUND SURFACE

CALICHE

CALICHE

EDGE OF
TRUE CRATER

DISTANCE FROM EPICENTER (FEET)
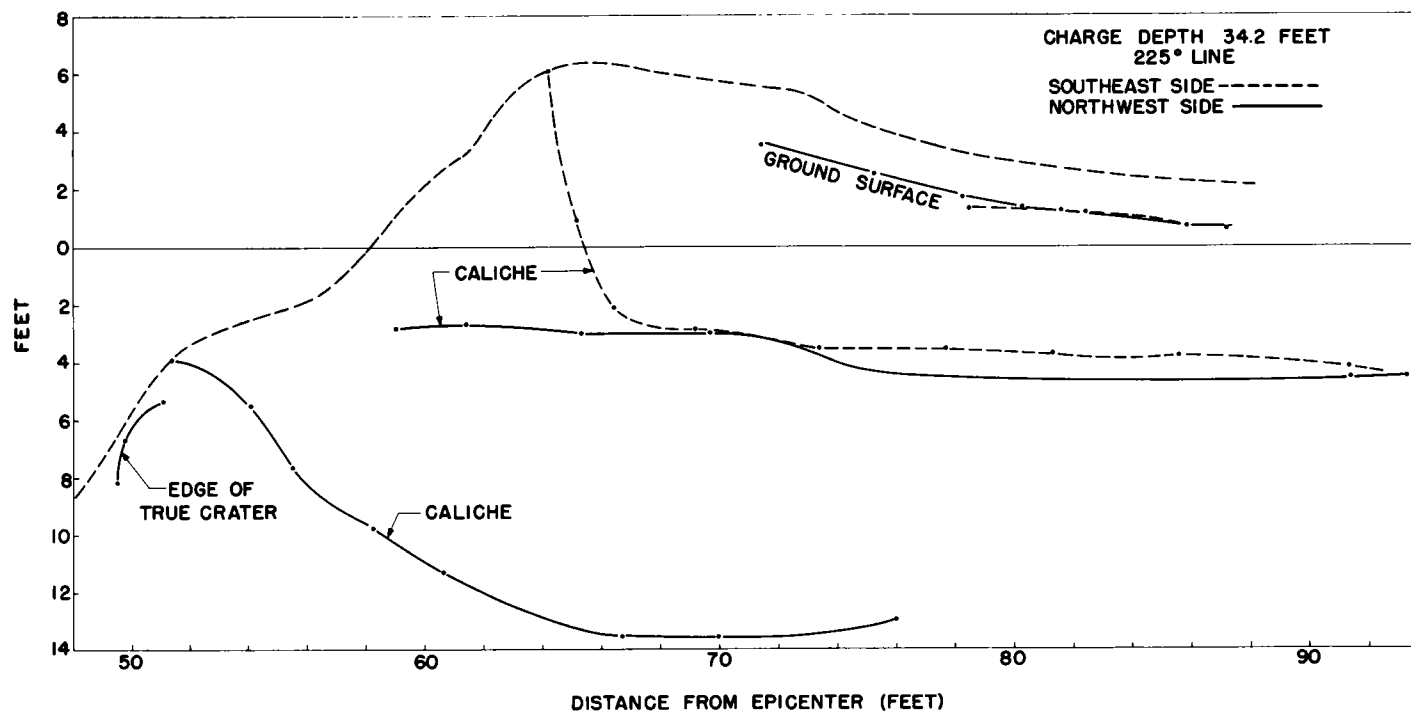
Fig. 11.8   Crater lip profile from a charge buried at 34.2 feet, 225° line.

appeared compressed or crushed. On both sides, the surface could be identified
at the crater edge. These edge sections, however, were isolated by crushed and
disturbed regions where the boundary was not clear. There was no crushing or
major disturbance which prevented surface identification beyond 74 feet. Iden-
tification of surface material so close to the edge of the apparent crater is
in marked contrast to that on the opposite side of this same crater and to that
of the crater previously discussed, where no surface material was found in the
crater lip nearly so close to the crater edge.

Charge Depth: 34.2 Feet

225° Line (Fig. 11.8). Note the sharp contrast to the profile on the 45-
degree line of the same crater.

Figure 11.8 illustrates the only case of excavation deep enough to permit
identification of the deep caliche layer. Because of talus on one side of the
trench, it was possible to observe this layer only on the northwest side. The
layer was thrust up nearly 10 feet above its normal depth of 13-1/2 feet. This
caliche layer was not as distinct as the shallower layer.

Note in the illustration the manner in which the shallower caliche layer
on the northwest side was raised only about 2 feet, slightly less than was the
deeper layer at a point directly below. It should also be noted that these
layers were badly crushed, although still identifiable only because caliche
crushed less easily than the surrounding material. By contrast, the southeast
side shows the same caliche layer folded sharply upward at the crater edge.
This can be seen in the photograph in Fig. 11.9. These two caliche layers
best demonstrate the great difference between the same layer as found on oppo-
site sides of the excavated trench. It points up clearly the asymmetries which
may occur within 20 to 30 feet along the circumference of the crater.

The surface on both sides of the trench was easily identifiable to the
distance shown. On the southeast side, it was badly crushed between the
caliche layer and the first surface point identified.

Charge Depth: 80 Feet

45° Line (Fig. 11.10). Note particularly the shear zones in the region
from 70 to 74 feet. This region is shown in Fig. 11.12. The material outside
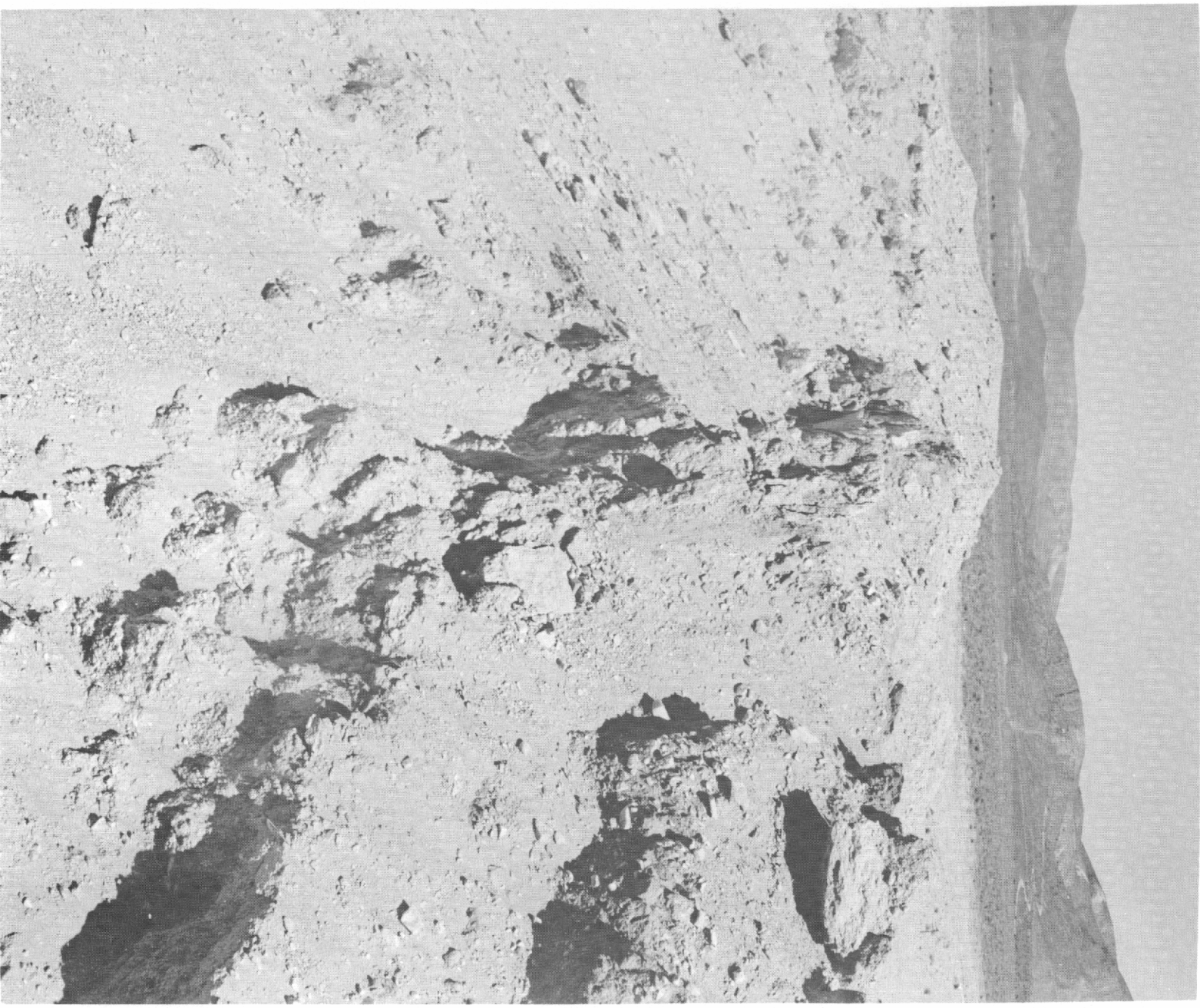
Fig. 11.9 Detail of the upthrust at crater lip.
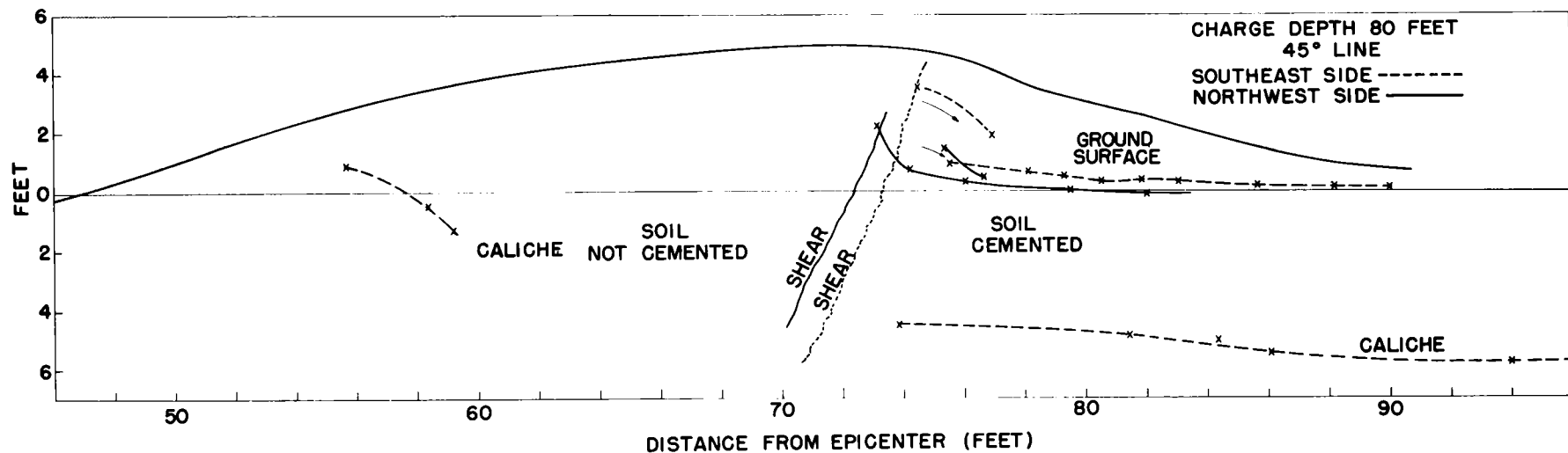
Fig. 11.10   Crater lip profile from a charge buried at 80 feet, 45° line.
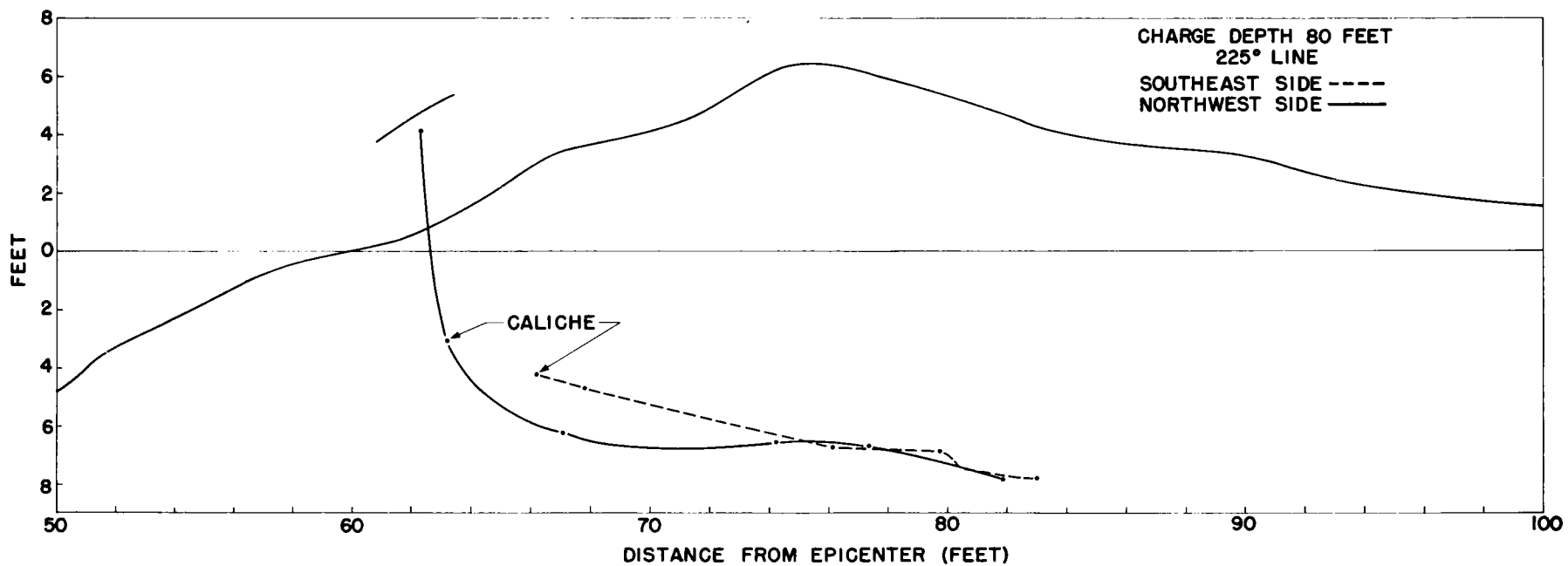
Fig. 11.11   Crater lip profile from a charge buried at 80 feet, 225° line.

Fig. 11.12 Detail of shear zone in crater lip from a charge buried at 80 feet.

the shear zone (to the left in the photograph) was quite stable and the side of the trench stood vertically. The region within the shear zone had no integrity. Strata which were intact and identifiable sloughed off with the first touching or disturbance of the region.

The caliche layer shows a gradual rise toward surface zero until a region near the shear zone is reached. One portion of the caliche layer was identifiable within the shear zone. At 75 feet, where the permanent displacement of this layer was about 1-1/2 feet, Fig. 11.3 shows a transient displacement of nearly 5 feet.

The surface also shows a gradual rise toward surface zero. Each side shows possible thrustovers. That for the southeast side is shown in the upper left quadrant of Fig. 11.12.

225° Line (Fig. 11.11). The high point on the northwest side requires an explanation. The profile of the crater is the center-line profile. The high point occurs because, at a point 16 feet away, the crater is 4 feet higher than the center-line profile. On that side, it was possible to identify the caliche layer all the way to the apparent crater surface, even though in that region it had been badly broken. Further evidence of asymmetries in regions 10 to 15 feet apart are shown in the different heights to which the caliche layers were raised. No information is shown on the original ground surface, since that surface was not identifiable.

Center. The firing circuit conduit was located 1-3/4 feet due north of the vertical axis through the charge. Postshot, its location was 2-1/2 feet from the axis on a N25°30'E bearing. Thus, the surface zero point shifted only a distance of about 1 foot.

11.3 CONCLUSIONS

The three Stagecoach craters were not cylindrically symmetrical. This lack of symmetry occurs in the true crater as well as in the apparent crater. The number of these asymmetries apparently increases with scaled burst depth. There has been considerable evidence in the past of variation or scatter in crater dimensions. Presented here, however, is evidence of scatter in dimensions and variations in shape within a single crater.

In the region where the mound or the base of the column joins the ground surface, there is evidence of compressive failure and overthrusting of the surface layers.

There will be no permanent vertical displacement of the ground surface beyond 1-3/4 crater radii. The ground surface remains continuous, rising gradually toward surface zero until about 1-1/2 crater radii. Closer than this point, the surface is crushed and broken. The caliche layer between 3 and 8 feet had no permanent vertical displacement beyond 1-1/2 crater radii for the shallower shots and 1-3/4 crater radii for the deep shot. It was possible to identify the caliche layer or some portion of it between 1 and 1-1/4 crater radii.

In several cases the caliche layer folded up to or just beyond the vertical, and the surface layers were over thrust. In no case was there a complete foldover of the surface layers as observed by Shoemaker[1] in the Teapot Ess and Arizona meteor craters.

REFERENCE

1. Shoemaker, E. M., Penetration Mechanics of High Velocity Meteorites, Illustrated by Meteor Crater, Arizona, Report of the International Geological Congress, XXI Session, Norden, 1960, Part XVIII, Copenhagen, 1960, p. 418.

Chapter 12
OPERATIONS by R. J. Burton, V. A. Harris, J. R. Heaston and
H. R. MacDougall

12.1 INTRODUCTION

Engineering, construction, and operational phases of Sandia's participation in Project Stagecoach are discussed in this chapter. Methods used in these experiments are detailed for guidance of field engineers who may be in charge of similar future experiments.

Although it is difficult to establish a standard set of rules for the planning, construction, and operation of high-explosive tests, some problems are common to all large-scale HE detonations. Presented here is the method used for three detonations in Project Stagecoach. Participants in the test, in addition to Sandia, included Naval Ordnance Laboratory (NOL), Ballistic Research Laboratories (BRL), Suffield Experimental Station (SES), and Boeing Airplane Company.

12.2 ENGINEERING AND DESIGN

Project Stagecoach was instituted by a request that three 40,000-pound HE detonations be conducted at various depths in desert alluvium at the Nevada Test Site (NTS) for the purpose of gathering data on cratering effects. A budget estimate of $275,600 was prepared for the project which is outlined in Table 12.1.

Construction of the detonation sites was originally planned to include casing and cavity umbrella design, since a preliminary soil analysis made by a subcontractor indicated that such structures would be needed to support a mass of noncohesive soil. Field tests made later by Holmes and Narver, Inc., showed that the soil was cohesive enough to permit substitution of a much lighter type of framing. Design and construction of these lighter structures reduced estimated construction costs by approximately $50,000. Further savings were realized by an increase in efficiency of HE loading; instead of three individual A-frames, each with its own pulley and hoist, a single

TABLE 12.1 STAGECOACH COSTS

Period Ending March 31, 1960

Item	Estimate	Obligated by Purch. Reqn.	March 1 costs	March 31 costs	Incurred costs not charged	Total
Engineering	$ 41,000					
Holmes and Narver, Inc.		$ 35,000	$ 19,582	$ 29,115	$ 3,000	$ 32,115
Construction	120,700					
Reynolds E. and E. Co.		100,000	71,805	82,481	--	82,481
Generators		5,000	0	1,122	--	1,122
Buckslip		5,000	2,463	4,222	--	4,222
Support	11,000					
Gage calibration, BRL		1,500	0	0	1,500	1,500
REECO Vehicles		5,523	5,523	5,523	--	5,523
HE handlers		8,760	0	4,521	--	4,521
MB technicians		16,500	4,461	14,424	--	14,424
Vehicles		10,000	4,187	5,053	3,000	8,053
MB vehicles		7,500	163	3,763	--	3,763
Contingency	17,100					
Subtotal	$189,800	$194,783	$108,184	$150,224	$ 7,500	$157,724
Sandia costs	85,800					
Material costs						
Field wire		1,092	0	0	1,092	1,092
TNT		11,800	7,790	7,790	3,010	11,800
Oscillators		5,225	0	0	5,225	5,225
Sources		3,500	0	0	3,500	3,500
Boosters, TNT		1,157	1,157	1,157		1,157
Pans		30	30	30		30
Salary			18,495	26,860		26,860
Overhead			17,550	25,500		25,500
Travel			5,913	10,658		10,658
Subtotal	$ 85,800	$ 22,804	$ 50,935	$ 71,995	$12,827	$ 84,822
Total			$159,119	$222,219	$20,327	$242,546
Total budget	$275,600					
Total costs	242,546					
Unobligated bal.	$ 33,054					
Engineering		$ 32,115				
Construction		87,825				
Support		37,784				
Subtotal			$157,724			
Sandia Costs			84,822			
Total			$242,546			

hoisting unit was constructed and mounted on a low-bed trailer so that it could be moved from site to site.

Construction plans were prepared by Holmes and Narver, Inc., who also surveyed locations for all instrumentation, photographic, and operational stations (Figs. 12.1 and 12.2). After aligning the three zero points on a north 45-degree east bearing and establishing local coordinates, the Holmes and Narver survey teams ran an instrumentation line on a true south bearing from each zero point. These directions were chosen primarily because they were the most advantageous for good photographic coverage in the early morning. Balloon and instrument positions which were dependent upon these bearings were determined at zero times by taking photographic profiles of the instrument-supporting balloons from two directions about 90 degrees apart. The survey teams also located, staked, and marked ground pressure-gage locations along the instrumentation lines. Targets were located in line with and adjacent to zero points as aids in photographic coverage. Survey work on location of radiation pellets and throwout collection pans is outlined in following sections.

Holmes and Narver subcontracted the job of preshot and postshot aerial surveys to American Aerial Survey Company of Covina, California. These provided Sandia with highly accurate contour maps of the area before and after detonations. A contract was negotiated with Reynolds Electrical and Engineering Company (REECO) for digging and backfilling the holes. Sandia Corporation assumed responsibility for handling HE at the site.

12.2.1 Site Location and Preparation

Stagecoach shots were to be detonated at depths of 80, 34.2, and 17.1 feet, respectively, in the same medium in which nuclear shots had been fired, so that comparative data on the two types of detonation could be obtained. The land in Area 10 slopes gently downward from east to west between the roads. The firing line along the north 45-degree east bearing could be adequately observed from an existing 35-foot steel tower about 6500 feet east of ground zero (GZ). On the basis of information gained from previous HE shots made in that area, holes for the Stagecoach detonations were spaced 600 feet apart along the firing line to prevent overlapping of craters or throwout. An area 1800 feet long and 600 feet wide (300 feet on each side of the firing line)

was lightly graded to remove underbrush and other possible obstructions to photography. A fence 200 feet in diameter, made of wooden posts and rope, was built around each GZ. A trailer was located at the gate of each area to control visitors during HE loading operations. The 200-foot diameter was considered a minimum safe distance for uncontrolled operations in view of the remote possibility of accidental detonation resulting from operation of radio transmitters.

Wooden 4- by 4-inch posts were spaced on a line from each GZ at 103, 137, 171, 205, and 274 feet (Fig. 12.3). An oiled strip 3 feet wide (1-1/2 feet wide on each side of the line of posts) was laid down on the graded surface to provide a plane of demarcation to define accurately the depth of throwout material caused by the detonation. To minimize dust disturbance to cameras, the area was wetted by a water truck over a 200-foot diameter around each GZ just before detonation.

12.2.2 Excavation and Casing of Chambers

During excavation for the three Stagecoach shots, soil density tests were made at designated intervals as shown in Fig. 12.4. (See also Table C.2, Appendix C.) Results of these tests were used to restore backfilling in the holes up to 95 to 100 percent of the original undisturbed soil density.

A timber A-frame equipped with a 2-speed electric hoist, a 3/8-inch cable, and a small bucket was used by the contractor for excavation. For loading the HE, a separate hoist and generator were mounted on a flat-bed trailer to enable them to be easily moved between sites (Figs. 12.5 through 12.8). Dimensions of the skip bucket were large enough to allow room in the shaft for the air ducts, sand chute, and ladder. The skip for lowering the HE was essentially a wooden shell over a frame of 1/2-inch steel rods. A door in the shell prevented the HE blocks from falling out, and a cover was added for personnel protection. The skip was guided in the shaft by shoes on the car which rode over 2- by 6-inch wooden guides mounted vertically in the shaft. Controls were mounted in the cab of the skip as well as at the surface, and a limit switch prevented the skip from being pulled all the way to the head frame. Magnetic brakes were provided on the hoist to prevent the skip from falling free in case of power failure.

Fig. 12.1 Location plan.

Fig. 12.2 Gage locations and footings.

PROFILE
NO SCALE

STA. 1003.03

STA. 1003.02

STA. 1003.01

GRADE 4322.1'

GRADE 4331.2'

GRADE 4341.6'

6.0' MIN. ABOVE GRADE
3.0' MIN. ABOVE GRADE
8.5' MIN. ABOVE GRADE
4.25' MIN. ABOVE GRADE
6.0' MIN. ABOVE GRADE
3.0' MIN. ABOVE GRADE

92.6'
136.8'
171.0'
205.2'
273.6'
NOT TO SCALE

17.1'
34.2'
79.0'
4262.53'

FOR DETAILS THIS AREA
SEE STRUCT. DWG. 010-1003-S1
(TYP. 3 PLACES)

4 X 4 POSTS 4'-0" O.C.

PLAN
SCALE: 1" = 100'

1800'
600'
300'
600'
600'
300'

STA.1003.03
N 879,212.07
E 683,712.07

STA.1003.02
N 879,636.23
E 684,136.23

STA.1003.01
N 880,060.39
E 684,560.39

8' X 16' BACKDROP (TYP.)
FENCE

FOR WINCH TL'R & FAN
SEE DWG JS-010-1003-M1
4 X 4 POST (TYP.)

FENCE - SEE NOTE No 3 (TYP.)

10' WIDE OILED STRIP (SEE NOTE 2)

181.0' (TYP.)

N 45° E

TO MOBILE CAMERA STA.
1200' S 45° E

BACKDROP
(3 REQUIRED)
DETAIL
SCALE 1" = 4'

16'-0"
8'-0"

PLYWOOD 1/2" THK. DOUGLAS FIR EXT. GR.
2 X 4 BLOCKING
TWO COATS FLAT BLACK

NOTE: LOCATED 20' FROM G.Z.

Fig. 12.3 Plan section and detail.

GENERAL NOTES:
1. SHADED AREA (600'x1800') TO BE BLADED FOR REMOVAL OF UNDER BRUSH
2. THREE STRIPS (10'x181') ARE TO BE SPRAYED WITH A HEAVY COATING OF ROAD OIL, MC-2 OR MC-3 -.3 GAL PER SQ. YD.
3. FENCE TO BE 200' DIA. CONST. OF 4"x4" WOOD POSTS 10'-0" C-C 4' ABOVE GRADE - STRING 3/4" MANILA ROPE BETWEEN, AT 18" & 36" HEIGHTS, AT ACCESS ROAD PROVIDE ROPE GATE 20' WIDE WITH SAFETY BELT FASTENERS, PROVIDE PLYWOOD SIGN 12"x26" TO HANG ON GATE TO READ "HIGH EXPLOSIVES BEING LOADED" IN RED LETTERS.

REFERENCE DRAWINGS
CIVIL 010-1003-C1
STRUCT JS-010-1003-S2
ELECT 010-1003-E1
MECH. JS-010-1003-M1
CIVIL JS-010-1003-C1 & C2

REVISIONS				
NO.	DATE	DESCRIPTION	CH'K'D	APP.
	12-17-59	REVISED STA No'S (01 WAS .03 .01 WAS .01) CHANGED DEPTHS TO ACCESS. REVISED DWG. REF. WAS 011-51 ADD 4x4 POST DEPTHS 1003.01		
	1-21-60	ADDED FENCES - NOTE 3 - REV DWG REF		
	2-10-60	REVISED MOBILE CAMERA STA. LOCATION CALLOUT FOR .01 & .03		
	4-12-60	AS BUILT-CORRECTED STA, ELEV'S. & BACK DROP LOC.A.		

I.D. 940906   USER APPROVAL

U. S. ATOMIC ENERGY COMMISSION
ALBUQUERQUE OPERATIONS OFFICE

HOLMES & NARVER, INC.
ENGINEERS — CONSTRUCTORS
A. E. C. FACILITIES DIVISION
849 SO. BROADWAY   LOS ANGELES 14, CALIFORNIA

CRATER EXPERIMENT-HE
PLAN SECTION & DETAIL
STA. 1003 01-02-03   AREA 10

DRAWN
CHECKED
APPROVED, H. & N.   S. E. Woods
DATE 12-8-59
SITE NTS

DRAWING NO.
010-1003-C2

Fig. 12.4 Soil density testing. Photos show Holmes and Narver personnel performing this work under typical field conditions.

Fig. 12.5 Explosives delivery van. Van is backed up to unloading platform at right. Left are tractor and low-bed trailer on which are mounted mobile hoisting drum and steel frame support. Second photo shows packaged explosives in cardboard cartons stacked on pallets inside van. Note blocking arrangements.
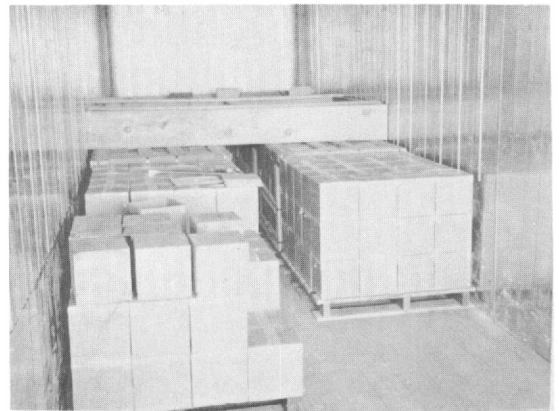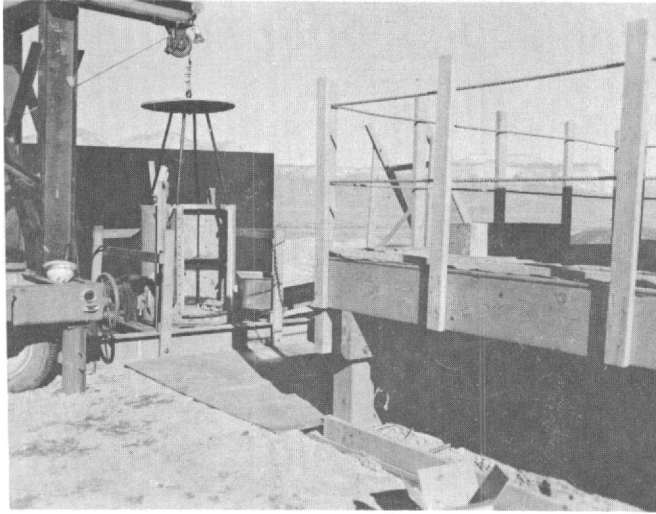
(a)
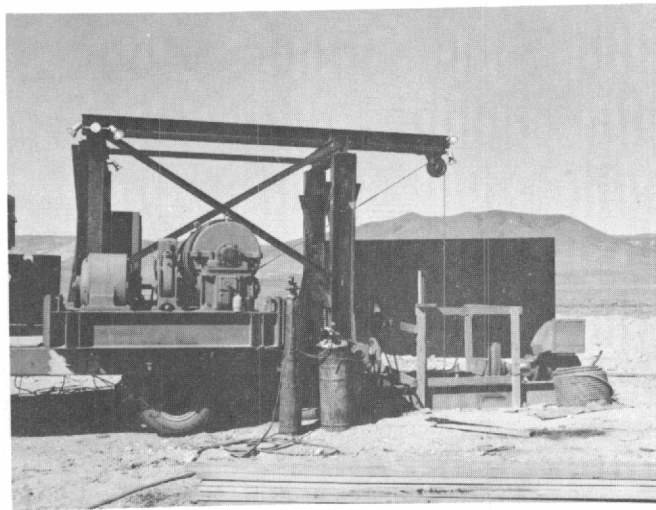
(b)
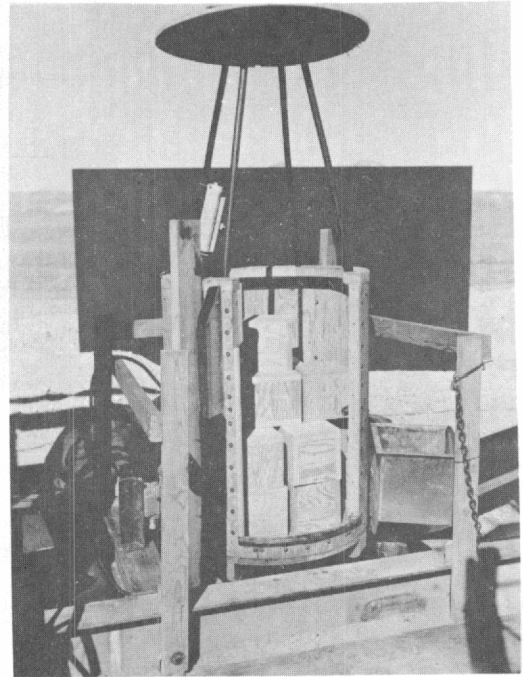
(c)

Fig. 12.6 Explosives handling equipment. Photos show (a) unloading platform, (b) hoist drum, and (c) lift cage. Photographic backboard is shown in background.
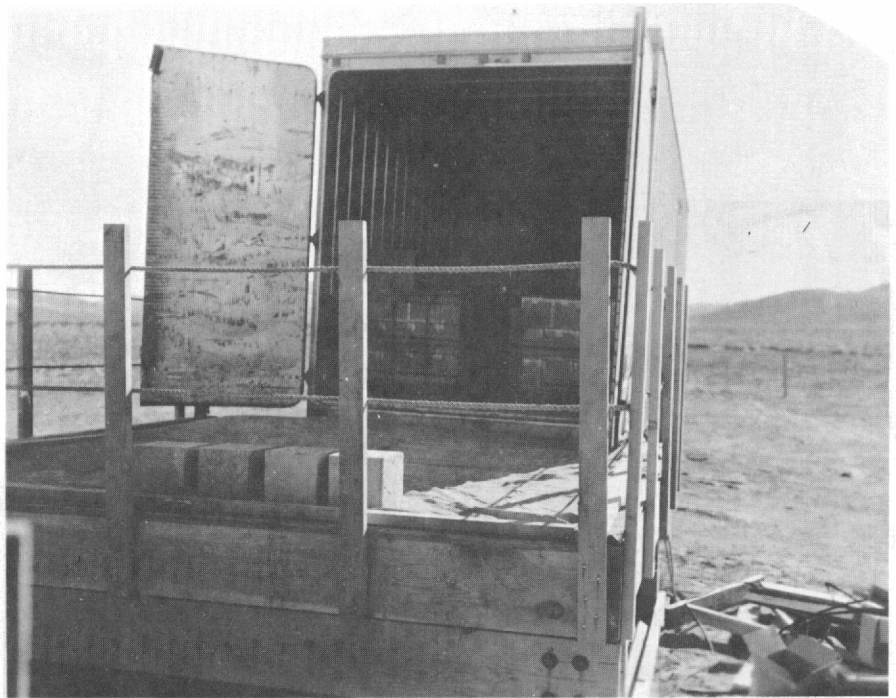
Fig. 12.7 Blocks of explosives on unloading platform. A 2-man crew was normally sufficient to unpackage individual blocks to be loaded on lift.

Fig. 12.8 Explosives lift cage. Steel and wood support structures were periodically removed as loading progressed.

The HE cavities were excavated to a bell shape at about 20 degrees from the vertical to allow working space around the edge of the stacked HE which had a circumference of 10 feet. To meet safe mining practices, corrugated steel segments, prefabricated on a 48-inch diameter with 3-inch internal flanges bolted together, were used in the Stagecoach excavations (see Fig. 12.9). A cavity umbrella was secured to the bottom of the shaft casing, and the entire mass was supported on the ground by a steel H-frame.

A sound-powered nonsparking telephone provided communication between cavity and surface. The cavity was illuminated by one large-wattage bulb set in an explosion-proof fitting. The entire electrical system was grounded through a series of rods driven into the ground and soaked with a saline solution. A grid of under-surface wires connected the rods in the area around the shaft opening and the hoist equipment. Ground wires were connected to all hoist equipment, ventilation machinery, sand chute, and shaft casing on the surface. Ground bus wires were taken down the shaft, and all sections of the casing, as well as the sand chute and the electrical conduit, were grounded.

Ventilation for the cavity was provided by a suction system which pumped air out of the cavity, causing fresh air to be pulled down the shaft. Air was completely changed every 3 minutes. Stale air was expelled at the surface through a filter system which removed any HE dust.

The sand used to fill the space around the HE stack as it was being built was supplied to the cavity through a lightweight pipe from the surface. A flexible neoprene tube on the end of the pipe allowed the sand to be directed to the desired location in the cavity. Since the cavity was larger than the HE sphere, a considerable amount of sand was required to fill the space around the blocks and to fill the space occupied by the shoring which was removed as the cavity became filled. In future tests of this type, an endeavor should be made to control the cavity size in order to minimize the magnitude of the sand backfilling.

When the cavity was completed, a 3/4-inch plywood platform, 6 feet square, was placed on a bed of sand to level and support the HE sphere. To support portions of the sphere not seated directly on the platform, wooden blocks of the same dimensions as the HE blocks were used.
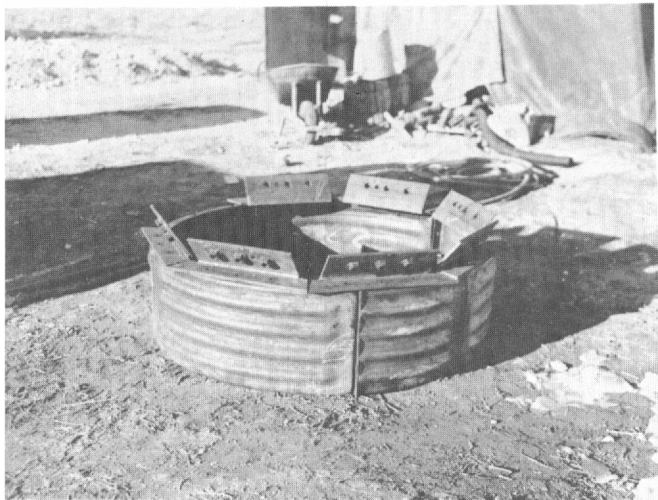
Fig. 12.9 Views show excavation methods using pneumatic digger and protective steel casing provided in each shaft.
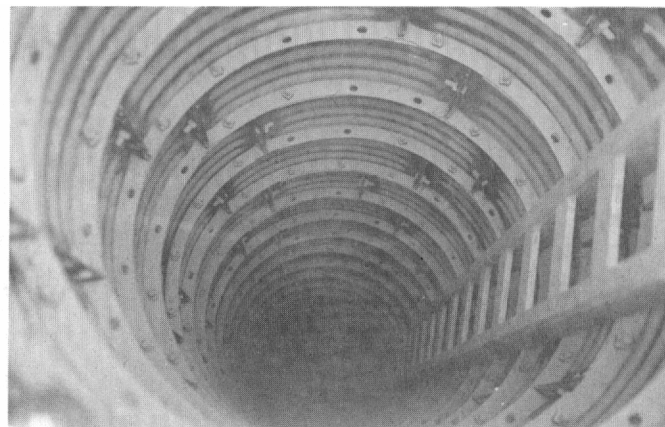
Fabricated hexagonal supporting rings were installed and secured with tie bars to the base of the steel casing. Heavy timbers were then inserted between the flanges of the beams to protect workers against cave-in. Some vertical timbers under the bottom ring of the sphere provided additional protection, but soil cohesion eliminated a requirement for other than normal mining precautions. The steel rings and wood shoring were removed periodically as the chamber became full of HE and sand backfill.

12.2.3 Security and Safety

The Sandia safety organization and scientific groups agreed that 5000 feet was a minimum distance beyond which personnel would be safe from missiles thrown out by 40,000 pounds of HE buried at the depths dictated for Stagecoach. A safety bulletin which warned that high explosives were being handled in the area was distributed. Roadblocks with flags and explosion-warning signs were erected on all roads leading to the zero points. To control traffic, a rope fence, signs, and flags were placed on a 100-foot radius around each zero point. A small house trailer which served as a combination washroom, lunchroom, and coffee area was installed at the gate to each GZ. The project coordinator or his alternate acted as control officer at this point. No smoking was permitted inside the 200-foot-wide cleared area, and radio transmissions were forbidden. To eliminate the expense of continuous security support, shot areas were completely cleared only about an hour before shot time.

Following each detonation, until aerial surveys were completed, two security guards in vehicles maintained traffic control to prevent effacement of crater lips and disturbance of throwout material. This precaution also helped to prevent visitors from falling into possible camouflets created by the detonations.

12.2.4 Preliminary Test Shot

Method of initiation was one of the chief problems connected with Stagecoach. Investigations of as many previous large shots as possible were made, and advice of experts from other companies was obtained. These investigations showed that very little work had been done on one-point detonation of large amounts of HE, and that there was a wide variety of opinion as to the best initiation methods. It was therefore decided that before one-point initiation

was tried with the full 40,000-pound sphere a test should be made of the initiating block design proposed for Stagecoach.

The basic demand was to initiate the explosion at the center of the sphere in such a way that the shock wave would reach the entire outside surface of the sphere at the same time. To answer this demand, a block was designed having a center sphere of Pentolite (50 percent TNT and 50 percent PETN), 4.3 inches in diameter, which would be initiated by a standard blasting cap. In order to furnish more brisance, this sphere was overcast with Cyclotol (75 percent RDX and 25 percent TNT), which produced a sphere 7.6 inches in diameter. The sphere was then overcast with TNT to form a cube 8.6 inches on a side, which was the same size as the HE blocks to be used in building up the 40,000-pound sphere. Two detonator wells, 5/8 inch apart, were then drilled from one side of the initiator block to 1/4 inch beyond the center of the Pentolite sphere. Type J-2 blasting caps were inserted into these wells.

Tests of the initiator block were made to show the manner in which it detonated, the shape of the shock wave produced by it, and the way in which the shock wave would progress in detonating a TNT mass. Cameras were used to obtain records of the shock wave; shock wave pressure was also measured to give an indication of yield and order of detonation.

Instrumentation for this experiment included 8- and 16-mm Fastax cameras operating at 12,000 and 6,000 frames per second, respectively (Figs. 12.10 and 12.11). The cameras were stopped down so that they would record only light from the initial portion of the explosion. Two plate cameras also were opened for 1/2 second during the burst; their plates recorded only as much light from the explosion as would be transmitted through a 3500-angstrom filter (Fig. 12.12). In this wavelength, the light comes, not from the burning of the explosive, but from the shock-excited air as the shock wave emerges from the mass. Two other cameras were also used for documentary coverage and light density measurements. The pressure of the wave was recorded by a 10-psi Wiancko gage operating in the 2.5-psi region. A consolidated system D was used for recording. As was true throughout Project Stagecoach, instrumentation and firing were activated remotely by a radio timing-firing system.

The first test consisted of firing the initiator block alone; it was mounted on a pedestal so that the shock wave characteristics could be studied

Fig. 12.10 Booster block film record. Film shows light from initial portion of explosion (taken with 8-mm Fastax, 12,000 fps, f/16, 4-inch, Dupont 931A).
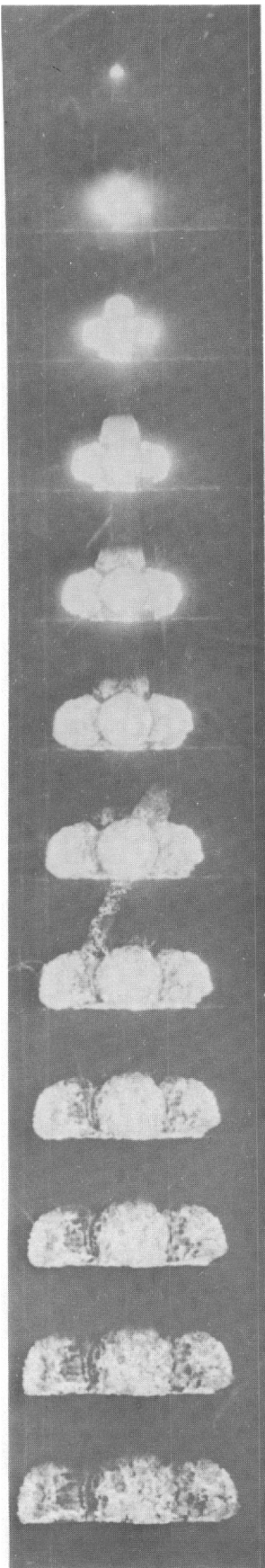
Fig. 12.11 Film record of 5000-pound shot. First six frames are shown (taken with 16-mm Fastax, 6000 fps, f/22, 4-inch, Dupont 931A).
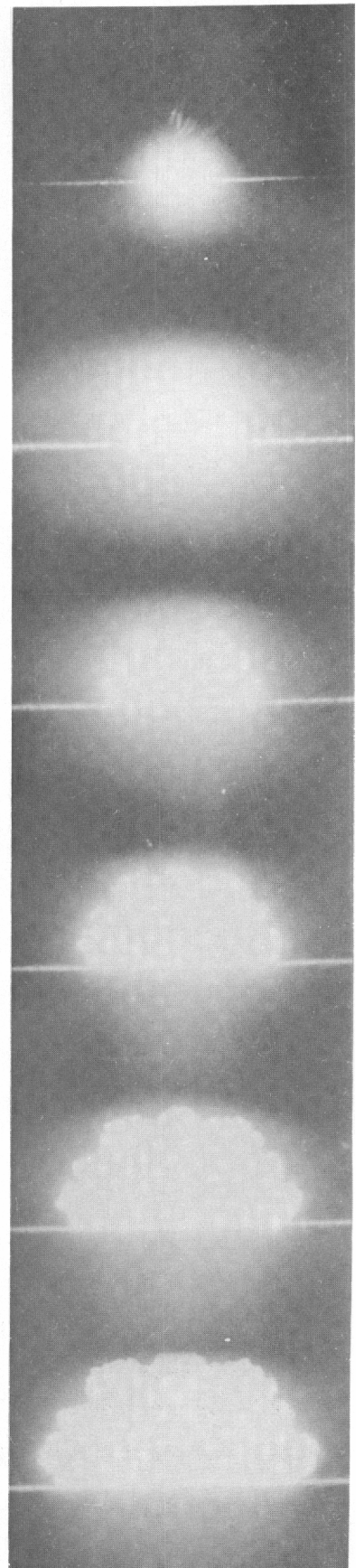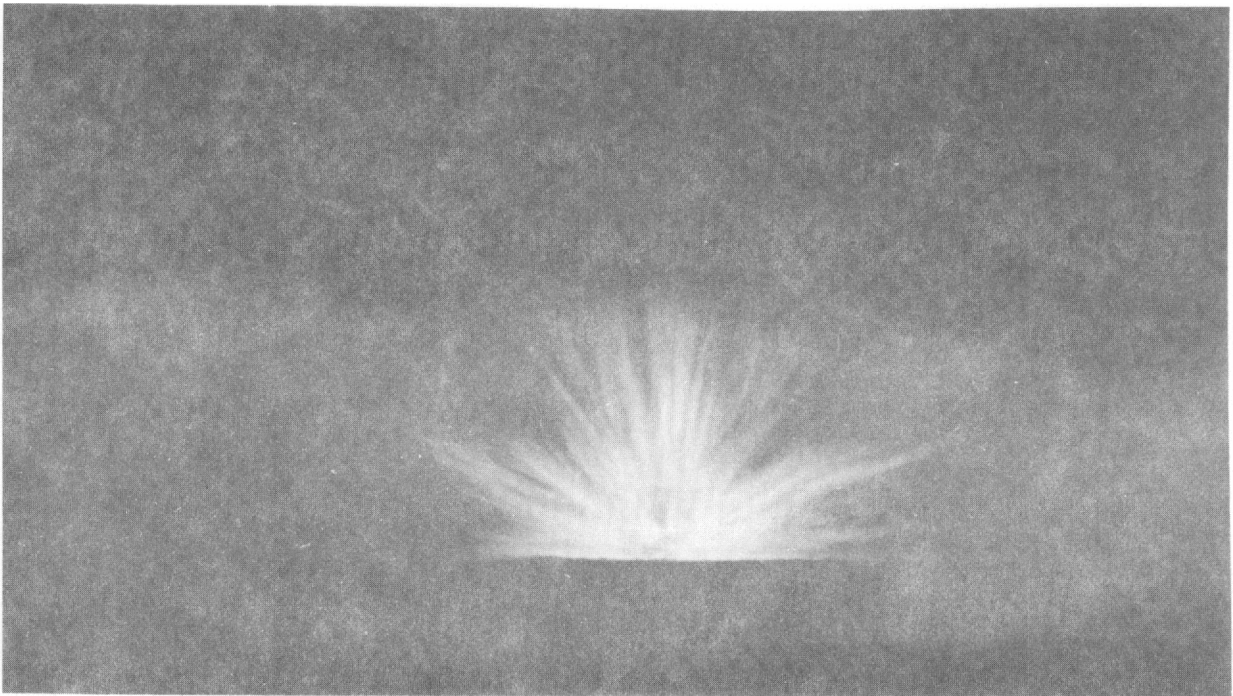
Fig. 12.12 Plate camera record of 5000-pound shot. Exposure, 0.5 sec; aperture, f/32; focal length, 12 inches; filter, 3500 angstroms; film, Ansco Comm. Ortho.
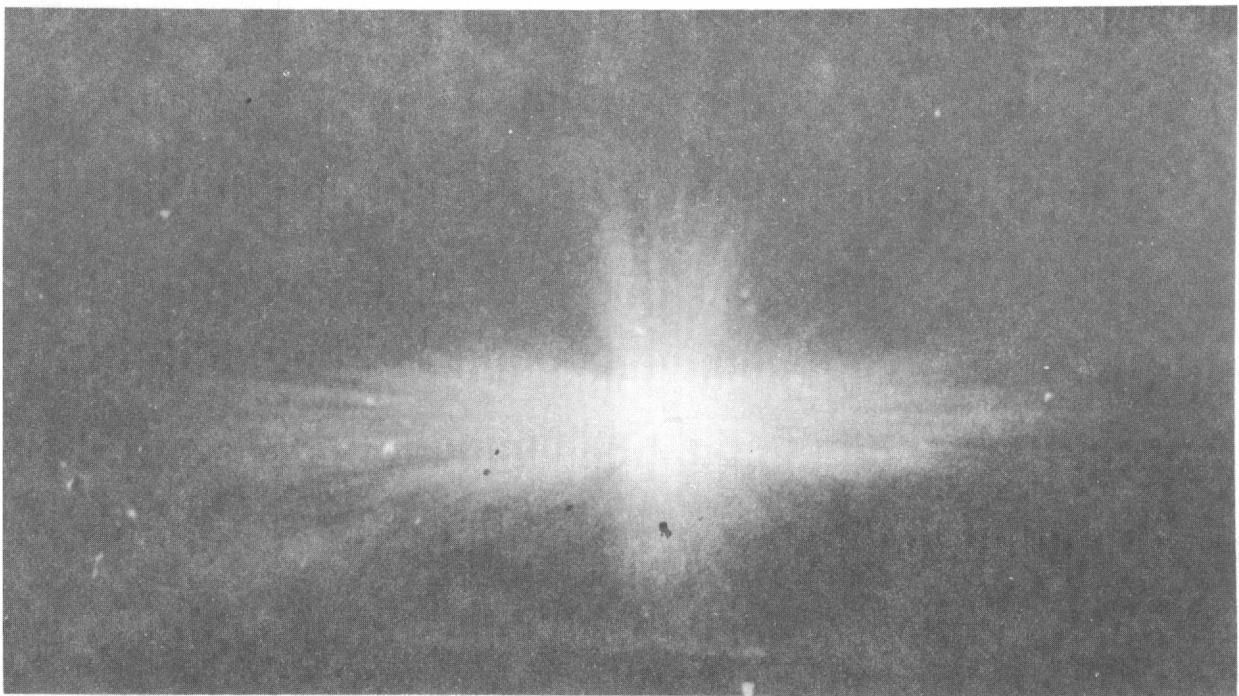
Fig. 12.13 Plate camera record of booster block. Exposure, 1 sec; aperture, f/32; focal length, 12 inches; filter, 3500 angstroms; film, Ansco Comm. Ortho.

through 360 degrees. High-speed photographs and film plates showed a spherical shock wave emerging from the block, with the initial explosion modified only slightly by the cubical overcast of TNT (Fig. 12.13).

Another initiator block was then placed at the center of 5000 pounds of TNT stacked in a spherical shape approximately 6 feet in diameter. The sphere was placed in the ground with the upper hemisphere above ground so that the shock wave could be investigated. The photographic and other measurements showed that both the shock front and the progression of the wave were more nearly spherical than those with the initiator block alone. The pressure recording made at 450 feet showed a wave with a fast rise time and an amplitude as predicted by theoretical studies for a high-order yield (Fig. 12.14).
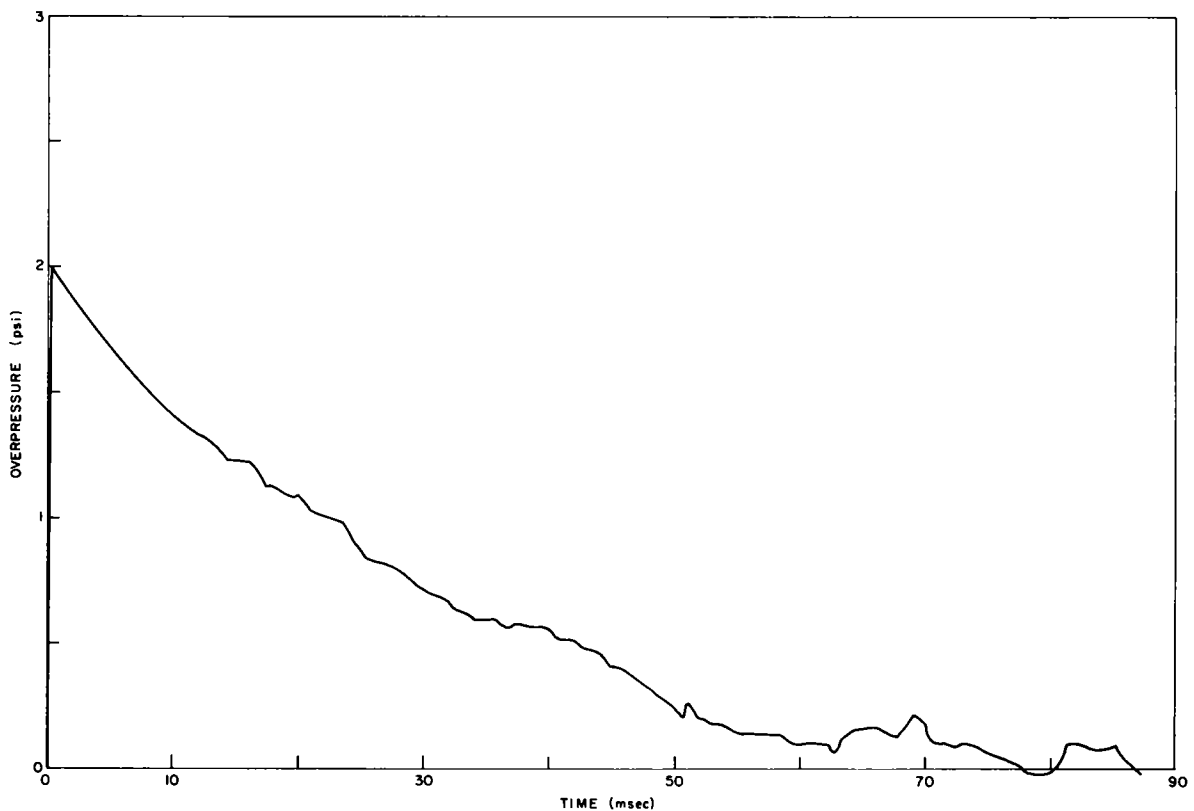
Fig. 12.14 Pressure recording made at 450 feet from block-initiated 5000-pound shot with upper hemisphere above ground. Note fast rise time and amplitude.

The next question which had to be considered was whether, if one 40,000-pound TNT sphere were detonated only 600 feet away from one which was ready to be detonated, the initiator block in the second sphere might not be shocked into initiation by the explosion of the first. To determine the sensitivity of the initiator block to this kind of shock, tests were conducted in the same medium which would be used in the Stagecoach events, as distances scaled to the weight of the initiator block. The block was armed with J-2 blasting caps, buried at a depth of 3 feet 4 inches, and backfilled with sand compacted nearly to the density of the undisturbed earth. A 36-pound block of TNT was armed with a jet perforator for initiation, then buried at the same depth 16 feet 8 inches away. When the TNT was detonated, the initiator block was not fired by the shock. The same test was then conducted at distances of 8 feet 4 inches, and 3 feet 4 inches, with the same results. The initiator block was then fired by one of the blasting caps which had been installed at the beginning of the test, and it performed as well as an unshocked block (see Fig. 12.15).

On the basis of these tests, the initiator block design was considered satisfactory as a means of supplying one-point detonation to the 40,000-pound spherical configurations of TNT in the main Stagecoach events.

12.2.5 Microbarograph Instrumentation

To record the blast-wave amplitudes during Stagecoach, 12 microbarograph (MB) sets were in operation. The sets were located at about 12,000, 40,000, and 75,000 feet from GZ on the range, at four points near Highway 95 and the Lee Canyon road, and at five points near St. George, Utah. These stations had been used during nuclear test shots for blast-overpressure experiments.

Communications were maintained between the control point and the stations by means of radio Net 12. A repeater had to be stationed temporarily near St. George, to maintain good contact with the locations in that vicinity. A zero marker was put on the MB record by broadcasting the "fire" tone over Net 12, thus actuating a marker pen.

The MB sets were prepared and checked at NTS for installation in both the stationary and mobile locations. New transistorized MB sets which, because of their lower power requirements were more adaptable for use with mobile stations than were older sets, were used as much as possible during Stagecoach, and a considerable amount of time was required to bring these sets to desired standards of rise time and amplification.
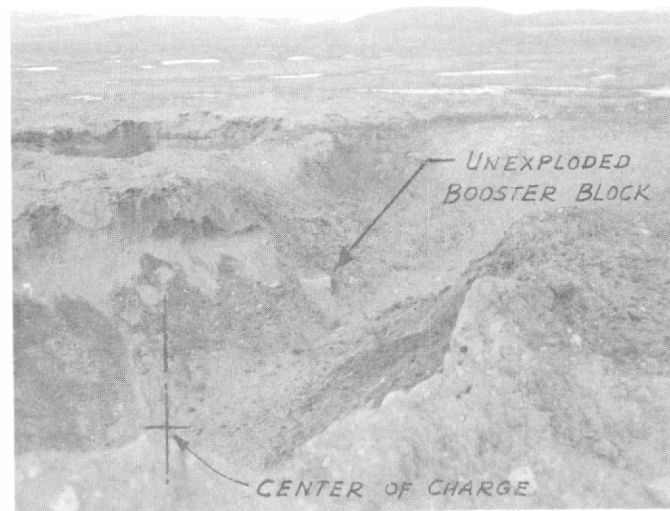
Fig. 12.15 Exposed undetonated initiator block. Photos show cavities made in tests prior to 40,000-pound shots.

Ten minutes before each Stagecoach shot, an MB calibration shot of 2400 pounds was fired about 2-1/2 miles from GZ. The pressure wave from this shot gave a propagation time calibration to the MB stations in addition to an amplitude calibration from a known yield of TNT.

The explosives used in these calibration shots were four 600-pound Navy depth charges, each detonated by a 3-pound granulated-TNT booster which was ignited by a J-2 blasting cap. The charges were fired by signals from the radio system. Three Wiancko pressure gages were mounted 300 feet from GZ, and the yield of the calibration shots was monitored by recording the pressure wave. The signal was taken from the gages to a trailer 1200 feet away and recorded on an oscillograph by means of a Consolidated carrier system. The pressure records were taken for comparison with those from previous tests.

A danger area having a radius of 5000 feet was established around the firing site for the calibration shots, since a considerable amount of shrapnel is hurled from the depth-charge containers. The area was cleared and barricaded before the charges were armed. Firing lines were connected to the relay behind a barricade 600 feet from the charges. Power was applied to the open fire relay contacts through the remote safing control.

The calibration charges were detonated on the surface of the ground and thus created some fairly large craters. In order that an equivalent coupling of the blast wave might be maintained on various shots, each crater was filled level with the surrounding surface before the next charge was fired. Preliminary results from pressure records on these calibration shots indicate that use of this noncompacted backfill material may have resulted in a double pressure-wave front, the first part of which comes directly from the explosion.

12.2.6 Explosive Used in the Stagecoach Shots

Units of HE used for Stagecoach were cubes of TNT 8-5/8 inches on a side, weighing about 36 pounds each. The cubical shape was chosen because it could be most conveniently assembled into a sphere. The weight was chosen simply for ease in handling. The blocks were manufactured at the Naval Ammunition Depot, Hawthorne, Nevada, by melting Army-surplus TNT flake and pouring it into wooden molds. The blocks were made to a dimensional tolerance of $\pm$ 1/8 inch. Blocks having cracks or cavities either in the interior or on the surface were rejected. After the melt was poured, the blocks were removed from

the molds, weighed and marked, packed in individual fiberboard containers, and placed on pallets in lots ready for shipment. Shipment was made to NTS by vans in 40,000-pound lots. The blocks were unloaded directly from the vans to the emplacement. A platform 12 feet square and 4 feet high was constructed near each GZ, and the blocks were carried individually from the vans to the platform, where the containers were removed and taken to an approved burn area for disposal. The blocks were then loaded from the platform into the skip prior to being lowered down the shaft. The usual load was 21 blocks, or 756 pounds. When the skip reached the cavity, the blocks were removed and stacked. During all handling of the HE, gloves and coveralls were worn by personnel to protect skin and clothing from contamination by toxic products.

A near-spherical shape was obtained by stacking the blocks according to a previously determined layer diagram. A plywood floor was constructed to support the first layer of blocks. Wooden blocks of the same size as the HE blocks were used on the first and second layers to give direct support to all blocks in the third layer. A total of 108 wooden blocks was used in each sphere. Fine sand was placed around the circumference of each layer to fill out the cavity and to support the sphere. The completed stacks consisted of 1114 blocks in 15 layers. Figure 12.16 shows blocks and stacking arrangements. Actual charge weights for the shots were: 17.1-ft burst depth--40,240 pounds, 34.2-ft burst depth--40,070 pounds, and 80-ft burst depth--40,120 pounds.

The HE sphere was detonated by the initiator block which was placed in the geometric center of the sphere. Two Army Engineers' special J-2 electric blasting caps were installed in the detonator wells, and the connections brought to the surface of the sphere by flat two-wire lines between rows of blocks. These leads were shorted and grounded at the top of the cavity while the sphere was being completed. A backup initiator block was placed in the second layer from the top of the sphere, where its wire leads, or the block itself, would not be subject to as much pressure and possible shifting as the central booster. After the HE sphere was completed, the electrical firing cables were connected to the cap leads through a conduit which entered the cavity from the surface. Current was furnished by firing lines from the fire relay actuated by the radio signal system. The relay and battery were installed in the camera trailer, together with the radio receiver for the timing signals. The firing circuit and the associated safing relay are shown in Fig. 12.17.
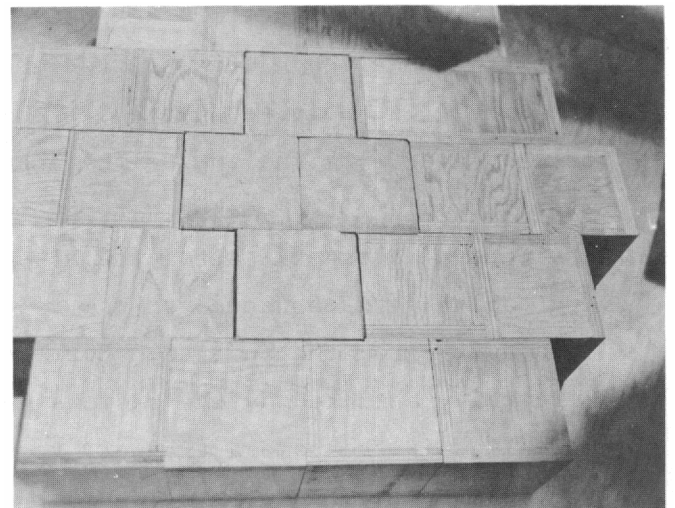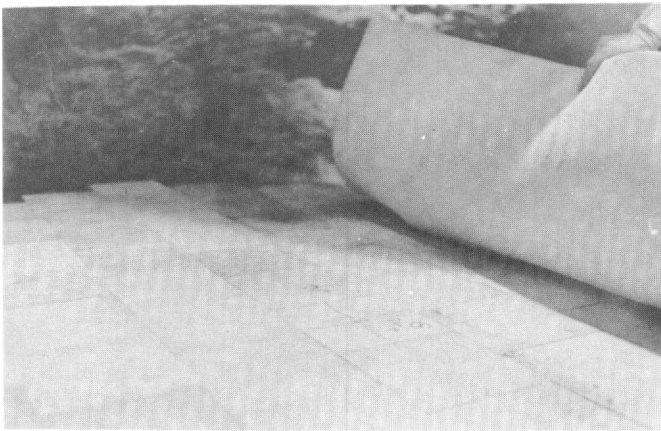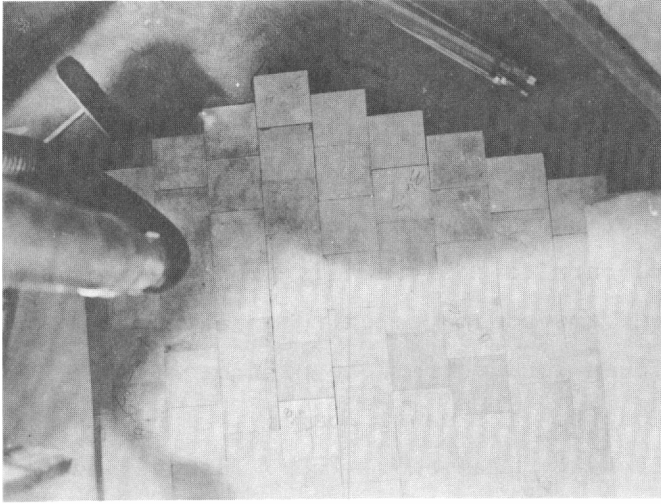
Fig. 12.16 Explosives stacking arrangements. Four views taken "down in the hole" show stacking arrangements, sand packing around edges, neoprene blanket to allow walking on explosive, and wooden supporting blocks.
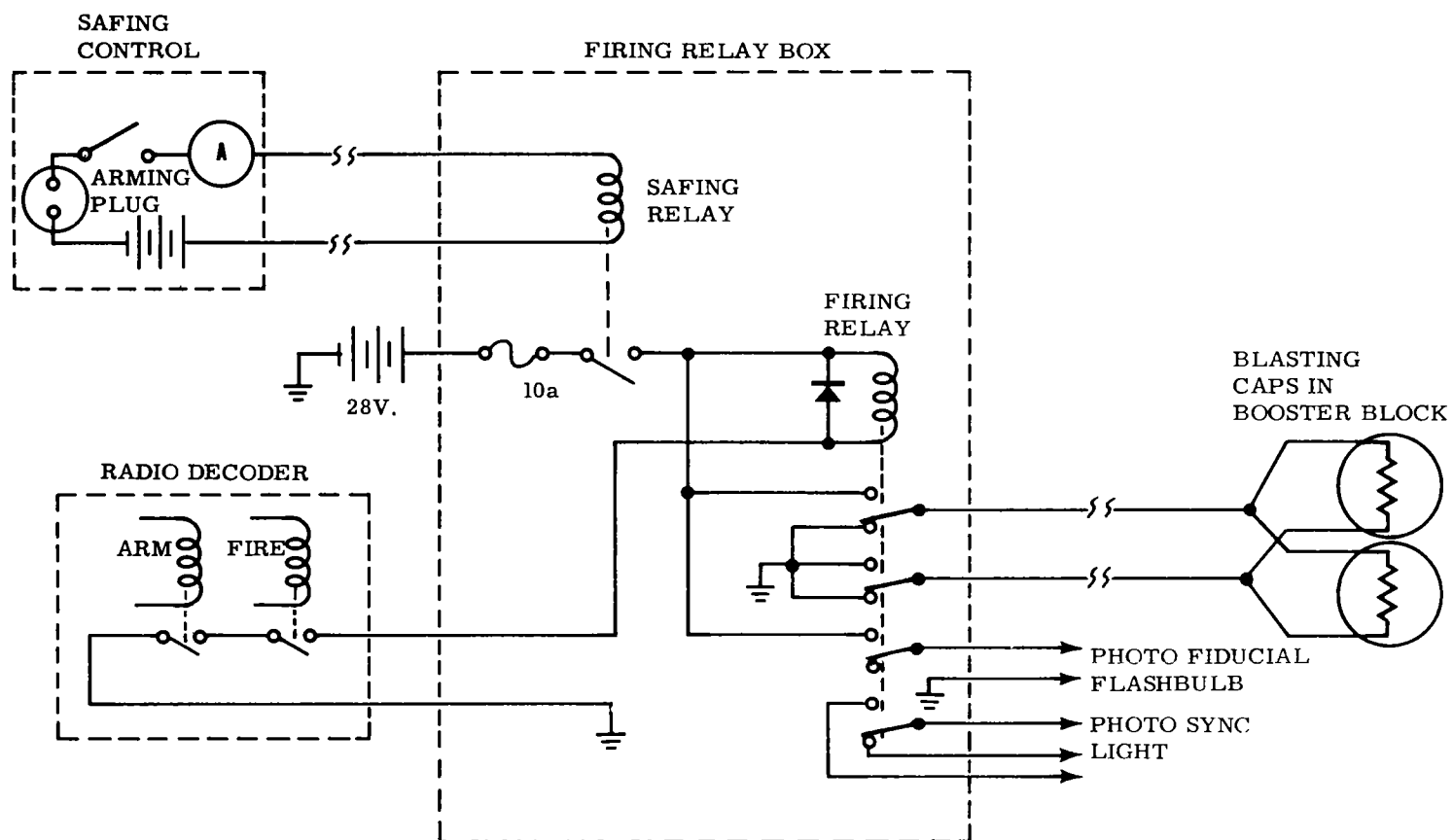
Fig. 12.17 Firing circuit and associated safing relay.

When loading and backfilling were completed and all instrumentation was ready, the area around GZ was cleared for arming, and roadblocks were established to keep the area clear of personnel. The firing leads into the blasting-cap bridgewire were checked by galvanometer readings, following which the firing lines were checked back to the fire relay. Check sheets were followed to maintain proper procedures and to furnish an arming record. After the lines were checked out, the firing leads were connected and the arming party was evacuated. Power was supplied to the open fire relay contacts when the safing relay was closed remotely at a safe distance from GZ.

12.2.7 Signal System and Communications

Communications were maintained at the site largely through the Net 8 radio system. Sets were available in most of the vehicles used during the operation; sets were also available in the control room and at various instrumentation and photographic stations. The radio system was particularly useful during the instrumentation and dry-run period preceding each shot. All stations inside the barricaded area which were manned during the shots used the Net 8 system for their primary communication channel to fire control. Other communication channels available to the manned stations included telephone, another radio net, or a standby set on Net 8. Off-site communications (primarily between control and the MB stations) were conducted over the low-frequency Net 12.

All required instrumentation timing and firing signals were transmitted and received by a radio system (Fig. 12.18). Signal relays were closed on receipt of the proper audiofrequency tone over Net 11 on the site, while the MB stations received a zero marker over Net 12. Signals were generated at the control console either by manual actuation or from mechanical cam-operated switches on a timer. Closure of the switch caused an audio tone to be generated which modulated the frequency of the transmitter carrier wave. When the proper tone was received, the frequency-sensitive relay was closed at the receiving station. A system which required two simultaneous tones was used to increase reliability and to provide protection against noise or other inadvertent relay actuation.

Three different signals were required on Net 11 to meet timing requirements, and three signals were sent on Net 12 to time the MB calibration shots and the zero marker on the MB records. These signals, as far as the user was
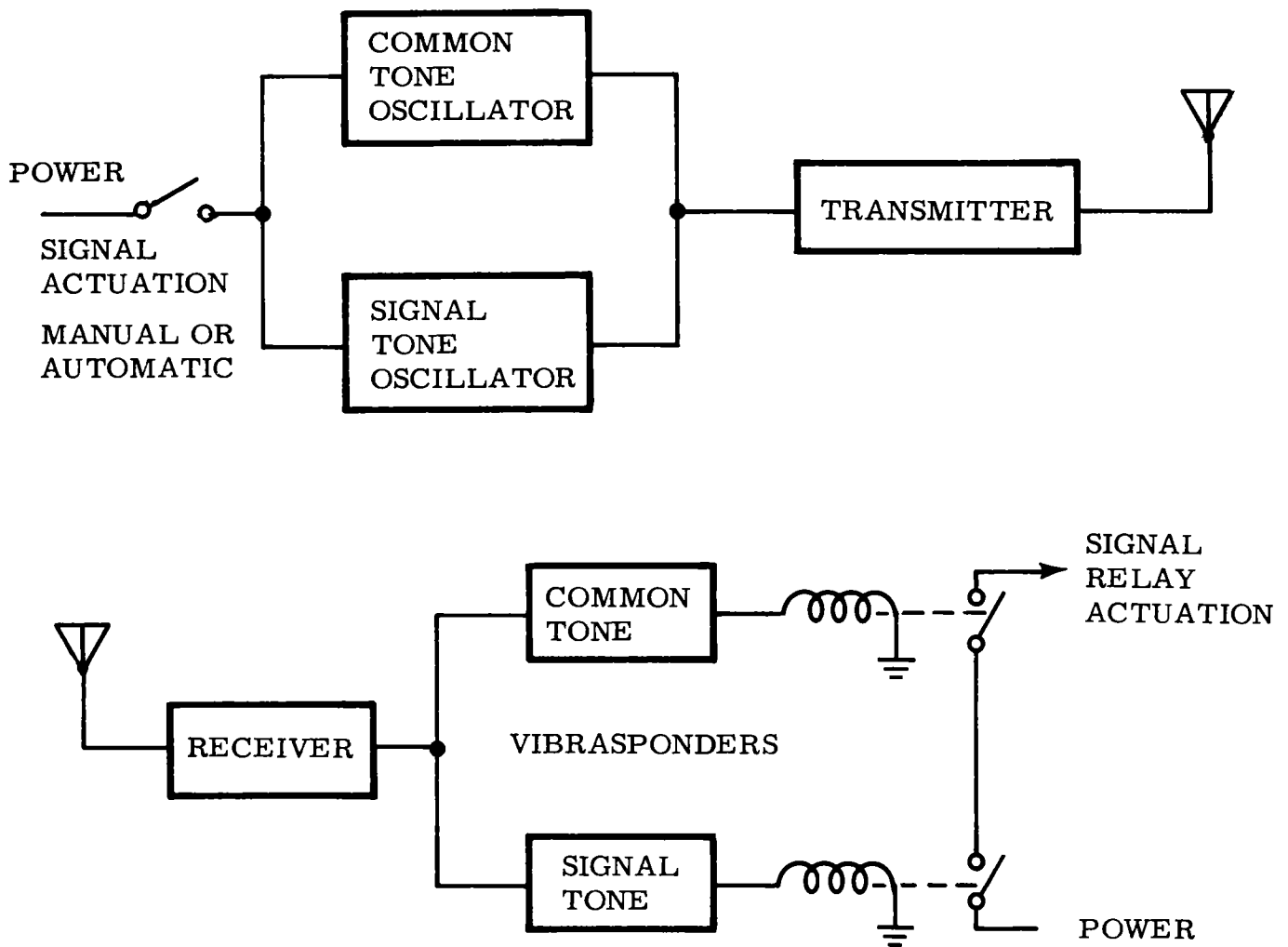
Fig. 12.18 Block diagram of radio signal system.

concerned, were 2-ampere contacts and involved a relay closure. For control
of larger currents, an intermediate relay had to be employed. Signals actuated
manually were guaranteed to $\pm$ 1/4 second in relation to zero time, while those
given during the last minute before firing came from a cam timer and were ac-
curate to $\pm$ 1/10 second. Some of the receiver tone strips and relays for the
zero signal were calibrated in relation to the firing relay with an accuracy
of $\pm$ 0.01 second. The signals were timed during the preshot sequence by a
clock set to WWV time so that the shots were fired with $\pm$ 1/2 second of world
time. During the preshot checkout period, the signal system was checked by a
complete set of signals sent to all receiving locations as shown in Table 12.2.

TABLE 12.2 SIGNAL CHART

Agency instrumentation	Stations	Signals Net 11	Net 12	Remarks
Microbarograph (Sandia)	St. George, Utah (2) Lee Canyon Hwy. 95 (4) On-site (3)		-10 min Zero	
Microbarograph calibration shot (Sandia)	Firing site No. 5 Pressure recording trailer		-10 min 4 sec -10 min -10 min 4 sec	Arm Fire
Photography (Sandia)	1200 feet SE of GZ 5000 feet S of GZ 5000 feet E of GZ	-2 sec -2 sec (voice count only)		Ground motion Balloon position 17- and 34-foot shots only
Air-blast pressure (NOL)	From 80 to 3000 feet S of GZ	-2 sec Zero		Wired from recording trailer 5000 feet S of GZ
Self-recording pressure gages (BRL)	80, 110, 160, 270, and 430 feet S of GZ	-2 sec		Wired from NOL trailer
Seismometers (SES)	3000, 4000, and 7000 feet S of GZ	Zero		Wired from 7000-foot station to others
Arming and firing (Sandia)	1200 feet SE of GZ	-10 sec Zero		Arm Fire

The countdown for the Stagecoach events was started an hour before zero, and the danger area was cleared of personnel before that time. Voice time announcements were given on Nets 8 and 12 at minus 1 hour, and again at minus 15 minutes. At minus 10 minutes 4 seconds, a signal was sent out to arm the MB calibration charges and to start the pressure-recording sequence. At minus 10 minutes, the calibration charges were fired and the marker signal sent to all MB stations. Voice time announcements then were made at minus 5 minutes, minus 1 minute, minus 30 seconds, and every second from minus 10 through zero. The automatic sequence timer was started at minus 40 seconds, and the remainder of the signals were actuated by the cam-operated switches. The arming signal was given at minus 10 seconds, and at minus 2 seconds a signal initiated a recording sequence for NOL, actuated BRL gages, and started the camera timing sequence. The fire signal closed the fire relay and at the same time furnished a marker on the SES seismometers in addition to placing a zero fiducial point on the MB records. The voice time announcements were continued through 30 seconds after zero time.

12.3 MISSILE THROWOUT, DENSITY, AND SIZE

The purpose of the missile throwout experiment was to secure data on missile hazard from partially contained high-explosive detonations. In order that data could be acquired in useful amounts, measurements were taken at distances of 80, 170, 365, and 775 yards from GZ, along two radii 180 degrees apart. At each measuring point throwout material was collected on a sheet of canvas 10 feet square (Fig. 12.19). After material from each shot was collected, it was screened and sized at the local Sandia warehouse and packaged for shipment to Sandia Laboratory at Albuquerque for further study. Data obtained were used to determine a scaling of safe distances for personnel in the vicinity of similar future detonations.

12.3.1 Distribution of Throwout

Collector pans used for determination of throwout distribution were ordinary aluminum cake pans, 9 inches in diameter and 1-1/4 inches deep. Samples were collected on only two of the three shots: those at the 17- and 34-foot depths. By use of standard survey techniques, 12 radii were located 30 degrees apart around GZ, with radius No. 12 oriented north. Pan distances from GZ were
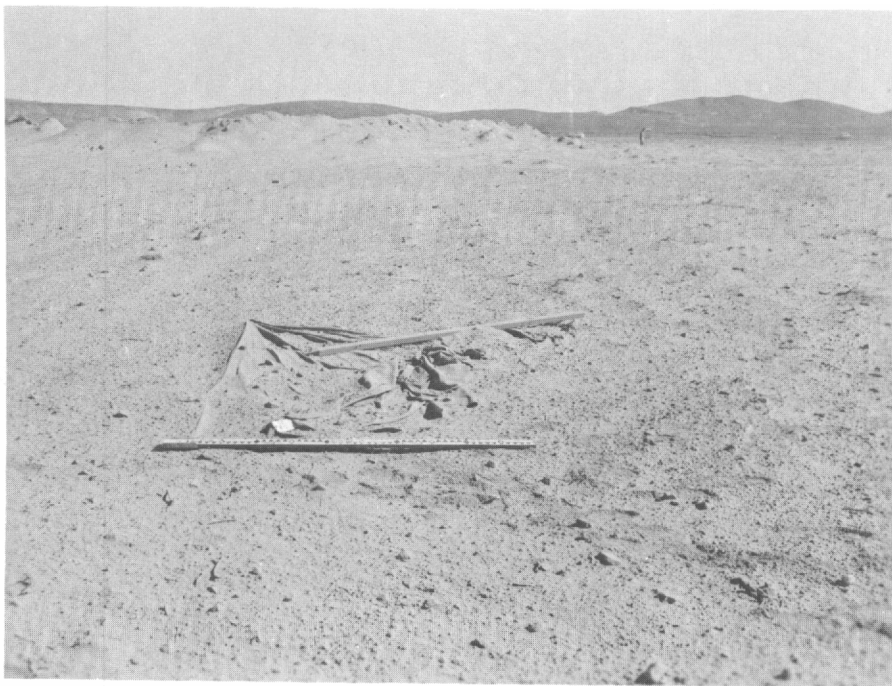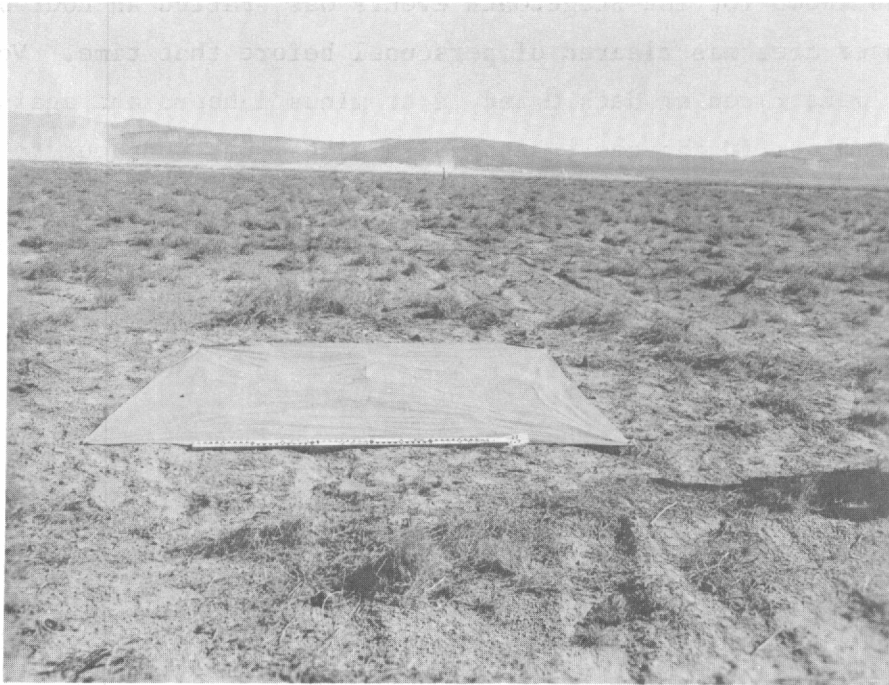
Fig. 12.19 Canvas collectors used in missile throwout test--
"before and after" views.

80, 115, 170, 250, 365, 530, 775, and 1150 yards (Fig. 12.20). Eight collectors were used on the north radius, making a total of 112 pans for each shot. For each collector location, an area 4 feet square was cleared and the earth stabilized with oil. The pans were placed on a 1-foot square of 1/4-inch plywood to insure against dirt adhering to the bottom of the pan (Fig. 12.21). Placement of the collectors was started at minus 3 hours by four 2-man teams. All 112 pans were in position for the first shot at minus 1 hour.

Access to the throwout-collection area was minimized until after the sampleᵣ were collected. The contents of each pan were carefully and completely emptied into individual plastic bags which were sealed and plainly marked as to shot number and collection location.

12.3.2 Particle Trajectory Study

Metal pellets which, to simplify recovery, contained radioactive material, were placed in the ground at various measured depths and distances from GZ. The radial position of the pellets was determined after each shot. Four 2-inch-diameter holes were drilled in a radial pattern from GZ for the tracer pellets at both the 17- and 34-foot detonations. Standard well-drilling techniques were used, and the holes were protected from cave-in damage until such time as the pellets were placed (Fig. 12.22).

The source used in the tracers was antimony 124, which has a half-life of 60 days. Because of the low background count of Area 10, it was felt that a strength of 600 millicuries per pellet was sufficient for easy detection and recovery. Specifications and procurement of the material were coordinated through Sandia's Health Physics Section, which also had responsibility for placement and recovery of the tracers. REECO Rad-Safe personnel assisted on the latter operation.

Twelve tracers were used for the 17-foot shot. The sources were delivered to the site in a lead shipping pig. As the pellets were removed from the pig, the serial numbers of the pellets and their placement in the hole were recorded. REECO personnel then removed the casing and filled the holes with moistened earth which was compacted up to the depth of the next tracer. To duplicate as closely as possible the undisturbed condition of the soil, light tamping of the dirt was required. The tracers were placed in the holes on the afternoon before shot day. Although the pellets did not create a health hazard while

W.P.
STA. 1003.02
& 1003.03

TYPICAL STATION DESIGNATION
SHOWN ON THIS LINE

H2

-30°
TYP.

A2
B2
C2
D2
E2
F2
G2

A
B
C
D 750'R
E 1095'R
F 1590'R
G 2325'R
H 3450'R

510'R
345'R

GENERAL NOTES:

1. 2" SQ. STAKE REQ'D AT EACH LOCATION SHOWN ON PLOT PLAN.
STAKE TO BE FLUSH WITH GRADE AND MARKED WITH THE
RESPECTIVE STA. DESIGNATION OF EACH LOCATION (A-1, A-2 ECT.)

2. AN AREA OF 4' RADIUS AROUND EACH STATION IS TO BE CLEARED
OF BRUSH AND TALL WEEDS. IF CLEARED AREA HAS TENDENCY TO BE
DUSTY, IT IS TO BE STABILIZED BY COVERING AREA WITH OIL.

3. ALL COLLECTOR PANS SHOULD BE PLACED ON A ONE SQUARE
FOOT PIECE OF 1/4" PLYWOOD.

4. ● ● STATIONS SHOWN THUS WILL HAVE DUPLICATE COLLECTOR
PLACED 2'-0" AWAY FROM OTHER COLLECTOR AT THAT STATION.

5. COLLECTORS WILL BE CYLINDERS OF MIN. DIMENSIONS DIA. OF 9"
AND DEPTH OF 1" (CAKE PANS)   WHICH WILL BE
MARKED PRIOR TO PLACEMENT WITH THE STATION DESIGNATION
AS A-1, A-2, A-3 ETC. COLLECTORS TO BE USER FURNISHED.

Fig. 12.20 Dust collector locations.

STATION LOCATION PLAN - DWG 010-1003-C1

ID 940906

△ 6'□ 10' — TARPS 15' OFFSET FROM RADIAL LINE

PLOT PLAN
SCALE : 1" = 400'

AS-BUILT

HOLMES & NARVER, INC.
Engineers — Constructors

Date 4-11-60   D.F.   CKD

Approved

4-11-60 AS BUILT - ADDED TARPS
NO. | DATE | REVISIONS

U. S. ATOMIC ENERGY COMMISSION
LAS VEGAS BRANCH OFFICE
LAS VEGAS, NEVADA

CRATER EXPERIMENT - H.E.
DUST COLLECTOR LOCATIONS
STA. 1003.02 & .03   AREA 10

SUBMITTED   APPROVED   RECOMMENDED   APPROVED

HOLMES & NARVER, INC.
ENGINEERS — CONSTRUCTORS
828 SO. FIGUEROA STREET   LOS ANGELES 17, CALIFORNIA

JOB: NTS

DRAWING NO.
JS-010-1003-C2

SCALE: NOTED

DRAWN BY: PH

257-258

Fig. 12.21 Collector pan and marker used in throwout distribution experiment.

Fig. 12.22 Protected drill hole for radioactive pellet placement in the particle trajectory experiment.

buried in the ground, radiation signs were placed at the locations. These were removed an hour before zero time by the arming and firing party.

Location of the tracers after the shot was carried out by REECO personnel who used standard radiation survey meters. When a pellet was located, its depth in the throwout and its serial number were recorded before it was returned to the lead pig. After a displaced tracer had been located, its final position was defined by NTS grid coordinates to within $\pm$ 1 foot and located as to elevation above its original location to within 0.1 foot.

Sixteen tracers were used for the 34-foot shot. Their placement and recovery were accomplished in the same manner as on the 17-foot shot. All 28 of the radioactive sources used in both shots were recovered.

12.4 OTHER REQUIREMENTS AND COVERAGE
12.4.1 Photographic Coverage

Documentary stills were taken of the drilling of the holes, the HE loading, and other facets of preparation for the experiment. One phase of this coverage consisted of taking a series of pictures of each HE layer until the explosive sphere was completed. Appendix A is devoted to photo coverage.

12.4.2 Vehicle and Generator Requirements

Vehicles for the program were rented from the REECO Motor Pool for approximately 5 dollars per week plus 7 cents per mile. Rental for vehicles which normally had very small mileage ranged up to 15 cents per mile, and power generators ranged from 3 to 5 dollars per use-time hour. Most of the small trailers, such as house trailers, were obtained on a flat charge of 30 dollars per month. The entire program, exclusive of the microbarograph participation described earlier, required:

9 sedans with Net 8 radio	4 portable generators (5 kw)
2 pickups with Net 8 radio	2 diesel generators (40 kw)
1 power wagon	1 photo-instrumentation trailer
1 field office trailer	1 Hydra-lift crane

The sedans averaged 500 miles per week during the major portion of the program from January through March, 1960. During the final days of the test detonations, demands on the existing vehicles were considerably increased because of visiting observers and the increased load of final preparations.

Generators were utilized as spot power sources in remote locations. Where major functions could be centrally located it was found advantageous to provide a larger type of diesel generator. Truck gasoline service for the generators was arranged on a daily basis except where continuous operations demanded a 50-gallon, gravity-feed drum for a particular generator.

12.4.3 Miscellaneous Support Contract

Previous field experience dictated the need for a small purchase order contract with REECO in the amount of $5000, designed to cover miscellaneous field expenses not provided for by the primary construction contract. These included such items as wooden mock-up blocks the same size as the HE blocks, for use as support under the bottom hemisphere; access road barricades; wire cages for burning HE containers; additional laborers to meet time schedules; extra photo targets to increase photographic data; trailer service and repair; and small stockroom items.

12.5 PARTICIPATION BY OTHER AGENCIES

Because the study of air blast from subsurface detonations in the range of Stagecoach geometries and charge sizes was favorable to contemporary research, NOL requested and was granted permission to measure air blast by means of approximately 15 pressure gages for each detonation. These measurements were made on the ground surface along the instrumentation lines south from GZ and from balloons supporting instruments at altitudes up to 500 feet. Pressures measured were extensively covered in the region of 0.25 to 5.0 psi. The gages were electromechanical, and the system utilized wired signal transmission to trailer-housed magnetic tape recorders at about 5000 feet from GZ.

Balloons were located at approximately 430, 750, 1600, and 3000 feet from GZ on two of the three shots. Construction for this program required only a 1/2-inch eyebolt 2 inches in diameter, anchored in a concrete block weighing about 1000 pounds, in addition to labor for balloon inflation and launching. Surveyors were required to lay out balloon and instrument locations; laborers were furnished by REECO to dig small square holes at these locations so that pressure gages could be installed at ground level. Jalbert Aerodynamic JX9A balloons

were used. These were 12 feet in diameter and 34 feet long. Pressure instruments, purchased by Sandia, were calibrated and operated by NOL.

Ballistic Research Laboratories conducted a backup program for NOL with similar pressure instruments and locations along the instrument line at ground surface only. The instruments were placed in the ground together with NOL's installation and, although measurements were taken independently, results served as confirmation of data obtained by NOL. Installation and data analysis were conducted by BRL on a contract with Sandia at a cost of $1500. No construction was involved other than the type already supplied for NOL.

Suffield Experimental Station at Ralston, Alberta, Canada, conducted a seismic effect program as a continuation of their broad study of ground-wave measurements created by surface and underground detonations of high explosives. The project consisted cf placing three Sprengnether, 3-component seismometers on the ground surface at 3000, 4000, and 5000 feet from GZ along the established instrument lines. The Sprengnether gages were standard, self-powered units and were initiated by an AC line at minus 6 seconds; they continued to operate to plus 30 seconds. A second line carried a thyratron generator pulse of 70 volts at 100 milliamperes to register zero time on the film. The units were modified to include a common base line mark, a zero-time marker, and a device to record time of arrival of air blast at the instrument. Additional tests were made of wire drag gages in the range of 0 to 350 feet. Association with the Canadian crew was quite harmonious and stimulating and, except for minor local supplies furnished by Sandia, no construction requirements were involved.

Boeing Airplane Company sent two men from their Aerospace Division at Seattle to make a study of dust fallout distribution created by the three detonations. Their program consisted of placing a pattern of 10-foot canvas squares on two lines 90 degrees from each other on a line from ground zero. By previous agreement, the project was to be conducted on a "noninterference" basis and, because of the Sandia program outlined above, it was possible to choose the distances and place the canvases at points which had already been surveyed. As a result of this operation a few hours ahead of firing time, it was rather easy to collect, weigh, photograph, and analyze the material deposited on the canvases.

Appendix A

PHOTOGRAPHY by L. J. Vortman

Locations of motion picture cameras are shown diagrammatically in Fig.
A.1 and are summarized in detail in Table A.1.

The major objectives of the motion picture photography were to record:

1. Early ground surface motion (displacement-time).

2. The rise of the mound and the manner of venting.

3. Throwout dispersion.

4. Cloud growth.

In addition to ground surface motion, the air shock front fortuitously
was visible on the Fastax pictures of the 17- and 34-foot shots.

To show positions of the NOL instrumented balloons, two 10- by 12-inch
photographic glass plates were exposed at zero time. One camera was placed
perpendicular to the balloon line and the other was placed 90 degrees away,
in line with the balloons. Targets were placed to show the tie-down points
of each balloon.

A photographic back drop, 8 feet high and 16 feet long, was placed behind
each surface zero. Five camera targets were placed 25 feet apart on centers
with the center one of the five at surface zero. The center target was 2
feet square and the others were 1 foot square. They were placed on 2- by
4-inch posts the bottom ends of which were set 2 feet below the ground surface.

Figures A.2 through A.13 are selected examples of still photography.
Figure A.14 shows a motion picture sequence of the Stagecoach 80-foot shot.

TABLE A.1   MOTION PICTURE CAMERA LOCATIONS

Location	Distance (feet)	Azimuth (degrees)	Camera	Film speed (frames per second)	Run time	Film	Lens	(feet) Object size (1/1000 inch)	Field of view (feet) Height	Width	Purpose
17-foot depth-of-burst											
Mound	5000	205	Bell and Howell, 16 mm	64	1+ min	Color	1 inch	5	1420	1900	Cloud and documentary
Tower	6000		Bell and Howell, 16 mm	64	1+ min	Color	1 inch	6	1704	2280	Cloud and documentary
Tower	6000		Fairchild, 16 mm	1000	5 sec	Color	35 mm	4.3	1310	1754	
Tower	6000		Mitchell, 35 mm	24	1+ min	Plus X pan	2 inches	3.0	1893	2604	
Mobile Sta	1200		Fastax, 16 mm	3000	2.5 sec	931 B W	4 inches	0.3	85	114	Surface motion
Mobile Sta	1200		Mitchell, 35 mm	100	60 sec	Plus X pan	10 inches	0.12	76	104	
Mobile Sta	1200		Warrick, 35 mm	1200	6 sec	Color	4 inches	0.3	189	261	
Mobile Sta	1200		Mitchell, 35 mm	100	60 sec	Plus X pan	1 inch	1.2	757	1042	
Mobile Sta	1200		Mitchell, 35 mm	100	60 sec	Plus X pan	6 inches	0.2	126	174	
Mobile Sta	1200		Fastax, 16 mm	3000	2.5 sec	931 B W	10 inches	0.12	34	46	Surface Motion
34-foot depth-of-burst											
Mound	5000	205	Bell and Howell, 16 mm	64	1+ min	Color	1 inch	5	1420	1900	Cloud and documentary
Tower	6000		Bell and Howell, 16 mm	64	1+ min	Color	1 inch	6	1704	2280	Cloud and documentary
Tower	6000		Fairchild, 16 mm	1000	5 sec	Color	35 mm	4.3	1310	1754	
Tower	6000		Mitchell, 35 mm	24	1+ min	Plus X pan	2 inches	3.0	1893	2604	
Mobile Sta	1200		Fastax, 16 mm	3500	2.3 sec	931 B W	4 inches	0.3	85	114	Surface motion
Mobile Sta	1200		Mitchell, 35 mm	100	60 sec	Plus X pan	10 inches	0.12	76	104	
Mobile Sta	1200		Warrick, 35 mm	1200	6 sec	Color	4 inches	0.3	189	261	
Mobile Sta	1200		Mitchell, 35 mm	100	60 sec	Plus X pan	1 inch	1.2	757	1042	Documentary
Mobile Sta	1200		Mitchell, 35 mm	100	60 sec	Plus X pan	6 inches	0.2	126	174	
Mobile Sta	1200		Fastax, 16 mm	3500	2.3 sec	931 B W	10 inches	0.12	34	46	Surface motion
80-foot depth-of-burst											
Mound	5000	205	Bell and Howell, 16 mm	64	1+ min	Color	1 inch	5	1420	1900	Cloud and documentary
Tower	6000		Bell and Howell, 16 mm	64	1+ min	Color	1 inch	6	1704	2280	Cloud and documentary
Tower	6000		Fairchild, 16 mm	1000	5 sec	Color	35 mm	4.3	1310	1754	
Tower	6000		Mitchell, 35 mm	24	1+ min	Plus X pan	2 inches	3.0	1893	2604	
Mobile Sta	1200		Fastax, 16 mm	1000	5 sec	931 B W	4 inches	0.3	85	114	Surface motion
Mobile Sta	1200		Mitchell, 35 mm	50	60 sec	Plus X pan	10 inches	0.12	76	104	
Mobile Sta	1200		Warrick, 35 mm	1200	6 sec	Color	4 inches	0.3	189	261	
Mobile Sta	1200		Mitchell, 35 mm	100	60 sec	Plus X pan	1 inch	1.2	757	1042	
Mobile Sta	1200		Mitchell, 35 mm	100	60 sec	Plux X pan	6 inches	0.2	126	174	
Mobile Sta	1200		Fastax, 16 mm	1000	5 sec	Color	10 inches	0.12	34	46	Surface motion

Note: All cameras running above 1000 frames per second have 1000 cycle timing (1 mark every millisecond).
All cameras running below 1000 frames per second have 100 cycle timing (1 mark every 10 milliseconds).
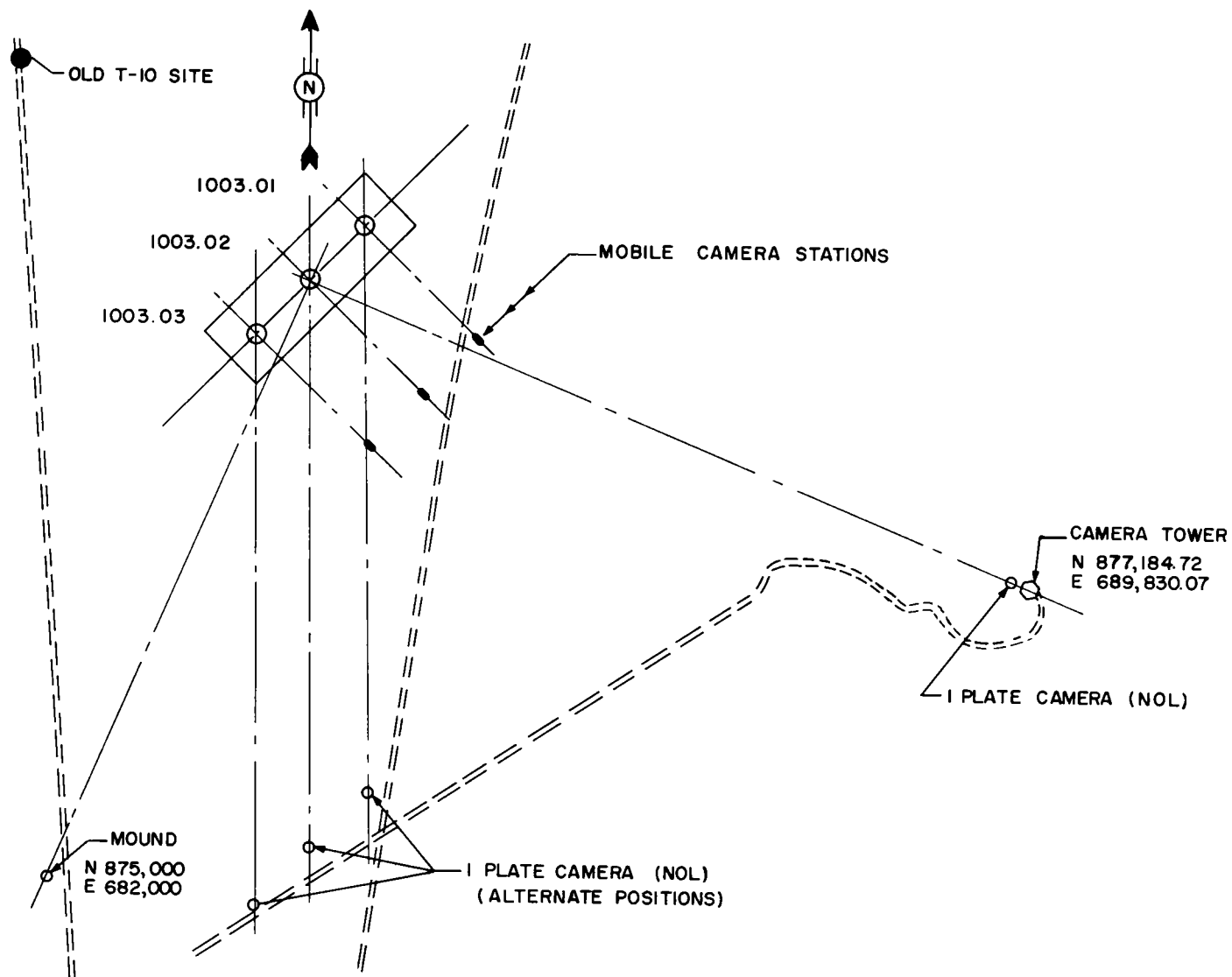
Fig. A.1 Location of camera stations.
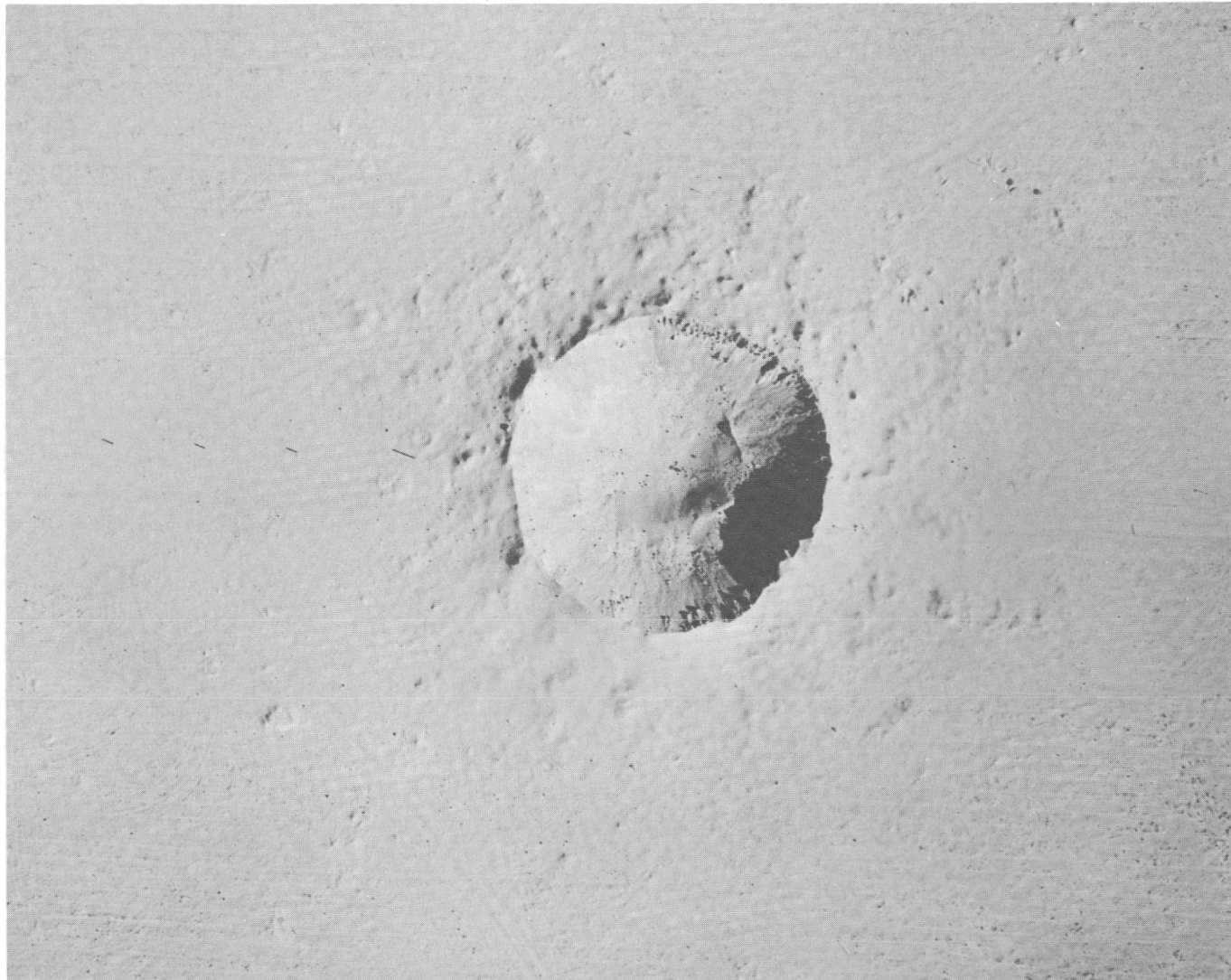
Fig. A.2 Crater from 20-ton charge buried at 17.1 feet.
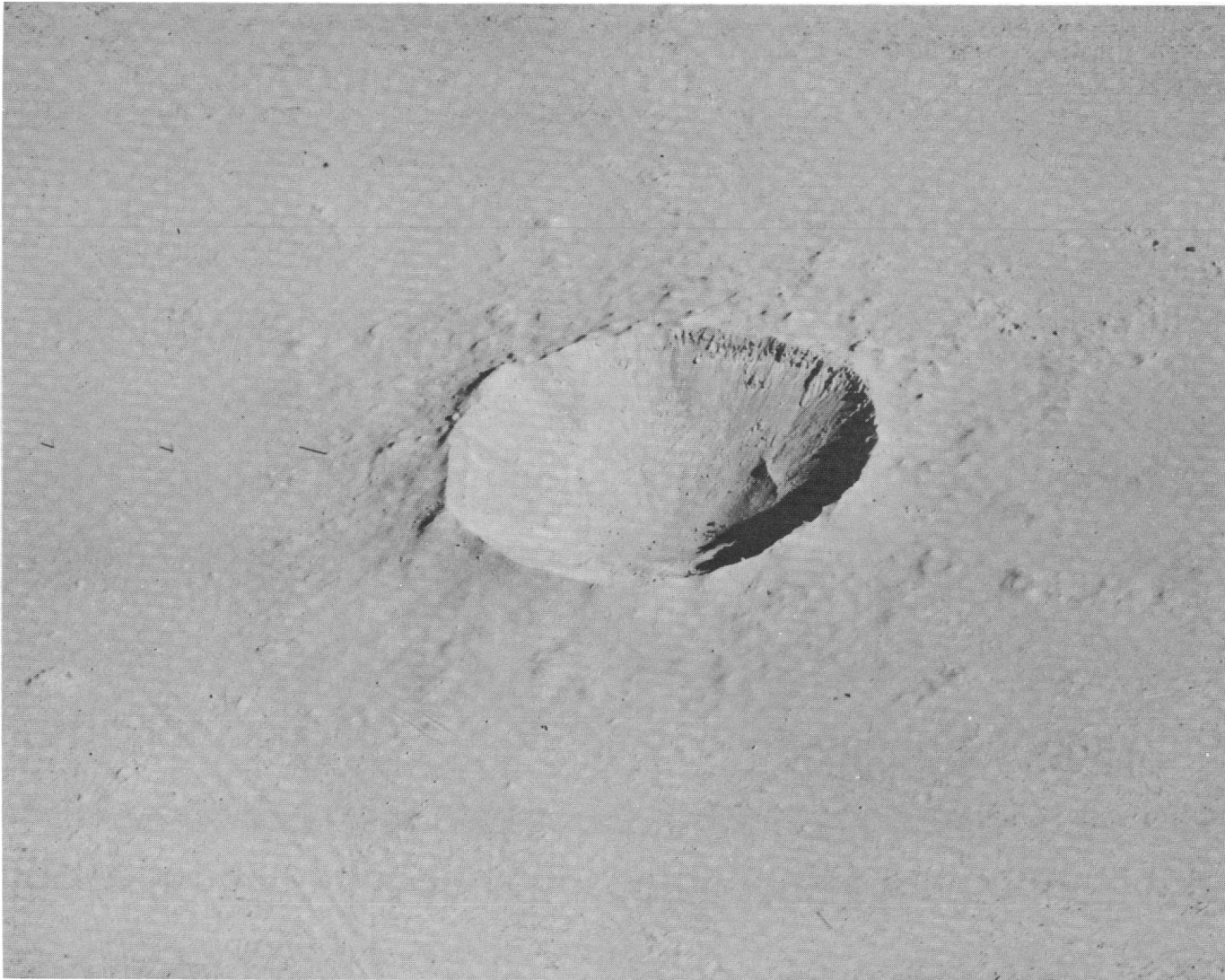
Fig. A.3 Crater from 20-ton charge buried at 17.1 feet.
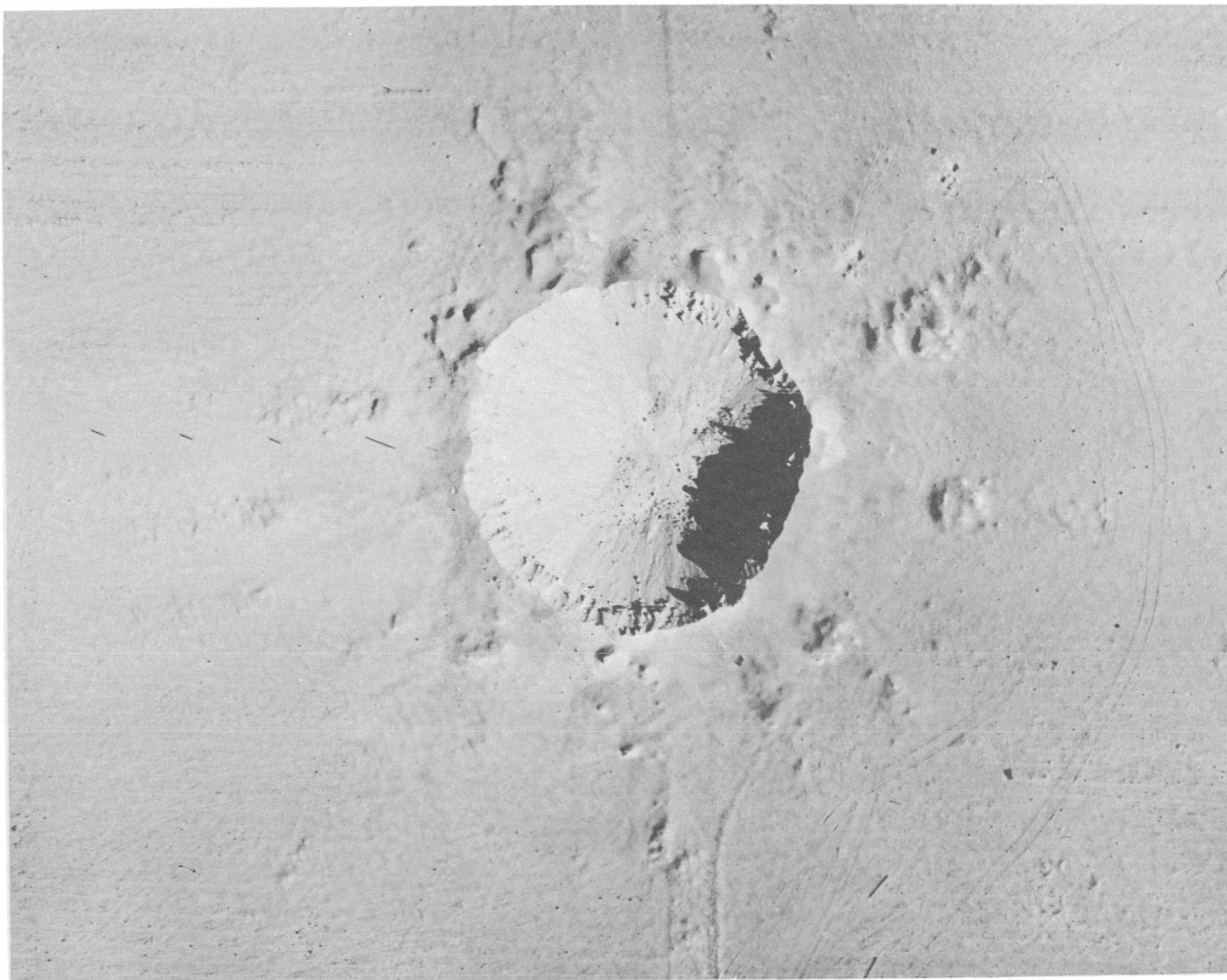
Fig. A.4 Crater from 20-ton charge buried at 34.2 feet.

Fig. A.5 Crater from 20-ton charge buried at 34.2 feet.

Fig. A.6 Crater from 20-ton charge buried at 80 feet.

Fig. A.7 Crater from 20-ton charge buried at 80 feet.
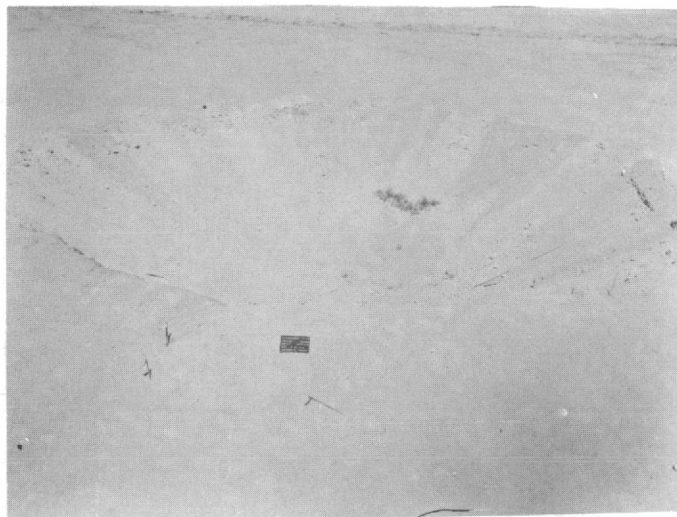
Fig. A.8 Crater from 20-ton charge
buried at 17.1 feet.
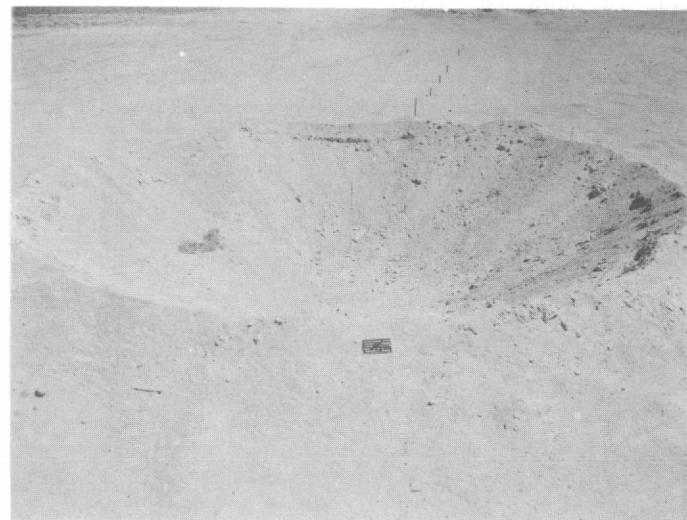
Fig. A.9 Crater from 20-ton charge
buried at 17.1 feet.
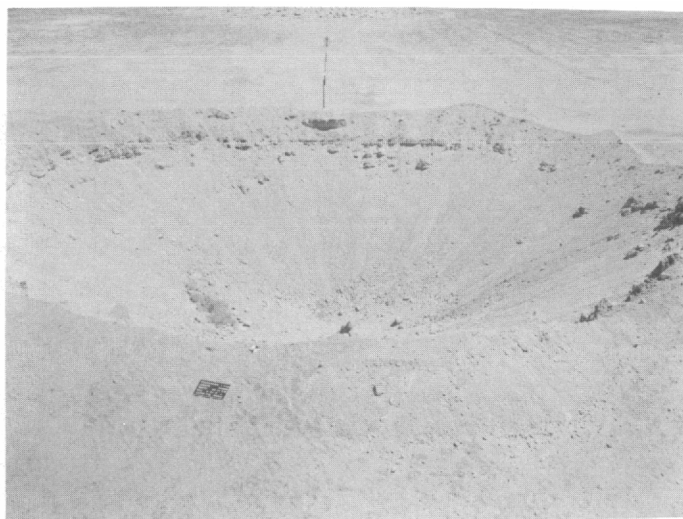
Fig. A.10 Crater from 20-ton charge
buried at 34.2 feet.

Fig. A.11 Crater from 20-ton charge
buried at 34.2 feet.
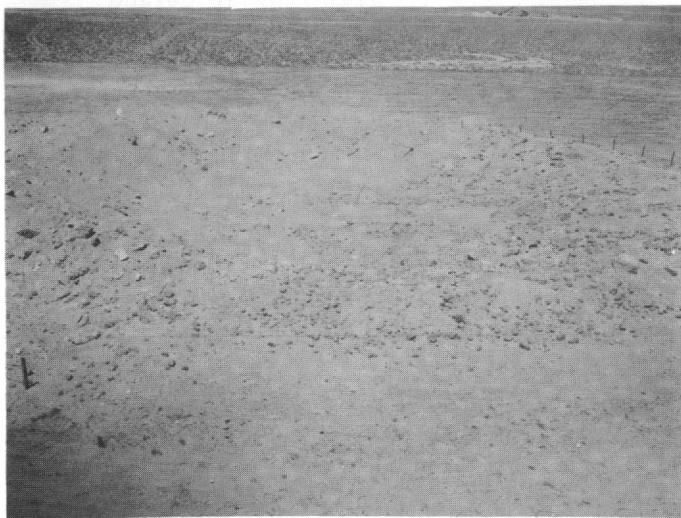
Fig. A.12 Crater from 20-ton charge
buried at 80 feet.

Fig. A.13 Crater from 20-ton charge
buried at 80 feet.
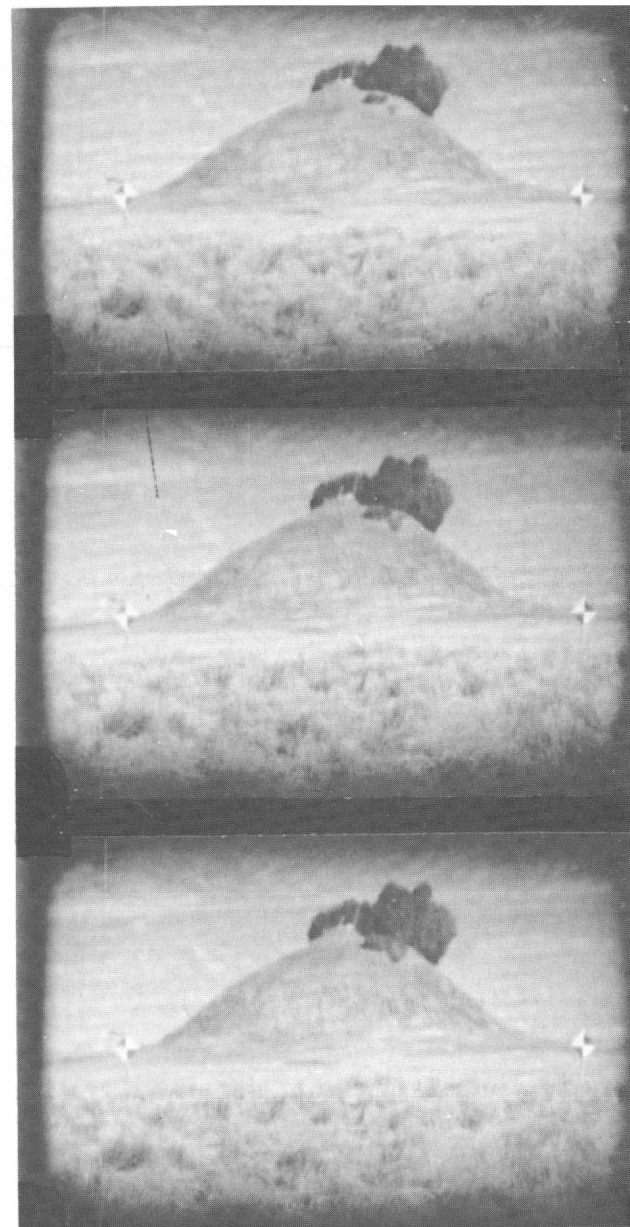
Fig. A.14 Motion picture sequence of the
Stagecoach shot buried at 80 feet.
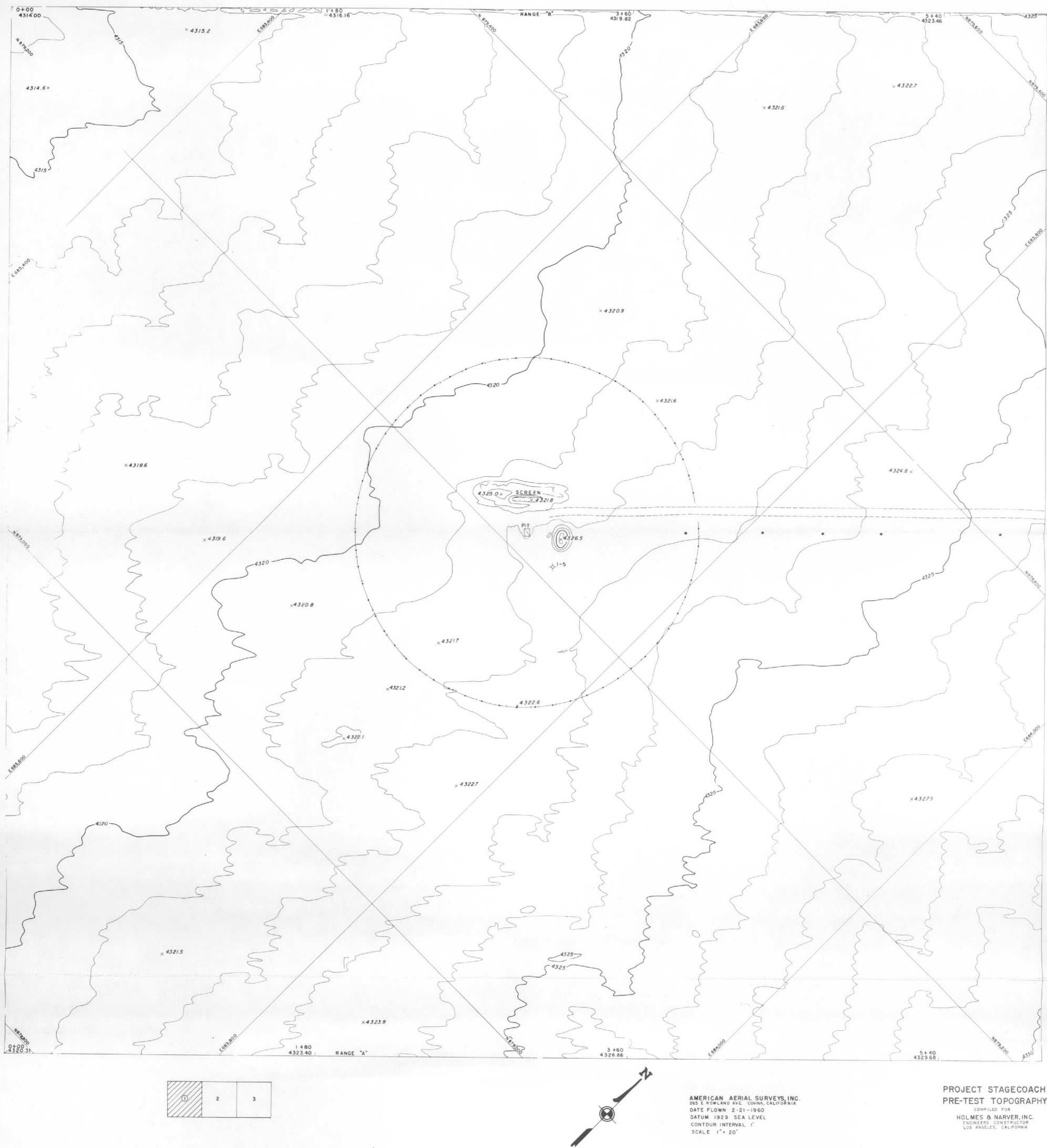
Fig. A.15   Preshot topography, Stagecoach charge at 17.1 feet.
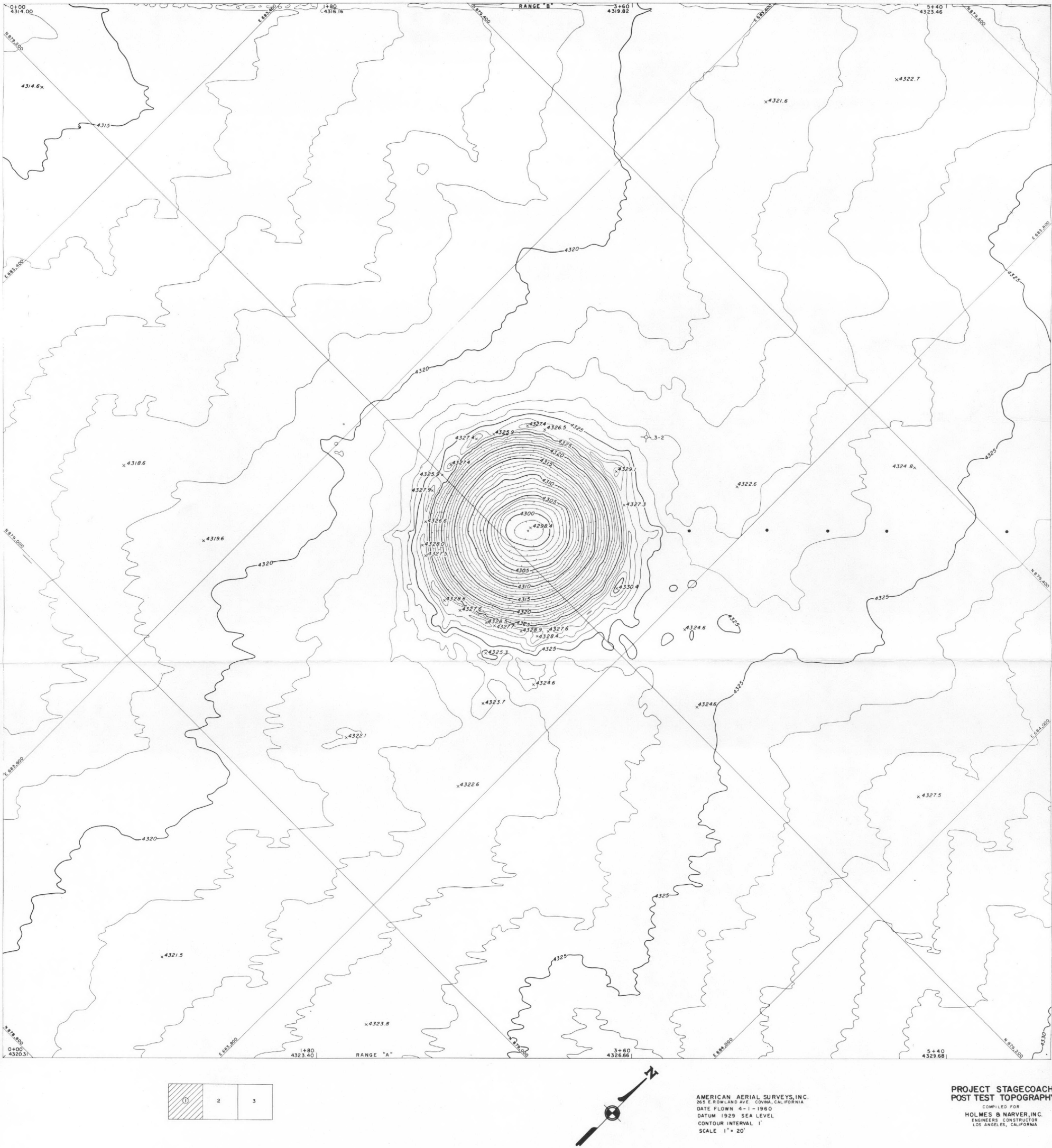
Fig. A.16 Postshot topography, Stagecoach charge at 17.1 feet.

Fig. A.17   Preshot topography, Stagecoach charge at 34.2 feet.

Fig. A.18 Postshot topography, Stagecoach charge at 34.2 feet.

Fig. A.19 Preshot topography, Stagecoach charge at 80 feet.
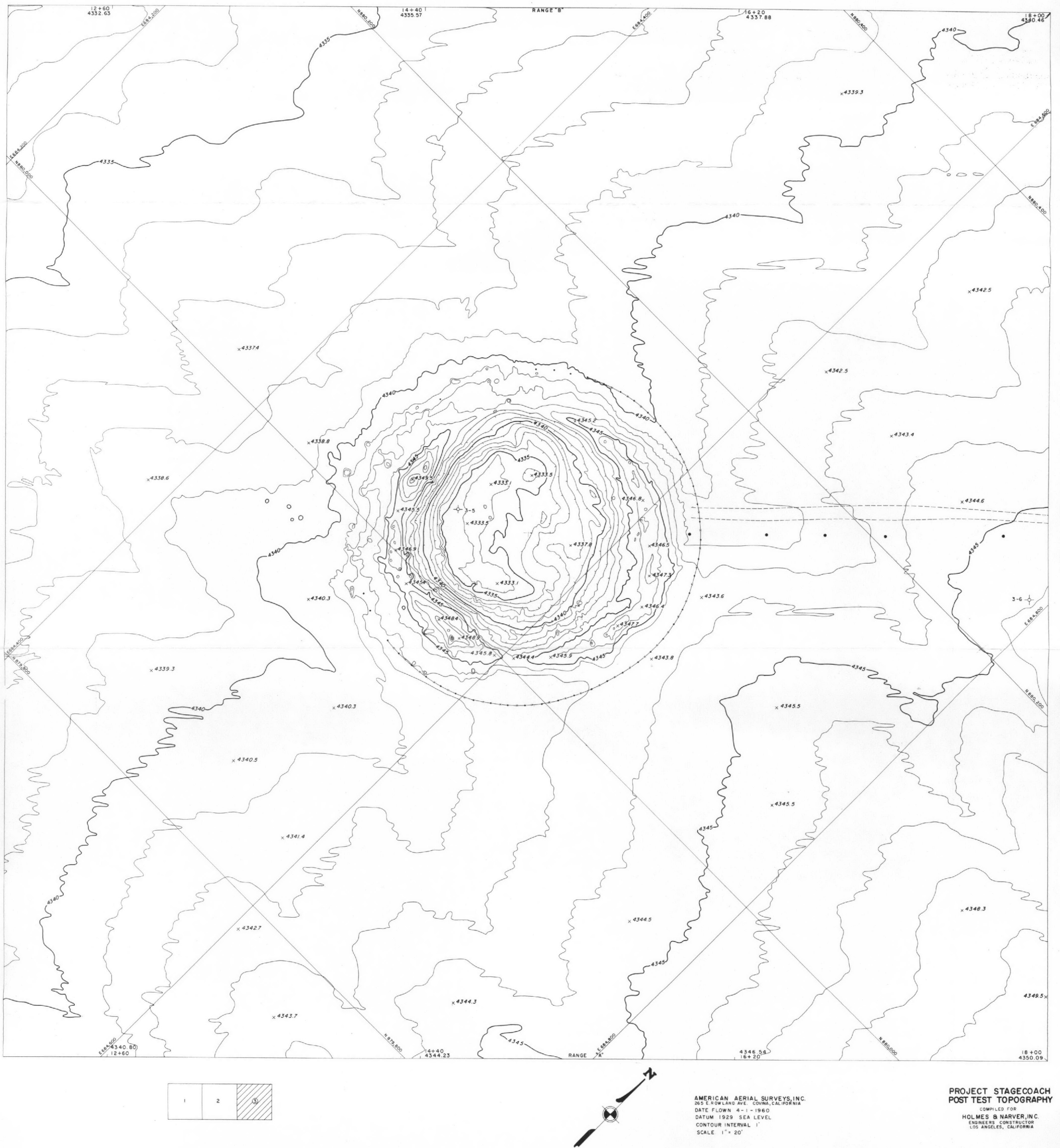
Fig. A.20 Postshot topography, Stagecoach charge at 80 feet.

Appendix B

WEATHER DATA by J. W. Reed

Condition: .1 altostratus   Stagecoach 80-foot shot
              .5 altocumulus   3/15/60   0900 PST
              .1 cirrus

Visibility: Unrestricted

Height (kft MSL)	Wind (deg/kts)	Pressure (mb)	Temperature (°C)	Relative humidity (%)	
4.330	300 ± 45/2 mph G16	875	÷5.3	34	
5.000	280/03	851	÷3.6	28	
6	310/10	821	÷1.8	26	Area 10 pilot balloon winds / Yucca Flat radiosonde data
7	330/16	791	-0.1	31	
8	330/25	762	÷1.5	29	
9	330/31	733	0.0	22	
10	330/30	705	-1.6	MSG	
15	325/46	580	-11.1	51	
20	330/74	474	-17.8	50	
25	330/68	385	-29.0	36	
30	330/60	309	-42.2	MSG	
35	330/60	245	-55.8	--	
40	330/78	192	-65.7	--	
45	310/39	150	-66.0	--	
50	300/51	117	-59.9	--	
55		92	-58.0	--	
60	295/40		-56.3		
70	325/15		-56.3		
80	Calm		-56.3		Tonopah rocket winds / ICAO Standard Temperatures
90	Calm		-49.0		
100	250/15		-39.9		
110	240/21		-30.8		
122	230/23		-19.8		
136	260/37		-7.3		
144	270/43		+0.6		
150	270/46		+5.8		
166	260/38		+9.7		
176	250/48		+7.1		

Sky condition: Clear   Stagecoach 17-foot shot
Visibility: Unrestricted   3/19/60   0800 PST

Height (kft MSL)	Wind (deg/kts)	Pressure (mb)	Temperature (°C)	Relative humidity (%)	
4.330	040 ± 15/10 mph ± 3.5	872	+12.4	24	
5.000	020/11	853	+11.4	25	
6	040/12	824	+10.6	24	Area 10 pilot balloon winds
7	070/11	793	+9.2	24	Yucca Flat radiosonde data
8	060/12	765	+6.5	25	
9	050/12	736	+4.0	27	
10	050/07	710	+3.2	21	
15	240/03	584	-7.3	MSG	
20	300/12	479	-18.7	--	
25	310/14	388	-30.6	--	
30	350/05	313	-42.6	--	
35	240/04	247	-55.6	--	
40	340/09	194	-61.0	--	
45	010/14	152	-61.0	--	
50	360/18	119	-62.6	--	
55	350/14	93	-62.4	--	
60	020/22	73	-62.8	--	

No rocket wind report

Sky condition: Clear
Visibility: Unrestricted

Stagecoach 34-foot shot
3/25/60   0800 PST

Height (kft MSL)	Wind (deg/kts)	Pressure (mb)	Temperature (°C)	Relative humidity (%)	
4.330	030 ± 25/8 mph ± 4	867	+14.2	35	
5.000	360/06	849	+12.9	25	
6	350/05	818	+11.8	24	Area 10 pilot balloon winds
7	350/04	788	+10.0	24	Yucca Flat radiosonde data
8	340/06	761	+8.8	25	
9	320/08	733	+6.1	27	
10	320/07	707	+3.6	30	
15	040/10	584	-8.2	37	
20	020/08	478	-18.3	MSG	
25	040/10	387	-31.3	--	
30	050/12	310	-43.7	--	
35	020/10	246	-55.8	--	
40	310/31	193	-62.6	--	
45	300/29	151	-60.0	--	
50	300/26	114	-62.0	--	
55	MSG	93	-63.0	--	
60	310/14	70	-61.8	--	
70	010/07	--	--	--	
80	Calm		-56.3		Tonopah rocket winds
90	Calm		-49.0		ICAO Standard Temperatures
100	Calm		-39.9		
107	210/8		-33.5		
113	270/21		-28.1		
116	270/21		-25.2		
124	280/34		-18.0		
140	270/34		-3.3		
149	260/42		+5.1		
150	270/55		+9.7		

Appendix C

THE AREA 10 MEDIUM by L. J. Vortman

Area 10, NTS, is part of an alluvial basin surrounded by mountains and comprises a wide variety of materials washed from the marginal slopes. Included are tertiary volcanics (rhyolite and tuff), limestone, dolomite, argillite, quartzite, conglomerate, and shale. The alluvial fans are a mixture of unassorted detritus from the surrounding mountains and are variable in size, composition, and cementation. In places this fill contains caliche deposits and fanglomerates.[1,2] The material is surface-water transported which results in interfingering thin sheets and interlacing tongues of material of different textures. Since the composition of the surrounding mountains determines the components of the alluvium, the components vary greatly from one place to another. Area 10 is a sufficiently small area that the variation throughout the region in which crater experiments have been carried out is relatively small.

Depth of the alluvium in Area 10 is from 600 to 1000 feet. Shoemaker[3] assigns the top 20 to 30 feet near Teapot Ess and Jangle U craters to recent deposits and deposits below this depth to the Pleistocene. Since deposition of the alluvium is a continuous process, it is difficult to conceive that the material in the two regions could differ except in so far as age may contribute to solidification and as the more humid climate of the Pleistocene may have altered the material or rate of deposition.

Wet densities from the surface to 16 feet at scattered locations in Area 10 show the following.[4]

Maximum	109.25	lb/ft^3
Average	99.5	lb/ft^3
Minimum	74.9	lb/ft^3

An early gradation analysis[5] gave the following 50-percent sizes for samples taken near the Stagecoach site.

Hole	Depth (ft)	50-percent size (in)
110	0 - 8	0.094
104	0 - 8	0.19
105	0 - 8.5	0.13

Seismic velocities for Area 10 were reported by Rugg:[5]

Depth from surface (ft)	Seismic velocity (ft/sec)
0 - 100	3000
100 - 350	4000 - 4500
350 - 500	5000 - 5500

Two 4-inch-diameter soil borings were made in the process of site selection.* The results were as shown in Table C.1.

Hole 1 was located midway between Stagecoach Stations 1003.01 and 1003.02, and hole 2 midway between Stations 1003.02 and 1003.03. Hole 1 was more moist throughout than hole 2, and both holes showed increasing density with depth. No tests after these two indicate a consistent trend with depth. The investigation indicated an ultimate angle of internal friction of between 38 and 43 degrees, and a coefficient of cohesion of zero. Gradation analysis of three samples is shown in Fig. C.1.

Soil density and water content were measured as the charge holes were excavated (Table C.2). There is no conclusive trend toward increasing density with depth as in the case of the exploratory holes. Although exploratory hole 1 was more moist than hole 2, a similar trend in Stations 1003.02 and 1003.03 which were adjacent to hole 1 is obscured by the contribution of rain and show at both stations. Average wet density is about 110 lb/ft^3.

Density and moisture content of the backfill were also obtained (Table (C.3).

*Ltr., Nevada Testing Laboratories, Ltd., to Holmes and Narver, Inc., dated November 6, 1959. Subject: Soil Borings for Crater Experiment Area 10, Nevada Test Site Laboratory No. 402.

Postshot, the deep shot showed a distinct difference in throwout from the two shallower shots. Instead of only fine materials and rocks, there was in addition a large number of blocks of relatively undisturbed soil. Table C.4 gives results of measurements made on material in the crater lip of the three shots. The loose material from the shot at 34.2 feet had a dry density below that of the other two shots. An unexpected result, however, was that the dry density from solid blocks from the deep shot was less than that from the loose material which, presumably, in situ had been the same as the material in the blocks. To be certain results were not due to error, additional measurements were obtained from the crater lip (Tables C.5 and C.6). The additional measurements confirmed that dry density of the block was less than that for the loose material, although both were lower than the earlier measurements. In an effort to better understand why this was so, additional observations were made on July 8, 1960. The blocks came from cemented fine sands and silts which occurred in alternating layers of cohesionless medium gravels and sands. Four laboratory tests were made from samples of both types:

1. Gradation analysis (Fig. C.2) showed a wide spread between the two types of soil, with the solid blocks showing a much higher percentage of fine material than indicated by earlier exploratory tests (Fig. C.1).

2. Maximum and minimum density determinations show that cemented soils have higher maximum density (Fig. C.3) and lower minimum density characteristics than loose soil (Fig. C.4), indicating better compaction characteristics for the compacted soil. (See Table C.7.)

3. In-place densities were determined on an undisturbed block sample of cemented fine sands and silts by use of the displacement method. (Table C.8.) The results of in-place density tests can be expected to vary from test to test because of varying amounts of gravel encountered at each test location.

4. Relative densities of both types of soil as found in the field were determined by use of maximum and minimum density relationships and the formula:

$$DR = \left(\frac{\frac{1}{WL} - \frac{1}{WF}}{\frac{1}{WL} - \frac{1}{WD}} \right) 100 \ ,$$

where   DR = relative density (unit dry weight) percent

WL = minimum dry unit weight (lbs/ft^3)

WD = maximum dry unit weight (lbs/ft^3)

WF = field dry unit weight (lbs/ft^3)

Relative density determinations indicate that cemented fine grained soils are in a denser state than uncemented gravelly soils.

Supplementing the above information are records of the excavation of the shafts. These are summarized in Figs. C.5, C.6, and C.7 and are subjective in that they are not the result of physical measurements, but are observations of the mining foreman and represent his judgment of the relative hardness of the material. Only the caliche layer between 5 and 10 feet is consistent in all three. A very hard band surrounded by medium hard material in the vicinity of 30 to 35 feet appears in two of the logs.

REFERENCES

1. Johnson, M. S., and Hibbard, D. E., A Geological Survey of the Atomic Energy Commission Area, Nye County, Nevada, WT-518, Armed Forces Special Weapons Project, April 1953.

2. Johnson, M. S., and Hibbard, D. E., Geology of the Atomic Energy Commission, Nevada Proving Ground Area, Nevada, U. S. Geological Survey Bulletin 1021-K, 1957.

3. Shoemaker, E. M., Penetration Mechanics of High Velocity Meteorites, Illustrated by Meteor Crater, Arizona. Report of the International Geological Congress, XXI Session, Norden, 1960, Part XVIII, Structure of the Earth's Crust and Deformation of Rocks, Copenhagen, 1960.

4. Piper, A. M., Geologic, Hydrologic, and Thermal Features of the Sites, WT-343, United States Geological Survey, May 1952.

5. Rugg, A. M., Seismic Refraction Survey for Nye County, Nevada, WT-327, United Geophysics Co., Inc., July 27, 1951.

TABLE C.1   RESULTS OF EXPLORATORY SOIL BORING

Hole	Depth (ft)	Wet density (lbs/ft^3)	Dry density (lbs/ft^3)	Moisture content (percent)
1	17	111.5	103.8	7.4
1	34	118.2	109.7	7.9
2	17	113.1	106.2	6.3
2	34	124.2	117.0	6.2
2	58	130	122.3	6.8

TABLE C.2   RESULTS OF SOIL TESTS OBTAINED FROM CHARGE HOLES

Station	Depth (ft)	Wet density (lbs/ft^3)	Dry density (lbs/ft^3)	Moisture content (percent)
1003.01 80-foot depth	2.3	112.9	106.0	6.7
	8.5	102.0	93.0	9.5
	17.1	102.3	98.1	4.8
	25.5	101.0	93.5	8.0
	31.3	103.0	97.5	5.8
	34.2	120.0	113.2	5.95
	46.1	103.2	98.6	5.0
	58	117.0	113.0	3.56
	80	102.5	97.2	5.5
1003.02 34.2-foot depth	2.0	116.0	109.0	6.0
	8.5	103.5	95.0	8.95
	17.0	114.8*	106.3	8.00*
	25.0	103.0	96.0	7.00
	25.0	103.3	99.5	4.7
1003.03 17.1-foot depth	2.0	106*	93.2	13.46*
	8.5	118	109	8.2*
	17.1	104.0	97	8

*Sample wet due to snow and rain.

TABLE C.3 RESULTS OF SOIL TESTS IN BACKFILL

Station	Depth (ft)	Wet density (lbs/ft^3)	Dry density (lbs/ft^3)	Moisture content (percent)
1003.01	69.5	116.7	107.1	9.0
80-foot depth	67.0	109.3	103.0	5.5
	63.0	115.9	105.1	10.0
	51.0	116.3	108.3	7.4
	48.5	113.1	103.7	9.1
	42.5	106.0	98.8	7.3
	38.0	110.0	99.5	10.6
	27.0	113.1	104.3	8.4
	7.0	112.3	105.4	6.4
	0.0	107.0	101.0	5.9
1003.02	21.5	107.0	101.0	6.1
34.2-foot depth	17.0	98.0	91.0	6.9
	8.5	107.0	99.2	7.9
	2.0	108.0	102.0	5.8
1003.03	4.0	107.0	102.0	4.3
17.1-foot depth	0.0	104.0	101.0	2.8

TABLE C.4 RESULTS OF SOIL TESTS ON CRATER LIP

Station	Azimuth (degrees)	Type of material	Wet density (lb/ft^3)	Dry density (lb/ft^3)	Moisture content (percent)
1003.01	180	Solid block	99.5	94.5	5.4
80-foot depth	180	Loose soil	99.7	95.0	4.9
		(at base of above)			
	180	Loose soil	110.7	106.5	3.9
	45	Loose soil	114.6	112.0	2.3
	45	Solid block	104.1	97.7	6.5
	225	Loose soil	114.2	109.8	4.04
	225	Solid block	104.0	99.4	4.8
1003.02	30	Loose soil	100.2	95.2	5.3
34.2-foot depth	150	Loose soil	104.0	97.6	6.6
	270	Loose soil	98.2	91.9	6.8
1003.03,	120	Loose soil	104	100	4.07
17.1-foot depth	240	Loose soil	110	106	3.8
	360	Loose soil	122.4	119	2.9

TABLE C.5   RESULTS OF ADDITIONAL SOIL TESTS ON CRATER LIP[*]

Station	Azimuth (degrees)	Type of material	Wet density (lb/ft^3)	Dry density (lb/ft^3)	Moisture content (percent)
1003.01a 80-foot depth	45 90	Solid block Loose soil	95 102.6	90.6 98.9	5 4
1003.02a 34.2-foot depth	150	Loose soil	94.3	89.0	6
1003.03a 17.1-foot depth	240	Loose soil	97.6	93.1	5

[*]Date of tests, May 1960.

TABLE C.6   RESULTS OF ADDITIONAL SOIL TESTS ON CRATER LIP[*]

Station	Azimuth (degrees)	Type of material	Wet density (lb/ft^3)	Dry density (lb/ft^3)	Moisture content (percent)
1003.01, 80-foot depth	45 90	Block Loose soil	81.5 103	76.4 97.1	6.6 6.0
1003.02 34.2-foot depth	150	Loose soil	121.5	113.1	7.5
1003.03 17.1-foot depth	240	Loose soil	111.7	104.9	6.5

[*]Date of tests, June 15, 1960.

TABLE C.7   DENSITY DETERMINATIONS

	Loose gravel and sand (lb/ft^3)	Compacted fine sand and silt (lb/ft^3)
Minimum dry density	91.6	78.7
Maximum dry density	109.3	113.0

TABLE C.8 IN-PLACE DENSITY AND RELATIVE DENSITY DETERMINATIONS

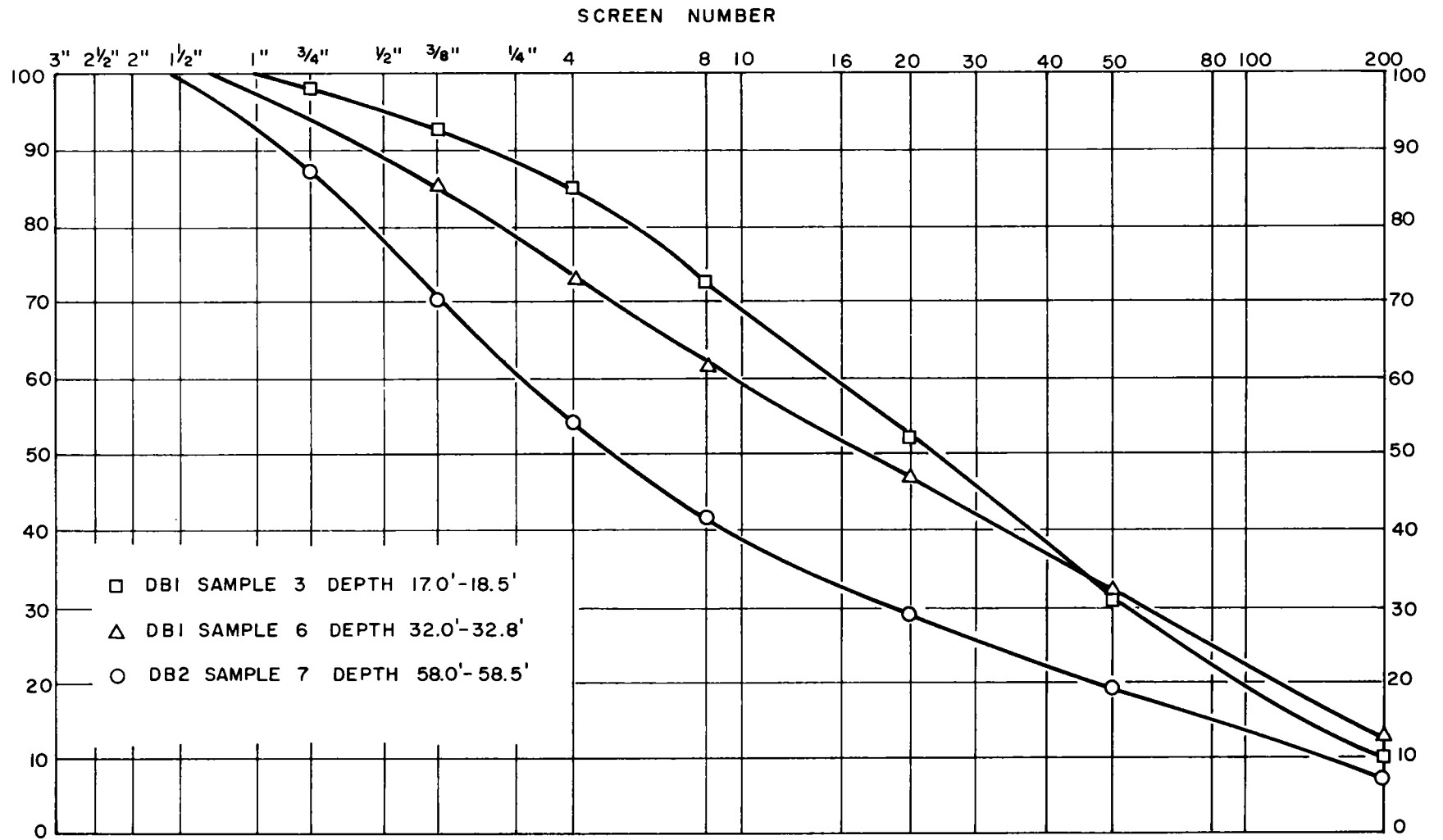| Type soil	determination	Dry density (lb/ft^3)	Moisture content (percent)	Relative density (percent)
Cemented brown fine sand and silt	Sand cone	94.7	1.2	56
Loose tan gravel and sand	Sand cone	97.6	2.5	37
Cemented brown fine sand and silt	Displacement	100.4	2.1	72

Fig. C.1 Aggregate chart.

SCREEN NUMBER

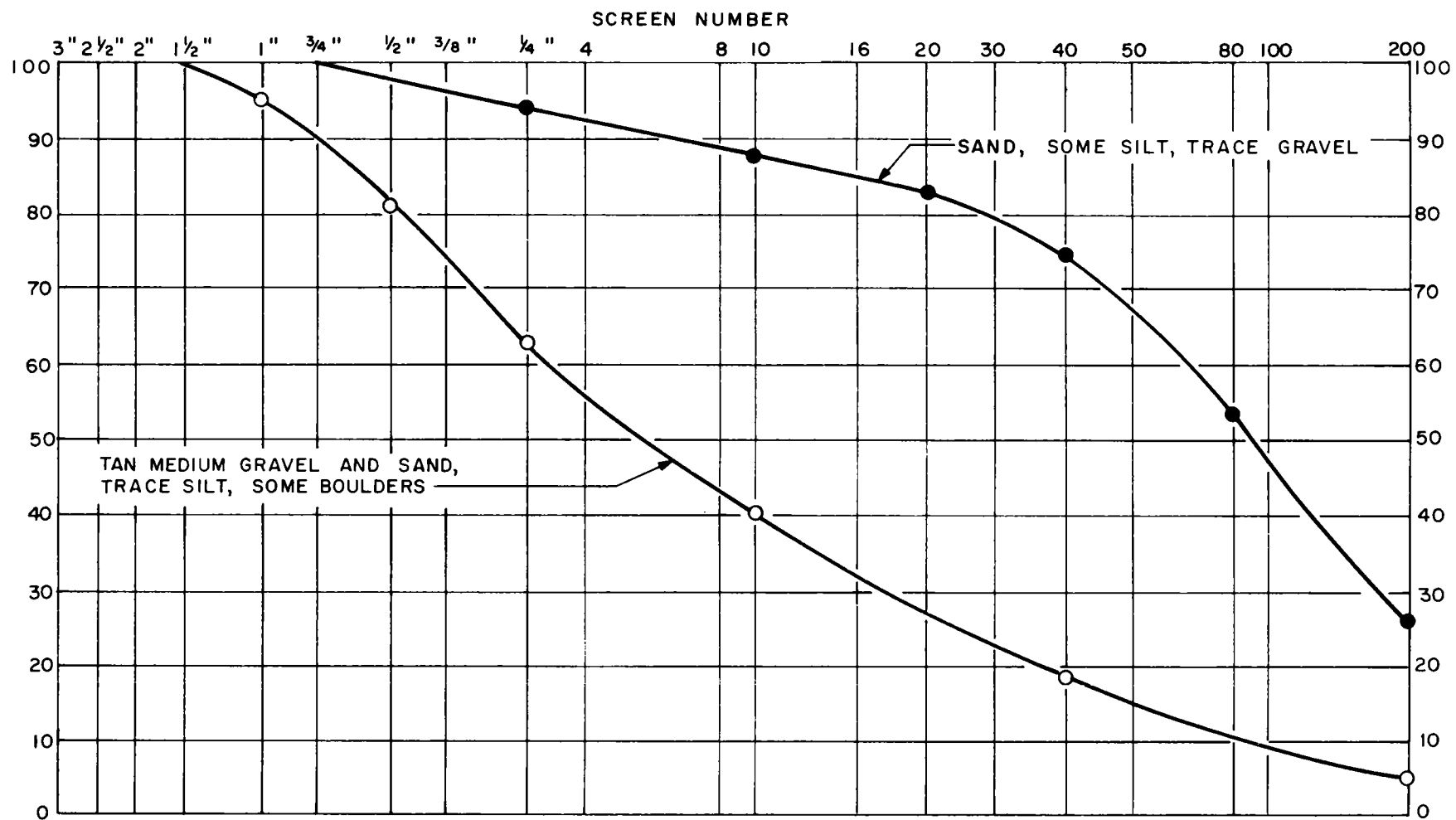
Fig. C.2 Aggregate chart.
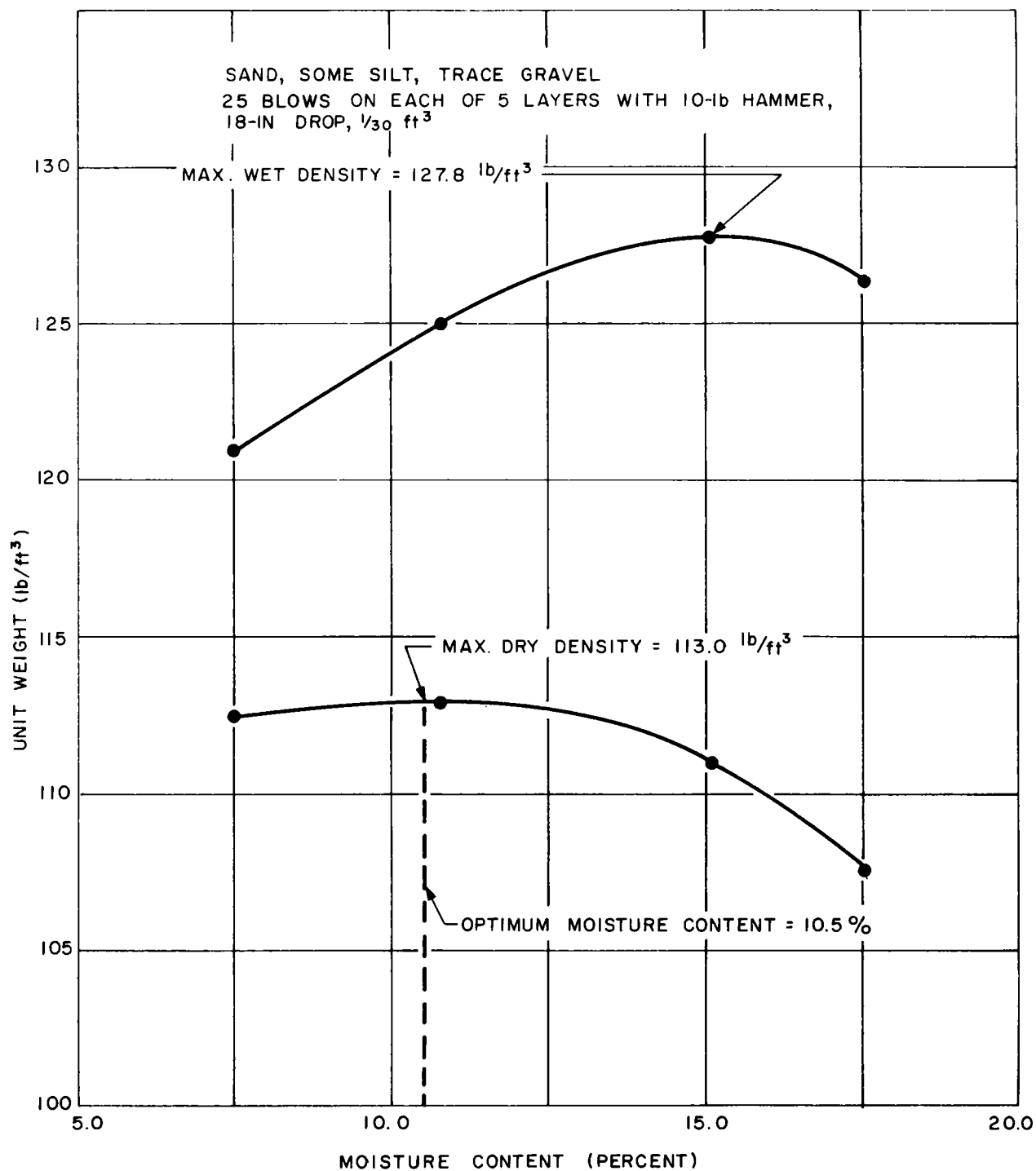
Fig. C.3 Moisture density curve.

Fig. C.4 Moisture density curve.

RELATIVE HARDNESS

COMPOSITION

DEPTH BELOW SURFACE (FEET)

0

5 — ROCK, SAND

CALICHE

10

ROCK, SAND, CLAY

15

SAND, CLAY

20

ROCK, SAND, CLAY

25

ROCK, SAND

30

CALICHE
SAND, BOULDERS

35 — ROCK, SAND

ROCK, SAND, CLAY

40

CALICHE
SAND, GRAVEL

45 — SAND, CLAY

50

NO
DATA

55

60

65 — ROCK, SAND

ROCK, SAND, CLAY

70 — SAND, BOULDERS

ROCK, SAND, CLAY
GRAVEL, SAND
75 — ROCK, SAND, CLAY
SAND, CLAY

80 — ROCK, SAND, CLAY

CALICHE
ROCK, SAND, CLAY
SAND
85

STAGECOACH

CHARGE DEPTH:
80 FEET

HOLE I

| | NO COMPACTION |
| VERY SOFT |
| SOFT |
| MEDIUM |
| MEDIUM HARD |
| VERY HARD |
| BROKEN ROCK |
| SAND |
| CALICHE |
| GRAVEL |
| LARGE BOULDERS |
| CLAY |
| AGGREGATE |

Fig. C.5 Shaft excavation record.

RELATIVE
HARDNESS

COMPOSITION

NO
COMPACTION

VERY
SOFT

SOFT

MEDIUM

MEDIUM
HARD

VERY
HARD

BROKEN
ROCK

SAND

CALICHE

GRAVEL

LARGE
BOULDERS

CLAY

AGGREGATE

0

5

10

15

20

25

30

35

40

45

50

55

60

65

70

75

80

85

SAND, CLAY

AGGREGATE

CALICHE
SAND, ROCK

ROCK, SAND, CLAY

ROCK, SAND

CLAY

ROCK, SAND

CLAY

ROCK, SAND

SAND, GRAVEL

ROCK, SAND, CLAY
ROCK, SAND

ROCK, SAND, CLAY

ROCK, SAND

ROCK, SAND, CLAY

STAGECOACH
CHARGE DEPTH:
34 FEET

HOLE 2
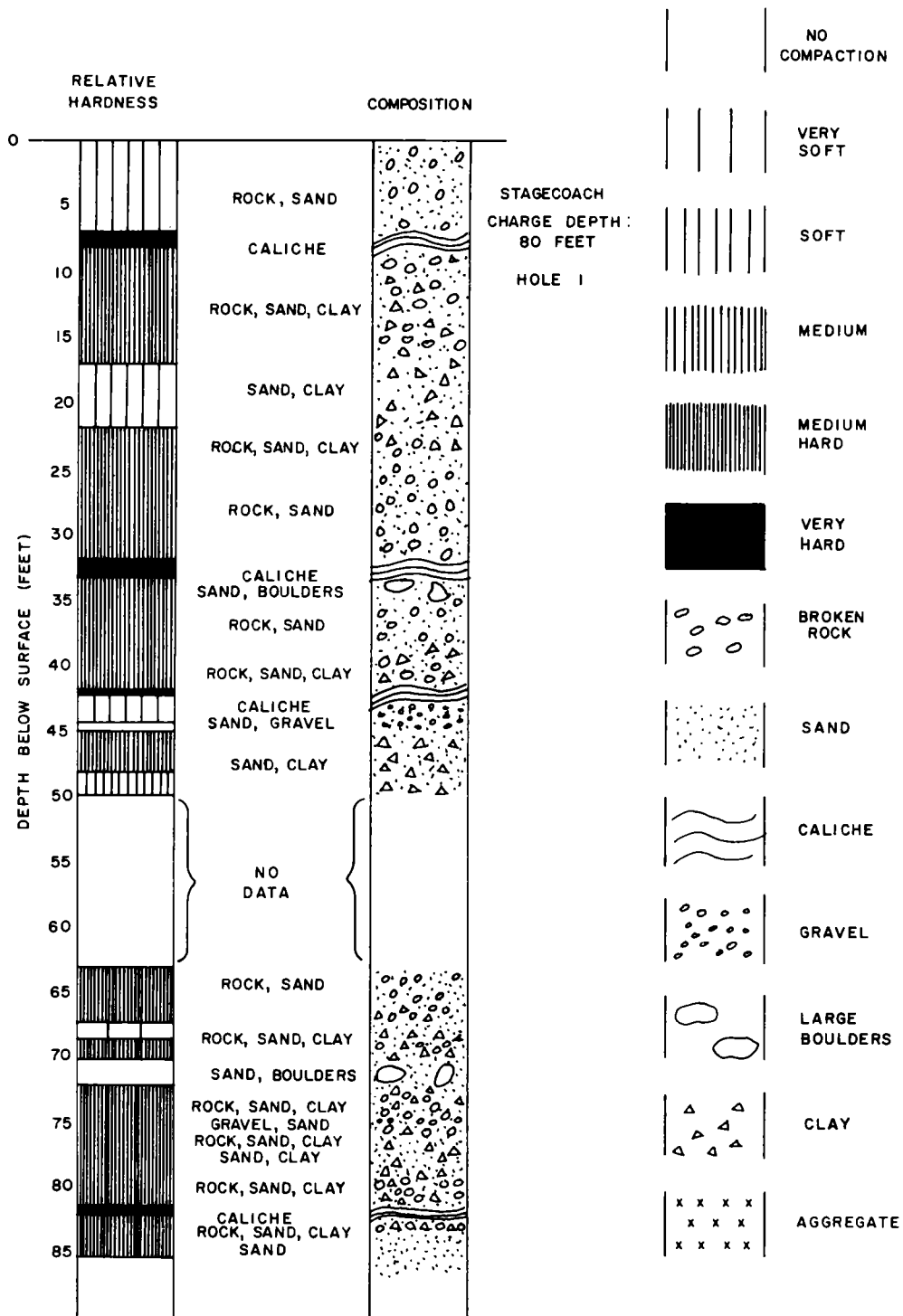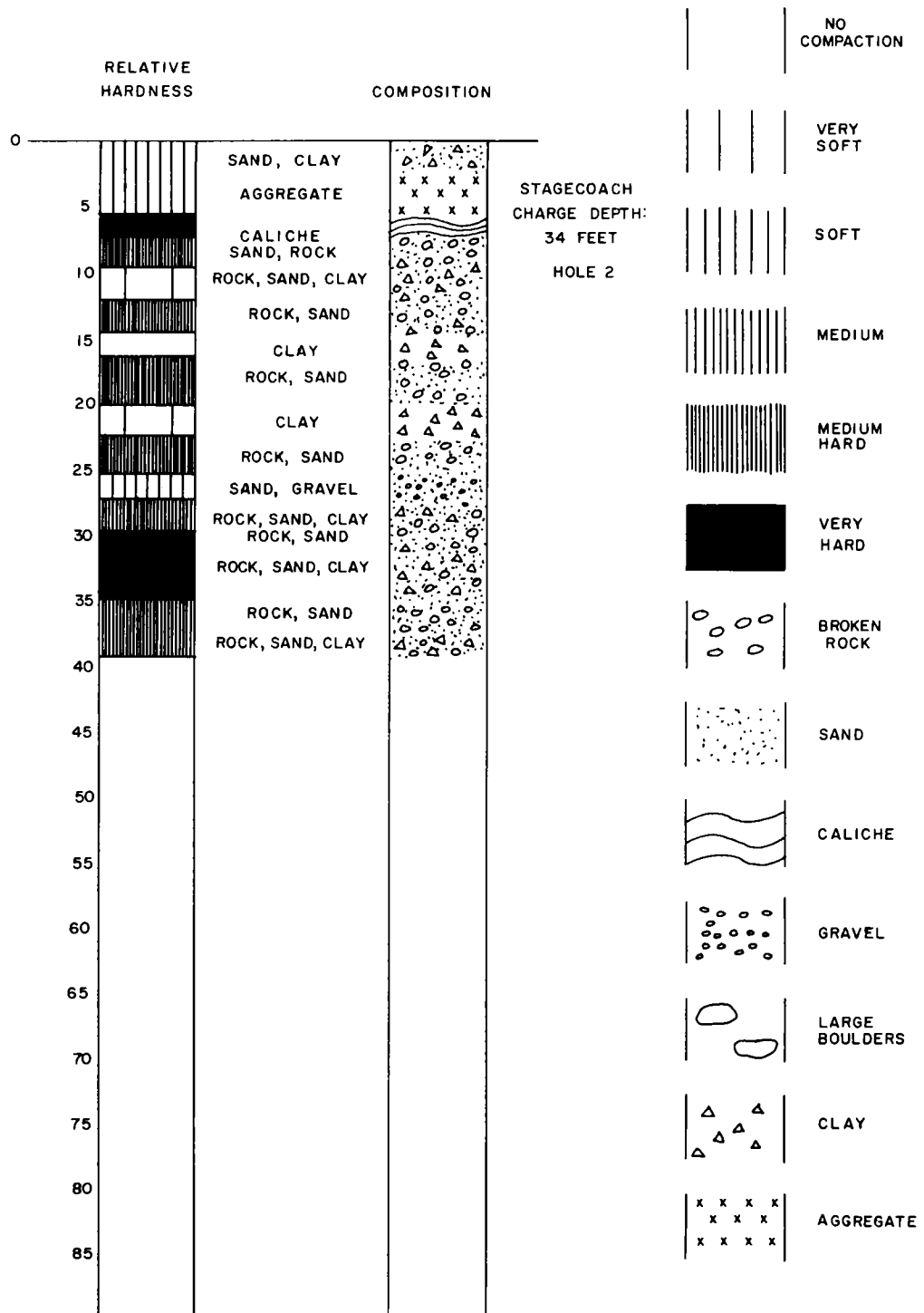
Fig. C.6   Shaft excavation record.
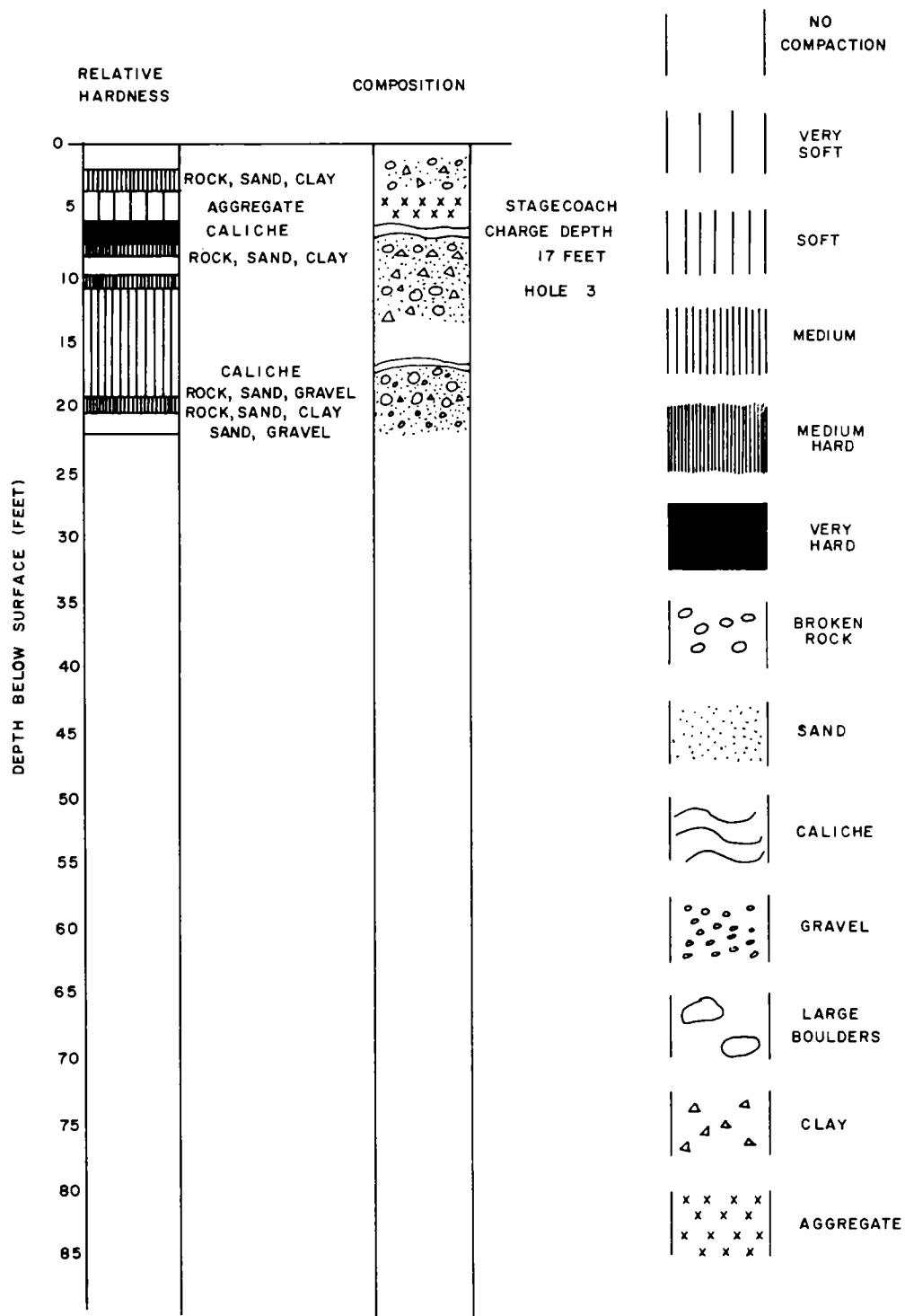
Fig. C.7 Shaft excavation record.

Brig. Gen A. W. Betts, AEC/Division of Military
Application
J. S. Kelly, AEC/DPNE (3)
Richard Hamburger, AEC/DPNE
William Oakley, AEC/DPNE
G. M. Dunning, AEC/DOS
L. A. Woodruff/H. E. Kendrick, AEC/LVB
K. F. Hertford, Mgr., ALO
P. W. Ager, ALO
D. W. King, ALO (2)
J. E. Reeves, NOO
R. E. Miller, NOO
R. F. Beers, NOO Consultant
P. Byerly, NOO Consultant
G. B. Maxey, NOO Consultant
T. F. Thompson, NOO Consultant
E. C. Shute, USAEC, San Francisco Operations Office,
211 Bancroft Way, Berkeley 4, Calif. (SAN)
Russell Ball, SAN
John Philip, SAN
Rodney Southwick, SAN
John Rinehardt, Colorado School of Mines,
Golden, Colo.
F. L. Smith, Colorado School of Mines,
Golden, Colo.
E. M. Purcell, Harvard University, Cambridge, Mass.
Charles W. Martin, 201 T and AM Lab, Iowa
State University, Ames, Iowa
Robert V. Whitman, MIT, Cambridge, Mass.
N. M. Newmark, University of Illinois, Urbana, III.
M. A. Cook, Explosives Research Group, Univ. of Utah
Ralph B. Baldwin, 1745 Alexander Rd. SE, East Grand
Rapids, Mich.
J. J. Gilvarray, Research Laboratories, Allis-
Chalmers Manufacturing Co., Milwaukee, Wis.
R. H. Carlson, Applied Physics Section, Mail Stop
21-31, Aerospace Division, Boeing Airplane Co.,
Seattle 24, Wash.
C. W. Lampson, BRL
B. Perkins, Jr., BRL
J. J. Meszaros, BRL
J. G. Lewis/J. Kelso, HQ/DASA
P. Holdsworth, Commissioner, Dept. of Natural
Resources, Box 1391, Juneau, Alaska
A. W. Patterson, Engineering Research and
Development Laboratory, Nuclear Power Branch,
Fort Belvoir, Va.
J. C. Mark, LASL
A. C. Graves, LASL
J. S. Foster/D. Sewell, LRL, Livermore
G. H. Higgins, LRL, Livermore (10)
M. D. Nordyke, LRL, Livermore
P. L. Randolph, LRL, Livermore
A. V. Shelton, LRL, Livermore
J. A. Berry, NOL
J. F. Moulton, NOL
L. Rudlin, NOL
M. Diamond, WSMR
F. B. Slichter, Office of the Chief of Engineers,
Washington 25, D. C. (OCE)
L. Machta, USWB, Washington
P. W. Allen, USWBRS/AEC-LVAO
G. B. Olmsted, AFTAC
W. H. Booth, OCE, Washington 25, D. C.
R. R. Philippe, OCE, Gravelly Point, Va.
M. D. Kirkpatrick, OCE, Gravelly Point, Va.
W. E. Clark, Oak Ridge National Laboratory
R. E. Grubaugh, E. H. Plesset Assoc. Inc., 1281
Westwood Blvd., Los Angeles 24, Calif.
D. T. Griggs, RAND Corp., 1700 Main Street,
Santa Monica, Calif.

R. B. Vaile, Jr., SRI, Menlo Park, Calif.
Chief Superintendent, Suffield Experimental Station,
Ralston, Alberta, Canada; Attn: G. H. S. Jones
W. K. Cloud, U. S. Coast and Geodetic Survey, San
Francisco Dist. Office, New Mint Bldg., San
Francisco, Calif.
L. M. Murphy, U. S. Coast and Geodetic Survey, San
Francisco Dist. Office, New Mint Bldg., San
Francisco, Calif.
L. Obert/W. E. Duvall/T. C. Atchison, U. S. Bureau
of Mines, Applied Physics Research Laboratory,
College Park, Md.
W. K. Boyd, Chief, Frozen Ground Applied Research
Branch; Snow, Ice, and Permafrost Research
Establishment, U. S. Corps of Engineers, 823
Emerson St., Evanston, Ill.
L. R. Page/A. Brown, USGS, Room 1033, GSA Bldg.,
Washington 25, D. C.
E. M. Shoemaker, USGS, 4 Homewood Place, Menlo Park,
Calif.
F. Byers, USGS, Denver Federal Center, Denver, Colo.
C. F. Romney, HQ/USAF, Air Force Technical Applica-
tions Center, Washington 25, D. C.
F. R. Brown, Waterways Experiment Station, P. O. Box
631, Vicksburg, Miss. (WES)
John Strange, WES, Vicksburg, Miss.
TID-4500 (16th Ed.), UC-35 (503 copies)
S. P. Schwartz, 1
R. W. Henderson, 100
A. B. Machen, 2300
G. C. Dacey, 5000
R. S. Claassen, 5100
T. B. Cook, 5110
C. R. Mehl, 5111
M. L. Merritt, 5112 (10)
L. J. Vortman, 5112
A. J. Chabai, 5112
D. M. Hankins, 5112
C. D. Broyles, 5113
J. D. Shreve, 5114
J. W. Reed, 5114
F. W. Nielson, 5130
B. F. Murphey, 5132
F. P. Hudson, 5150
J. W. Easley, 5300
M. J. Norris, 5420
R. M. Betz, 6010
G. A. Fowler, 7000
D. B. Shuster, 7200
W. T. Moffat, 7240
B. C. Benjamin, 7241
J. C. Eckart, 7250
R. J. Burton, 7254
V. A. Harris, 7254
J. R. Heaston, 7254
G. P. Stobie, 7255
C. L. Gomel, 7256
L. E. Lamkin, 7500
W. J. Howard, 8100
L. E. Hollingsworth, 8120
H. R. MacDougall, 8133
W. A. Jamieson, 8233
Mrs. B. R. Allen, 3421-1
Mrs. M. G. Randle, 3421-2
R. K. Smeltzer, 3421-3
W. F. Carstens, 3423, Attn: J. M. Zanetti, 3423-1
G. R. Miller, 3423-1
R. C. Smelich, 3466-1 (5)